REAL-TIME OBSERVATION AND ANALYSIS OF COHERENCE AND ALIGNMENT IN MOLECULAR SYSTEMS:
ISOLATED MOLECULES AND CHEMICAL REACTIONS

Thesis by
John Spencer Baskin

In Partial Fulfillment of the Requirements
for the Degree of
Doctor of Philosophy

California Institute of Technology
Pasadena, California

1990
(Submitted September 28, 1989)

ACKNOWLEDGMENTS

It is a pleasure to acknowledge first and foremost my faculty advisor, Professor Ahmed Zewail, for affording me the rare opportunity of collaborating on many interesting and exciting scientific projects as a member of his research group. His ideas and direction are heavily imprinted on all the work described in this thesis. I thank him for his encouragement, and for the understanding he has exhibited on the many occasions during my tenure at Caltech that I have failed to meet the challenges and opportunities presented. I acknowledge him also, in conjunction with the National Science Foundation (Grant DMR-8521191), for the financial support which has made it possible for me to be here. I owe thanks also to the ARCS Foundation for additional financial support provided in the form of an ARCS fellowship awarded for the academic year 1984-85.

Among the many members of the Zewail group whom I have worked beside through the years, I wish to thank in particular: Peter Felker and David Semmes for introducing me to the nuts and bolts and joys of laser spectroscopy in 036 Noyes and for later collaborations; and Isaac Xavier for his generous help and patience in initiating me to various other aspects of experimental research. Though I have never met Bill Lambert, I feel I also owe him a fundamental debt of gratitude for his role in the construction of 036, which has proved an excellent and versatile laboratory for time-resolved spectroscopy.

I must also acknowledge the role of many members of the Chemistry and Applied Physics staff who in one way or another have worked to make possible the research described in this thesis. Without intending to minimize the contributions of others too numerous to list by name, I would like to give special mention to a few people who have been particularly instrumental. I thank Tom Dunn for the frequent application of his expertise to repair equipment essential to the operation of our laboratory. Tina Wood must receive credit for a great deal of typing and revising of manuscripts over the past two years, including that done in the preparation of one section of this thesis. For rendering the

preparation of the remainder of the thesis as pleasant as I suppose it is possible for such a thing to be, I thank Dave Malerba, who has been responsible for maintaining the Chemistry Division computing (and word processing) facilities at peak performance as well as in high spirits through a critical period.

My general acknowledgement goes to my parents, my brothers and their families, other family members and friends. Their influence has shaped the course of my career in many and subtle ways. Again, it is impractical to make an exhaustive list, but I think it is safe to say that without the specific encouragement, motivation and cajoling provided by three people, it is most unlikely that I would have pursued the course that has brought me, by many twists and turns, to this present culmination. These people are my brother Leland Baskin, presently of Waxahachie, Texas, Professor Jim Tanner of the Georgia Institute of Technology, Atlanta, Georgia, and Susan Cone of Decatur, Georgia. Each of them has swayed me at certain junctures of my life to consider options that I might otherwise have overlooked. If my work here has been of value, or if the foundation laid shall enable me to perform valuable services in the future, a large measure of credit must go to them.

I dedicate this thesis to my students and colleagues
at the Institut Kizito, Isiro, Republic of Zaire, 1978-81.

ABSTRACT

Picosecond time-resolved rotational coherence spectroscopy is developed as a probe of excited state rotational level structure and alignment. The measurement technique employs a combination of supersonic cooling by molecular beam expansion, coherent picosecond pulsed laser excitation, and time-resolved and polarization-analyzed detection of spectrally dispersed fluorescence. The requisite measurement system response time of approximately 50 picoseconds is attained using time-correlated single photon counting and a microchannel plate detector.

In the case of purely rotational coherence (PRC), i.e., when rotation may be treated in the rigid rotor approximation, analysis of the polarization-analyzed fluorescence provides direct information about the rotational constants and structure of the molecule's excited vibronic state. This method of structural determination of excited states has the inherent advantages over conventional frequency-domain spectroscopy of sub-Doppler resolution and insensitivity to ground state structure. As a result, it is particularly valuable in investigations of large molecules and complexes. Analyses of PRC measurements on eight different molecular systems are detailed in this thesis. These provide illustrative examples of various aspects of the technique while permitting the derivation of new information about the excited states of six of the eight molecules or complexes studied. Principal among the findings are values of the sum of rotational constants B' and C' of the *t*-stilbene S_1 electronic state ($B' + C' = 0.5132 \pm .0008$ GHz) and of all three S_1 rotational constants of anthracene.

We also report measurements of time-resolved and polarization-analyzed fluorescence as a function of excess vibrational energy in the S_1 electronic states of both *t*-stilbene and anthracene. We are able to distinguish the contribution of purely rotational coherence from the contributions of purely vibrational (or rovibrational) coherence to the evolution of fluorescence from the vibrationally excited molecule. Our results provide a test of the extent of coupling between vibrational and rotational motion and its influence on intramolecular vibrational energy redistribution.

Measurements of polarization-analyzed fluorescence of dissociation products demonstrate that rotational coherence of the reagent can be transferred to its fragments. In order to interpret the results of these and related experiments, a classical model of fluorescence anisotropy in prompt, impulsive dissociation reactions is developed.

TABLE OF CONTENTS

Chapter 1

Introduction

A primary determinant of chemical reactivity in polyatomic molecules is the extent to which energy deposited in one of the many degrees of freedom remains localized or is redistributed.[1] For this reason, understanding the mechanisms and time scales of energy flow has been a goal of fundamental importance in chemical physics. Experimental studies of redistribution processes in isolated molecules, particularly in excited electronic states, have focused on the vibrational degrees of freedom in an effort to quantify the roles of density of states, coupling strengths, and mode and symmetry restrictions in the onset of intramolecular vibrational energy redistribution (IVR).[2] Ultrafast pulsed laser and molecular beam techniques have made it possible to trace in real-time the consequences of dynamic behavior in isolated molecules and have thereby contributed greatly to these investigations.[3]

As clear indications of the involvement of rotational degrees of freedom in redistribution processes came to light in the early 1980's,[4] a number of experiments were undertaken to illuminate the nature of the interactions. Fluorescence polarization measurements, both steady state[5] and time-resolved,[6,7,8] were motivated by the understanding that coupling between vibration and rotation which results in a breakdown of the rigid rotor approximation will affect the degree of polarization anisotropy.[9] The extremes of complete separability of vibration and rotation and complete randomization of vibrational-rotational energy, within the constraints of angular momentum conservation, constitute the so-called regular rotor and statistical rotor limits of molecular rotation, respectively.

The time-resolved polarization studies presented in this thesis began with the objective of clarifying the role of rotations in the well documented IVR behavior in the S_1 electronic states of the molecules *t*-stilbene and anthracene.[3] In the early course of this work, polarization transients related to free regular rotor rotation rather than to vibration-rotation coupling were observed. The origin of these transients is purely rotational coherence or, in other words, coherence within a superposition of multiple rigid rotor-like rotational quantum states.[10]

Although fluorescence depolarization as a probe of molecular rotational diffusion in liquids had long been known[11] and studied extensively using laser excitation on the nanosecond and picosecond time scales,[12] there had been no analogous studies of the free rotation of isolated molecules. The characteristics of rotational dephasing due to free rotation had received some theoretical attention in the 1960's,[13] but the expected dephasing rates were not accessible to measurement with the techniques of the day. By the time the above-mentioned investigations of the role of vibration-rotation coupling in IVR were undertaken, improvements in laser and molecular beam apparatus had brought the picosecond and sub-picosecond realm of molecular rotation into the reach of direct experimental observation. In order to correctly extract from polarization experiments on those time scales effects originating in nonrigid rotation, it therefore became essential to understand the manifestations of rigid-rotor rotation associated with purely rotational coherence (PRC). The advancement of this understanding has been the primary goal of this thesis. Based on the knowledge acquired, it has then been possible to examine fluorescence polarization measurements of vibrationally excited molecules for evidence of deviation from regular rotor behavior.

Beyond its use as a diagnostic for rotational involvement in IVR, studies of molecular alignment also play an important role in the field of unimolecular and bimolecular reaction dynamics. When a reaction is initiated from an anisotropic population of precursors, details of the dynamic interactions may be manifested in preferential product alignment or angular distributions. The extraction of these details from experimental observations has been the subject of much interest.[14] For reactions, as for isolated molecules, the effect of rotation must be accounted for in the analysis of alignment sensitive observables. In particular, the interpretation of product fluorescence anisotropy requires an understanding of the consequences of rotation of both reactants and products and the correlation between the two. Each isolated phase of this rotational evolution can be treated classically in a manner which is formally equivalent to the classical treatment of purely rotational coherence. In conjunction with studies of dissociation dynamics in our laboratory,[15] time-resolved fluorescence anisotropies of dissociation products have also been measured. In order to interpret the results of these and similar measurements, a classical model of the evolution of alignment and angular momentum in an impulsive dissociation reaction has been developed.

In addition to the preceding dynamic implications, the opportunity for a completely distinct and unexpected application of time-resolved polarization measurements was presented by one aspect of our observations. This was the presence of intensity recurrences or rephasings at times related to the structural parameters of the excited state.[16] Frequency resolution and assignment of the individual rotational lines of vibronic transitions has long been employed for the precise determination of the rotational constants of excited electronic states of small molecules. In order to extend this technique to larger molecules, whose spectra have denser rotational structure, ultra-high resolution lasers and strongly collimated molecular beams to reduce the Doppler linewidths are required.[17] For sufficiently dense spectra, as measured on the scale of the natural linewidth, due either to size, asymmetry, or direction of the transition moment, this technique is not applicable. Purely rotational coherence spectroscopy is found to offer an alternative, effectively Doppler-free, time domain approach to the determination of excited-state rotational constants. Due to the nature of the phenomenon of PRC, this approach has criteria for applicability completely different from those of the frequency domain measurement. In particular, because the time scale of recurrences lengthens as the rotational constants get smaller, the technique is readily applicable to large molecules. A major focus of the work presented in this thesis is demonstration of the practical utility of PRC spectroscopy for determination of excited-state rotational constants and structures. Results have shown that the usefulness of the technique is not severely limited by requirements of symmetry or dipole direction and that the information obtainable is comparable and complementary to that derived from high resolution frequency domain spectroscopy. Moreover, PRC recurrences have now been observed by a variety of detection schemes, including multi-photon ionization,[18] fluorescence depletion,[19] and laser induced fluorescence.[20] These facts and the inherent advantages of the technique suggest it can find broad application in the study of excited electronic states of large molecules.

Briefly, the organization of the remaining chapters is as follows. Chapter 2 is intended to give the reader a thorough grounding in the theoretical foundation of PRC. Section I of that chapter gives an overview of the phenomenon and describes the principle features of the quantum mechanical treatment, which has been fully developed elsewhere.[10] Section II takes a detailed look at the classical treatment of alignment phenomena. In Part A, a general classical derivation of polarization anisotropy is given. Application both to isolated, stable molecules and to dissociation products, under the restriction of symmetric top motion, is the subject of Part B. Section III focuses on the implications of molecular asymmetry both for the observable characteristics of PRC and for its numerical calculation from the quantum mechanical expression. Chapter 3 is devoted to a description of the experimental apparatus and procedures employed in the measurement of time-resolved and polarization-analyzed fluorescence. The methods of analysis of this data, principally involving comparison and fitting to numerical simulations of PRC signals, is described in Chapter 4. Finally, experimental results are presented and discussed in Chapter 5. The arrangement of that chapter is detailed in its own introduction.

References

1. N. Bloembergen and A. H. Zewail, J. Phys. Chem. **88**, 5459 (1984).
2. For reviews, see: C. S. Parmenter, J. Phys. Chem. **86**, 1735 (1982); and R. E. Smalley, J. Phys. Chem. **86**, 3504 (1982).
3. For a review, see: P. M. Felker and A. H. Zewail in *Advances in Chemical Physics* Vol. LXX Part 1 (John Wiley, New York, 1988).
4. For a discussion, see: W. D. Lawrence and A. E. W. Knight, J. Chem. Phys. **92**, 5900 (1988), and references therein.
5. G. M. Nathanson and G. M. McClelland, Chem. Phys. Lett. **114**, 441 (1985); J. Chem. Phys. **84**, 3170 (1986).
6. V. Matsumoto, L. H. Spangler, and D. W. Pratt, Chem. Phys. Lett. **95**, 343 (1983).
7. N. F. Scherer, J. F. Shepanski, A. H. Zewail, J. Chem. Phys. **81**, 2181 (1984).
8. D. K. Negus, D. S.Green, and R. M. Hochstrasser, Chem. Phys. Lett. **117**, 409 (1985).
9. G. M. Nathanson and G. M. McClelland, J. Chem. Phys. **81**, 629 (1984).
10. P. M. Felker and A. H. Zewail, J. Chem. Phys. **86**, 2460 (1987).
11. F. Perrin, J. Phys. Rad. **5**, 497 (1934); **7**, 1 (1936).
12. T. Tao, Biopolymers **8**, 609 (1969); T. J.Chuang and K. B. Eisenthal, Chem. Phys. Lett. **11**, 368 (1971); G. R. Fleming, J. M. Morris, and G. W. Robinson, Chem. Phys. **17**, 91 (1976); K. G. Spears and L. E. Kramer, Chem. Phys. **30**, 1 (1978); D. P. Millar, R. J. Robbins, and A. H. Zewail, J. Chem. Phys. **76**, 2080 (1982).
13. R. G. Gordon, J. Chem. Phys. **43**, 1307 (1965).
14. See References 21 through 32 of Chapter 2.
15. D. H. Semmes, J. S. Baskin, and A. H. Zewail, J. Am. Chem. Soc. **109**, 4104 (1987).
16. J. S. Baskin, P. M. Felker, and A. H. Zewail, J. Chem. Phys. **84**, 4708 (1986) and Appendix I of this thesis.

17. For example, see: W. A. Majewski and W. L. Meerts, J. Mol. Spectrosc. **104**, 271 (1984); W. A. Majewski, D. F. Plusquellic, and D. W. Pratt, J. Chem. Phys. **90**, 1362 (1989).

18. N. F. Scherer, L. Khundkar, T. Rose, and A. H. Zewail, J. Phys. Chem. **91**, 6478 (1987).

19. J. F. Kauffman, M. J. Côté, P. G. Smith, and J. D. McDonald, J. Chem. Phys. **90**, 2874 (1989).

20. M. Dantus, R. M. Bowman, and A. H. Zewail, to be submitted for publication.

Chapter 2

Theory of Rotational Coherence and Alignment

Portions of this chapter are taken from the following published articles:

"Purely Rotational Coherence Effect and Time-resolved Sub-Doppler Spectroscopy of Large Molecules. II. Experimental," by J. S. Baskin, P. M. Felker, and A. H. Zewail.

Reprinted with permission from The Journal of Chemical Physics, Volume 86, p. 2483. Copyright 1987 American Institute of Physics.

and

"Determination of Excited-State Rotational Constants and Structures by Doppler-Free Picosecond Spectroscopy," by J. S. Baskin and A. H. Zewail.

Reprinted with permission from The Journal of Physical Chemistry, Volume 93, p. 5701. Copyright 1989 American Chemical Society.

I. Purely Rotational Coherence in Symmetric Top Molecules

As an introduction to the theory of purely rotational coherence (PRC), we describe here a simple, physically intuitive picture of the phenomenon. It is based on the fact that the properties (e.g., time and polarization dependence) of PRC fluorescence signals can be understood as arising from the classical motion of each molecule-fixed transition dipole as the molecules of the sample rotate freely in space. This classical motion, coupled with the quantization of angular momentum, reproduces the quantum mechanical manifestations of PRC both qualitatively and, to a great degree, quantitatively.[1]

For example, Figure 1 illustrates the classical rotation of a rigid prolate symmetric top of moment of inertia I_a about the figure axis and I_b about any axis perpendicular to it. (We designate the unique axis of the top by the term figure axis instead of symmetry axis since the latter has more general applications. The figure axis of an accidentally symmetric top need not even be a true symmetry axis.) This can be described as consisting of two motions: 1) a precession or nutation of the figure axis about the total angular momentum vector $\vec{J}$, at angular frequency ω_1 or frequency $\nu_1 = \omega_1/(2\pi)$; and 2) a rotation about the figure axis of the body at angular frequency ω_2. Although the first motion is commonly referred to as precession, nutation is the more proper technical term when the motion is not induced by the action of a torque. Fig. 1 shows the position of the body at two different times separated by half of the nutation period. The angle θ between the figure axis and $\vec{J}$ remains constant so that the component of $\vec{J}$ along the figure axis ($\equiv \vec{K}$) has constant magnitude. The frequencies ν_1 and ν_2 are given by[2]

$$\nu_1 = \frac{1}{2\pi}|\vec{J}|/I_b = \frac{J\hbar}{2\pi}\frac{4\pi B}{\hbar} = 2BJ \tag{1.1}$$

$$\nu_2 = \frac{1}{2\pi}|\vec{J}|\cos\theta\left(\frac{1}{I_a} - \frac{1}{I_b}\right) = \frac{K\hbar}{2\pi}\left(\frac{4\pi A}{\hbar} - \frac{4\pi B}{\hbar}\right) = 2(A-B)K \tag{1.2}$$

where J and K are the magnitudes of $\vec{J}$ and $\vec{K}$, respectively, in units of $\hbar$ and the definitions of the rotational constants $B = \hbar/(4\pi I_b)$ and $A = \hbar/(4\pi I_a)$ have been used. (For an oblate top, ν_2 simply changes to $2(B - C)K$.)

Thus, it is seen that a dipole that is parallel to the figure axis partakes only of the nutational motion, sweeping out a cone in space at the frequency $\nu_1 = 2BJ$. As a result, the radiation from this dipole in any given direction returns to its original value at the period $1/(2BJ)$. It is clear then that the intensity may be modulated only by the nutation frequency, and possibly higher harmonics thereof, but not by the rotation frequency. By contrast, when the dipole is perpendicular to the figure axis, it undergoes both nutational and rotational motion so frequencies based on both ν_1 and ν_2 may appear. For ν_2, only the second harmonic, i.e., $4(A - B)K$, is relevant since a rotation about the figure axis of 180° returns the dipole to its original direction. Both the time dependence and polarization dependence of the fluorescence from individual molecules can be derived from this model.

In practice, the measured fluorescence signals to be considered in this thesis arise from excitation by a linearly polarized pulse of macroscopic samples containing molecules in a large number (typically thousands) of different rotational states. At $t = 0^+$, the dipoles of the excitation transition are partially aligned along the direction of the excitation polarization. The molecules thereafter undergo various forms of the motion described above, producing their own individual modulation or beat patterns with a wide range of modulation frequencies determined by the angular momentum and the excited state rotational constants $B'$and A'. The alignment and synchronization imposed by the excitation pulse and the postulate that J and K may assume only integral values then lead to the following quantitative picture of the macroscopic behavior of PRC when the dipoles of the excitation and detection transitions have the same orientation in the molecule: 1) For parallel transitions (dipole parallel to the figure axis), a total spatial realignment or rephasing of dipoles occurs at the fundamental nutation frequency $2B'$, since all molecules nutate at some multiple of that frequency. 2) For perpendicular transitions, rephasings occur at $4(A' - B')$, which is twice the fundamental rotation frequency, as well as at the fundamental nutation frequency $2B'$, but these rephasings are only partial unless the two frequencies are commensurable. Recurrences in fluorescence (or absorption) intensities associated with such patterns of dipole rephasings constitute the principle observable consequences of PRC in symmetric tops. The exact nature of the recurrences will depend on the fluorescence component detected. For example, in the cases described above, the major recurrences will clearly be positive in the fluorescence component with polarization vector parallel to that of the excitation pulse (henceforth referred to as parallel fluorescence). If, on the other hand, the excitation and detection dipoles are perpendicular to each other, parallel fluorescence will display negative recurrences. In each case, recurrences of opposite phase will appear in the perpendicular component of fluorescence. These properties and specific cases will be discussed in more detail in Section II of this chapter.

The preceeding picture of PRC as a consequence of the orientational evolution of isolated molecules has its quantum mechanical analog in the evolving character of a coherent superposition of rotational eigenstates. This superposition is prepared by the coherent excitation of multiple excited electronic state rotational levels from a single ground state rotational level, as permitted by the appropriate electromagnetic transition selection rules and the laser bandwidth. Since these excited state levels may in turn emit to certain common ground state levels, quantum interference effects (quantum beats) are expected in fluorescence when the detection does not resolve the separate emission channels[3]. In this case, the fluorescence will be modulated at frequencies corresponding to the energy splitting between the interfering excited state rotational levels, with amplitudes which depend on the particular excitation/emission channels involved. Since fluorescence polarization also varies with rotational state, the resultant beat pattern is detection polarization dependent. This is a common feature of all quantum beats arising between rotational levels, such as Zeeman[4] or Stark[5] quantum beats. In those cases, however, the beats appear only in the presence of an applied field and correspond to a precession of the molecules induced by the torque on a permanant dipole.

For a rigid prolate symmetric top molecule, the rotational levels in the excited state have energies E given by

$$E/h \equiv F(J', K') = B'J'(J'+1) + (A' - B')K'^2 \tag{1.3}$$

where J' and K' are the quantum numbers for total angular momentum and projection of angular momentum along the figure axis, respectively. Selection rules for electric dipole excitation are $\Delta J = 0, \pm 1$, $\Delta K = 0$ for parallel dipole transitions and $\Delta J = 0, \pm 1$, $\Delta K = \pm 1$ for perpendicular dipole transitions. For the present considerations, selection rules on the magnetic quantum number (i.e., the quantum number for the z component of total angular momentum), M, are not of concern, since M does not affect the rotational energy. Thus, for a given vibronic transition from a single ground state (J_0, K_0) level, three and six different excited state levels may be reached for parallel and perpendicular transitions, respectively, when the laser coherence width $\Delta\nu_{\mathrm{coh}}$ is sufficiently broad. This process is illustrated for a parallel transition in Fig. 2, which is reproduced from Ref. 1. $\hat{\epsilon}_1$ is used to designate the polarization of the excitation pulse. Emission paths for detection polarization $\hat{\epsilon}_2 \parallel \hat{\epsilon}_1$ are also shown explicitely, showing the sharing of final states that is essential to quantum interference. The upward pointing arrows represent the possible use of alternate probe schemes in which the second transition is absorption rather than emission. The three energy differences, and hence possible beat frequencies, between the three states comprising the parallel transition-induced superposition state are always multiples of $2B'$, whatever the initial (J_0, K_0) level. This may be easily confirmed by consideration of Eq. (1.3) for $\Delta K = 0$. Five of the fifteen differences between the six energy levels for a perpendicular transition take on identical values, so at most ten distinct frequencies may be involved. Again, three are multiples of $2B'$, the fourth is a multiple of $4(A' - B')$, and the six others are sums and differences of the fourth frequency and each of the first three. These last are not, in general, multiples of any combination of molecular constants.

The actual beat frequencies depend, for both dipole directions, on the initial (J_0, K_0) level involved, so that the rotational beat patterns arising from different initial states will be different. The frequencies present in the rotational quantum beat patterns of individual molecules are found to match closely those of the fluorescence modulations derived from the classical rotational motion. For example, Fig. 3 shows the expected parallel fluorescence intensity when the $(J_0 = 6, K_0 = 3)$ rotational level of a symmetric top molecule with rotational constants approximating those of *t*-stilbene is excited by a delta function pulse. This M quantum number has been summed over to obtain this intensity, so that it corresponds to an average over spatial orientations rather than to a true single molecule. The fundamental nutation period of *t*-stilbene is $1/2B' = 1.95$ ns, and the pertinent transition dipoles are both assumed parallel. The signal is seen to repeat exactly with the 1.95 ns period. It also shows a major quasi-periodic oscillation resulting from the superposition of beat frequencies at $J_0 \cdot 2B' = 12B'$ and $(J_0 + 1) \cdot 2B' = 14B'$. This pair of frequencies is the quantum analog of the single classical nutation frequency of the $J_0 = 6$ molecules. The smaller recurrence also has its classical equivalent due to the fact that the figure axis is approaching a complete reversal of direction at the midpoint of its nutation trajectory (see Section II).

Since commensurability of the frequencies of individual molecules is a shared characteristic of quantized classical fluorescence modulations and quantum beat patterns, previous comments on the effect of thermal averaging on the former apply equally to the latter. Thus, although signals such as that of Fig. 3 are not observed experimentally, macroscopic recurrences at the fundamental frequencies $2B'$ and, for a perpendicular transition, $4(A' - B')$ do appear in the fluorescence intensity. Numerous examples of such thermally averaged signals may be seen in later sections.

In the quantum mechanical description of PRC, the simple consideration of rotational selection rules and energies has been sufficient to derive the modulation frequencies which may appear in the fluorescence signal. To confirm other properties predicted by the classical picture, such as the phase dependence of recurrences for given dipole directions and detection polarization, a detailed calculation is required. Derivation of the appropriate quantum mechanical expressions has been given in Ref. 1 employing a density matrix formulation. An alternate derivation is given in the remainder of this section, permitting a simple statement of the basic equation for PRC beats. Reduction of this basic equation to the specific analytical expressions given in Ref. 1 can be done, but it involves fairly laborious algebraic manipulations. In the treatment of Ref. 1, powerful tensor algebra and symmetry properties could be exploited to carry out this reduction efficiently.

Consider a polyatomic molecule in which we assume the electronic (q_a), nuclear (q_α), and rotational (α, β, γ) coordinates are completely separable. Ignoring spin, the total wavefunction of the molecule can be written as follows:

$$\psi = \psi_{\text{el}}(q_a) \cdot \psi_{\text{vib}}(q_\alpha) \cdot \psi_{\text{rot}}(\alpha, \beta, \gamma) \ . \qquad (1.4)$$

In the electric dipole approximation, the composition of the coherent superposition prepared in an excited electronic state by the excitation pulse is governed by the transition dipole matrix element $\langle \psi_0 | \hat{d}_K | \psi_1 \rangle$. Here the operator $\hat{d}_K$ is the component of the electric dipole moment $\hat{d}$ along the direction of polarization of the linearly polarized excitation. The nuclear contribution to the electric dipole gives no contribution to the transition dipole for a transition between electronic states, since it does not operate on the orthogonal electronic wavefunctions. It is sufficient, therefore, to let $\hat{d}$ be the electric dipole due to electrons only: $\hat{d} = \sum_a -e \cdot \vec{r}_a$. If this operator in the chosen molecule-fixed coordinate frame has components $\hat{d}_i^m$, $i = x, y, z$, then $\hat{d}_K$ is given in terms of these components and the direction cosine operators relating the two reference frames by

$$\hat{d}_K = \sum_i \hat{d}_i^m \cos\theta_{Ki} = \hat{d}_x^m \cos\theta_{Kx} + \hat{d}_y^m \cos\theta_{Ky} + \hat{d}_z^m \cos\theta_{Kz} \ . \tag{1.5}$$

Substituting Equations (1.4) and (1.5) into the dipole matrix element, one finds

$$\langle\psi_0|\hat{d}_K|\psi_1\rangle = \sum_i \left(\int \psi^*_{\mathrm{vib}_0}\psi_{\mathrm{vib}_1}\, d\tau_{\mathrm{vib}}\right)\left(\int \psi^*_{\mathrm{rot}_0} \cos\theta_{Ki}\, \psi_{\mathrm{rot}_1}\, d\tau_{\mathrm{rot}}\right) \times \left(\int \psi^*_{\mathrm{el}_0} \hat{d}_i^m \psi_{\mathrm{el}_1}\, d\tau_{\mathrm{el}}\right) \ . \tag{1.6}$$

The first integral is the standard vibrational Franck-Condon factor, f_{FC}. The electronic integral is the ith component of the transition dipole moment, designated by d_i^m. The integral over rotational coordinates is referred to as the direction cosine matrix element. For symmetric top rotational wavefunctions[7,8] this matrix element is a function of the initial and final values of the rotational quantum numbers J, K, and M. In the notation of Ref. 8,

$$\begin{aligned}\int \psi^*_{\mathrm{rot}_0} \cos\theta_{Ki}\, \psi_{\mathrm{rot}_1}\, d\tau_{\mathrm{rot}} &= \langle J_0K_0M_0|\cos\theta_{Ki}|J_1K_1M_1\rangle \\ &\equiv \left(\Phi_{Ki}\right)_{J_0K_0M_0;J_1K_1M_1} \ .\end{aligned} \tag{1.7}$$

Then Eq. (1.6) reduces to

$$\langle\psi_0|\hat{d}_K|\psi_1\rangle = f_{FC} \sum_i \left(\Phi_{Ki}\right)_{J_0K_0M_0;J_1K_1M_1} d_i^m \ . \tag{1.8}$$

Explicit expressions for $\left(\Phi_{Ki}\right)_{J_0K_0M_0;J_1K_1M_1}$ are given in Ref. 8 in which the symmetric top figure axis is the z axis, and angular momentum is quantized along the space-fixed Z axis. The electric dipole rotational selection rules for electronic transitions simply state the combinations of parameters for which these expressions are nonzero.

The superposition state excited from a single ground state, for given transition dipole moment and excitation polarization directions, may now be specified.

The Z axis is chosen in the direction of the excitation polarization without loss of generality. It is assumed that a delta function excitation pulse at $t = 0$ accesses a single upper vibronic state ($|S_1 v_1\rangle$ in Fig. 1) and that all $|J_1 K_1 M_1\rangle$ rotational states for which $\sum_i (\Phi_{Zi})_{J_0 K_0 M_0; J_1 K_1 M_1} d_i^m$ is nonzero are within reach of the excitation bandwidth. The rotational wavefunction in the excited state at $t = 0$ is then

$$\psi_{\rm rot}(0) = f_{FC} \sum_{J_1 K_1 M_1} \Big(\sum_i (\Phi_{Zi})_{J_0 K_0 M_0; J_1 K_1 M_1} d_i^m \Big) |J_1 K_1 M_1\rangle \; . \qquad (1.9)$$

If the sum in parentheses is abbreviated by $\mathrm{M}_Z^{\{0;1\}}$, the time evolution of the superposition state is given by

$$\psi_{\rm rot}(t) = f_{FC} \sum_{J_1 K_1 M_1} \mathrm{M}_Z^{\{0;1\}} \, |J_1 K_1 M_1\rangle \, \exp\left(-i \frac{E(J_1, K_1, M_1)}{\hbar} t \right) \qquad (1.10)$$

where $E(J_1, K_1, M_1)$ is the energy of the eigenstate $|J_1 K_1 M_1\rangle$. In the absence of applied fields, E does not depend on M_1.

The fluorescence intensity of polarization L from this superposition state to the state $|J_2 K_2 M_2\rangle$ is proportional to $\left|\langle \psi_{\rm rot}(t) | \hat{d}'_L | J_2 K_2 M_2 \rangle\right|^2$, and the total detected intensity is

$$I_L(J_0, K_0, M_0, t) \propto \sum_{J_2 K_2 M_2} \left| \langle \psi_{\rm rot}(t) | \hat{d}'_L | J_2 K_2 M_2 \rangle \right|^2 \; . \qquad (1.11)$$

The emission dipole need not be the same as the absorption dipole, as indicated by the prime on the dipole operator. The range of J_2 is always $J_0 - 2$ to $J_0 + 2$. The maximum ranges of K_2 and M_2 are $K_0 - 2$ to $K_0 + 2$ and $M_0 - 1$ to $M_0 + 1$, with the chosen convention of excitation polarization. On substituting Eq. (1.10) in Eq. (1.11), one finds the final expression for the polarization-analyzed fluorescence intensity for arbitrary dipole and detection polarization directions:

$$I_L(J_0, K_0, M_0, t) \propto$$

$$\sum_{J_2 K_2 M_2} \left| \sum_{J_1 K_1 M_1} \mathrm{M}_Z^{\{0;1\}*} \langle J_1 K_1 M_1 | \hat{d}_L' | J_2 K_2 M_2 \rangle \exp\left(i \frac{E(J_1, K_1, M_1)}{\hbar} t \right) \right|^2$$

$$\propto \sum_{J_2 K_2 M_2} \left| \sum_{J_1 K_1 M_1} \mathrm{M}_Z^{\{0;1\}*} (\mathrm{M}')_L^{\{1;2\}} \exp\left(i \frac{E(J_1, K_1, M_1)}{\hbar} t \right) \right|^2 \qquad (1.12)$$

where $(\mathrm{M}')_L^{\{1;2\}}$ is equal to $\sum_i (\Phi_{Li})_{J_1 K_1 M_1; J_2 K_2 M_2} d_i^{m'}$.

The origin of the PRC modulations may be easily recognized in Eq. (1.12). For certain values of J_2, K_2, and M_2, the interior sum over excited-state rotational quantum numbers has more than one term with nonzero coefficient. (In a representation like Figure 2 or 3, such a final state is one that is reached by more than a single path.) When the square modulus is taken in these cases, one obtains not only time independent diagonal contributions but also time dependent cross-terms with frequencies fixed by the energy differences between contributing excited states. Each cross-term is complex, but it is paired with its complex conjugate so that their sum is real. Since the total intensity is given by a square modulus, it is positive as well. The terms contributing to the sum depend on the directions of the transition dipoles and of the detection polarization, so that when these change, the beat modulations change accordingly.

Equation (1.12) is the expression for the true single molecule PRC intensity, showing the dependence on all three rotational quantum numbers of the initial state. Such an equation must be used when the rotational energy depends on M as well as J and K. The results of Ref. 1 for field-free single initial rotational levels are obtained from this equation by summing over M_0. For actual comparisons with experiment, a further weighted summation over all populated rotational levels of the ground state is required.

II. Classical Time-dependent Fluorescence Anisotropy of Symmetric Top Molecules

A. General derivation

This section begins with a derivation of the time evolution of probe signal intensities following excitation of an isotropic sample by a linearly polarized delta function light pulse. The nature of the molecular motion following excitation remains arbitrary in this derivation. The consequences of symmetric top motion will be examined subsequently. The probe process of primary interest is polarization-analyzed fluorescence detection, but probing by a properly chosen polarized excitation/detection sequence is equally suitable. The derived time-dependence will be applicable to the latter case when the signal observed is proportional to the total population of the terminal state of the pump/probe excitation sequence.

Many facets of the present derivation, and many of the conclusions drawn, can be found in an extensive literature of theoretical treatments of molecular alignment phenomena. These have treated fluorescence of both stable molecules[9-20,1] and of dissociation products,[21-24] as well as dissociation fragment angular distributions[25-31] and Doppler profiles.[32] In many cases both classical and quantum mechanical derivations have been given, demonstrating that the classical treatments give very satisfactory results for most situations of practical interest. Previous treatments have often been adapted to special cases, dealing with, e.g., time-integrated fluorescence, rotational diffusion in liquids, linear molecule rotation, or specific transition dipole directions. The derivation here of classical time-resolved and polarization-analyzed fluorescence is intended to be general enough to admit application both to stable molecules and photodissociation products. Particular attention is given to all factors which may influence measured fluorescence evolution, since direct comparison with experimental results is the ultimate goal.

We describe first the nature of the experiment to be considered and define the physical parameters and nomenclature. An initially isotropic population of ground-state molecules forms the sample under study. We designate a molecule in this sample by M_1. $\hat{\epsilon}_1$ is a unit vector designating the direction of polarization of the linearly polarized excitation pulse. Excitation (as well as detection) is assumed to be via an electric-dipole allowed vibronic transition, with a transition dipole moment $\vec{d}_1$ whose direction is fixed in the molecular frame. The instant of excitation defines $t = 0$. Because the probability for absorption of the polarized pump pulse is dependent upon the orientation of $\vec{d}_1$ relative to $\hat{\epsilon}_1$, there will be created at this instant an excited-state population (M_1^*) with a well-defined spatial alignment. At some later time t, a transition of the molecule M_2 is probed, where M_2 is either equal to M_1^* or is one of its photoproducts. The instantaneous transition probability of each M_2 is determined by the orientation of the dipole moment $\vec{d}_2$ of the probe transition to the probe polarization vector $\hat{\epsilon}_2$. Thus the time evolution of alignment of dipole moments $\vec{d}_2$ in the sample will be reflected in a time-dependent polarization anisotropy of the signal. In order to calculate the time dependence of the probe signal as a function of probe polarization, the rotational motion of each dipole must be traced continuously from $t = 0$, the moment when the alignment of the population is created by the excitation pulse.

As in previous treatments it will be shown that the quantity governing the polarization dependence of intensities is η, the time dependent laboratory angle between the evolving direction of $\vec{d}_2$ and the direction of $\vec{d}_1$ at $t = 0$. Final intensity expressions derived here and elsewhere are distinguished by the specific distribution of $\eta(t)$ in the ensemble. Note that the classical treatment of molecular rotational motion that is employed here corresponds in the quantum mechanical description to coherent excitation spanning all rotational branches of the pertinent transitions. In a branch resolved excitation and detection sequence, no such time evolution is manifested.

As initial conditions for the pump/probe experiment, we assume that a very large number N of M_1 molecules in a single vibronic state are accessible to the pump laser. The normalized rotational state distribution is given by $p_J(\{i\})$, where $\{i\}$ represents any complete set of rotational coordinates for M_1. This leads to an expected population $P_J(\{i\}) = N\,p_J(\{i\})$ in rotational state $\{i\}$. The molecules have transition moments and angular momenta distributed uniformly over 4π steradians, though these distributions are not, in general, independent of each other. Since absorption of a photon can change the angular momentum or any of its components by at most $\hbar$, in the classical limit the rotational state of M_1^* will be assumed identical to that of M_1. The orientational evolution which is pertinent to the pump/probe process is completely expressed in the function $\eta(t)$ as defined above. This is evident since interaction of the radiation fields and the molecules is solely through the dipoles. Therefore, we may treat each subset of M_2 molecules characterized by a specific $\eta(t)$ as a distinguishable final state, and designate the set of parameters on which $\eta(t)$ depends by $(\{f\})$. Note that since $(\{f\})$ must specify all rotational motion after $t = 0$, in the case of dissociation it may depend on the rotation of M_1^* as well as of M_2. The designation "final" might then be more properly replaced by "post-pump." Intensities calculated for each $\{f\}$-state will be referred to as state-resolved since they may exhibit classically distinguishable evolution, but no direct correspondence to quantum-mechanical states is implied. Finally, we define $p_{i\rightarrow f}$ as the branching ratio from initial to final state, giving the expected fraction of those molecules excited in state $\{i\}$ which yield fragments in state $\{f\}$.

To derive the probe signal intensity from molecules characterized by arbitrary $\{f\}$ and for an arbitrary sequence of pump/probe polarizations, we refer to the geometry of Fig 4. The probe polarization vector $\hat{\epsilon}_2$ is rotated from $\hat{\epsilon}_1$ by an angle delta in the laboratory. Since the population excited by the pump pulse must have cylindrical symmetry about $\hat{\epsilon}_1$ at all time, the choice of azimuthal orientation of $\hat{\epsilon}_2$ about $\hat{\epsilon}_1$ is arbitrary. We write first the probability for absorption during a delta-function pump pulse by a molecule in state $\{i\}$ with $\vec{d}_1$ as shown. In the linear or low intensity regime

$$p_a = C_a\big(\{i\}\big)\ \cos^2\alpha = \frac{C_a\big(\{i\}\big)}{3}\big(1+2P_2(\cos\alpha)\big) \tag{2.1}$$

where $P_2(x) = \frac{1}{2}(3x^2-1)$ is the second order Legendre polynomial and C_a is a constant of proportionality which is independent of the laboratory orientation of the dipole. C_a will depend in general on the specific vibronic transition and the characteristics of the pump pulse, and may depend on the initial rotational state, particularly when the frequency spread of rotational transitions is as great as, or greater than, the pump bandwidth. Explicit indication of this and other functional dependences will generally be dropped in the following equations for readability.

We require next the conditional probability $p_{pr/a}$ for *detection* of probe absorption or emission by M_2 in state $\{f\}$ with dipole $\vec{d}_2$ at time t, given that it was excited by the pump at $t=0$. For the particular $\vec{d}_2$ orientation shown, we may write

$$p_{pr/a}(t) = C_{pr}\big(\{f\},t\big)\ \cos^2\beta = \frac{C_{pr}\big(\{f\},t\big)}{3}\big(1+2P_2(\cos\beta)\big) \tag{2.2}$$

where, again, the first term has no angular dependence, but may depend on the rotational state. This probability should be interpreted as follows: if, of all M_2 in the specified $\{f\}$ rotational state, a large number n have dipoles oriented, at time t, in the indicated direction, the number of detected probe transitions expected from these molecules in a single measurement (single probe pulse or single fluorescence channel width) is $n\,p_{pr/a}(t)$. Note that the population n does not depend on vibronic state, so it changes in time only as the dipoles rotate. If the probe process is absorption, C_{pr} is determined by the same factors as C_a but now may vary in time since the vibronic state of the fragment may be time dependent. When the probe is fluorescence detection in a direction normal to $\hat{\epsilon}_2$, C_{pr} depends on the spontaneous emission strength (probability for a downward transition) at wavelengths within the spectral window of detection, and also accounts for the solid angle of fluorescence collection and detection efficiency. In this case, C_{pr} *must* be time-dependent since the probability of the fragment remaining in the excited vibronic state decreases with time. In the simplest case, the probability per unit time for emission by an excited M_2 will be constant and C_{pr} will decay exponentially, as it may also for an absorption probe from an excited state. However, for either type of probe, the vibronic state of the fragment may also be subject to nonradiative evolution (as, for example, when the vibrational character of the molecule is altered by intramolecular vibrational energy redistribution) leading to temporal changes in absorption or emission strength at the probe wavelength. A special case of this type is the spectral shift of a probe transition caused in the early stages of dissociation by the proximity of the two fragments.[33] Similarly, in the case of predissociation, the spectrum will shift from that of M_1^* to that of M_2 when the separation of fragments occurs. Such a time dependence may be a function of $\{f\}$ but cannot depend on the orientation of the molecule in the lab frame.

The probability for excitation of M_1 in state $\{i\}$ with dipole $\vec{d}_1$ as shown, creation of M_2 in state $\{f\}$, *and* detection of a probe transition at a time t for which the angle between $\vec{d}_1(0)$ and $\vec{d}_2$ is η, can be found by combining the above results and averaging over possible directions of $\vec{d}_2$:

$$\begin{aligned} p_{a+pr}(t) &= p_a p_{i\to f} \Big\langle p_{pr/a}(t) \Big\rangle_{\phi'} \\ &= \frac{C_a}{3}\, p_{i\to f}\, \frac{C_{pr}(t)}{3} \big(1 + 2P_2(\cos\alpha)\big) \Big\langle 1 + 2P_2(\cos\beta) \Big\rangle_{\phi'} \; . \end{aligned} \tag{2.3}$$

Each value of ϕ' is weighted equally in this average since the azimuthal orientation of the molecule about $\vec{d}_1$ at $t = 0$ was isotropic. The average in Eq. (2.3) may be carried out simply by referring to Figure 3 and applying the addition theorem for spherical harmonics to $P_2(\cos\beta)$.[34] This gives

$$p_{a+pr}(t) = \frac{C_a}{3}\, p_{i\to f}\, \frac{C_{pr}(t)}{3} \big(1 + 2P_2(\cos\alpha)\big)\big(1 + 2P_2(\cos\eta)P_2(\cos\gamma)\big) \; . \tag{2.4}$$

The total number of transitions expected from molecules in the state $\{f\}$ when the sample is probed at time t is found by multiplying Eq. (2.4) by $P_J(\{i\})$, averaging over the uniform initial distribution of $\vec{d}_1$, and summing (or integrating) over initial states. Multiplication by $h\nu_{pr}$, where ν_{pr} is the probe transition frequency, then gives the detected energy. The state resolved average probe intensity over the spatial and temporal extent of the probe beam or detector, will be proportional to this energy with a proportionality constant C completely determined by the characteristics of the probe. Thus,

$$I_\delta(\{f\},t) = C\sum_{\{i\}} P_J(\{i\})\, h\nu_{pr}\Big\langle p_{a+pr}(t)\Big\rangle_{(\alpha,\phi)_{4\pi}} . \tag{2.5}$$

Following the average of $P_2(\cos\gamma)$ over phi, one obtains

$$\begin{aligned} I_\delta(\{f\},t) = C&\left(\sum_{\{i\}} P_J(\{i\})\,\frac{C_a}{3}\,p_{i\to f}\right) h\nu_{pr}\,\frac{C_{pr}(t)}{3} \\ &\times\Big\langle\Big(1+2P_2(\cos\alpha)\Big)\Big(1+2P_2(\cos\delta)P_2(\cos\eta)P_2(\cos\alpha)\Big)\Big\rangle_{\alpha_{4\pi}} \end{aligned} \tag{2.6}$$

where terms which cannot depend on the initial state have been factored from the summation. The notation $\alpha_{4\pi}$ recalls that the remaining average is part of the original average over a sphere: $\langle\ldots\rangle_{(\alpha,\phi)_{4\pi}} = \frac{1}{2\pi}\int_0^{2\pi}\frac{1}{2}\int_0^{\pi}\ldots\sin\alpha\,d\alpha\,d\phi$. This average is zero for $P_2(\cos\alpha)$ and $\frac{1}{5}$ for $P_2^2(\cos\alpha)$. Furthermore, note that if $P_j(\{f\})$ is defined as the total number of M_2 fragments created in the state $\{f\}$, one has

$$\begin{aligned} P_j(\{f\}) &= \sum_{\{i\}} P_J(\{i\})\,\frac{C_a}{3}\Big\langle 1+2P_2(\cos\alpha)\Big\rangle_{(\alpha,\phi)_{4\pi}} p_{i\to f} \\ &= \sum_{\{i\}} P_J(\{i\})\,\frac{C_a}{3}\,p_{i\to f}\ , \end{aligned} \tag{2.7}$$

which is precisely the sum appearing in Eq. (2.6). If the remaining alignment independent factors $C\,h\nu_{pr}\,\frac{1}{3}C_{pr}(t)$ are combined into a single function $a(\{f\},t)$, the final generally applicable intensity expression can be written

$$I_\delta(\{f\},t) = P_j(\{f\})\,a(\{f\},t)\left[1+\frac{4}{5}P_2\Big(\cos\delta\Big)P_2\Big(\cos\eta(\{f\},t)\Big)\right] \tag{2.8}$$

where the complete functional dependence of each term is indicated. The macroscopic signal is then obtained by a sum over all product states:

$$I_\delta(t) = \sum_{\{f\}} I_\delta(\{f\},t) \ . \tag{2.9}$$

From these equations, several well-known general properties of the polarization-analyzed intensities are immediately evident. These deal specifically with intensities measured at $\delta = 0°$, $54.7°$, and $90°$, designated $I_\parallel$, $I_{54.7°}$ (magic angle intensity), and $I_\perp$, respectively. (It is assumed in the following that the detection efficiency, and hence $C_{pr}(t)$, is independent of δ. In practice this condition is often not met and data collected at different angles must be normalized to compensate for this bias.) First, from Eq. (2.8) one finds $I_\parallel + 2I_\perp = 3P_j(\{f\})a(\{f\},t)$, which is independent of the orientational evolution of the population. Physically, this reflects the equivalence of all directions of perpendicular polarization, and the fact that the sum of intensities from a dipole emitter measured with polarizations along any set of three orthogonal axes is independent of the orientation of the dipole. Secondly, because $P_2\big(\cos(54.7°)\big)$ is zero, $I_{54.7°} = P_j(\{f\})a(\{f\},t) = \frac{1}{3}(I_\parallel + 2I_\perp)$, and hence is also insensitive to orientational effects. Thirdly, applying the general definition of polarization anisotropy ($r \equiv (I_\parallel - I_\perp)/(I_\parallel + 2I_\perp)$) to the state resolved intensities, one finds the simple relations

$$r(\{f\},t) = 0.4\, P_2\big(\cos\eta(t)\big) \tag{2.10}$$

and

$$I_\delta(\{f\},t) = P_j(\{f\})\, a(\{f\},t)\, \Big(1 + \alpha_\delta r(\{f\},t)\Big) \ , \tag{2.11}$$

where α_δ has the value $2P_2(\cos\delta)$. Eq. (2.10) shows that the initial anisotropy is equal to 0.4 in the usual case that the pump and probe dipoles have the same orientation in the molecule-fixed frame. It also shows that the anisotropy of an isotropic sample has a minimum value of -0.2 which it reaches at times when $\eta(t) = \frac{\pi}{2}$, meaning that every $\vec{d}_2$ has reached a position such that it is perpendicular to the direction of $\vec{d}_1$ at $t = 0$. Finally, the anisotropy of the macroscopic intensities [Eq. (2.9)] is given by a weighted sum of the state resolved anisotropies:

$$r(t) = \sum_{\{f\}} P_j(\{f\})a(\{f\},t)r(\{f\},t) \Big/ \left(\sum_{\{f'\}} P_j(\{f'\})a(\{f'\},t) \right) . \qquad (2.12)$$

Since the anisotropies contain all available information about the dipole orientation, it will be convenient in the following discussions to restrict our attention to Equations (2.10) and (2.12) whenever possible. If the intensity for arbitrary delta is required, it may be recovered from the anisotropy by use of Eq. (2.11) or, for the macroscopic intensity, by

$$\begin{aligned} I_\delta(t) &= \big(1 + \alpha_\delta r(t)\big) \times \left(\sum_{\{f\}} P_j(\{f\})a(\{f\},t) \right) \\ &= \big(1 + \alpha_\delta r(t)\big) \times I_{54.7^\circ}(t) \qquad (2.13) \end{aligned}$$

where Equations (2.9), (2.11), and (2.12) have been used. From the experimental point of view, Eq. (2.13) confirms the sufficiency of measuring only the two principal polarization components, $I_\parallel$ and $I_\perp$, because both $I_{54.7^\circ}$ and $r(t)$ can be derived from them.

A simplification of practical utility is achieved in the above equations when separability of the state and temporal dependence of $a(\{f\},t)$ according to the perscription $a(\{f\},t) = B(\{f\})\,A(t)$ is assumed. This can usually be considered a reasonable approximation, in which $B(\{f\})$ reflects the strength of the probe transition for the particular rotational state, and $A(t)$ depends only on the evolution of the vibronic state. (This assumption is actually less restrictive than it might appear since $A(t)$ need be constant only over those rotational states for which $B(\{f\})$ has a substantial amplitude.) When the above separation is made, $A(t)$ may be factored from all final state sums. In particular, the weights in Eq. (2.12) reduce to $P_j(\{f\})B(\{f\})$, which are related to time-integrated spectroscopic data, and the time dependence of $r(t)$ is completely attributable to the rotational dynamics manifested in $\eta(t)$. A full characterization of the intensities depends additionally only on the measurement of the macroscopic magic angle intensity, which is in this case equal to $A(t)$ to within a multiplicative constant.

For all calculations presented in this thesis, it will be assumed either that a common temporal envelope A(t) characterizes all pertinent rotational states or that the sum in Eq. (2.9) may be separated into at most two parts to account for contributions from two different population components having different A's. It is further assumed that B depends only on the position of the transition frequency of each state within the spectral window of the probe, and therefore depends only on the energy of the state. This spectral sensitivity is then determined from the overlap of the rotational band contour with the probe pulse bandwidth in absorption or the monochromator bandpass in fluorescence. The spectrally broad picosecond or femtosecond pulses used in the time-resolved experiments will typically span the entire rotational contour with approximately constant intensity. Thus, uncertainty in B, even in the abscence of satisfactorily resolved and assigned time-integrated spectra of congested rotational bands, will usually not be of great concern. In the classical picture being developed here, it would appear that the final state weights in Eq. (2.12) could be changed arbitrarily by varying the choice of B to obtain many different forms of macroscopic anisotropy. This is actually not the case, however, since time dependence can only be observed when the probe pulse coherently spans multiple branches of the rotational band contour, as mentioned at the beginning of this section.

Eq. (2.10) reveals the central role played by the function $\eta(t)$ in the evolution of the signals we wish to calculate. We now derive the form of this function for the specific case that all motion of the dipole $\vec{d}_2$ for $t > 0$ is associated with the free rotation of a symmetric M_2. This situation applies both for excitation of a stable symmetric M_1 and for very rapid dissociations that give rise to a symmetric fragment M_2.

Symmetric top rotation was described in Section I of this chapter and illustrated in Fig. 1. Referring again to that figure, we recall that the motion is characterized by a constant total angular momentum vector $\vec{J}$ and a constant angle Θ between $\vec{J}$ and the figure axis. A complete specification of the orientation of the top in a space-fixed frame can be given by means of a commonly employed[35] set of Euler angles (Θ, Φ, Ψ), as shown in Fig. 5. To be consistent with the definition of the angle Θ defined in Fig. 1, the space-fixed frame (X, Y, Z) is chosen with the Z axis along $\vec{J}$ while the z axis of the molecule-fixed frame coincides with the figure axis of the molecule. Since the directions of the pertinent angular momentum and of the principal inertial axes may change in a dissociation, we reserve the use of capital letters ($\vec{J}$, (Θ, Φ, Ψ)) for the description of M_1, while $\vec{j}$ and (θ, ϕ, ψ) will apply to M_2.

Using the Euler angle description, the form of $\eta(t)$ for symmetric M_2 can be easily derived. We first determine the motion relative to the space-fixed X, Y, and Z of the principal axes of M_2. This is described by a uniform change in ϕ at rate ω_1 (nutation about $\vec{j}$) and in ψ at rate ω_2 (rotation about the figure axis). The equations of motion of unit vectors along the top axes are therefore

$$\begin{aligned}\hat{x}(t) = &\big(\cos(\psi_0 + \omega_2 t)\cos\omega_1 t - \cos\theta\sin(\psi_0 + \omega_2 t)\sin\omega_1 t\big)\hat{X}\\ &+ \big(\cos\theta\sin(\psi_0 + \omega_2 t)\cos\omega_1 t + \cos(\psi_0 + \omega_2 t)\sin\omega_1 t\big)\hat{Y}\\ &+ \sin\theta\sin(\psi_0 + \omega_2 t)\hat{Z} \qquad (2.14a)\end{aligned}$$

$$\begin{aligned}\hat{y}(t) = &\big(-\sin(\psi_0 + \omega_2 t)\cos\omega_1 t - \cos\theta\cos(\psi_0 + \omega_2 t)\sin\omega_1 t\big)\hat{X}\\ &+ \big(\cos\theta\cos(\psi_0 + \omega_2 t)\cos\omega_1 t - \sin(\psi_0 + \omega_2 t)\sin\omega_1 t\big)\hat{Y}\\ &+ \sin\theta\cos(\psi_0 + \omega_2 t)\hat{Z} \qquad (2.14b)\end{aligned}$$

$$\hat{z}(t) = \sin\theta\sin\omega_1 t\,\hat{X} - \sin\theta\cos\omega_1 t\,\hat{Y} + \cos\theta\,\hat{Z} \qquad (2.14c)$$

where the arbitrary value of ϕ_0 has been taken as 0. The classical angular frequencies are as given in Section 1: $\omega_1 = 4\pi B_\perp j$ and $\omega_2 = 4\pi(B_\| - B_\perp)j\cos\theta$, where now $B_\|$ and $B_\perp$ are the rotational constants of the molecule about its figure axis and about any axis perpendicular to it, respectively. Note that the frequencies in this form are also valid for oblate tops, for which $B_{\|} = C$ and ω_2 is negative. For now, no distinction need be drawn between the dimensionless $j = |\vec{j}|/\hbar$ in these expressions and the quantum number j associated with the eigenvalue $j(j+1)$ of the angular momentum squared. This correspondence must be treated more carefully, however, when recurrences are considered.

Given the projections of $\vec{d}_1$ and $\vec{d}_2$ on the M_2 principal axes, it is now straightforward to calculate

$$\cos(\eta(t)) = \frac{\vec{d}_1 \cdot \vec{d}_2(t)}{d_1 d_2} = \frac{1}{d_1 d_2}\Big(d_{1x}\hat{x}(0) + d_{1y}\hat{y}(0) + d_{1z}\hat{z}(0)\Big) \cdot \Big(d_{2x}\hat{x}(t) + d_{2y}\hat{y}(t) + d_{2z}\hat{z}(t)\Big) \quad (2.15)$$

by using Equations (2.14) to reduce the time-dependent basis vectors to a common lab-fixed frame. d_1 and d_2 in Eq. (2.15) are the amplitudes of vectors $\vec{d}_1$ and $\vec{d}_2$. Note that while both $\vec{d}_1$ and $\vec{d}_2$ must be expressed in terms of projections on the M_2 principal axes, because $\vec{d}_1$ is associated with a transition of M_1, there need be no symmetry restrictions on its components even for a rigorously symmetric M_2.

B. Applications

i. Isolated stable molecules

Our principal interest in discussing the anisotropy of isolated stable molecules undergoing free rotation is to establish a connection between the theoretical development of the preceding section and the results of previous classical and quantum mechanical treatments.[1,13,20] We demonstrate thereby the validity of the present formalism and develop further insight into its implementation in treating specific cases. Comparisons with quantum mechanical results available in the domain of stable molecules permit an objective assessment of the applicability of the classical model, which may, by extrapolation, serve as a guideline in applications to dissociation.

According to the preceding derivation, Equations (2.10), (2.14), and (2.15) provide a complete prescription for calculation of the state-resolved probe signal anisotropies. The latter two equations show that these may be functions not only of time, but also of j (through the frequencies), θ (both explicitly and through ω_2), and ψ_0. Thus the pertinent final state coordinates for symmetric top motion are $(\{f\}) = (j, \theta, \psi_0)$. As an example of an elementary though important application of these equations, consider the case of $\vec{d}_1$ and $\vec{d}_2$ parallel to the figure axis of M_2. The relation of the two transition moments to the M_2 figure axis is designated by the notation $(\|, \|)$. With $\vec{d}_1 = d_1 \cdot \hat{z}(0)$ and $\vec{d}_2(t) = d_2 \cdot \hat{z}(t)$, application of Equations (2.14) and (2.15) leads to the following expression for $\cos\eta(t)$:

$$\cos\eta(t) = \sin^2\theta \cos\omega_1 t + \cos^2\theta \ . \tag{2.16}$$

Substitution into Eq. (2.10) gives the state resolved anisotropy

$$\begin{aligned} r_{\|,\|}&(j, \theta, \psi_0, t) \\ &= \frac{3}{5}\sin^4\theta\,\cos^2\omega_1 t + \frac{6}{5}\sin^2\theta\,\cos^2\theta\,\cos\omega_1 t + \frac{3}{5}\cos^4\theta - \frac{1}{5} \\ &= \frac{1}{10}\left(3\cos^2\theta - 1\right)^2 + \frac{6}{5}\sin^2\theta\,\cos^2\theta\,\cos\omega_1 t + \frac{3}{10}\sin^4\theta\,\cos(2\omega_1 t) \ . \end{aligned} \tag{2.17}$$

Expressions equivalent to Eq. (2.17) were derived classically for this special case in both Ref. 1 and Ref. 20.

A unique aspect of this expression is traceable to the fact that rotation about the figure axis has no effect on the motion of a parallel dipole. As a result, r depends neither on the rotation frequency ω_2 nor on ψ_0. Absence of a dependence on ψ_0 means that the same anisotropy is displayed by all fragments occupying a common energy level: $r_{\|,\|}(j, \theta, \psi_0, t) = r_{\|,\|}(j, \theta, t)$.

Eq. (2.17) is an analytical expression of the behavior which was predicted in the discussion of Section I. The anisotropies are seen to be periodic with the nutation period $2\pi/\omega_1 = 1/(2B_\perp j)$, independent of θ. The initial anisotropy is equal to 0.4, as expected. A situation of particular interest and simplicity is that of $\theta = \frac{\pi}{2}$ which applies to all linear M_2 when electronic and spin angular momenta may be neglected. The anisotropy then reduces to[12,20]

$$r_{\|,\|}(j, \frac{\pi}{2}, t) = 0.1 + 0.3\cos(2j\omega_{n0}t) \tag{2.18}$$

which oscillates at twice the nutation frequency. Here ω_1 has been replaced by $j\omega_{n0}$ where $\omega_{n0} = 4\pi B_\perp$ in order to show the dependence on j explicitly. ω_{n0} will be referred to as the fundamental nutation frequency of the molecule. For a linear molecule without electronic or spin angular momenta, nutation and rotation are interchangable terms since there is no rotation about the figure axis.

Eq. (2.17) may also be compared with the results of the full quantum mechanical treatment.[1] Eq. (2.12) gives the anisotropy after averaging over an isotropic sample, so comparison with the M summed quantum results is required. As stated above, Eq. (2.17) gives both $r_{\|,\|}(j, \theta, \psi_0, t)$ and $r_{\|,\|}(j, \theta, t)$, and therefore corresponds to the quantum result for energy level $(j, k \equiv j\cos\theta)$. For example, Fig. 6a shows the case of $I_\| \propto 1 + 2r(t)$ for $j = 6$ and $\theta = \pi/3$, i.e. $k = 3$. The B rotational constant was chosen to permit direct comparison with Fig. 3. The two plots begin in a similar fashion but diverge near half the fundamental nutation period. Use of $j = \sqrt{6 \cdot 7} = 6.48$, corresponding to the actual total angular momentum of the quantum level of Fig. 3, also fails to exactly reproduce the quantum behavior at long times.[1] This discrepancy can be resolved, as pointed out in Ref. 20, by replacing the classical frequencies $\omega_1 = j\omega_{n0}$ and $2j\omega_{n0}$ by $\frac{1}{2}[j\omega_{n0} + (j+1)\omega_{n0}]$ and $(2j+1)\omega_{n0}$ for integral j. These are the exact quantum beat frequencies for the $(\|, \|)$ dipole case, as easily found from Eq. (1.3). When this substitution is made, the $I_\|$ shown in Fig. 6b results. While not identical to the quantum result, this calculation reproduces the recurrence behavior of Fig. 3 quite well. From comparisons such as this, one is lead to conclude that the classical treatment can be useful even at very low values of angular momentum.

For all other dipole cases, it is found that the classical state resolved anisotropy depends on ψ_0. For symmetric M_2, ψ_0 specifies only the rotational phase of the M_2-fixed frame in the $\vec{j}$-fixed reference frame at $t = 0$ and does not affect the energy. Comparison of the classical results with quantum mechanical energy level resolved expressions for other than the $(\|, \|)$ case therefore requires application of Eq. (2.12) with the summation over states limited to an integration over ψ_0 only. The weight accorded to each state is $P_j(\{f\})a(\{f\}, t)$. When it is assumed that $a(\{f\}, t) = B(\{f\})\,A(t)$ and that B depends only on the rotational energy, as discussed previously, $a(\{f\}, t)$ may be factored from Eq. (2.12) and canceled. For the thermal samples under consideration, the rotational state populations $P_j(j, \theta, \psi_0)$ also depend only on the rotational energy. Thus the general classical expression for the anisotropy of the (j, θ) energy level involves an integration over ψ_0 with uniform weighting:

$$r(j,\theta) = \frac{1}{2\pi}\int_0^{2\pi} r(j,\theta,\psi_0)\ . \tag{2.19}$$

$r(j, \theta, \psi_0)$ is found using Equations (2.10), (2.14), and (2.15) as before.

The classical anisotropy as a function of energy level has been derived according to this formula for the four distinct symmetric top principal axis dipole cases: $(\|, \|)$, $(\|, \perp)$, $(\perp, \|)$, and $(\perp, \perp)$. These are found to agree exactly with the high j limits of the quantum expressions for these cases, which were given explicitly in Ref. 1. In particular, the $(\perp, \perp)$ case can be derived by letting both $\vec{d}_1$ and $\vec{d}_2$ lie along either the x or y molecular axis. Choosing x one finds, after some simplification,

$$\begin{aligned}\cos\eta(t) = \hat{x}(0)\cdot\hat{x}(t) = -\cos\theta\sin\omega_1 t\ \sin\omega_2 t + \cos\omega_1 t\ \cos\omega_2 t + \\ (1-\cos\omega_1 t)\sin^2\theta\ \sin\psi_0\ \sin(\psi_0+\omega_2 t)\ .\end{aligned} \tag{2.20}$$

When this is substituted into Equations (2.10) and (2.19), the following result is obtained:

$$\begin{aligned}r_{\perp,\perp} = {}& \frac{1}{40}(3\cos^2\theta - 1)^2 + \frac{3}{10}\cos^2\theta\ \sin^2\theta\ \cos\omega_1 t + \frac{3}{40}\sin^4\theta\ \cos(2\omega_1 t) \\ & + \frac{9}{80}\sin^4\theta\ \cos(2\omega_2 t) + \frac{3}{40}(1+\cos\theta)^2\sin^2\theta\ \cos\big((\omega_1 + 2\omega_2)t\big)\end{aligned}$$

$$+\frac{3}{40}(1-\cos\theta)^2\sin^2\theta\,\cos\big((\omega_1-2\omega_2)t\big)+\frac{3}{160}(1+\cos\theta)^4\,\cos\big(2(\omega_1+\omega_2)t\big)$$
$$+\frac{3}{160}(1-\cos\theta)^4\,\cos\big(2(\omega_1-\omega_2)t\big)\ . \qquad (2.21)$$

One finds again that the detailed calculation confirms the properties expected from the simple considerations of Section I. Modulations of the anisotropy are due to both nutation and rotation but only the first harmonic of the rotation frequency appears.

While Eq. (2.21) agrees exactly with the high j limit of the $(\perp,\perp)$ case given in Ref. 1, it is in disagreement with the high j expression for this case given in Eq. (12) of Ref. 20. For comparison with that result, the last four terms of Eq. (2.21) can be rewritten as

$$\ldots+\frac{3}{20}(1-\cos^4\theta)\cos\omega_1 t\,\cos(2\omega_2 t)+\frac{3}{80}(1+6\cos^2\theta+\cos^4\theta)\cos(2\omega_1 t)\,\cos(2\omega_2 t)$$
$$-\frac{3}{10}\cos\theta\,\sin^2\theta\,\sin\omega_1 t\sin(2\omega_2 t)-\frac{3}{20}\cos\theta(1+\cos^2\theta)\sin\omega_1 t\,\sin(2\omega_2 t)\ . \qquad (2.22)$$

The last two terms in Eq. (2.22) are omitted in Ref. 20 with the explanation that terms in $\sin(2\omega_2 t)$ cancel in the ensemble average. As pointed out, because $2\omega_2 \propto k$, $\sin(2\omega_2 t)$ is an odd function in k, and positive or negative k are equally probable. The terms associated with positive and negative k do not cancel, however, because $\cos^n\theta \equiv (k/j)^n$ is also an odd function of k for odd n. Thus, each complete term is even in k, and the identical anisotropies calculated for positive and negative k add constructively rather than cancel. Such must be the case physically, for the choice of a positive reference direction for the specification of k is completely arbitrary for any particular molecule.

We now consider calculation of the macroscopic anisotropy, based on the full summation over final states indicated in Eq. (2.12). The evaluation of Eq. (2.12) must in general be carried out numerically for a Boltzmann distribution in the stable molecule problem. The general features of the resulting anisotropies can, however, be illustrated fairly accurately by a situation for which an analytical solution is possible. This is the case of a linear or diatomic M_2 when it is assumed that the product of P_j^l and B, expressed as a function of the one dimensional variable j, is a Gaussian centered at j_0 with half-width at $1/e$ of Δj. Considering first $j_0 = 0$ and j continuously distributed over 0 to $+\infty$, upon substitution for $r(j,t)$ from Eq. (2.18), the integration of Eq. (2.12) can be carried out exactly to give

$$\begin{aligned} r_{\parallel,\parallel}(t) &= \int_0^\infty e^{-\left((j-j_0)/\Delta j\right)^2}\left(0.1 + 0.3\cos(2j\omega_{n0}t)\right)dj \Bigg/ \left(\int_0^\infty e^{-\left((j-j_0)/\Delta j\right)^2}dj\right) \\ &= 0.1 + 0.3e^{-(\Delta j\omega_{n0}t)^2} \ . \end{aligned} \tag{2.23}$$

Thus, the initial anisotropy of 0.4 decays nonexponentially with a rotational coherence time of $\tau_c = (\Delta j\omega_{n0})^{-1}$ to the asymptotic value of 0.1. Allowing only integral j does not alter the dephasing time even if Δj is as small as 2 or 3. Two differences are noted, however. First, the asymptote in the discrete case increases to $0.1 + .15/\left(\sum_j e^{-(j/\Delta j)^2}\right)$ because the constant contribution to the anisotropy (of 0.4) associated with $j = 0$ is no longer of infinitesimal measure. Secondly, full recurrences in the anisotropy occur at times $t = n/(4B_\perp)$ for integer n. (The asymptote above is less than the time average of $r(t)$ because of these positive recurrences.) These features are suggestive of expected distinctions between the quantum mechanical and classical behavior, but they should not be considered quantitatively accurate due to the approximate nature of the classical to quantum frequency correspondence. Of primary importance to us here is the fact that comparisons of measured and calculated early time behavior will be sensitive to the choice of a discrete or continuous distribution of angular momenta only for $\Delta j \leq 5$.

If the above Gaussian distribution is displaced to a nonzero center frequency j_0, the integration can still be carried out if the distribution is extended to $-\infty$. This gives a result which approaches the integral of the actual distribution, which is truncated at $j = 0$, for $j_0 \gg \Delta j$ and also provides a good approximation for $j_0 \geq \Delta j$. One finds in this case a damped oscillation of the anisotropy:

$$r_{\parallel,\parallel}(t) = 0.1 + 0.3\cos(2j_0\omega_{n0}t)e^{-(\Delta j\omega_{n0}t)^2} \tag{2.24}$$

The coherence decay rate as revealed by the damping of the oscillations is proportional to Δj, as before. The initial decay of the anisotropy is now determined primarily by j_0 and is faster than before, since $j_0 \geq \Delta j$. For example, a diatomic thermal distribution at a high enough temperature so that the most probable j is much greater than 1/2 can be reasonably approximated by a Gaussian for which $j_0 \simeq 1.13\Delta j$. When these values are substituted into Eq. (2.24), the initial decay of $r(t)$ is followed by a clearly discernible dip below the 0.1 asymptote before the coherence is completely lost. The basic properties of the time dependence of $r_{\parallel,\parallel}$ displayed in Eq. (2.24), although derived for a diatomic M_2 and an ideal distribution of angular momenta, can nevertheless be recognized in the behavior of more complicated systems.

If the Gaussian distribution in Eq. (2.23) is replaced by the high j, one dimensional Boltzmann distribution $2je^{-\frac{1}{2}Bhj^2/(k_BT)}$ for a diatomic at rotational temperature T, the macroscopic $r_{\parallel,\parallel}(t)$ can be given exactly by expanding the exponential and cosine, and integrating term by term. The result is expressible as a series expansion in the product $\left(\frac{k_BT}{I}\right)t^2$, as recognized by Gordon.[12] One finds

$$r_{\parallel,\parallel} = 0.1 + 0.4 \cdot \sum_{n=0}^{\infty} (-1)^n \cdot 3 \cdot 2^{(3n-2)} \frac{n!}{2n!} \left(\frac{k_BT}{I}\right)^n t^{2n} \ . \tag{2.25}$$

Thus, the time evolution of the signal scales as $\sqrt{I/(k_bT)} \propto (TB)^{-\frac{1}{2}}$. This scaling has also been shown to be valid to good approximation for thermal distributions of nonlinear molecules.[1]

ii. Time dependent alignment of dissociation products

In this subsection, we are concerned with the time evolution of product alignment under collisionless conditions following a unimolecular dissociation or "half-collision," which is initiated by pulsed laser excitation. The systems considered dissociate into atom + molecule, i.e.,

$$\mathrm{M}_1 \quad \xrightarrow{h\nu} \quad \mathrm{M}_1^* \quad \longrightarrow \quad \mathrm{M}_2 + \mathrm{A} \ . \tag{2.26}$$

M_2 may range from a diatomic to a large polyatomic, under the restriction, however, that only symmetric top motion will be treated in detail. The reaction is illustrated in Fig. 7 for a single molecule. $\hat{\epsilon}_1$, $\hat{\epsilon}_2$, $\vec{d}_1$, $\vec{d}_2$, and δ have been previously defined. In the particular case shown, $\vec{d}_1$ and $\vec{d}_2$ are both parallel to the figure axis of M_2. The time evolution of alignment of the dipole moments ($\vec{d}_2$) of the product molecules will be reflected in a time-dependent polarization anisotropy of the signal.

Two types of dissociation process will be considered in this thesis: those for which the initially excited state is bound, such as the various types of predissociation; and those for which the initial excitation is to an unbound state of the system, as to a repulsive electronic potential surface. In the case of predissociation, a finite time t_d is required for transition from the initially excited state to an unbound state of equal total energy. In the second type of process described above, $t_d = 0$. We will refer henceforth to any case for which t_d is negligible on the scale of rotational motion as prompt dissociation. In it, the motion of free M_1^* can be ignored, resulting in a much simpler treatment. The results may also serve as a useful approximation for cases in which t_d is not completely negligible but still short compared to the period of rotation of the parent M_1.

In order to calculate the time dependence of the probe signal as a function of probe polarization for the reaction described by Eq. (2.26), the rotational motion of each dipole must be traced continuously from $t = 0$, the moment when the alignment of the reactant population is created by the excitation pulse. This requires a knowledge not only of the free motion of M_1^* preceeding dissociation ($t < t_d$) and that of the free M_2 following complete separation of the fragments, but also a knowledge of any motion occurring while the fragments are in close proximity, during which time the partition between potential, translational, and rotational energy is still evolving. Such a detailed calculation is possible only when the interaction potential of the fragments is precisely defined. Single particle trajectory calculations of this type for specific model potentials, similar to those carried out in the investigation of product rotational energy distributions,[22,36,37] may be instructive, revealing unique consequences of the final state interactions. However, the data available on excited electronic potential surfaces is often insufficient to warrant such a precise treatment on a case by case basis. To permit a simple, unified treatment of the generic fast dissociation reaction, it will be assumed here that the duration of the "transition state" between reactant and free product is negligible when compared with the rotational periods entering significantly into the calculation. In this "impulsive dissociation" approximation, only the initial geometry, the direction of the impulse in the molecular frame and the available energy E' need be specified. Failure to achieve detailed quantitative agreement between the predictions of this simple model and experimental results may serve as an indicator of the importance of final state interactions in the particular system under study.

Referring again to Fig. 7, we now define those quantities specific to the dissociation problem. The position occupied by A within M_1, relative to the center of mass of M_2, is designated by $\vec{r}$. In the impulsive approximation adapted here, M_2 acquires an angular momentum $\vec{j}$ instantaneously at t_d. The translational motion of the fragments in the M_1^* center of mass frame is characterized by separation of the centers of mass of M_2 and A with equal and opposite linear momenta, along trajectories which are displaced from each other by the impact parameter b. The energy difference E' between the internal energy of M_1^* and that of the products appears as kinetic energy of rotation and translation. Conservation of total angular momentum yields the condition

$$\vec{j} + \vec{L} = \vec{J} \tag{2.27}$$

where $\vec{L}$ is the angular momentum of separation of A and M_2, referred to as the orbital angular momentum of the products. $\vec{L}$ is determined completely by b and the velocities of separation.

In prompt, impulsive dissociations, only M_2 rotation is important, so $\eta(t)$ is determined as it was for stable molecule rotation by the three parameters j, θ, and ψ_0. The classical state resolved anisotropies $r(j,\theta,\psi_0,t)$ are thus identical for the two cases. It is only the different weights in the summation of Eq. (2.12) which distinguish the two. The divergence will begin in general even with the integration over ψ_0 to find the anisotropies of individual energy levels, for, while ψ_0 is uniformly distributed over 2π for a thermal distribution of stable molecules, the distribution of ψ_0 following dissociation will normally be very nonuniform (*vide infra*).

In one case, however, differences in the distribution of ψ_0 are unimportant. This is the $(\|,\|)$ dipole case, for which it was found that $r(j,\theta,\psi_0,t)$ is independent of ψ_0. Consequently, $r_{\|,\|}(j,\theta,t)$ following prompt, impulsive dissociation is identical to that for the excitation of an isotropic sample of stable, freely rotating symmetric top molecules, as given in Eq. (2.18) and previously derived.[1,20] Even in this simple case, macroscopic anisotropies can differ substantially if the distribution of dissociation products over rotational energy levels is not similar to a thermal distribution.

In all other situations of interest, values for the weights in Eq. (2.12) are required. $P_j(j,\theta,\psi_0)$, the distribution of final rotational state populations, is again the factor of greatest concern. It is this distribution that establishes the link between time-resolved anisotropy and the geometric and dynamic details of dissociation. These details determine the state-to-state branching ratio $p_{i\rightarrow f}$ which appears in the general expression for P_j [Eq. (2.7)]. P_j itself is most generally only an intermediate product of the calculation of $r(t)$ using Equations (2.7) and (2.12). In certain cases, however, P_j may be derived from measured distributions of dissociation products. These measurements give the populations of rotational energy levels, $P_j'(j,\theta)$, leaving only the ψ_0 dependence of the full distribution to be determined. When this dependence is known or can be approximated (as, e.g., for $(\|,\|)$ dipoles) the time evolution of the macroscopically observable anisotropy will be completely determined by $P_j'(j,\theta)$ and the spectral window opened by the probe. However, even in this case, the dynamic origins of P_j are of fundamental interest. In the remainder of this section, P_j will be related directly to the three physical sources of M_2 rotation: initial rotation of M_1, the torque applied by repulsion between M_2 and A as they dissociate, and initial vibration of M_1.

When a rotating rigid body falls apart without release of internal energy ($E' = 0$) the kinetic energy and hence the velocities of all its constituant parts are conserved. In the present context, M_2 and A will separate with the instantaneous relative velocity of their centers of mass, and M_2 will have angular momentum $\vec{j}_r$ determined by the instantaneous angular velocity $\vec{\omega}_0$ of M_1 at $t = 0$. With $\mathbf{I\!I}'$ and $\mathbf{I\!I}$ representing the inertia tensors of M_1 and M_2, respectively, one has $\vec{\omega}_0 = (\mathbf{I\!I}')^{-1}\,\vec{J}$ and therefore

$$\vec{j}_r = \mathbf{I\!I}(\mathbf{I\!I}')^{-1}\vec{J}\,. \tag{2.28}$$

(For a linear M_1, for which the inertia tensor is not invertible, the inertia tensors may be replaced by the scalar moments about the perpendicular axes.) In this general form, Eq. (2.28) is understood to require the evaluation of all terms relative to parallel cartesian coordinate axes at $t = 0$. However, it is more convenient and appropriate to represent $\vec{J}$ and $\mathbf{I\!I}'$ in the M_1 principle axis frame (frame 1), while $\vec{j}$ and $\mathbf{I\!I}$ are naturally represented in the M_2 principle axis frame (frame 2). Using the subscripts 1 and 2 to indicate the reference frame of the representation, one may write

$$\begin{aligned}\vec{j}_{r2} &= \mathbf{I\!I}_2\left(\mathbf{U}(\mathbf{I\!I}'_1)^{-1}\mathbf{U}^{\mathrm{T}}\right)\left(\mathbf{U}\vec{J}_1\right)\\ &= \mathbf{I\!I}_2\mathbf{U}(\mathbf{I\!I}'_1)^{-1}\vec{J}_1\end{aligned} \tag{2.29}$$

where $\mathbf{U}$ is the matrix of the unitary transformation from frame 1 to frame 2. $\mathbf{I\!I}'_1$ and $\mathbf{I\!I}_2$ are both diagonal with diagonal elements I_i and I'_i, $i = x, y, z$. As a simple example of the use of Eq. (2.29), when $\mathbf{I\!I}'$ and $\mathbf{I\!I}$ are diagonal in the same reference frame, a fraction I_i/I'_i of the M_1 angular momentum along the ith coordinate axis is transferred to M_2.

The unitary matrix U may be given explicitly for principal axis coordinate systems of M_1 and M_2 which are applicable for all symmetric top M_2 as well as for any system in which the atom A lies in a symmetry plane of M_2. In these situations the choice and/or labeling of axes of the M_2 coordinate system can be made in such a way that the atom A lies in its yz plane. We are concerned primarily with symmetric M_2, for which, as usual, the figure axis is taken as the z axis. The principle moments of inertia of M_2 are I_x, I_y, and I_z, and the components of the vector $\vec{r}$ locating A in the M_2 frame (with origin at the M_2 center of mass) are $(0, y_{\mathrm{A}}, z_{\mathrm{A}})$. From these data, the inertia tensor of M_1 relative to an axis system with axes parallel to the M_2 principle axes may be written

$$\mathbb{I}'_2 = \begin{pmatrix} I_x + \mu r^2 & 0 & 0 \\ 0 & I_y + \mu z_{\mathrm{A}}^2 & -\mu\, y_{\mathrm{A}} z_{\mathrm{A}} \\ 0 & -\mu\, y_{\mathrm{A}} z_{\mathrm{A}} & I_z + \mu y_{\mathrm{A}}^2 \end{pmatrix} \tag{2.30}$$

where μ is the reduced mass of M_2 and A. With the axes of the M_1 principle axis frame labeled so that $I'_y > I'_z$, the principle moments of M_1 are

$$\begin{aligned} I'_x &= I_x + \mu r^2 \\ I'_y &= \frac{1}{2}(I_y + I_z + \mu r^2) + \frac{1}{2}\sqrt{w^2 + (2\mu\, y_{\mathrm{A}} z_{\mathrm{A}})^2} \\ I'_z &= \frac{1}{2}(I_y + I_z + \mu r^2) - \frac{1}{2}\sqrt{w^2 + (2\mu\, y_{\mathrm{A}} z_{\mathrm{A}})^2} \end{aligned} \tag{2.31}$$

where $w = I_y - I_z + \mu(z_{\mathrm{A}}^2 - y_{\mathrm{A}}^2)$. Finally, defining $D_\pm$ as

$$D_\pm = \sqrt{(\mu\, y_{\mathrm{A}} z_{\mathrm{A}})^2 + \frac{1}{4}\left(w \pm \sqrt{w^2 + (2\mu\, y_{\mathrm{A}} z_{\mathrm{A}})^2}\right)^2}\ , \tag{2.32}$$

the transformation matrix U, composed of the eigenvectors of $\mathbb{I}'_2$, is

$$\mathbf{U} = \begin{pmatrix} 1 & 0 & 0 \\ 0 & \frac{\mu\, y_{\mathrm{A}} z_{\mathrm{A}}}{D_-} & \frac{\mu\, y_{\mathrm{A}} z_{\mathrm{A}}}{D_+} \\ 0 & \frac{-\mu\, y_{\mathrm{A}} z_{\mathrm{A}}}{D_+} & \frac{\mu\, y_{\mathrm{A}} z_{\mathrm{A}}}{D_-} \end{pmatrix}\ . \tag{2.33}$$

The corresponding equations of transformation for matrix **A** and vector $\vec{y}$ are

$$\mathbf{A}_2 = \mathbf{U}\mathbf{A}_1\mathbf{U}^{\mathrm{T}}\ ,\ \vec{y}_2 = \mathbf{U}\vec{y}_1\ . \tag{2.34}$$

If we consider next a stationary rigid M_1 which is split apart by an impulsive force, the resulting angular momentum of M_2 can be calculated by invoking conservation of energy and momentum. Recall that $\vec{r}$ locates A in the M_2 frame (Fig. 7). Taking $\hat{f}$ as a unit vector in the direction of the force on M_2, $\hat{t}$ a unit vector in the direction of $\vec{r} \times \hat{f}$ (i.e., in the direction of the torque on M_2), $b_0 = |\vec{r} \times \hat{f}|$, and μ the reduced mass of A and M_2, $\vec{j}_t$ is given by

$$\vec{j}_t = \left(\frac{2E'}{\frac{1}{\mu b_0^2} + \left(\mathbb{I}^{-1}\hat{t}\right) \cdot \hat{t}} \right)^{\frac{1}{2}} \hat{t} \,. \tag{2.35}$$

Frame 2 is the natural frame of representation for all quantities in this equation.

When a rigidly rotating molecule dissociates impulsively, the final angular momentum of M_2 is composed of two independent contributions:

$$\vec{j} = \vec{j}_r + \vec{j}_t \tag{2.36}$$

with $\vec{j}_r$ and $\vec{j}_t$ calculated by Equations (2.29) and (2.35). The key to this independence is the assumption of impulsive dissociation under which all interaction is complete before any relative motion of the products can occur. Note, however, that although $\vec{j}_t$ does not depend directly on $\vec{J}$, if the assumption of rigidity is relaxed, the initial rotational motion may affect $\vec{j}_t$ indirectly by inducing distortion of M_1 and thereby changing the direction of $\hat{f}$.

Vibrations of M_1 that involve displacement of A affect the final rotation of M_2 in a more complicated manner. The $\vec{j}$ produced from a given $\vec{J}$ may be different at each point of the vibrational trajectory due to varying geometry, instantaneous angular velocity of M_2, and available vibrational potential energy. In the cases we will consider, the vibrational energy initially in the M_2–A bond is small compared to the total kinetic energy of the products. In view of the very approximate nature of the impulsive dissociation mechanism used to determine the partitioning of most of this energy between rotation and translation, a detailed treatment of the small vibrational contribution is not warranted here. The constant sum of kinetic and potential vibrational energy will simply be incorporated into E' and partitioned as determined by the resulting "effective" impulse. The effect of initial geometry on $\vec{\jmath}$, and on $\vec{\jmath}_t$ in particular, can be major, however, so the distribution of geometries associated with vibrational motion may not be neglected in general. A simple model of the role of vibration can be realized by averaging the rigid body dissociation described by Eq. (2.36) over a distribution of positions of A along the appropriate coordinate. We therefore proceed to derive the P_j arising from a single fixed geometry, bearing in mind that a final vibrational average may be required to yield the final distribution.

Writing Eq. (2.36) as $\vec{\jmath} = \mathbf{I\!I}(\mathbf{I\!I}')^{-1}\vec{J} + \vec{\jmath}_t$, we see that for fixed $\vec{\jmath}_t$ the mapping of initial $\vec{J}$ to final $\vec{\jmath}$ is one-to-one. (This is true in three dimensions only if both $\mathbf{I\!I}'$ and $\mathbf{I\!I}$ are invertible, but similar results are applicable in two dimensions for linear molecules.) Thus $p_{i\to f}$ is simply a delta function corresponding to the mapping defined by Eq. (2.36). That is, in the discrete formulation of Eq. (2.7), the desired population $P_j(\vec{\jmath})$ is

$$P_j(\vec{\jmath}) = \frac{C_a}{3}\, P_J\big(\vec{J}(\vec{\jmath})\big) \tag{2.37}$$

where $\vec{J}(\vec{\jmath})$ is found by inverting Eq. (2.36):

$$\vec{J}(\vec{\jmath}) = \mathbf{I\!I}'\mathbf{I\!I}^{-1}(\vec{\jmath} - \vec{\jmath}_t)\ . \tag{2.38}$$

As discussed in connection with Eq. (2.28), Eq. (2.38) can be written in a form more suitable for calculations with specification of the representation used for each quantity:

$$\vec{J}_1 = \mathbf{I\!I}'_1\mathbf{U}\mathbf{I\!I}_2^{-1}(\vec{\jmath}_2 - \vec{\jmath}_{t2})\ . \tag{2.39}$$

If the angular momentum is to be treated as continuously distributed, the population functions $P_J(\vec{J})$ and $P_j(\vec{\jmath})$ are defined so that $\iiint P_J\, d^3J = N$ for a nonlinear molecule and $\iiint P_J\, d^2J = N$, $(j_z \equiv 0)$ for a linear molecule, and likewise for P_j. In this case, when applying the change of coordinates from J to j space defined by Eq. (2.38), the absolute magnitude of the Jacobian determinant of the transformation must be included in Eq. (2.37) to account for the change in volume element.

In the calculations to follow, we will consider only situations for which the initial angular momentum distribution is thermal. The correct high J limit for M_1 of arbitrary structure is

$$P_J(\vec{J}) = \frac{N}{\pi Q} e^{-(E(\vec{J})/kT)} \tag{2.40}$$

where $E = h(B_x J_x^2 + B_y J_y^2 + B_z J_z^2)$ for $\vec{J}$ in the M_1 principle axis frame and the classical rotational partition function Q is equal to $\sqrt{\pi k^3 T^3/(h^3 B_x B_y B_z)}$ for nonlinear M_1 or $kT/(Bh)$ for linear M_1. To facilitate the transformation to j space, E/kT may be written as

$$E(\vec{J})/kT = \left(\mathbf{F}\vec{J}_1\right)^2 \tag{2.41}$$

where

$$\mathbf{F} = \sqrt{\frac{h}{kT}} \begin{pmatrix} \sqrt{B_x} & 0 & 0 \\ 0 & \sqrt{B_y} & 0 \\ 0 & 0 & \sqrt{B_z} \end{pmatrix} . \tag{2.42}$$

With the definition $\mathbf{G} = \mathbf{\Pi}'_1 \mathbf{U} \mathbf{\Pi}_2^{-1}$, Equations (2.37), (2.39), (2.40), and (2.41) may be combined to give the explicit dependence of product population on the vector $\vec{j}$, following dissociation of a thermally equilibrated sample:

$$P_j(\vec{j}_2) = \frac{C_a}{3} \frac{N}{\pi Q} \exp\left(-(\mathbf{F}\mathbf{G}\vec{j}_2 - \mathbf{F}\mathbf{G}\vec{j}_{t2})^2\right) ||\mathbf{G}|| . \tag{2.43}$$

The Jacobian determinant, $|\mathbf{G}|$, of the linear transformation is a constant.

Equations (2.43), (2.35), and (2.12) constitute the general framework for calculation of the anisotropies of dissociation products. Specific examples of such calculations are discussed in Section IV of Chapter 5.

III. Purely Rotational Coherence of Asymmetric Top Molecules

In the first two sections of this chapter, a detailed picture of rotational coherence in symmetric top molecules was developed. By restricting the discussion to symmetric tops, the major features of the phenomenon could be revealed with a minimum of complication. However, because most molecules are not symmetric tops, the quantitative analysis of experimental results is principally dependent on a detailed understanding of rotational coherence in asymmetric top molecules. Such is clearly the case for the measurements discussed in Section II of Chapter 5. The rigorous quantum mechanical theory of PRC in asymmetric tops was developed in Ref. 1. Later in this section, we will review the details of this theory as they relate to the implementation of efficient simulation and fitting procedures used in the analysis of our experimental data. First, we attempt to give some physical insight into the way in which asymmetry alters the by now well-known characteristics of PRC as manifested in symmetric top molecules.

Consider again the picture of PRC as developed in Section I and based on the classical rotation displayed in Fig. 1. For a prolate symmetric top such as the one pictured, the figure axis, as the axis of smallest moment of inertia, is the a axis. When the two principal moments of inertia about axes perpendicular to the a axis differ, the axis are designated b and c according to the convention $I_a < I_b < I_c$. The rotation of the asymmetric top is naturally more complicated than that shown in Fig. 1, with the degree of deviation depending both on the degree of asymmetry and the direction of $\vec{J}$ in the molecule. When $\vec{J}$ is near either the a or c axis (corresponding to the highest and lowest rotational energies, respectively, for the given $J = |\vec{J}|$), the motion is very close to that of a symmetric top with the role of the figure axis played by the principal axis nearest $\vec{J}$. The nutation frequencies in the two limits differ, however, as they depend on the average of the moments about the axes perpendicular to the effective figure axis. Moreover, for a range of intermediate energies determined by the degree of asymmetry, the motion is very irregular, with no principal axis maintaining even an approximately constant angle with $\vec{J}$. This leads to a loss of commensurability of the periodicities associated with different initial states so that the regularly spaced sharp recurrences seen following thermal averaging in the symmetric limits are expected to broaden (initially) and diminish as the asymmetry increases.

Considering the problem from the quantum mechanical perspective, we recall that PRC recurrences in symmetric tops were a consequence of the regular spacing of rotational energy levels. Asymmetry shifts rotational levels away from this regular spacing, with the shift strongly dependent on the corresponding symmetric limit K value. This produces just the result expected: quantum beats from different initial levels are not commensurable, and the frequencies are associated in some sense with the direction of $\vec{J}$ relative to the principal axes of the molecule. Macroscopic recurrences will be weakened accordingly. In fact, strictly periodic recurrences are not expected since no single frequency will be shared by all molecules of the sample. However, simulations have shown that, even for fairly large asymmetries, the equal spacing of clearly defined nutation-like recurrences is retained to good approximation. In contrast, distinct, periodic rotation recurrences are seen only for very small asymmetries. We will refer to the (quasi-) periods associated with these two types of recurrences as τ_1 and τ_2, respectively.

Due to the incommensurability of beats in the asymmetric top, the relationship between excited-state rotational constants and PRC recurrence periods is no longer trivial. In the following, approximate expressions for the rotational energies of an asymmetric top are used to investigate this relationship. Because it is based on rotational energy expansions that are accurate at low J only, this treatment is only applicable to samples at low rotational temperatures, such as those encountered in molecular beam experiments.

For low values of J, it is possible to represent the energies of an asymmetric rigid rotor in power series expansions in $J(J+1)$ and the asymmetry parameter $b = \frac{1}{2}(C-B)/[A-\frac{1}{2}(B+C)]$, which goes to zero in the prolate symmetric limit.[38] (An equivalent expansion in $b^* = \frac{1}{2}(A-B)/[C-\frac{1}{2}(A+B)]$ is preferred when the molecule is near oblate. The discussion below is based on the prolate case.) Energy levels are each designated by a value of K from 0 to J with two levels for each nonzero K. From these expansions, the following conclusions may be drawn: 1) For small b, the energy expressions are approximated by those of a symmetric top with B replaced by $\bar{B} \equiv \frac{1}{2}(B+C)$. A first estimate of rotational constants is thus provided by the modified symmetric top relations

$$B' + C' \simeq 1/\tau_1 \tag{3.1}$$

and

$$4[A' - \frac{1}{2}(B' + C') \simeq 1/\tau_2 \ . \tag{3.2}$$

2) Leading corrections to the symmetric top-like expressions are of second order in b for all levels, except for a first-order splitting of the $K = 1$ levels. Since a pure level splitting (i.e., without displacement of the average energy) results in quantum beat frequencies symmetrically displaced from the unperturbed value, it will affect recurrence amplitudes but have little effect on recurrence periods in thermally averaged PRC signals. Therefore, the b^2 terms are the first terms capable of causing deviations from the expressions given above.

Including expansion terms up to b^2, but neglecting asymmetry splitting, one obtains the following expression for rotational energy:

$$\begin{aligned} E/h \equiv F(J,K) = {} & \left[\bar{B} + \frac{1}{4}(A-\bar{B})b^2\right] J(J+1) + (A-\bar{B})(1-\frac{3}{8}b^2)K^2 \\ & + \frac{1}{8}\eta(K)(A-\bar{B})b^2 J^2(J+1)^2 \end{aligned} \tag{3.3}$$

which can be written

$$F(J,K) = B^* J(J+1) + (A-B)^* K^2 + f(J,K) \ . \tag{3.4}$$

The function $\eta(K)$ is equal to $1/(K^2-1)$ for all K other than 1, while $\eta(1) = -\frac{1}{4}$. It may be noted that B^* is equal to $B + \Delta B^K_{\text{eff}}$ as defined by Herzberg in his discussion of asymmetric top spectra.[39]

Without the term $f(J,K)$, these energies would lead to recurrence periods given by $1/(2\bar{B}^*)$ and $1/[4(A-B)^*]$ by analogy with the symmetric top. Unfortunately, $f(J,K)$ plays a significant role and the effect of its dependence on both J and K defies any simple expression.

Consider for example the spacings between adjacent J levels at fixed K, which are responsible for the symmetric top nutation period. These are

$$\Delta^K_{J-1,J} \equiv F(J,K) - F(J-1,K) = \left[2B^* + \frac{1}{2}\eta(K)(A-\bar{B})b^2J^2\right]J \tag{3.5}$$

and

$$\Delta^K_{J,J+1} = \left[2B^* + \frac{1}{2}\eta(K)(A-\bar{B})b^2(J+1)^2\right](J+1)\ . \tag{3.6}$$

With an effective rotational constant B_{eff} defined by

$$\begin{aligned} B_{\text{eff}}(J,K) &= B^* + \frac{1}{4}\eta(K)(A-\bar{B})b^2(J^2+J+\frac{1}{2}) \\ &= \bar{B} + \frac{1}{4}(A-\bar{B})b^2\left[1+\eta(K)(J^2+J+\frac{1}{2})\right]\ , \end{aligned} \tag{3.7}$$

these may be written

$$\Delta^K_{J-1,J} = \left[2B_{\text{eff}}(J,K) - \delta(J,K)\right]J \tag{3.8}$$

and

$$\Delta^K_{J,J+1} = \left[2B_{\text{eff}}(J,K) + \delta(J,K)\right](J+1) \tag{3.9}$$

where

$$\delta(J,K) = \frac{1}{4}\eta(K)(A-\bar{B})b^2(2J+1)\ . \tag{3.10}$$

These two splittings and their sum, $2B_{\text{eff}}(J,K)(2J+1) + \delta(j,K)$, are then the beat frequencies associated with the quasi-nutation of the molecule in the single level with initial quantum numbers J and K. These frequencies are not exactly commensurable due to $\delta(J,K)$, but this last term is generally very small relative to $2B_{\text{eff}}(J,K)$. Thus, the single level rotational coherence will be nearly periodic with a fundamental frequency given to good approximation by $2B_{\text{eff}}(J,K)$. The primary contribution of $\delta(J,K)$ will be simply to slowly damp the recurrences.

Of more concern than the effect of $\delta(J,K)$ is the fact that B_{eff} is a function of J and K. Because of this, single-molecule rotational coherences at many different fundamental frequencies will contribute to the macroscopic PRC signal. This is precisely the circumstance that the qualitative description at the beginning of this section led us to anticipate. Macroscopic recurrences will still be seen, however, when the fundamental frequencies of a substantial fraction of the sample population lie close enough together that peaks in the corresponding beat patterns partially overlap and reinforce each other. The resultant frequency $1/\tau_1$ will then be a weighted average of the frequencies $2B_{\text{eff}}(J,K)$ of the contributing levels, or

$$1/\tau_1 = \big\langle 2B_{\text{eff}}(J,K)\big\rangle = 2\bar{B} + \frac{1}{2}(A-\bar{B})b^2\Big[1 + \big\langle \eta(K)(J^2+J+\frac{1}{2})\big\rangle\Big] \qquad (3.11)$$

where the angle brackets denote the required average. If we define a parameter α by

$$\alpha = \frac{1}{2} + \frac{1}{2}\langle \eta(K)(J^2+J+\frac{1}{2})\rangle \qquad (3.12)$$

and approximate $(A-\bar{B})$ in Eq. (3.11) by $\big(A-1/(2\tau_1)\big)$, we may give the following correction to Eq. (2.1):

$$B' + C' = 1/\tau_1 - \alpha\big[A' - 1/(2\tau_1)\big]b^2 \ . \qquad (3.13)$$

We refer to the second term of the right-hand side of this equation as the asymmetry correction. A similar correction could, of course, be derived for the rotation period given by Eq. (3.2). A clear example of rotation recurrences has not been seen experimentally, however, so there has been no practical requirement for such a correction. PRC simulations indicate that Eq. (3.13) accounts well for the dependence of the asymmetry correction on b. The practical application of this equation will be discussed after consideration of the parameter α.

Due to the nature of the superposition process, the weights in the average of Eq. (3.12) are not simply determined by the level populations and intensities, so an analytical evaluation of α appears impossible. For the purpose of making a reasonable estimate of its value, we note that $\eta(K)$ is always positive unless $K = 0$ or 1. (Recall that $\eta(K) = -1, -1/4, 1/3, 1/8, 1/15, \ldots$, for $K = 0, 1, 2, 3, 4, \ldots$.) The large size of $\eta(0)$ makes the frequencies of $K = 0$ levels differ greatly both from those of all other K levels and from each other for different J, minimizing the possibility of constructive interference. The contribution of $K = 0$ is further reduced by its single weight. For $K = 1$, due to the rapid increase with J of the asymmetry splitting, constructive (in-phase) addition of beats from its two components alternates with out-of-phase addition (for changes of a few quanta or less in J in the asymmetry range considered), so many $K = 1$ levels have little or no potential of contributing to PRC recurrences. And again, as for $K = 0$, peaks that do appear are relatively unlikely to overlap with the peaks of higher K level beats because of the size and sign of η. These considerations suggest, and simulations confirm, that the prominent macroscopic recurrences in asymmetric top PRC are associated with the $K \geq 2$ manifolds. Thus, the quantity $\langle \eta(K)(J^2 + J + \frac{1}{2}) \rangle$ may be well approximated by $\langle (J^2 + J)/(K^2 - 1) \rangle$.

J and K in the above average are both low integers with $J \geq K \geq 2$. For $J < 15$ individual terms range from 1.08 up to 70, yielding an average always greater than, but of the order of, 1. For the molecules and conditions relevant to the experimental studies in Chapter 5 of this thesis, values ranging from ~ 2 to 8 have been derived by comparison with PRC simulations. The higher values are associated with the more prolate molecules as might be expected due to the low population of high K levels. By contrast, for oblate tops the largest populations are found in levels with $K = J$, and a value of $\langle (J^2 + J)/(K^2 - 1) \rangle = 1.6$ was derived from a PRC simulation for a set of rotational constants much nearer the oblate symmetric top limit ($b^* = -0.167$).

If the average $\langle \eta(K)(J^2 + J + \frac{1}{2}) \rangle$ were 0, Eq. (3.11) tells us that $1/\tau_1$ would be equal to $2\bar{B} + \frac{1}{2}(A - \bar{B})b^2 \equiv 2B^*$, as predicted from Eq. (3.4) when $f(J, K)$ is neglected. However, from Eq. (3.12) and the fact that the average is greater than 1, we conclude that the asymmetry correction is actually at least twice as large. The result for the prolate top is a recurrence period τ_1 such that $\tau_1 < 1/(2B^*) < 1/(2\bar{B})$. For the oblate top, the corrections are of opposite sign, since A' is replaced by C' in Eq. (3.13), and $C' - 1/(2\tau_1)$ is negative.

Although α is found to be molecule and temperature dependent, Eq. (3.13) may still be of practical value. From PRC simulations covering the range of rotational constants and temperatures of interest in our experiments, we found that the empirically determined asymmetry correction was given to within $\sim 50\%$ accuracy by Eq. (3.13) with $\alpha = 3$. From this result we conclude that, given an experimentally determined recurrence period and approximate values of A' and b, one may apply Eq. (3.13) with $\alpha = 3$ to quickly obtain a fairly good idea of the size of the asymmetry correction. It can then be decided whether a full PRC simulation is required. For many of the experimental determinations of rotational constants discussed in Chapter 5, the estimated correction was much smaller than the experimental error, and no simulation was required. Uncertainties in A' and b further reduce the accuracy of Eq. (3.13), but these uncertainties are equally present in asymmetry corrections determined from simulations. Simulations can be advantageous in reducing these uncertainties only if one attempts to fit the PRC beat pattern.

We now turn to a detailed examination of the calculation of simulated PRC signals in asymmetric tops. The principle of these calculations is identical to that developed in Section I and expressed in Eq. (1.12). The only difference will be that the rotational eigenstates take a different form, giving different direction cosine matrix elements [Eq. (1.7)] and different rotational energies.

The rotational energy eigenstates of an asymmetric top are designated by the quantum numbers J and M, which have the same meaning as for symmetric tops, and an index τ: $|J\tau M\rangle$. As for symmetric tops, the energy does not depend on M. There are $2J+1$ energy levels with quantum number J, which converge in the symmetric top limit to the levels associated with each of the $2J+1$ values of K from $-J$ to J. For convenience, the index τ is also taken to run from $-J$ to J. Because the eigenstates of the symmetric and asymmetric top are both also eigenstates of the total angular momentum and the Z component of angular momentum, the symmetric top eigenstates $\{\,|JKM\rangle : K = -J \ldots J\,\}$ form a basis for the subspace of asymmetric top eigenstates with the same J and M. The matrix elements of the asymmetric top Hamiltonian in the chosen (either oblate or prolate) symmetric top basis are easily derived.[40] The coefficients of the expansion

$$|J\tau M\rangle = \sum_{K=-J}^{J} a(J\tau K)\,|JKM\rangle \tag{3.14}$$

are elements of the eigenvectors of this matrix and depend on the relative sizes of the rotational constants. For computational efficiency, an alternate basis of the (JM)-subspace which is closely related to the symmetric top $|JKM\rangle$ basis is actually used to calculate the a coefficients. In this alternate basis, the $(2J+1)$-dimensional Hamiltonian is block diagonal with four blocks of dimension $\sim (2J+1)/4$. The eigenstates of each block are associated with a different rotational symmetry species. (See below.)

Serving as the basis for our asymmetric top PRC simulations is the following expression for the time evolution of polarization-analyzed and thermally averaged fluorescence derived in Ref. 1:

$$I(t,\hat{\epsilon}_1,\hat{\epsilon}_2,T) \propto \sum_{\Gamma_0} \frac{G(\Gamma_0)e^{-E_{\Gamma_0}/k_B T}}{Q} \left[\sum_{\Gamma_1\Gamma_1'} f(J_0,J_1,J_1',\tau_0,\tau_1,\tau_1') \times \exp\left(-i\frac{E_{\Gamma_1}-E_{\Gamma_1'}}{\hbar}t\right)\right] e^{-\gamma t} \,. \tag{3.15}$$

The subscript 0 in this equation denotes quantities associated with the ground or initial state, while the subscript 1 refers to the excited state. The terms preceeding the bracketed quantity represent the summation over the ground state manifold $\Gamma_0 = \{J_0\tau_0\}$, with the contribution of each level scaled by its statistical weight, $G(\Gamma_0)$, and its thermal population. (Magnetic quantum number summations have already been carried out in this equation.) Q is simply the rotational partition function. Within the brackets is a summation over all pairs of excited state rotational levels which are reached via excitation from a given ground state level. Each such pair gives rise to an interference term which is modulated at a beat frequency proportional to the energy difference between the levels. Multiplication by a single exponential excited state decay envelope, where γ is the radiative lifetime of the excited state, is also indicated. Other forms of vibronic state temporal evolution may also be used, however, as discussed in Section II of this chapter, and demonstrated in Section III of Chapter 5.

The dependence of the intensity on time (t) and on sample rotational temperature (T) are shown explicitly in Eq. (3.15). Only the angle between the excitation and detection polarization directions ($\hat{\epsilon}_1$ and $\hat{\epsilon}_2$, respectively), is important and appears in the expression for the Fourier amplitudes of the interference terms:

$$
\begin{aligned}
f(J_0, J_1, J_1', \tau_0, \tau_1, \tau_1') = &\sum_{q_1 q_1'} \sum_{q_2 q_2'} \sum_{L_1} \sum_{K_1 K_1'} \sum_{K_1'' K_1'''} \sum_{K_0 K_0'} D_{00}^{(L_1)}(\phi, \theta, 0) \\
&(-1)^{J_0 + J_1 + J_1' + K_1 + K_1'' + K_0' + L^1 + Q_1 + Q_2} (2J_0 + 1)(2J_1 + 1)(2J_1' + 1)(2L_1 + 1) \\
&a_0(J_0\tau_0K_0)a_0(J_0\tau_0K_0')a_1(J_1\tau_1K_1)a_1(J_1'\tau_1'K_1')a_1(J_1\tau_1K_1'')a_1(J_1'\tau_1'K_1''') \\
&\mu_1^{1,q_1}\mu_1^{1,-q_1'}\mu_2^{1,q_2}\mu_2^{1,-q_2'} \begin{pmatrix} 1 & 1 & L_1 \\ Q_1 & -Q_1 & 0 \end{pmatrix} \begin{pmatrix} 1 & 1 & L_1 \\ Q_2 & -Q_2 & 0 \end{pmatrix} \\
&\begin{pmatrix} L_1 & 1 & 1 \\ q_2' - q_2 & -q_2' & q_2 \end{pmatrix} \begin{pmatrix} J_1 & 1 & J_0 \\ -K_1 & q_1 & K_0 \end{pmatrix} \begin{pmatrix} J_1' & 1 & J_0 \\ -K_1' & q_1' & K_0' \end{pmatrix} \\
&\begin{pmatrix} J_1 & J_1' & L_1 \\ K_1'' & -K_1''' & q_2 - q_2' \end{pmatrix} \begin{Bmatrix} J_1 & J_1' & L_1 \\ 1 & 1 & J_0 \end{Bmatrix}
\end{aligned}
\tag{3.16}
$$

Primes serve in this equation to distinguish quantities associated with the two interfering excited state levels. Unprimed and double-primed terms indicate one level, while single and triple primes indicate the other. The Euler angles $(\phi, \theta, 0)$ fix the relative orientation of $\hat{\epsilon}_2$ and $\hat{\epsilon}_1$. However, the element $D_{00}^{(L_1)}(\phi, \theta, 0)$ of the Wigner rotation matrix does not depend on ϕ and is equal to the Legendre polynomial $P_{L_1}(\cos\theta)$. The components of the transition dipoles in a spherical vector representation are $\mu_i^{1,q_i}, q_i = -1, 0, 1$ where $i = 1$ and 2 for the excitation and detection transition, respectively. The sums over $q_i^{(\prime)}$ are then equivalent to the sums over dipole components (i in Eq. (1.9)) implicitly contained in Eq. (1.12). Q_1 and Q_2 are indices which determine the polarization state of the excitation and detection pulses: 0 for linear polarization and ±1 for right- and left-hand circular polarizations.

The subscripts on the eigenstate expansion coefficients indicate that the rotational eigenstates of the ground and excited electronic states will in general be different due to differing rotational constants. Under the assumption of negligible vibration-rotation interaction, the rotational levels of any molecule may be classified according to their behavior with respect to C_2 rotations about the principal axes of inertia. The resulting rotational symmetry species are designated $++$, $+-$, $-+$, and $--$ in Dennison's notation,[41] and rotational levels for a given J are divided approximately equally among the four. These species are distinguished by restrictions on the properties of the a_i coefficients, and through them, the radiative selection rules are implicitly contained in Eq. (3.16). Specifically, only even or only odd K terms that are either symmetric or antisymmetric in K may contribute to the eigenstates of a given species. It is easy to see from these properties and the fourth and fifth 3-j symbols in Eq. (3.16) that only certain combinations of species will yield nonzero amplitudes for a given dipole component. In fact, each Cartesian component of the dipole will induce transitions connecting each species with one of the other three. Thus, transitions from the state $|J\tau M\rangle$ may occur to about 1/4, 1/2, or 3/4 of the

$6J + 3$ rotational levels satisfying the J selection rule ($\Delta J = 0, \pm 1$) when the dipole has respectively, one, two, or three nonzero components along principal axes of the molecule. In this rigid rotor limit, the point group of the molecule will play a role only through restrictions which symmetry may place on the direction of the transition dipole. It is appropriate to point out here that computation times for PRC frequency spectra, which increase as the square of the number of transitions, become significantly longer for off-axis dipole moments.

In practice, all experiments for this thesis were performed with linearly polarized excitation and detection. Thus in the programs employed for simulation and fitting, such as those in Appendix II and Appendix III, the values of Q_1 and Q_2 are set equal to zero. Either of the first two 3-j symbols then shows that f is zero unless L_1 is 0 or 2. The fourth and fifth 3-j symbol permit us to make the substitutions $q_1 = K_1 - K_0$ and $q_1' = K_0' - K_1'$, eliminating the independent summations over the q_1's. Likewise, the sixth 3-j symbol requires that $q_2' = -K_1''' + K_1'' + q_2$. Noting furthermore that $(-1)^{K_i}$ is a constant for any summation over a specific rotational state (from the symmetry species properties), and, as a result, that $(-1)^{K_1+K_1''}$ is always equal to 1, we may reduce Eq. (3.16) to a form which more closely resembles that employed in the computer implementation. This is

$$
\begin{aligned}
f(J_0, J_1, J_1', \tau_0, \tau_1, \tau_1') = (-1)^{J_0+J_1+J_1'+K_0'}(2J_0+1)(2J_1+1)(2J_1'+1) \\
\left[\sum_{K_0 K_1} a_0(J_0\tau_0K_0)a_1(J_1\tau_1K_1)\mu_1^{1,K_1-K_0}\begin{pmatrix} J_1 & 1 & J_0 \\ -K_1 & K_1-K_0 & K_0 \end{pmatrix}\right] \\
\left[\sum_{K_0' K_1'} a_0(J_0\tau_0K_0')a_1(J_1'\tau_1'K_1')\mu_1^{1,K_0'-K_1'}\begin{pmatrix} J_1' & 1 & J_0 \\ -K_1' & K_1'-K_0' & K_0' \end{pmatrix}\right] \\
\sum_{L_1=0,2}(2L_1+1)P_{L_1}(\cos\theta)\begin{pmatrix} 1 & 1 & L_1 \\ 0 & 0 & 0 \end{pmatrix}^2 \begin{Bmatrix} J_1 & J_1' & L_1 \\ 1 & 1 & J_0 \end{Bmatrix} \\
\sum_{K_1'' K_1'''} a_1(J_1\tau_1K_1'')a_1(J_1'\tau_1'K_1''')\begin{pmatrix} J_1 & J_1' & L_1 \\ K_1'' & -K_1''' & K_1'''-K_1'' \end{pmatrix} \\
\sum_{q_2}\mu_2^{1,q_2}\mu_2^{1,K_1'''-K_1''-q_2}\begin{pmatrix} L_1 & 1 & 1 \\ K_1''-K_1''' & K_1'''-K_1''-q_2 & q_2 \end{pmatrix}. \qquad (3.17)
\end{aligned}
$$

The (K_0, K_1) sums, primed and unprimed, are completely contained in their respective brackets. Note that these sums over the dummy K variables differ at most by a sign when Γ_1 is equal to Γ'_1. They can also be shown to be pure real or pure imaginary.

The evaluation of Eq. (3.17) has been greatly accelerated by utilizing the properties of the expansion coefficients. For example, it can be shown that $f(J_0, J_1, J'_1, \tau_0, \tau_1, \tau'_1)$ and $f(J_0, J'_1, J_1, \tau_0, \tau'_1, \tau_1)$ are real and equal, so that only one of the two must be calculated. This fact also ensures that I is real and modulated only by cosine terms. It is, of course, self-evident that I is real when it is expressed in the form of Eq. (1.12), so the demonstration thereof for the above equations serves only as a test of the correctness of the equations themselves.

The proof that $f(J_0, J_1, J'_1, \tau_0, \tau_1, \tau'_1)$ and $f(J_0, J'_1, J_1, \tau_0, \tau'_1, \tau_1)$ are real and equal can be conveniently carried out in two steps, showing first that the two f's are complex conjugates of each other, then showing that f is always real. The proof relies on the fact that for a given $J_0\tau_0 \rightarrow J_1\tau_1$ transition, only a single Cartesian component of the transition dipole produces a nonvanishing contribution to the (K_0, K_1) sum. Thus, the properties of f depend only on the particular set of dipole components responsible for the two interfering excitation channels. There are nine such sets: (x, x), (x, y), etc. In practice, the ordering of the components is unimportant, and the three diagonal cases, in which both excitation transitions are induced by the same dipole moment, can be treated together, leaving six distinct cases to consider. (The above sets of excitation components should not be confused with the dipole pairs discussed in Section II and Ref. 1 which refer to the excitation/detection sequence of principal axis dipoles.)

In the same way that the equality of $f(J_0, J_1, J'_1, \tau_0, \tau_1, \tau'_1)$ and $f(J_0, J'_1, J_1, \tau_0, \tau'_1, \tau_1)$ makes it possibly to restrict the $\Gamma_1\Gamma'_1$ sums to $J'_1 \geq J_1$ and $\tau'_1 \geq \tau_1$ for $J'_1 = J_1$, it can be shown that the (K_0, K_1) sums need be carried out only over positive K_0 terms, since negative K_0 terms are simply related to them. ($K_0 = 0$ must be accounted for separately.) The 3-j symbols restrict K_1 to K_0 or $K_0 \pm 1$, so the above restriction on K_0 yields a time savings of about 50%.

Finally, quantities which appear repeatedly in the course of PRC calculation have been evaluated once in advance and stored in memory for recall. The (K_0, K_1) sums, which each depend on only one of the two excited states, provide one example in which repetitive calculations are avoided in this manner. Values from a single storage array are called by both primed and unprimed versions of the sum, with a sign change when needed. An even larger economy has been realized by calculating all of the very small number of distinct q_2 sums before beginning the ground state manifold summation in Eq. (3.15).

References

1. P. M. Felker and A. H. Zewail, J. Chem. Phys. **86**, 2460 (1987).
2. G. Herzberg, *Molecular Spectra and Molecular Structure* (Van Nostrand Reinhold, New York, 1945), Vol. II, p. 23.
3. S. Haroche, in *High Resolution Laser Spectroscopy*, edited by K. Shimoda (Springer, New York, 1976), p. 254.
4. R. Wallenstein, J. A. Paisner, and A. L. Schawlow, Phys. Rev. Lett. **32**, 1333 (1974); P. J. Brucat and R. N. Zare, J. Chem. Phys. **78**, 100 (1983); M. Dubs, J. Mühlbach, and J. R. Huber, J. Chem. Phys. **85**, 1288 (1986).
5. M. Brieger, A. Hese, A. Renn, and A. Sodiek, Chem. Phys. Lett. **76**, 465 (1980); P. J. Brucat and R. N. Zare, Mol. Phys. **55**, 277 (1985).
6. G. Herzberg, *Molecular Spectra and Molecular Structure* (Van Nostrand Reinhold, New York, 1966), Vol. III, p. 128–131.
7. H. Rademacher and F. Reiche, Zeits. f. Physik **41**, 435 (1927).
8. P. C. Cross, R. M. Hainer, and G. W. King, J. Chem. Phys. **12**, 210 (1944).
9. F. Perrin, J. Phys. (Paris) **7**, 390 (1926); J. Phys. Rad. **5**, 497 (1934); *ibid* **7**, 1 (1936).
10. R. Memming, Z. Physik. Chem. NF, **28**, 168 (1961).
11. P. P. Feofilov, *The Physical Basis of Polarized Emission* (Consultants Bureau, New York, 1961)
12. R. G. Gordon, J. Chem. Phys. **43**, 1307 (1965).
13. R. G. Gordon, J. Chem. Phys. **45**, 1643 (1966).
14. T. Tao, Biopolymers **8**, 609 (1969).
15. T. J.Chuang and K. B. Eisenthal, J. Chem. Phys. **57**, 5094 (1972).
16. A. Szabo, J. Chem. Phys. **72**, 4620 (1980); **81**, 150 (1984).
17. G. W. Loge and C. S. Paramenter, J. Chem. Phys. **74**, 29 (1981).
18. A. P. Blokhin and V. A. Tolkachev, Opt. Spectrosc. (USSR) **51**, 152 (1981).
19. G. M. Nathanson and G. M. McClelland, J. Chem. Phys. **81**, 629 (1984); **85**, 4311 (1986).

20. A. B. Meyers and R. M. Hochstrasser, J. Chem. Phys. **85**, 6301 (1986).

21. D. A. Case, G. M. McClelland, and D. R. Herschbach, Mol. Phys. **35**, 541 (1978).

22. A. H. Zewail, J. Chem. Soc. Faraday Trans. 2 **85**, 1221 (1989).

23. R. Heather and H. Metiu, Chem. Phys. Lett. **157**, 505 (1989).

24. M. Dantus, R. M. Bowman, J. S. Baskin, and A. H. Zewail, Chem. Phys. Lett. **159**, 406 (1989).

25. L. C. Biedenharn in *Nuclear Spectroscopy, Part B* edited by F. Azjenberg-Selove (Academic, New York, 1960) p. 732.

26. D. A. Case and D. R. Herschbach, J. Chem. Phys. **64**, 4212 (1976).

27. R. N. Zare and D. R. Herschbach, Proc. IEEE **51**, 178 (1963); R. N. Zare, Molec. Photochem. 4, 1 (1972); R. N. Zare, Chem. Phys. Lett. **156**, 1 (1989).

28. M. D. Morse, K. F. Freed and Y. B. Band, J. Chem. Phys. **70**, 3604 (1979); M. D. Morse and K. F. Freed, J. Chem. Phys. **74**, 4395 (1981).

29. J. A. Beswick and W. M. Gelbart, J. Phys. Chem. **84**, 3148 (1980).

30. M. Shapiro and R. Bersohn, Ann. Rev. Phys. Chem. **33**, 409 (1982).

31. C. H. Dugan and D. Anthony, J. Phys. Chem. **91**, 3929 (1987).

32. G. E. Hall, N. Sivakumar, D. Chawla, P. L. Houston, and I. Burak, J. Chem. Phys. **88**, 3682 (1988); G. E. Hall and P. L. Houston, Ann. Rev. Phys. Chem. (in press 1989).

33. P. Arrowsmith, F. E. Bartoszek, S. H. P. Bly, T. Carrington, Jr., P. E. Charters, and J. C. Polanyi, J. Chem. Phys. **73**, 5895 (1980); J. C. Polanyi and R. J. Wolf, J. Chem. Phys. **75**, 5951 (1981); P. R. Brooks, R. F. Curl, and T. C. Maguire, Ber. Bunsenges. Phys. Chem. **86**, 401 (1982); J. H. Foth, J. C. Polanyi, and H. H. Telle, J. Phys. Chem. **86**, 5027 (1982).

34. For example, see Ref. 26.

35. For example, see: L. D. Landau and E. M. Lifshitz, *Mechanics*, Third Edition (Pergamon Press, Oxford, 1976) p. 110; H. Goldstein, *Classical Mechanics*,

Second Edition (Addison-Wesley, Reading, Massachusetts, 1980) p. 146.

36. R. Bersohn and M. Shapiro, J. Chem. Phys. **85**, 1396 (1986).
37. K. Kühl and R. Schinke, Chem. Phys. Lett. **158**, 81 (1989).
38. S. R. Polo, Can. J. Phys. **35**, 880 (1957).
39. G. Herzberg, *Molecular Spectra and Molecular Structure* (Van Nostrand Reinhold, New York, 1966), Vol. III, p. 256.
40. For example, see: I. N. Levine, *Molecular Spectroscopy*, (John Wiley and Sons, New York, 1975) p. 214.
41. D. M. Dennison, Rev. Mod. Phys. **3**, 280 (1931).

Figure Captions

1. Classical motion of a rigid symmetric top. The top is shown at two times separated by half a nutation period. The total angular momentum vector $\vec{J}$ and its component $\vec{K}$ along the figure axis are indicated. ω_1 and ω_2 are the angular frequencies of nutation and of rotation about the figure axis, respectively.
2. Level diagram illustrating the quantum mechanical origin of purely rotational coherence in a symmetric top molecule. The particular pathways shown are those appropriate to the case of parallel excitation and detection transition dipoles and detection polarization $(\hat{\epsilon}_2)$ parallel to excitation polarization $(\hat{\epsilon}_1)$. (This figure is reprinted from Ref. 1.)
3. Purely rotational coherence signal for parallel detection $(I_{||})$ associated with a single ground state rotational energy level of a *t*-stilbene-like symmetric top. The scheme of excitation and detection is shown explicitly in the upper righthand corner of the figure. Summation over all equally weighted M_0 states has already been carried out. Thus this signal is that to be expected for excitation of an isotropic sample of molecules, and not of molecules in a single quantum state. The calculated signal is strictly periodic with a period of 1.95 ns, corresponding to the fundamental nutation period.
4. Geometric relations and angles in the lab-fixed frame used in the derivation of Eq. (2.8).
5. Euler angles specifying the orientation of the molecule-fixed reference frame (x, y, z) relative to the space-fixed frame (X, Y, Z). For our purposes, Z is always chosen to coincide with the angular momentum of the molecule, and z with the molecular figure axis.
6. a) Classical time-resolved parallel fluorescence intensity for an isotropic distribution of symmetric top molecules with angular momentum $6\hbar$ and $\theta = \pi/3$. The intensity is calculated from Equations (2.17) and (2.11). It is strictly periodic at the nutation frequency $\omega_1 = 6 \cdot 2B'$ where $1/(2B') = 1.95$ ns.

b) Time-resolved parallel fluorescence intensity based on Eq. (2.17) with $\theta = \pi/3$, but with the two classical frequencies replaced by the three quantum mechanical frequencies associated with the ground state level $j = 6$. See text for details.

7. Geometry of the dissociation problem $M_1 \rightarrow M_2 + A$. The pump pulse, with polarization $\hat{\epsilon}_1$, excites the dipole $\vec{d}_1$ of M_1 at left. After dissociation, the dipole $\vec{d}_2$ of fragment M_2 is probed with probe polarization $\hat{\epsilon}_2$ (right).

Figure 1

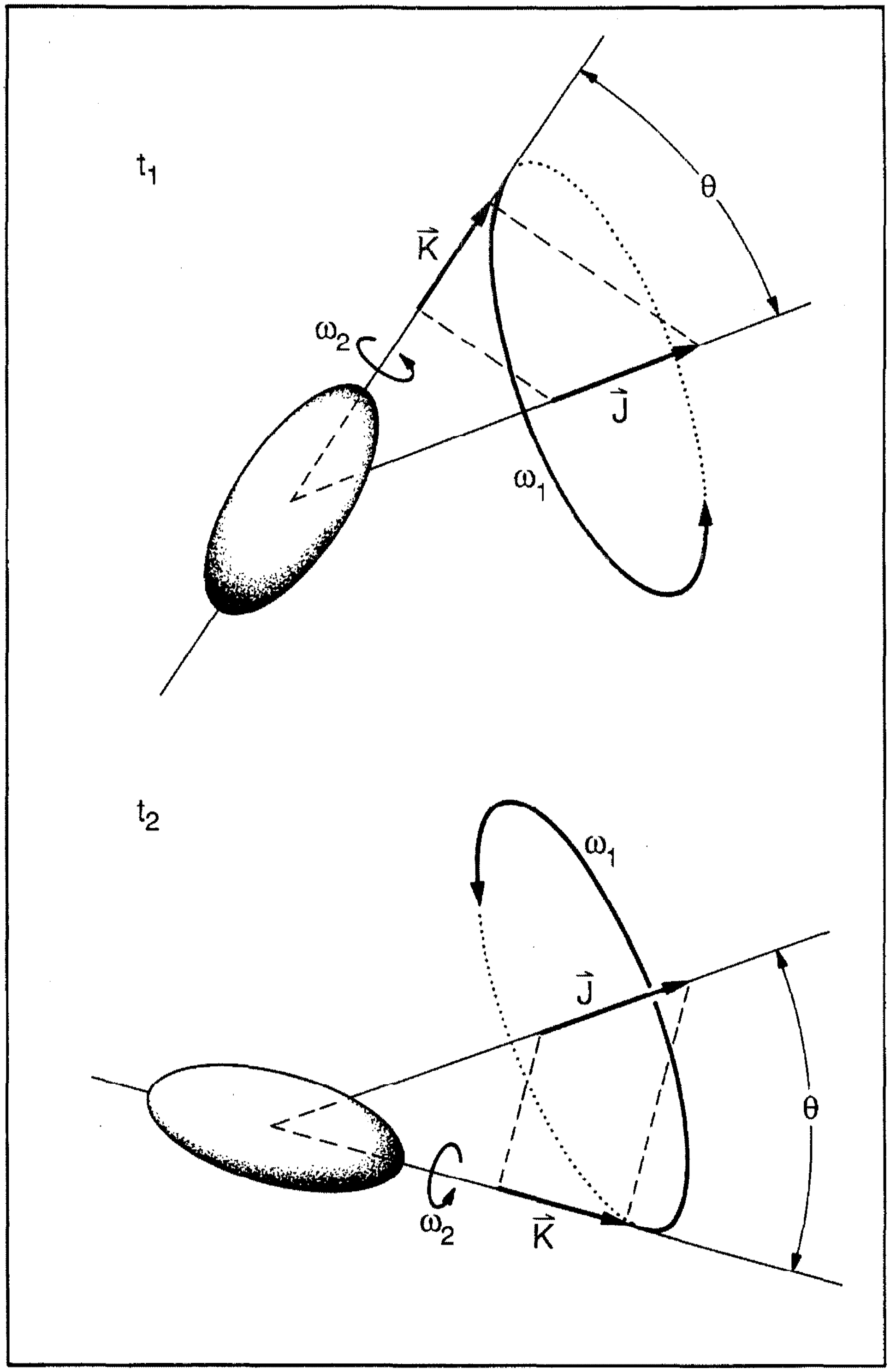

Figure 2

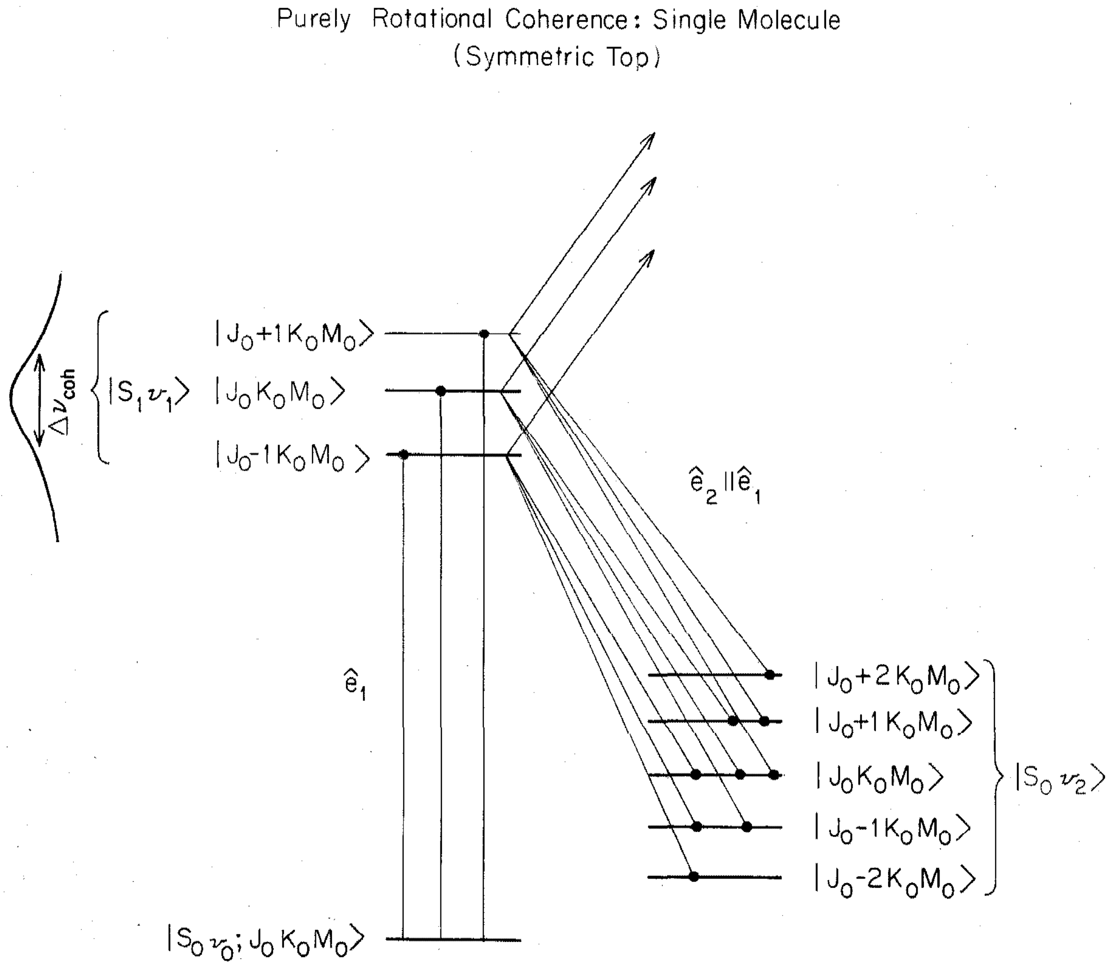
Purely Rotational Coherence: Single Molecule
(Symmetric Top)
$\Delta\nu_{coh}$
$|S_1 v_1\rangle$
$|J_0+1\, K_0 M_0\rangle$
$|J_0 K_0 M_0\rangle$
$|J_0-1\, K_0 M_0\rangle$
$\hat{e}_2 \parallel \hat{e}_1$
$\hat{e}_1$
$|J_0+2\, K_0 M_0\rangle$
$|J_0+1\, K_0 M_0\rangle$
$|J_0 K_0 M_0\rangle$
$|J_0-1\, K_0 M_0\rangle$
$|J_0-2\, K_0 M_0\rangle$
$|S_0 v_2\rangle$
$|S_0 v_0; J_0 K_0 M_0\rangle$

Figure 3

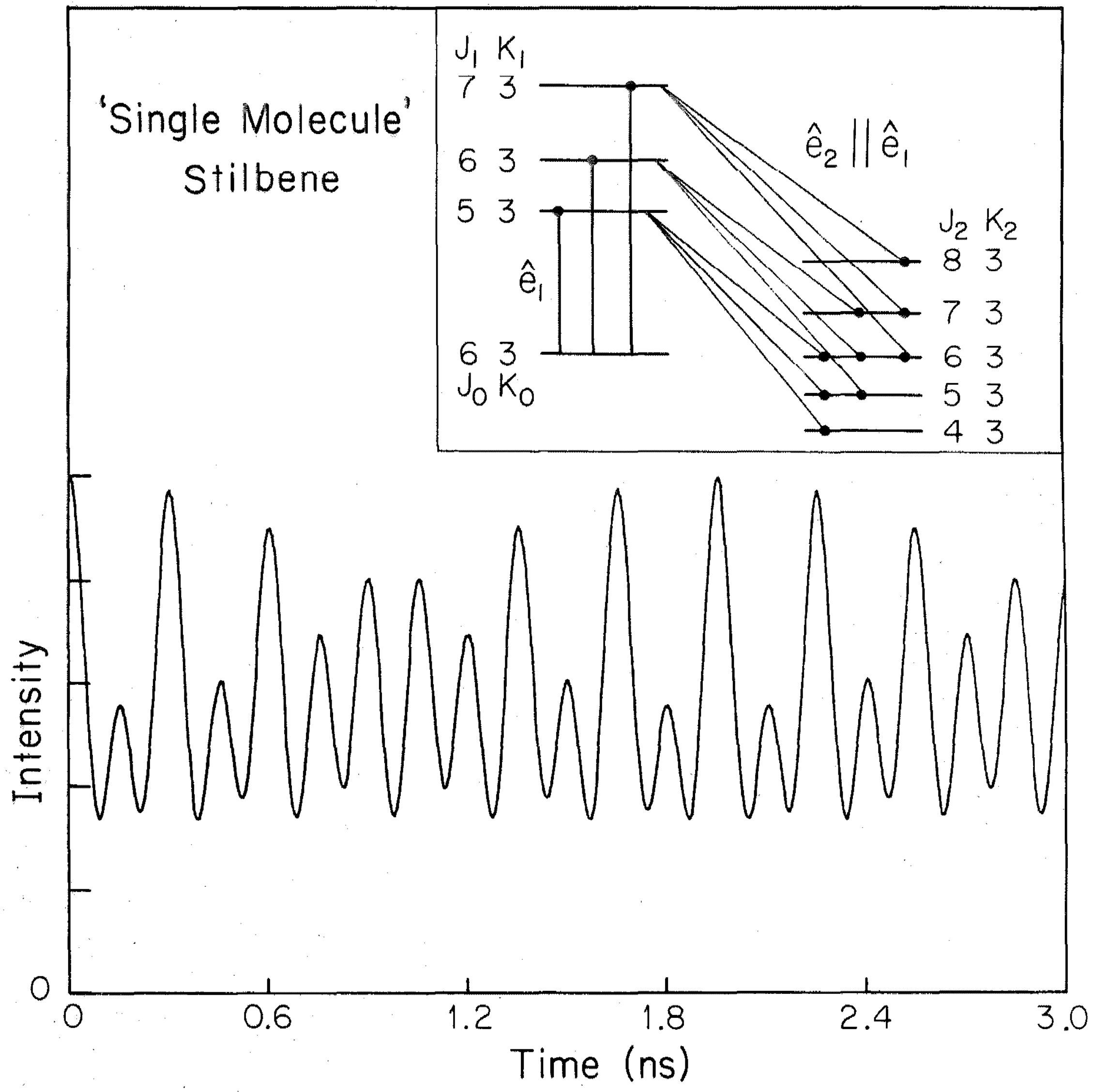
'Single Molecule'
Stilbene
J_1 K_1
7 3
6 3
5 3
$\hat{e}_1$
6 3
J_0 K_0
$\hat{e}_2 \| \hat{e}_1$
J_2 K_2
8 3
7 3
6 3
5 3
4 3
Intensity
0
0
0.6
1.2
1.8
2.4
3.0
Time (ns)

Figure 4

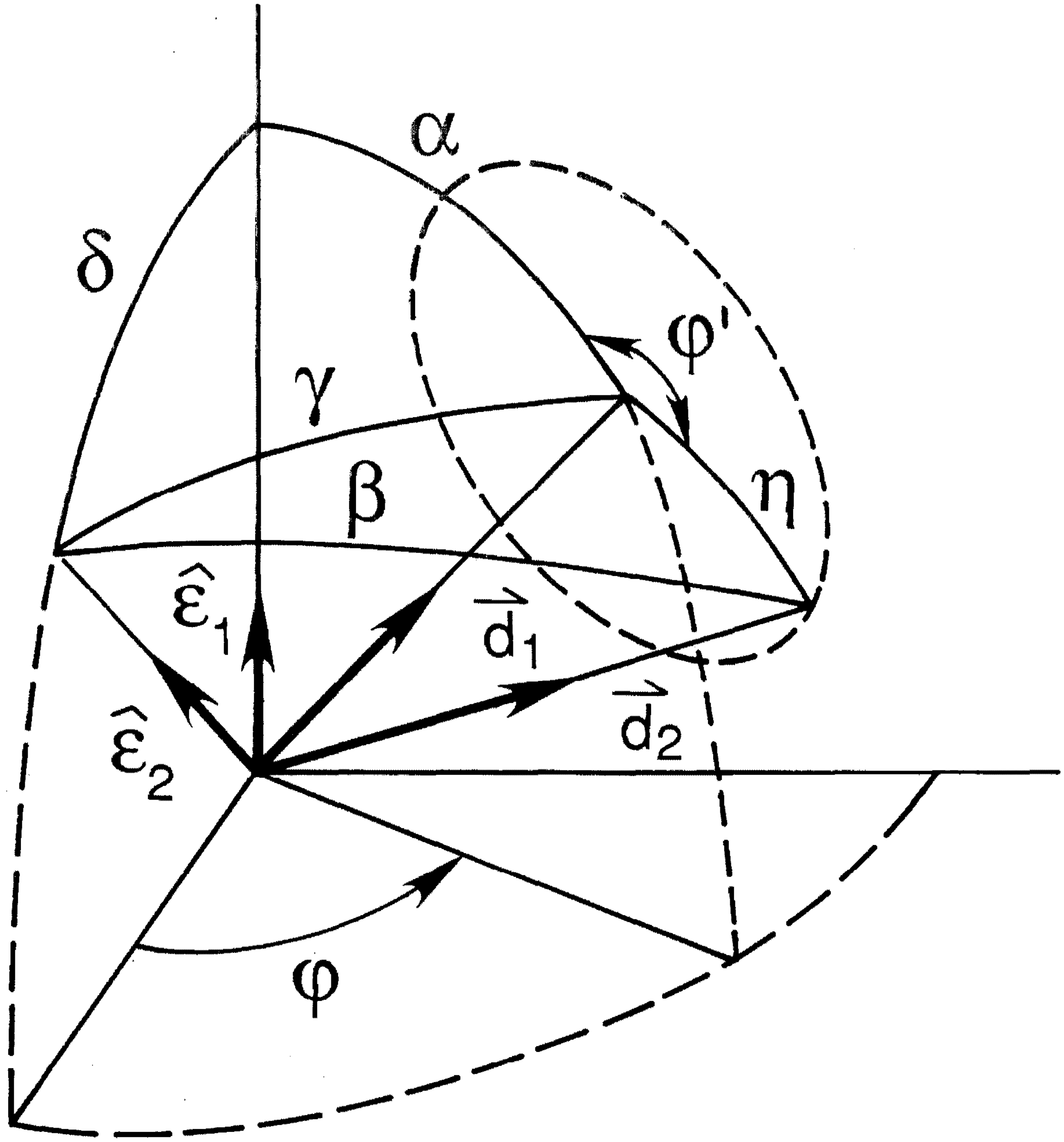

Figure 5

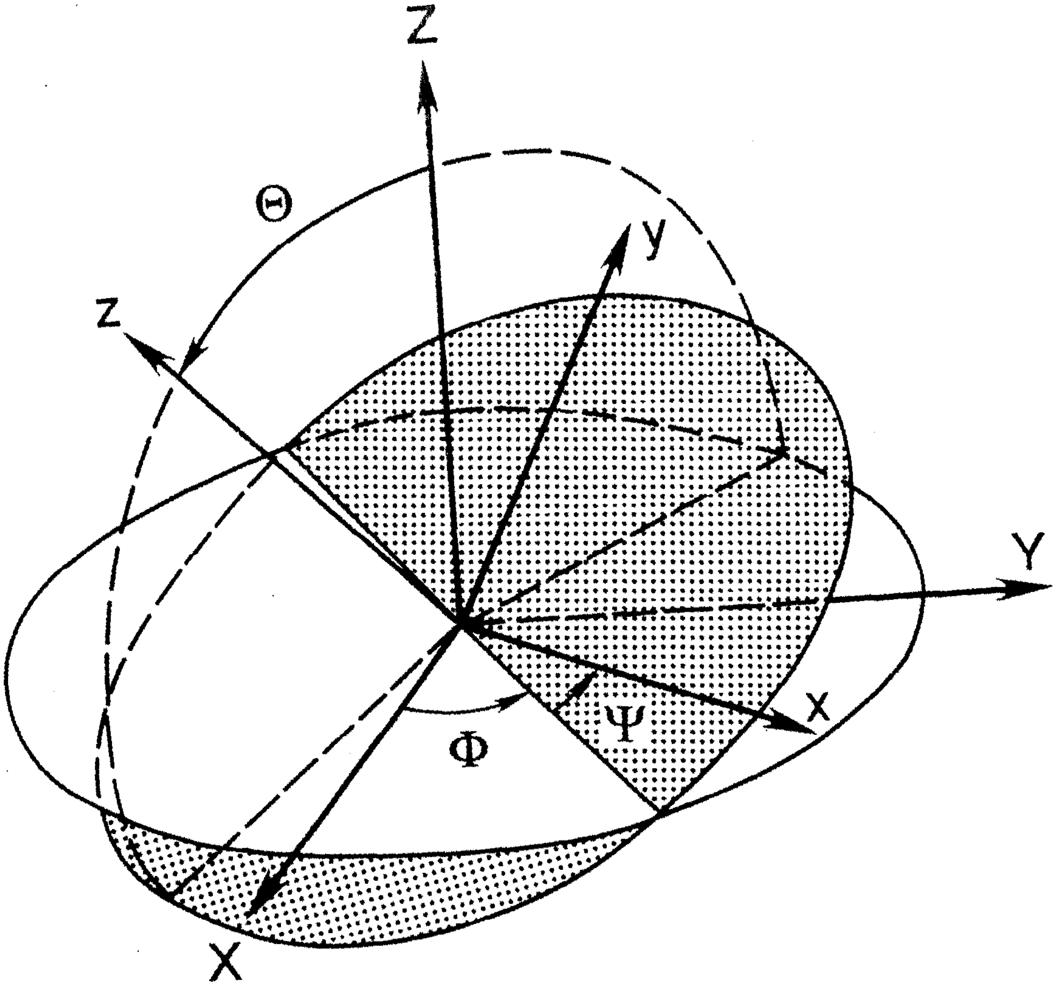

Figure 6

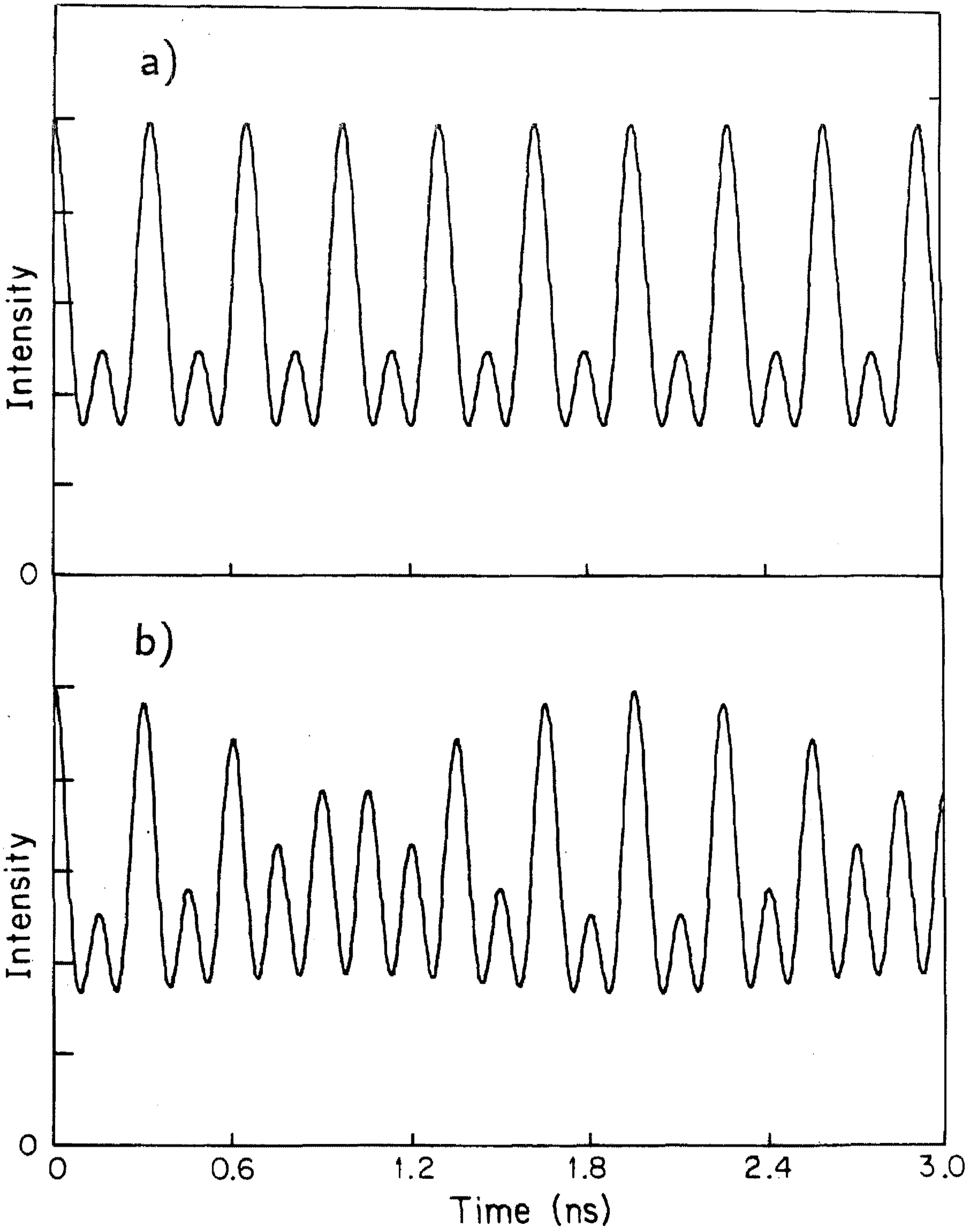

Figure 7

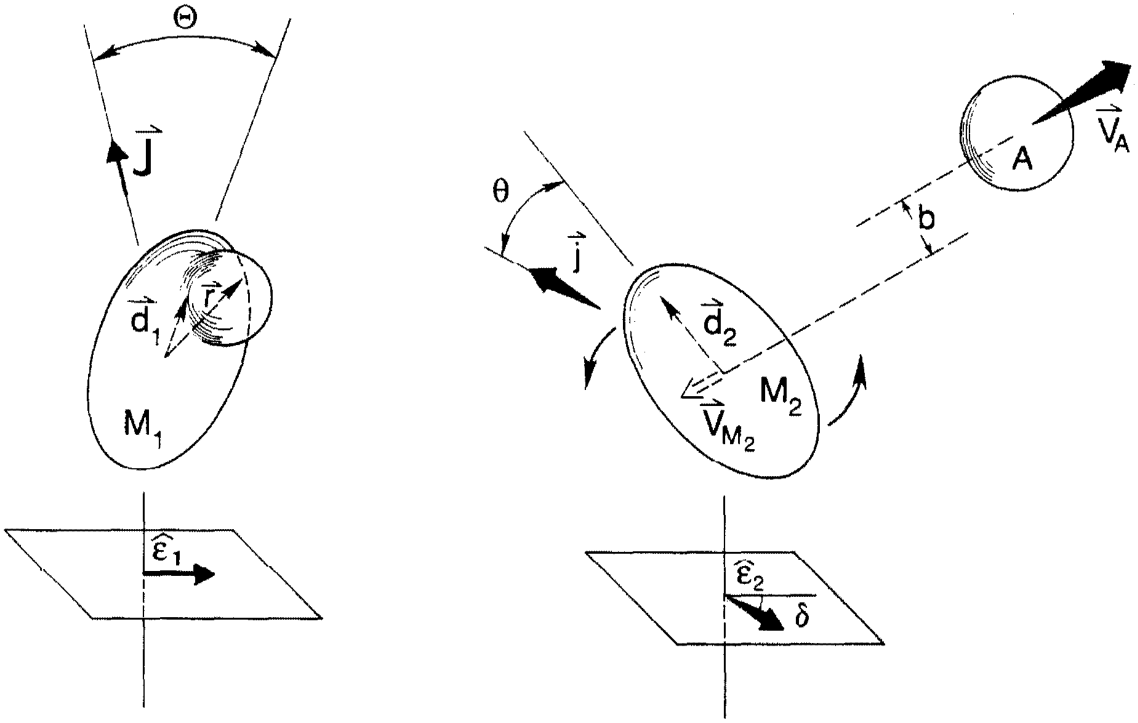

Θ
$\vec{J}$
$\vec{d}_1$
$\vec{r}$
M_1
$\hat{\varepsilon}_1$
θ
$\vec{j}$
$\vec{d}_2$
M_2
$\vec{V}_{M_2}$
b
A
$\vec{V}_A$
$\hat{\varepsilon}_2$
δ

Chapter 3

Experimental

Portions of this chapter are taken from the following published articles:

"Purely Rotational Coherence Effect and Time-resolved Sub-Doppler Spectroscopy of Large Molecules. II. Experimental," by J. S. Baskin, P. M. Felker, and A. H. Zewail.

Reprinted with permission from The Journal of Chemical Physics, Volume 86, p. 2483. Copyright 1987 American Institute of Physics.

and

"Determination of Excited-State Rotational Constants and Structures by Doppler-Free Picosecond Spectroscopy," by J. S. Baskin and A. H. Zewail.

Reprinted with permission from The Journal of Physical Chemistry, Volume 93, p. 5701. Copyright 1989 American Chemical Society.

I. General Apparatus

Measurements of time-resolved and polarization-analyzed fluorescence of jet-cooled molecules, to be presented in Chapter 5, form the experimental basis of this thesis. The experimental apparatus employed for these measurements is described in the four subdivisions of this section. In Fig. 1 are represented schematicly all components of the experimental system, except for those related to polarization selection and analysis. Reference is made to this figure throughout Sections A, B, and C. Details concerning polarization aspects of the experiments are considered in Section D.

A. Ultraviolet Excitation Source — Laser system and Second Harmonic Generation

The first requirement of our experiments was the generation of picosecond pulses of tunable ultraviolet light. A Spectra Physics Model 171 argon ion laser in mode-locked operation served as the primary energy source in the generation scheme. Mode-locking refers to the creation of a regime in which a single short light pulse circulates in the laser cavity.[1,2] If such a regime can be established, at each reflection of the circulating pulse from the partially transmissive front mirror, or output coupler, a fraction of its energy is transmitted, resulting in a periodic train of output pulses. The temporal separation of these pulses is equal to the time required for the circulating light pulse to make one round trip in the laser cavity. This time is given by $2L/c$, where L is the effective (optical) length of the laser cavity. For the 1.8 meter length of the 171 laser, the round trip time was approximately 12 ns.

The mode-locking element used in our laboratory was a prism located near one end of the laser cavity (ML, for mode-locker, in Fig. 1). A radio frequency transducer attached to one side of the prism was driven at a resonant frequency of the prism to set up an acoustic standing wave across the path of the laser beam. The result was a diffraction grating of temporally periodic diffraction efficiency. Mode-locking was accomplished by precisely synchronizing the cavity round trip time (by adjustment of the cavity length) with the periodicity of the low-diffraction or high-transmittance windows of this grating. Since there are two of these windows for each full cycle of the acoustic wave, the required driving frequency was around $\frac{1}{2}(12\text{ns})^{-1} = 41$ MHz.

The duration of mode-locked pulses depends not only on the characteristics of the mode-locking element but also on the characteristics of the gain medium. Pulsed operation at a period of $2L/c$ requires lasing at not one, but a series of frequencies at a frequency spacing of $c/(2L)$. The infinite sinusoidal waves associated with each of these longitudinal cavity modes are "locked" together (hence the name mode-locking) to produce pulses in the time domain. By the Fourier relation between the frequency and time domains, the sharper the temporal pulse, the more modes required to produce it. Thus the spectral breadth of a region of positive gain sets a lower limit on the pulse width that may be obtained for lasing in that region. The optimal combination of power and short pulse duration among argon ion lasing transitions is found in the 514.5 nm line. In our laboratory, 150 to 200 ps pulses and average powers of .5 to .8 W were typically attained for operation at this wavelength. Mode-locking was also achieved at the strong 488 nm transition, but due to the narrowness of the gain profile, pulse widths less than 1 ns FWHM could not be produced.

The argon ion output described above was used to synchronously pump a Spectra Physics Model 375 tunable dye laser with Spectra Physics Model 344 cavity dumper (DL and CD in Fig. 1). The dyes Rhodamine 590 and DCM provided coverage of the wavelength range 597 nm to 722 nm needed for these experiments. The dye was dissolved in a solvent of sufficient viscosity to produce a stable laminar sheet when forced into air from a thin metal nozzle. When the pump beam was focused into this sheet, the dye absorbed the 514 nm light; lasing at longer wavelengths could then occur to any one of the unpopulated higher-lying ground state levels of the dye. Tuning was accomplished with a three-plate birefringent filter, alone or in combination with an ultra-fine tuning etalon. Synchronous pumping, achieved by matching the pulse round-trip time in the dye laser cavity to that of the pump laser, served to mode-lock the dye laser. The slow build-up and rapid depletion of the gain of the dye, coupled with the broad bandwidth of the dye gain, resulted in dye laser pulses that were much shorter than the pump pulses. Pulse widths were not directly measured in the course of these experiments, but typical values for a system of this type are about 15 ps FWHM.[3]

In the dye laser configuration shown in Fig. 1, the four mirrors forming the doubly folded cavity, including the two end mirrors, were full reflectors. Light pulses could only be extracted from the cavity by the cavity dumper, at a repetition rate selectable from single shot to 4 MHz. The active element of the cavity dumper was an acousto-optic cell, located at the focus of the second confocal arrangement of mirrors in the dye laser cavity (as shown). The light pulse circulating in the cavity traversed this cell twice in each round trip. At intervals determined by the selected repetition rate, an acoustic wave train was sent across the cell, diffracting energy from the cavity into the exit path of the laser. Interference of the light diffracted on the two passes through the crystal helped to produce efficient dumping into the primary dumped output pulse and to suppress dumping of adjacent secondary pulses. Secondary pulses were always present, but their intensities relative to the primary pulse was usually less than 1:200. Reduction of the laser repetition rate by cavity dumping was indispensible when working with molecules having fluorescence lifetimes of the order of or longer than the inherent mode-locked pulse separation. Cavity dumping also significantly increased the energy of individual output pulses, which was of great value in increasing the efficiency of second harmonic generation (see below). The cavity dumper was normally operated at a repetition rate of 4 MHz, with output pulses in the five to ten nanojoule range.

Ultraviolet pulses were produced from the visible pulses which exited the cavity dumper by second harmonic generation[1,4,5] in a lithium iodate ($LiIO_3$)

crystal (SHG in Fig. 1). The generation of harmonics of a monochromatic signal by transmission through a nonlinear medium is a general phenomenon. Thus passage of light through a crystal of nonlinear susceptibility results in an output containing harmonics of the driving frequency. Even harmonics are produced only when the response is anisotropic. This means that ultraviolet light is generated as visible light propagates through a noncentrosymmetric nonlinear crystal. Because of dispersion within the crystal, the propagtion velocities of the visible and ultraviolet light are generally different, and infinitesimal contributions to the ultraviolet are created with continuously varying relative phase. Interference between these contributions is typically constructive for very short path lengths only, and the effectiveness of the conversion process is severely limited. However, for certain birefringent crystals the directions of propagation and polarization may be chosen to make the two propagation velocities equal. This process is referred to as phase-matching.[1] All ultraviolet contributions then have zero relative phase and add constructively to produce a greatly enhanced resultant. For all excitation wavelengths needed in our experiments (298 nm to 361 nm), phase-matching could be achieved by angle tuning one of two appropriately cut 1 cm thick $LiIO_3$ crystals. Conversion efficiencies of several percent were typical and depended quadratically on the intensity of the visible light. The bandwidth of the ultraviolet pulses was determined to be no greater than 5 cm^{-1} without and 2 cm^{-1} with the etalon in place, based on spectrometer scans of scattered laser light.

The second doubling crystal was designed to permit generation of second harmonic light down to the shortest wavelength for which phase-matching in $LiIO_3$ is possible. This blue doubling limit is reached when the propagation direction of the incident beam is perpendicular to the optic axis. Since the dependence of phase-matched wavelength on angle in this wavelength region was not accurately known to the crystal supplier (Cleveland Crystals), measurements were performed in our laboratory to determine the optimum angle of cut for such a crystal. In these measurements, the blue limit for phase-matching in $LiIO_3$ at room temperature was found to be 293 nm. Since the range of the first crystal ended at 315 nm, a tuning range for the second crystal of 293 to $\sim$ 320 nm was desired. The measured (internal) phase-matching angles at these wavelengths differed by $\sim 26°$. This range corresponds to a range of external angles of incidence of $\pm 25°$, which could be reasonably accommodated by choosing a wide-angle mounting cell. It was therefore specified that the crystal be cut so that the normal to its optical faces and its optic axis form an angle of $90 - 26/2 = 77°$. Although the doubling range is centered at $\sim$ 305 nm, the wavelength that is phase-matched at normal incidence for this design is 298.3 nm.

B. Samples, molecular beam apparatus, and expansions

Samples of *trans*-stilbene and anthracene with stated purities $\geq 96\%$ were obtained from commercial sources (Aldrich, MCB, Pfaltz and Bauer). Extensive earlier work on these molecules carried out in this laboratory[3,6,7,8,9] demonstrated that further purification had no effect on observed characteristics of the samples in the spectral region of interest. Fluorene was purchased from Aldrich with purity $\geq 98\%$. Residual impurities in the sample were of no concern, since only the strong $S_1 \leftarrow S_0$ 0_0^0transitions of fluorene and the fluorene-Ar_1 van der Waals complex[10] were investigated.

These samples were studied in the form of cold isolated molecules prepared by expansion in a continuous supersonic jet. The apparatus consisted of a sample reservoir and nozzle mounted horizontally within a translatable, heated metal jacket on the axis of a cylindrical vacuum chamber. The expansion of the seeded carrier gas occurred through a pinhole in the nozzle. For expansions under low backing pressures, the reservoir and nozzle were formed of Pyrex tubing, and the carrier gas was introduced via a simple double o-ring compression fitting. The thick-walled capillary tube forming the nozzle was drawn out and sealed, then sanded down to reopen a pinhole in its tip. Pinhole diameters were measured by optical microscope and ranged from 60 to 80 microns. For backing pressures exceeding 100 psig, a stainless steel sample reservoir was used. The nozzle on this reservoir was formed by a screw cap designed to hold commercially available drilled metal disks with a metal to metal seal. Pinhole diameters from $12\frac{1}{2}$ to 50 microns were used.

Experiments on bare (i.e., uncomplexed) molecules were generally conducted using neon at a pressure of approximately six atmospheres. The choice of backing gas and pressure were dictated by the need to achieve maximum cooling of rotations.[11,12] Helium complexes with *t*-stilbene were formed using backing pressures of pure helium up to 45 atm. For the formation of van der Waals complexes with argon, neon was again used as the principle carrier gas with low concentrations of argon mixed in. The mixing was regulated by means of a supersonic needle valve which allowed continuous variation of the argon concentration. The advantage of this arrangement was the ease with which observed complex signals could be optimized and checked for their dependence on argon concentration, an important clue to stoichiometry. It must be noted, however, that due to mechanical instabilities a constant mixing ratio over the course of lengthy experiments was often difficult to maintain by this method.

The temperature of the nozzle assembly was controlled by two independent coils of heating wire: one extending over the full length of the sample reservoir and one in the immediate vicinity of the nozzle only. Thermocouples were attached to the metal jacket surrounding the sample tube both at its front edge, to monitor the nozzle temperature, and near the center, where the bulk of the sample is located. Cited sample temperatures refer to readings of this second thermocouple and ranged from 120 C to 180 C for the solid sample compounds discussed in Chapter 5. Heater settings were chosen to maintain the temperature reading at the nozzle approximately 50 C higher than that of the reservoir. If this was not done, clogging of the nozzle tip by solidified sample became a problem.

The vacuum chamber in which the nozzle assembly was mounted was 12 in.

in diameter and 36 in. long. An Edwards 18B4A 12 in. oil vapor booster pump, backed by a Kinney KT150 single stage mechanical pump, was connected to a right angle pneumatic valve mounted on the end of the chamber, downstream from the molecular beam. With this pumping arrangement, the background pressure was maintained below a few millitorr under normal operating conditions, and always less than 20 millitorr.

After leaving the $LiIO_3$ crystal, the remaining visible and newly created ultraviolet laser beams reached a mirror of high reflectance at the ultraviolet wavelength. This mirror directed the ultraviolet beam upward through a Brewster angle quartz window into the vacuum chamber (see Fig. 1), while permitting a major part of the visible beam to pass on undeflected. A final quartz lens in the vacuum chamber focused the ultraviolet excitation beam tightly into the expanding free jet. The distance X of the laser from the nozzle was continuously adjustable with a value of two or three mm used for the typical experiment. Pertinent expansion conditions, including X, the nozzle diameter (D), the reservoir temperature, carrier gas, and backing pressure were routinely recorded and will often be cited in Chapter 5 as specific results are presented. In many cases checks for collisions or hot band formation were made by studying the effects of changing backing pressure or X/D.

C. Fluorescence detection

Fluorescence from the interaction region of the crossed molecular and laser beams was collected at right angles to both beams by an $f/2$ collimating lens and focused by a second lens onto the entrance slit of a microprocessor controlled 0.5 meter Spex spectrometer (see Fig. 1). In order to trace the time evolution of fluorescence intensity the technique of time-correlated single photon counting (TCSPC)[13] was implemented as follows. At the exit slit of the spectrometer, single photons were detected by a Hammamatsu 1564U microchannel plate photomultiplier. The photomultiplier output pulses were amplified, discriminated, and used to trigger the start channel of an Ortec Model 457 biased time to pulse height (amplitude) converter (TAC). The stop channel was supplied by the similarly processed output of a fast photodiode detecting the visible laser pulses (PD in Fig. 1). For each valid sequence of start/stop pulses received, the TAC, as its name implies, gives an output pulse of amplitude proportional to the time between the two input pulses. The amplitude of the TAC output following detection of a fluorescence photon in our experiments was therefore a measure, on a time scale with an offset fixed by various optical and electronic delays, of the time which elapsed between the passage of the excitation pulse and the emission of the photon. By feeding the TAC output pulses to a Tracor Northern Model TN-1706 multichannel analyzer (MCA) in pulse height analysis mode, the desired histogram of photon emission times was produced. After accumulation of a sufficient number of counts per channel, the data were transferred to a DEC PDP 11/23 computer for storage and analysis.

The time base for our measurements was calibrated by detecting visible dye laser pulses at the full 82 MHz repetition rate of the argon laser. This procedure and other observations bearing on the accuracy of absolute time interval measurements will be described later in this chapter. Biasing of photon detection to early times (pulse pile-up) can occur in TCSPC when there is a significant probability for collection of two or more photons for a single excitation pulse. This could be avoided simply by maintaining detection count rates below 40 KHz. In practice, saturation of the microchannel plate imposed a more stringent upper limit to detection rates of several kilohertz only. The flow of emitting molecules out of the field of view of the collection optics could also cause a gradual loss of signal at times exceeding 10 ns. These transit time effects could produce at most slight, systematic distortions of detected signal on the time scale of rotational coherence measurements. These were generally of no concern.

The temporal instrument response for the system was measured by advancing the tip of the nozzle into the path of the laser beam and detecting the scattered laser light. In our efforts to minimize the response width, it was observed that the disparity in optical path lengths for different paths through the spectrometer could contribute significantly to the response time. For example, rays of 300 nm wavelength light which traverse opposite edges of our 76,800 groove grating have transit times differing by 77 ps in first spectral order. Therefore, during these experiments, a mask was placed immediately in front of the grating to reduce by more than two-thirds the width accessible to illumination. Figure 2 shows the optimum response of 40 ps FWHM obtained for the detection system described above, with the grating mask in place. Response widths were more typically around 60 ps. Since the measured response was observed at times to be very sensitive to certain variables of the measurement procedure (spectrometer slit widths and grating position, and exact scattering geometry) and these factors were, in general, necessarily different for response and decay measurements, the measured response may be expected in some cases to differ from the one actually operative for the decay collection. Broadening due to long term instabilities is an additional impediment to precise determination of the effective response width for lengthy experiments. For accurate characterization of decays, the response of the system was measured both before and after the transient measurement.

D. Polarization measurements

Our basic objective in experiments discussed in this thesis was to separately detect components of fluorescence having polarizations oriented at selected angles with respect to the excitation polarization. The high degree of linear polarization required of the excitation source resulted naturally from the process by which the ultraviolet pulses were generated. A soleil compensator was used to orient the excitation polarization perpendicular to the direction of fluorescence collection, as shown in Fig. 3. Analysis of the fluorescence into components was provided by a Glan-air prism polarizer placed before the entrance slit of the spectrometer. This device is formed by cutting a rectangular parallelepiped of the birefringeant mineral calcite into two right triangular prisms, then mounting the two halves with a thin air gap between the faces of the cut.[4] Light entering along the normal to an uncut face of the polarizer crosses a triangular wedge of calcite to the air gap. For a proper angle of cut, the angle of incidence of the light on the calcite-air interface lies between the critical angles of the ordinary and extraordinary rays, as determined by their respective indices of refraction, n_o and n_e. The ordinary ray is then totally internally reflected while the extraordinary ray is transmitted across the gap and continues across the second wedge to exit the prism undeviated. This mechanism of polarization selection has a very high extinction ratio and relatively high transmittance, but it also has the disadvantage of a limited acceptance angle. If light falls on the gap at too large an angle, both components are reflected while if the angle is too small, both are transmitted. The cut-off angle, which depends on n_e, and the leakage angle, which depends on n_o, change with wavelength, but the acceptance angle, which is the difference between them, is about nine degrees throughout the ultraviolet. Since this angle surpassed slightly the acceptance angle of the $f/7$ spectrometer, no unanalyzed light could reach the detector when the prism was correctly positioned. At the upper end of the wavelength range, this entailed biasing the prism normal slightly from the optical axis of the collection system in order to maintain a field of view symmetric about that axis.

The effect of the finite angle of fluorescence collection on mixing of polarization components was shown empirically to be minor by measuring decays with both our standard two lens $f/2$ collection optics and a single lens arrangement of $f/7$ with no apparent effect on results obtained. An indication of the polarization selectivity of the complete excitation/detection system was provided by measurements of scattered laser light. These tests showed the system adequate to provide a detection bias toward the selected polarization of no worse than 30 to 1.

An alternative but equivalent arrangement has also been employed for the detection of perpendicular fluorescence in which the compensator is removed, leaving the excitation polarization parallel to the direction of fluorescence collection. Both polarization components propagating along the collection axis are then perdendicular to the excitation, and the prism analyzer may be removed. Not only is twice as much light available in this configuration, but transmission losses in the prism of about 40% are eliminated, resulting in a significant increase in signal at the detector.

II. Time base calibration

One major application of rotational coherence spectroscopy developed in our laboratory is the measurement of rotational constants of molecules in excited electronic states. The accuracy of rotational constants so measured depends fundamentally on the accurate determination of the time scale of our experimental apparatus. Many calibration methods of varying degrees of accuracy have been developed and applied to time measurement systems of this type.[14] In this section we describe in detail a calibration procedure suited to the equipment and accuracy demands of our experiments. Tests undertaken to verify the accuracy of the established time base are also discussed.

The full time range of the TAC–MCA combination during all experiments described in this thesis was 16 ns or less. To calibrate the detection system, an easily reproducible phenomenon with a time dependence on this time scale was needed. The pulse trains from either of the two synchronously mode-locked lasers used in our experiments provided just such a calibration standard. The repetition rate of the argon ion laser was locked to twice the frequency of the acoustic wave in the mode-locker crystal as described in Section I of this chapter. The driving signal for the mode-locker was derived from a stabilized frequency source which also governed the dye laser cavity dumper. The accuracy of the displayed mode-locker frequency was confirmed by its agreement to better than 10 ppm with the dye laser repetition rate measured by a Hewlett-Packard Model 5340A frequency counter (accounting for reduction of the latter rate by cavity dumping). These considerations show that the average separation of laser pulses produced by the system could be determined to 5 digit accuracy.

To perform a calibration of the 16 ns time range, scattered laser light was collected and recorded in a calibration file showing two well defined laser pulses. The separation in channels of the recorded pulses was then equated to the true separation calculated from the mode-locker frequency. Under the assumption of strict periodicity of the laser pulses and both stability and linearity of the TAC–

MCA combination, uncertainty in the measured channel separation became the limiting uncertainty in the time base calibration. Repeated calibrations showed that the estimation of pulse positions by eye was sufficient to give an upper limit of half a channel width uncertainty in the typical measurement of an 800 channel separation, equaling a relative uncertainty of less than 0.07%. When two recorded pulses were regular in shape and extended over several data channels, their separation could be more precisely established by determining the shift in channels required to bring one pulse into congruence with the other. In such cases, a clear degradation of the overlap of the pulses occurs for changes of less than 1/5 channel in the shift.

The most convenient choice of pulses to use in the calibration were visible dye laser pulses. In particular, the dumped primary and following secondary pulse could be measured by simply scattering laser light through the normal fluorescence detection optics. (Visible instead of ultraviolet light was detected because secondary pulses are virtually eliminated from the ultraviolet by the quadratic power dependence of second harmonic generation.) Detecting dye laser pulses instead of argon ion pulses for the calibration offered the advantages of minimum pulse widths as well as simplicity of implementation. Disadvantages included the difference in detected pulse intensity and possible distortion of the suppressed pulse. This latter is due to the inequivalent positions occupied by the primary and secondary pulses within the cavity-dumped pulse train and raises the possibility that their average separation (as measured in data accumulated over hundreds of millions of pulse pairs) is shifted from the average separation of all mode-locked pulses. However, if a variation in separation of pulse maxima were induced by interaction with the cavity dumper acoustic wave, the observed separation should change with changes in the phase and timing of the cavity-dumping rf signal relative to the circulating cavity pulses. The negative outcome of attempts to observe such an effect was taken as evidence that any deviations from constant pulse separation is not detectable within the current precision of our measurements. Cavity dumped pulses were therefore used for all calibrations. The large difference in intensities of the pulses was typically reduced by detuning the phase and timing of the cavity dumper.

The validity of the assumptions of stability and linearity mentioned above has also been investigated. Both the short- and long-term stability of the time base were tested by frequent calibration. The results showed that variations over spans of days and months often did not exceed the uncertainty in a single calibration. Periods of fluctuation and abrupt changes of the order of one percent have been observed, however. Therefore, for measurements requiring the highest degree of accuracy the time-base was calibrated before and after the experiment.

If either the TAC or MCA has a nonlinear response, a calibration of the system establishes only an average time scale, while the true local time scale will vary from position to position. Since the time interval over which PRC recurrences were measured was often much different from that of the calibration standard, recurrence periods derived on the assumption of linearity may be subject to systematic error. Preliminary linearity tests were performed by measuring at different positions in the calibration range the delay associated with a short cable. These showed no nonlinearity to the .5% level.

After measurements of recurrence periods on a number of molecules were completed, it became clear that measurement errors due to other sources could be limited to about 0.1%. It was therefore desirable to ascertain the linearity of the time base to a similar degree of precision. A standard test of linearity consists of measuring the arrival times of randomly distributed photons.[15] Since these events occur with equal probability in each time division of equal length, the number of counts accumulated in each channel is a measure of the duration to which that channel corresponds. In order to clearly demonstrate deviations from linearity of the order of 0.1%, count totals of approximately 10^6 would be required. Since the typical window of observation in our experiments (~ 16 ns per laser pulse) recorded only about 1/15 of all events (see below), a count total of 10^6 in each of the 1000 observed channels would entail detection of 1.5×10^{10} random pulses, assuming no loss of events due to electronic dead time. At the maximum count rate of the TAC of 140 kHz, as determined by the 7 μs duration of the reset sequence, this signal would require a collection time of 30 hours. Even if our interest is restricted to trends on a scale of hundreds of picoseconds (tens of channels), collection times of several hours are needed. Moreover, a large percentage of start pulses are lost at the maximum count rate, leading to severe pulse pile-up distortion. These circumstances rendered it impractical to carry out extensive linearity studies. For a limited investigation of long range nonlinearity, we used a high gain photomultiplier as the random pulse generator at count rates of $\sim$ 30 kHz. Even at these rates, the influence of pulse pile-up is not negligible at the 0.1% sensitivity level. Pulse pile-up effects must, therefore, be considered in the analysis of our linearity measurements. The calculation of these effects is described next.

In the TCSPC technique, events are timed relative to the periodic stop pulse (of period T) from the laser; therefore, the measurement system time coordinate (t') is limited to the interval $(0, T)$. Only a segment of this interval, between t_1 and t_2, is actually observed. The probability density over t' for the arrival of a photon from a source uncorrelated with the laser is a constant $p_a = 1/T$. If f is the expected number of photons per laser cycle, the number of photons arriving in any real time interval Δt has a Poisson probability distribution with expectation $f\,\Delta t/T$,

$$p(N; \Delta t) = \exp(-f\,\Delta t/T)\frac{(f\,\Delta t/T)^N}{N!} \; . \tag{2.1}$$

The probability that no photons arrive is then $p(0; \Delta t) = \exp(-f\,\Delta t/T)$. The probability density $p_r(t)$ for a photon that arrives in a given cycle to successfully trigger the start channel of the TAC at time t' is the product of p_a and the probability that the electronics are not "dead" at that time. The latter is the probability that no other photon has arrived since the last stop pulse ($t' = 0$) or the last resetting of the electronics ($t' - t_d$), whichever is more recent. Because the reset process, which lasts many complete laser cycles, begins with a stop pulse, t_d is expected to have a fairly constant value. When t_d is not in (t_1, t_2), the same one of the two times, either 0 or t_d, is more recent for each t' in the observation window. Calling this time t_0, we have

$$p_r(t') = \frac{1}{T} \exp\big(-f(t' - t_0)/T\big) \tag{2.2}$$

for $t_1 < t' < t_2$. The probability for a recorded event is thus not constant but falls monotonically at a rate determined by the photon arrival rate f/T. The fractional change in p_r from t_1 to t_2 is

$$\frac{[p_r]|_{t_1}^{t_2}}{p_r} = \big(p_r(t_2) - p_r(t_1)\big)/p_r(t_1) = \exp\big(-f(t_2 - t_1)/T\big) - 1 \ . \tag{2.3}$$

This expression, being independent of t_0, applies to the cumulative distribution of recorded events, even if t_0 varies from photon to photon, as long as it does not fall between t_1 and t_2. For small f, the exponential may be expanded to give

$$\frac{[p_r]|_{t_1}^{t_2}}{p_r} \simeq -f(t_2 - t_1)/T \ . \tag{2.4}$$

Two independent linearity tests as described above were carried out on our detection system for one of the time ranges used in our experiments. These showed no deviations of the local time scale from the average scale exceeding .25%. However, a least squares fit to a straight line of the test of highest signal-to-noise, corrected for the influence of pulse pile-up by equation (2.4), showed a trend of deviations above and below the mean channel count that was about equal to the standard deviation of the measured values (.18%). If such a trend were present during a recurrence measurement made over the first half of the calibration range, the derived period would be about 0.1% too long. This error is greatly reduced when the measurement spans the full range of the calibration. Results of many of the measurements discussed in Chapter 5 appear to support the presence of such a bias. The linearity tests described here confirm that errors introduced by this effect are not outside the uncertainties estimated from all other sources, but also indicate that a fuller characterization of the system linearity is essential to push the accuracy of the technique beyond the current level.

When the time range was shorter than the laser 12 ns pulse separation, an indirect method of calibration was required. The most convenient was the insertion of a calibrated cable in the pulse circuit to delay the measured position of the scattered laser pulse by a known length of time. The cable delay was measured on a longer time scale which was itself calibrated against the laser repetition rate. The accuracy of the average time scale established by this simple and rapid method was estimated at .25%. Alternatively, when the MCA conversion gain was set at 2048 channels, a time range between 6 and 12 ns could be calibrated by using the MCA digital offset to shift the observed time "window" from the fundamental to the secondary pulse, thereby permitting the total channel separation of the two pulses to be determined. The fact that the two pulses were not recorded simultaneously reduced the accuracy with which the absolute separation could be determined, but the larger number of channels between the pulses resulted in a relative error comparable to that achieved by the direct calibration.

From comparison of calibrations at different settings on the MCA, it also appears that the MCA conversion gain results in a precise scaling of the time range, suggesting that experiments on at a conversion gain setting of 2048 may be calibrated in the usual manner by decreasing the conversion gain to 1024 for the calibration. This procedure was not used here, however. By contrast, the time range settings of the TAC are very approximate and a calibration of one range may be in error by up to 5% if applied to another range based on the nominal scaling.

We note here one other novel calibration technique which has already been employed in our laboratory on a time range of 4 ns. This is the utilization of rotational coherence recurrences themselves as the time standard. The recurrence period of *t*-stilbene has been used to calibrate measurements of short time phenomena in the fluorescence of *t*-stilbene or its van der Waals complexes.[16] An accuracy of 1% or better is easily and conveniently obtained. This accuracy is more than adequate for characterizing fast fluorescence rises and decays. The potential for the use of recurrences of other molecules in this manner is great. A molecule like I_2, for example, whose recurrences have now been observed,[17] displays time markers at a separation of approximately 600 ps, or 300 ps when the out-of-phase recurrence is included. This separation is well-known (to at least 6 digit accuracy, if centrifugal distortion is neglected) and is discretely variable as a function of the excited vibration. Smaller molecules have correspondingly shorter recurrence spacings and could be used to calibrate even shorter time ranges.

References

1. A. Yariv, *Quantum Electronics* (John Wiley and Sons, New York, 1975).
2. A. E. Siegman, *Lasers* (University Science Books, Mill Valley, California, 1986).
3. W. R. Lambert, P. M. Felker, and A. H. Zewail, J. Chem. Phys. *ibid.* **81**, 2217 (1984).
4. E. Hecht and A. Zajac, *Optics* (Addison-Wesley, Reading, Massachusetts, 1974).
5. N. Bloembergen, *Nonlinear Optics* (W. A. Benjamin Inc., New York, 1965).
6. J. A. Syage, W. R. Lambert, P. M. Felker, A. H. Zewail, and R. M. Hochstrasser, Chem. Phys. Lett. **88**, 266 (1982); J. A. Syage, P. M. Felker, and A. H. Zewail, J. Chem. Phys. **81**, 4685 (1984).
7. W. R. Lambert, P. M. Felker, J. A. Syage, and A. H. Zewail, J. Chem. Phys. **81**, 2195 (1984).
8. P. M. Felker and A. H. Zewail, J. Phys. Chem. **88**, 6106 (1984); P. M. Felker, W. R. Lambert, and A. H. Zewail, J. Chem. Phys. **82**, 3003 (1985).
9. W. R. Lambert, P. M. Felker, and A. H. Zewail, J. Chem. Phys. **75**, 5958 (1981); *ibid.* **81**, 2209 (1984); P. M. Felker and A. H. Zewail, J. Chem. Phys. **82**, 2975 (1985); *ibid.* **82**, 2994 (1985).
10. W. L. Meerts, W. A. Majewski, and W. M. van Herpen, Can. J. Phys. **62**, 1293 (1984).
11. B. W. Keelan and A. H. Zewail, J. Phys. Chem. **89**, 4939 (1985).
12. B. W. Keelan and A. H. Zewail, J. Chem. Phys. **82**, 3011 (1985).
13. C. C. Lo, B. Leskover, P. R. Harteg, and K. Sauer, Rev. Sci. Instrum. **47**, 1113 (1976); D. V. O'Connor and D. Phillips, *Time-correlated single-photon counting* (Academic Press, London, 1984).
14. For example, see: H. E.Taylor, Nucl. Instr. Methods **68** (1969); Z. H. Cho and C. Bohm, Nucl. Instr. Methods **84** (1970).
15. Ortec product information, Model 457 Biased Time to Pulse Height

Converter Operating and Service Manual #2924 01C 0778, Ortec Incorporated, Oak Ridge, Tennessee.

16. D. H. Semmes, J. S. Baskin, and A. H. Zewail, J. Am. Chem. Soc. **109**, 4104 (1987); D. H. Semmes, J. S. Baskin, and A. H. Zewail, submitted for publication.
17. M. Dantus, R. M. Bowman, A. H. Zewail, to be submitted for publication.

Figure Captions

1. Overview of the experimental arrangement for the measurement of time-resolved fluorescence of jet-cooled molecules. Key to symbols: ML – mode-locker; DL – dye laser; CD – cavity dumper; SHG – second harmonic generation; PD – photodiode; MCP – microchannel plate; TAC – time to amplitude converter; and MCA – multichannel analyzer.
2. Temporal response of the fluorescence detection system to scattered laser pulses. The spectral resolution is $\simeq 2\ \text{cm}^{-1}$. A mask restricts the width of the spectrometer diffraction grating accessible to illumination. The long trailing edge is typical of the microchannel plate detector.
3. Detailed sketch of the experimental arrangement for polarization selective excitation and detection of fluorescence of jet-cooled molecules. $\hat{\epsilon}_1$ is the polarization vector of the excitation pulse. $\hat{\epsilon}_2$ is the polarization component of the collected fluorescence that is selected by the prism analyzer for detection. Two possible orientations of $\hat{\epsilon}_2$ are shown. MCP is a microchannel plate photomultiplier. Pulse processing and timing electronics are incorporated in the "photon counter" black box.

Figure 1

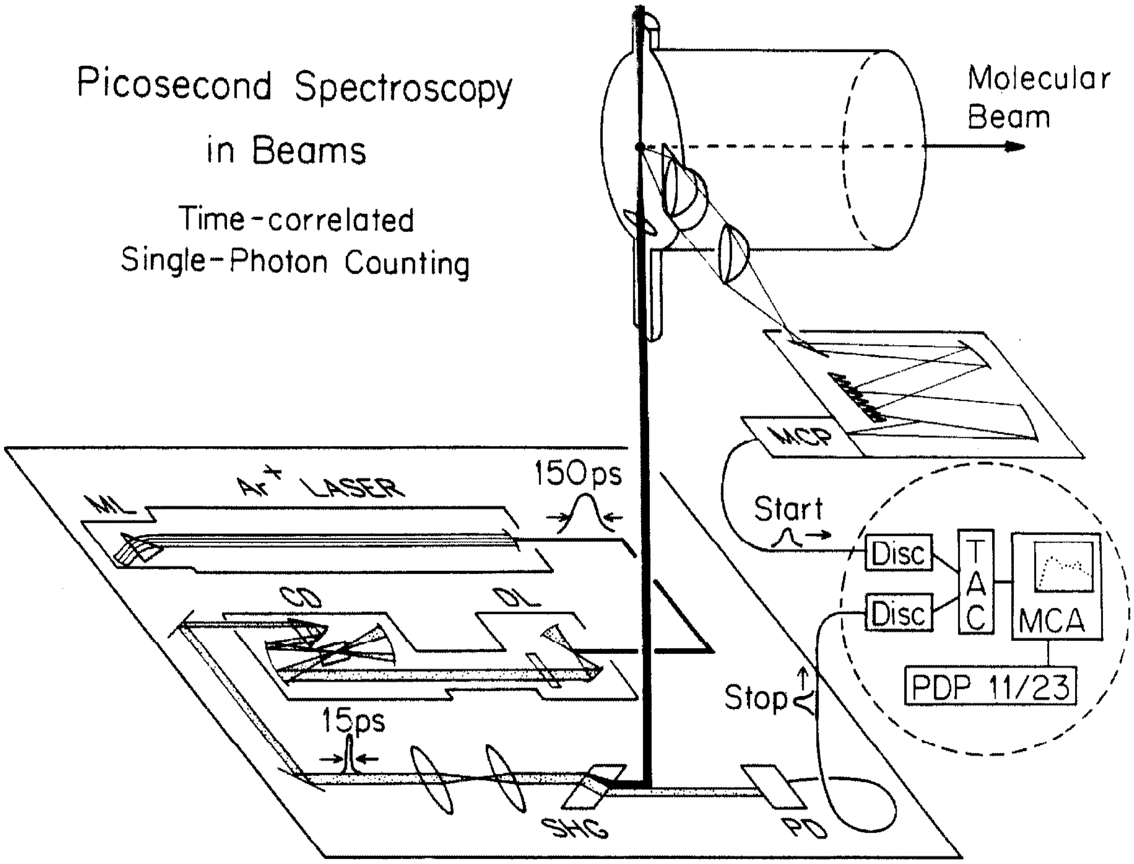
Picosecond Spectroscopy
in Beams
Time-correlated
Single-Photon Counting
Molecular
Beam
MCP
Ar+ LASER
ML
150ps
Start
Disc
Disc
T
A
C
MCA
PDP 11/23
CD
DL
Stop
15ps
SHG
PD

Figure 2

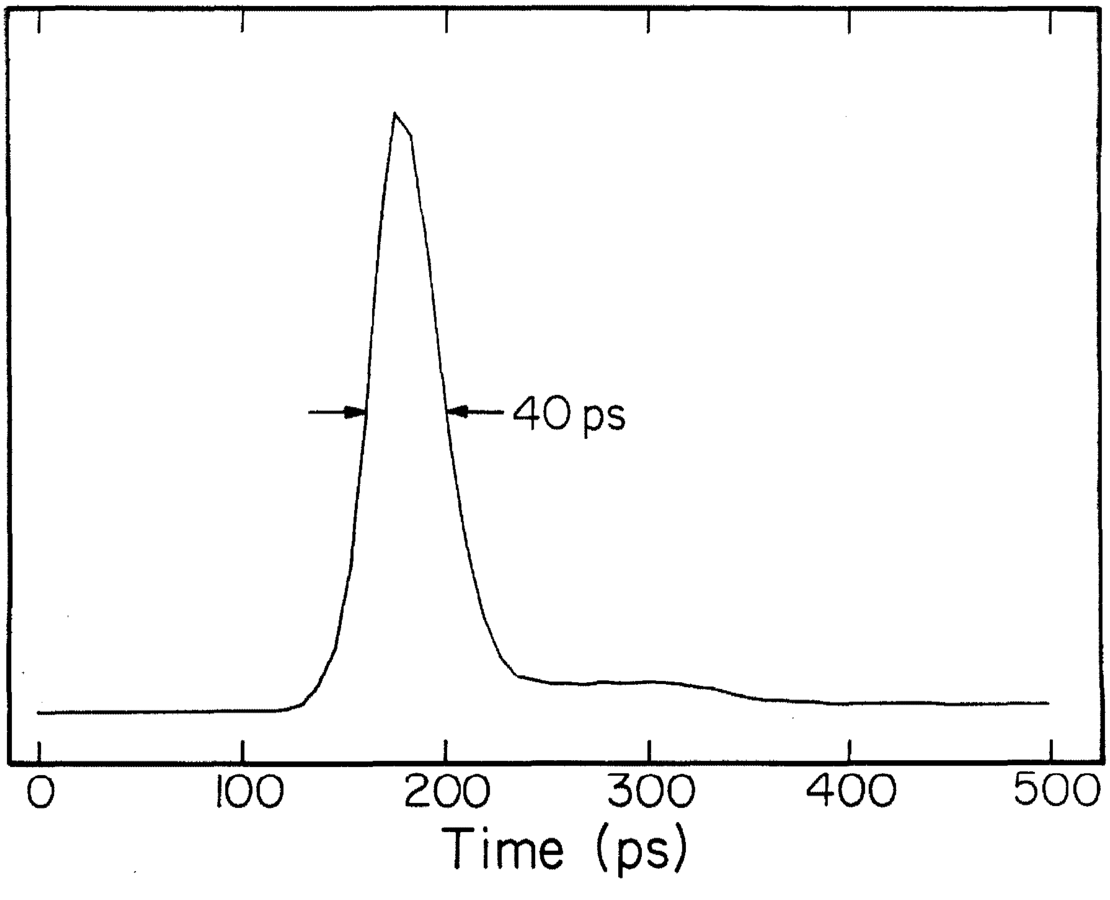

Figure 3

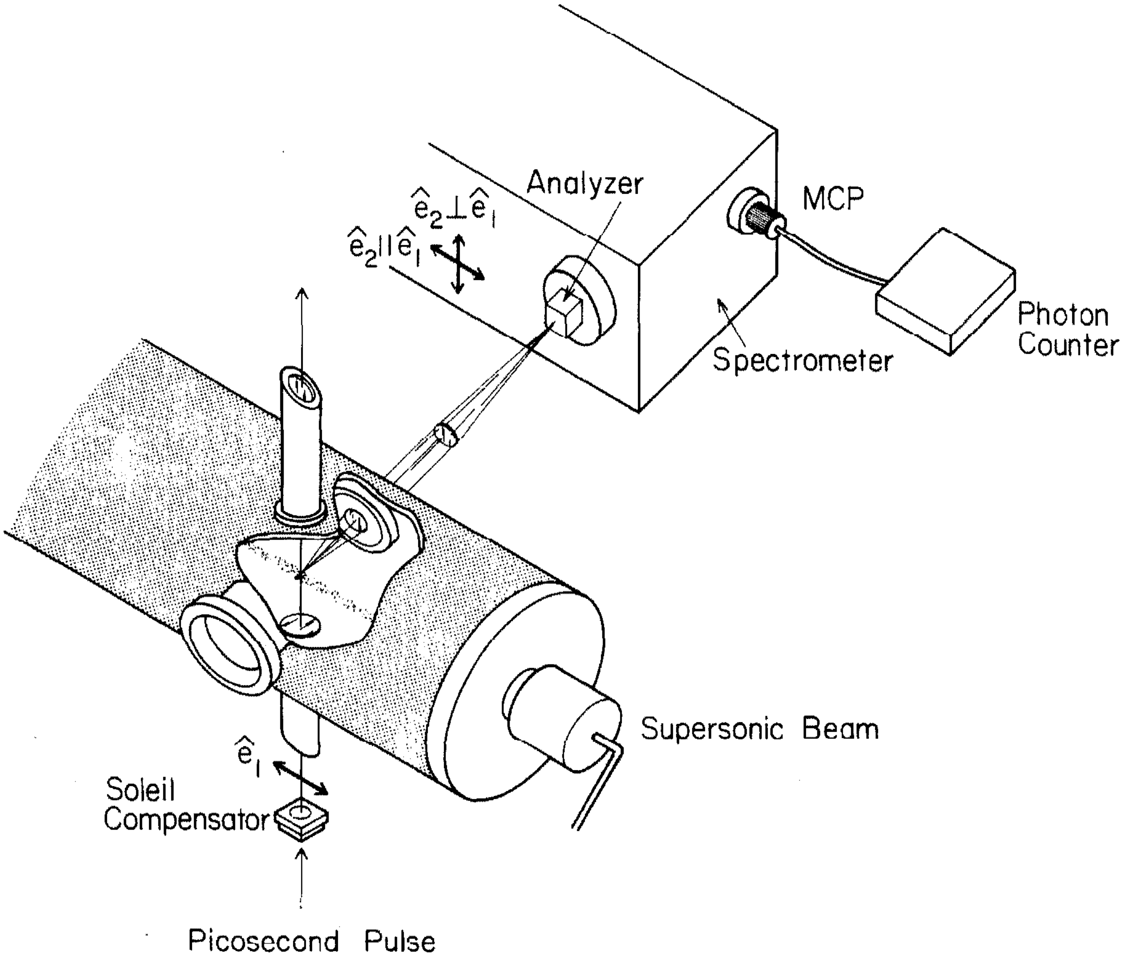

Picosecond-Molecular Beam Polarization Apparatus

Chapter 4

Data Analysis

Portions of this chapter are taken from the following published articles:

"Purely Rotational Coherence Effect and Time-resolved Sub-Doppler Spectroscopy of Large Molecules. II. Experimental," by J. S. Baskin, P. M. Felker, and A. H. Zewail.

Reprinted with permission from The Journal of Chemical Physics, Volume 86, p. 2483. Copyright 1987 American Institute of Physics.

and

"Determination of Excited-State Rotational Constants and Structures by Doppler-Free Picosecond Spectroscopy," by J. S. Baskin and A. H. Zewail.

Reprinted with permission from The Journal of Physical Chemistry, Volume 93, p. 5701. Copyright 1989 American Chemical Society.

In this chapter we give a detailed account of the various procedures employed in the interpretation of our measurements. Methods applied to extract excited-state parameters from measurements of polarization-analyzed fluorescence are described first. Details pertinent to the calculation of the van der Waals molecule potential energy surfaces discussed in Section II B of Chapter 5 are then given.

The nature of purely rotational coherence lends itself to two semi-independent types of analysis. The first is the determination of recurrence periods and the second is the fitting of data to numerical simulations. For the first, the optimal time range for data collection includes many recurrence periods. For the second, resolution of details of recurrence shapes and amplitudes is of primary importance and a shorter time scale is usually preferable. A full description of the procedure employed for each of these methods of analysis follows.

Rotational recurrence periods and associated error bars were determined in the following manner. Recurrence positions in a measured decay were located by inspection, and uncertainties corresponding roughly to 90% confidence intervals were estimated for each one. Short fluorescence lifetimes were first removed to prevent biasing of the positions. This was accomplished by multiplying the data by $e^{t/\tau}$ where τ was the measured lifetime. A weighted least squares fit to the estimated positions yielded the recurrence period. The quoted uncertainties were found conservatively by considering the maximum and minimum periods consistent with the error bars on the extreme recurrences. For the values reported here, these conservative error estimates have been reduced only when warranted by the good agreement between a series of independent measurements.

Fig. 1 presents an example of a rotational coherence measurement used to determine the recurrence of *t*-stilbene. The decaying curve is the measured signal with the polarization analyzer set to select parallel fluorescence. Also shown at the top of the figure is the same data after elimination of the decay. In this, the regularly spaced in-phase recurrences may be located and their positions accurately measured. On the basis of a single measurement of this type, the

PRC recurrence period of *t*-stilbene could be determined with an uncertainty as low as ~ 4 ps.

As seen in Section III of Chapter 2, precise values for the rotational constants of asymmetric tops are not given directly by PRC recurrence periods as in the symmetric top case. Even the approximate expressions derived in that section do not permit the determination of independent $B'$and C' values without some additional constraint (such as the assumption of planarity). To extract as much potential information as possible from the experimental data therefore requires comparison with numerical simulations designed to accurately reproduce the conditions of the measurement.

The fundamental component of these simulations is the expression derived by Felker and Zewail[1] and discussed at length in Chapter 2. There are three important assumptions involved in each PRC simulation in this thesis, which are: 1) The initial ground state population distribution is assumed Boltzmann. 2) A rigid-rotor rotational Hamiltonian is assumed. 3) The possibility of axis switching in excitation is neglected. By this last, we mean that the equilibrium principle axes of inertia of the ground and excited states are assumed to coincide.[2] It should be kept in mind that any of these assumptions may lead to inaccuracies since they need not be justified in all cases. Further limitations are placed on the accuracy of the calculations by the finite temporal and frequency resolution, frequency bandwidth, and range of ground-state rotational levels included. However, checks were made to ensure that the choice of these parameters had no significant influence on the results. Typical values used for final calculations were 4 ps and 1 MHz for temporal and frequency resolutions and 50 GHz for the frequency bandwidth. The temporal resolution used during fitting was that of the measured data, either 8 or 16 ps. The frequency bandwidth was also set at 35 GHz during preliminary fitting. This lower value had no noticeable effect after convolution with our ~ 50 ps response. An energy cutoff was set for the inclusion of ground-state rotational levels. This was preferable to a simple limit on J_0 since the overlap of J manifolds is very pronounced in many of the molecules studied. It was found that simulated intensities reached their asymptotic values when ground-state levels with J_0 up to 25 – 35 (depending on temperature and molecule) were included in the summation. Again, preliminary fitting was done with somewhat lower ground state limits, chosen to give about 99% of the asymptotic intensity.

The contributions of minor isotopic species due to the natural abundance of ^{13}C have also been considered and will be discussed in relation to the *t*-stilbene results in Chapter 5. These contributions can be important but were negligible for the purposes of the present work.

The calculations of PRC intensities requires, in principle, the specification of 11 parameters: the rotational temperature, six rotational constants (A'', B'', C'', A', B', C'), and the directions of the absorption and emission dipoles ($\theta_1, \phi_1, \theta_2, \phi_2$). The ground-state structure exerts an influence on PRC in two ways: the ground-state energies determine the initial state distribution, and the eigenstates govern the transition strengths to each upper state. However, it has been found that results of simulations are quite insensitive to the exact values of the ground-state constants, as might be expected since the beat frequencies responsible for the appearance of recurrences depend only on the excited-state energies. Thus, it is sufficient in practice to specify a single set of rotational constants. In addition, in the cases considered in Chapter 5, a single electronic transition is involved in both absorption and emission, implying a single transition moment. This reduces the effective number of simulation parameters to six. The computer fitting routines that have been employed in the data analysis for this thesis treat only four of these six as variables, leaving the transition moment fixed.

To perform the least-squares fitting, calculated intensities were convoluted with an instrument response function and compared to the experimental data. This comparison entailed the introduction of two additional fitting parameters: a scaling factor to adjust the simulation amplitude and a time shift to synchronize the temporal evolution of the two files.

The experimental data could be fit either in the form of parallel fluorescence or of polarization anisotropy. As discussed in Chapter 2, the fluorescence polarization anisotropy is defined as

$$r(t) \equiv \frac{I_{\parallel}(t) - I_{\perp}(t)}{I_{\parallel}(t) + 2I_{\perp}(t)} \tag{1}$$

where $I_{\parallel}(t)$ and $I_{\perp}(t)$ are the fluorescence intensities with polarizations parallel and perpendicular, respectively, to that of the excitation. The anisotropies presented have been calculated by the formula

$$R(t) \equiv \frac{[F_{\parallel}(t) - BL_{\parallel}] - a[F_{\perp}(t-t') - BL_{\perp}]}{[F_{\parallel}(t) - BL_{\parallel}] + 2a[F_{\perp}(t-t') - BL_{\perp}]} \tag{2}$$

where $F_{\parallel}(t)$ and $F_{\perp}(t)$ are the measured decays, $BL_{\parallel}$ and $BL_{\perp}$ are their respective dark current imposed baselines, and a and t' are two adjustable parameters. Here the upper case R is employed (following the notation adopted by Negus et al.[3]) to emphasize that the effects of limited temporal response are directly incorporated into $R(t)$ and must be accounted for when comparing results with theory. The value of a was chosen to reproduce the theoretically expected[1] asymptotic value of the anisotropy, and t' was adjusted by consideration of the decay rises and very early behavior of $R(t)$. The need for these parameters arises from unavoidable changes in detection efficiency and time origin which are coincident with the change of detection polarization (i.e., the physical rotation of the analyzer). They may also, of course, be used to compensate for systematic detection bias (particularly the polarization dependence of the spectrometer grating efficiency) and drifts in the detection system or the excitation power.

Because $R(t)$ near $t = 0$ (taken as the instant that the decay amplitudes depart their baseline values) is very sensitive to small changes in t' as well as suffering from very low signal to noise, precise early time anisotropy values could not be derived. In Fig. 2 is shown, for example, the effect of small variations in the value of t' on $R(0)$ in a measurement of the polarization anisotropy of t-stilbene fluorescence. Note, however that values of $R(t)$ at longer times are relatively insensitive to the choice of t', so that, in particular, the positions and amplitudes of recurrences are well determined. Similarly, apparent $R(0)$ values are strongly affected by even small response drifts, which again have negligible impact on $R(t)$ at other times.

Methods employed to find the best-fit PRC parameters to a given set of data included a simple grid search of likely regions of the parameter space and optimization routines either without constraint or constrained by the condition of planarity. In choosing initial values for the rotational constants, two generally applicable relations were useful. The first is

$$A^{-1} \geq C^{-1} - B^{-1} \; , \tag{3}$$

which holds (to very good approximation) for any set of rotational constants. (This relation is not rigorous for effective rotational constants; i.e., A^{-1} may be slightly smaller than $C^{-1} - B^{-1}$ as a result of averaging over the vibrational state.) The second depends on the measured nutation recurrence period (τ_1) and is by now well known:

$$B' + C' \approx 1/\tau_1 \tag{4a}$$

if the molecule is prolate or

$$A' + B' \approx 1/\tau_1 \tag{4b}$$

if it is oblate. The rotational constants of the ground state could either be held fixed at predetermined values or be equated to the excited-state values. A χ^2 test was used to judge the goodness of fit. Poisson statistics apply to decays collected by single photon counting. For $R(t)$, approximate expressions[4] based on Eq. (2) were used to characterize the distribution, which is not Poisson. The standard deviation of each anisotropy value was given by

$$\sigma_R = \frac{3a}{\left[F_{\parallel} - BL_{\parallel} + 2a(F_{\perp} - BL_{\perp})\right]^2} \sqrt{(F_{\perp} - BL_{\perp})^2 F_{\parallel} + (F_{\parallel} - BL_{\parallel})^2 F_{\perp}} \; . \tag{5}$$

When parallel fluorescence was fitted, the decay lifetime was eliminated from the fitting process by multiplying the data by $e^{t/\tau}$, with a corresponding adjustment of weights used in the χ^2 calculation. The measured response with which the simulation was convoluted was also multiplied by $e^{t/\tau}$. The rational for this was as follows. We may write the fluorescence intensity as a product $I(t) = A(t)e^{-t/\tau}$, where all evolution within the excited state is represented in the function $A(t)$ and $e^{-t/\tau}$ accounts for the excited-state population decay. If the temporal response of the detection system is $S(t)$, the measured signal is then the convolution $F(t) = I(t) \circ S(t)$, or

$$F(t) = \int_{-\infty}^{+\infty} I(t-t')S(t')\,dt' = e^{-t/\tau} \int_{-\infty}^{+\infty} A(t-t')e^{t'/\tau}S(t')\,dt' \ . \qquad (6)$$

Thus the function $F(t)e^{t/\tau}$ that we wish to fit is equal to the convolution of $A(t)$ with $e^{t/\tau}S(t)$. The precision of the lifetime measurement is not critical to this process. Since the PRC signal is known to vary around a constant DC level, it is only necessary that no long range trends appear in the residual of the exponential fit to the data.

The Fortran program ATFIT2 in Appendix III is the most general fitting routine employed in the analysis of experimental data discussed in this thesis. In ATFIT2, all three excited state constants are varied independently, along with the rotational temperature and the parameter T0 that fixes the temporal synchronization of the data and the simulation. The amplitude scaling can also be optimized, but it was found that no significant improvement in χ^2 could be obtained by varying the scale from that determined by normalization of the two files. The ground state rotational constants are held at predetermined values in this program. The gradient of the χ^2 function in the parameter space of the five remaining adjustable parameters was determined analytically by calculations in which each parameter was displaced above and below its current value. For efficiency, the dependence of χ^2 on T0 was determined by shifting a single simulated data set plus and minus one channel. This is generally a very gross adjustment, and a finer step may be worth the extra computation time involved. Since the temperature enters only in the final step of the PRC frequency spectrum calculation, spectra for three different temperatures were obtained at essentially the price of one computation.

The minimization algorithm used in ATFIT is not completely effective when parameters are correlated. A particular problem was presented by the correlation between T0 and the absolute magnitude of the rotational constants as a set. To see this, note that PRC frequencies, even for the asymmetric top, are linearly proportional to the rotational constants. Thus, multiplication of all constants by a scaling factor γ results in a scaling of the PRC time domain signal by γ^{-1}. Since the experimental data cover a fixed time range which is positioned relative to the simulation by the parameter T0, T0 must be adjusted when the simulation time scale is expanded or contracted. For a given T0, the program ATFIT was found effective at optimizing the shape of the PRC pattern; that is, the correct ratios of rotational constants was determined. However, to find the optimum scaling factor and the corresponding T0, the program ATGRID1 was used. In this program, the simulation time scale and T0 were varied simultaneously in such a manner as to maintain the center of the data at a fixed position in the simulation. The plot numbered 1 in Fig. 22 of Chapter 5 is an example of such an optimization. The value of T0 was decreased by 37 ps, or about $2\frac{1}{2}$ channels, over the range of the plot to compensate for the contraction of the simulation time scale.

For many of the most time-consuming calculations of asymmetric top PRC intensities, a near-symmetric treatment was used. This treatment is based on the fact that the asymmetric top eigenfunctions $|J\tau M\rangle$ must transform smoothly into symmetric top eigenfunctions as B and C (or A and B) converge. Thus, only a single coefficient in the expansion of each eigenfunction,

$$|J\tau M\rangle = \sum_{K=-J}^{J} a(J\tau K)|JKM\rangle \ , \qquad (7)$$

can have appreciable amplitude for small asymmetries. In the near-symmetric treatment, all other coefficients are assumed negligible in the evaluation of Eq. (3.15) of Chapter 2. This has much the same result as applying the approximate selection rules $\Delta K_{sym} = 0, \pm 1$ where K_{sym} stands for K_{pr} or K_{ob}, the designation of the closest symmetric top limit. In this approximation, the only consequence of asymmetry is the shift in rotational energies that causes changes in PRC beat frequencies. This treatment was used regularly for preliminary fitting and off-axis dipole calculations and was found to give satisfactory results even for moderately large degrees of asymmetry while providing a substantial ($> 50\%$) savings in computer time. Near-symmetric and full asymmetric calculation options are provided in the program ATFIT, to be selected at each execution.

The evaluation of Eq. (3.14) of Chapter 2 (disregarding the exponential decay factor) is essentially a Fourier transformation from the frequency to the time domain. Recalling that $f(J_0, J_1, J_1', \tau_0, \tau_1, \tau_1') = f(J_0, J_1', J_1, \tau_0, \tau_1', \tau_1)$, the direct calculation requires the sum over all distinct frequencies ω of $A\cos(\omega t)$ at each temporal data point. The amplitude A is either f or $2f$, depending on whether J_1 and τ_1 are different from J_1' and τ_1' or not. In practice the frequencies are recorded in an array of finite resolution so that the calculated frequencies must be rounded to the nearest value in the periodic grid. (For symmetric tops this actually need not introduce any limitations in accuracy, since all frequencies fall exactly on a grid of spacing $2B'$.) If the number of distinct frequencies of significant amplitude is called INU, and the number of time points NPTS, the number of cosine evaluations is INU·NPTS.

Since values of either INU or NPTS or both may be in the thousands, it is natural to consider alternative implementation of this transformation by a fast Fourier transform (FFT) algorithm. In an FFT the calculation time is proportional to N log(N) where N is the number of equally spaced points in either the time or frequency domain, since both must be equal. When the frequency and time resolutions are designated by ν_{res} and CT respectively, the total time range involved in the FFT calculation ($\equiv$ N·CT) is equal to $1/\nu_{\mathrm{res}}$, and the calculated temporal function is periodic with this period. Since this periodicity is a necessary consequence of the chosen frequency resolution and the associated rounding of frequencies, the calculated function near the end of the time range may be completly unrelated to the true function. Since signal differences of less than 1% are important in PRC analyses (see Chapter 5), the useful part of the calculated time range will, in fact, be quite small. Consider, for example, a modulation term of true frequency ν. If this frequency falls midway between two grid values, it will be recorded as ν' such that $|\nu - \nu'| = \frac{1}{2}\nu_{\mathrm{res}}$. The true and calculated intensities will be $I = A\cos(\Phi)$ and $I' = A\cos(\Phi')$, where the phase $\Phi = 2\pi\nu t$ or the phase difference is

$$\Delta\Phi = \pi\nu_{\mathrm{res}}t \ . \tag{8}$$

The maximum intensity difference for a given (small) $\Delta\Phi$ is equal to $A \cdot \Delta\Phi$. An upper limit on $\Delta\Phi$ of .02 will insure that the calculated intensity does not differ from the true intensity by more than 1% of the total amplitude of the modulation ($\equiv 2A$). Since the unmodulated intensity is typically from 1.5 to 3 times greater than the sum of all modulation amplitudes, and the average frequency defect $|\nu - \nu'|$ is, in general, smaller than $\frac{1}{2}\nu_{\mathrm{res}}$, calculations with the above limit placed on $\Delta\Phi$ can be expected to accurately reproduce features of 1% amplitude. From Eq. (8), t is equal to $\Delta\Phi/(\pi\nu_{\mathrm{res}})$. We find then that data from an FFT calculation may be expected to be reliable for $t \leq .02/(\pi\nu_{\mathrm{res}})$, or less than 1% of the entire calculated time range. Comparison of actual calculations at different frequency resolutions showed that limited resolution introduced errors of about $\frac{1}{2}$% of the signal at 5% of the time range, and $\leq$ .1% at $1\frac{1}{2}$% of the range.

As the preceeding considerations demonstrate, the time range of the FFT calculation must be a factor of 20 or more longer than the time range of interest. This determines an upper limit for the value of ν_{res}). For detailed comparisons with experimental results, the temporal resolution must be a multiple of the experimental value. This establishes a minimum frequency range of 1/CT. A further restriction is the limitation of N to integral powers of 2. In contrast, each parameter can be set independently at an appropriate value for the direct calculation. Thus the direct calculation gains a factor of at least 20 by the fact that the time range can be set as needed. Similarly, 1/CT is typically much higher than the range of frequencies that need otherwise be included. Another factor that reduces the advantage of the FFT is the sparseness of the frequency array. In the direct calculation, the time loop is not executed for frequencies with amplitudes below a minimum threshold. Depending on the resolution and span of frequencies, this may reduce the time for the direct calculation by another order of magnitude relative to the FFT. From a comparison in which only 2% of the FFT time range was considered useful and 388 temporal data points were required, the FFT transformation was found to be about 30% slower than the direct method. For larger NPTS, the FFT computation time scales as NPTS log(NPTS). Assuming that the frequency array is already sparse, as it is in our calculations, direct calculation for larger NPTS scales as NPTS, since the smaller ν_{res} that is required does not significantly affect the value of INU. An improved FFT algorithm or a higher error tolerance would change the balance in favor of the FFT, but the advantage is not expected to be significant for calculations of high accuracy. On the other hand, direct transformation has the general advantage that PRC signals for various time ranges, resolutions, and starting times can be calculated from a single frequency spectrum, without regard for the values of the frequency domain parameters. Note also that calculation of the frequency spectrum itself consumes more than half of the computation time, so further gains in transformation speed have diminishing returns.

Because the PRC calculation begins with the calculation of a Fourier spectrum, comparison of experimental data and simulation in the frequency domain could greatly improve the efficiency of PRC fitting. This procedure has not been investigated. Problems to be addressed include proper weighting of the least square sum and the effect of temporal shifts between the data and the measured response.

In some cases, the influence of noise on our measurements has been tested by the addition of random noise to simulated data. Poisson statistics were assumed for this purpose. An algorithm due to Knuth[5] was used to generate Poisson distributed data for low count totals. A more efficient algorithm was used to calculate Gaussian noise for count totals above 15, since for such values the Poisson distribution differs negligibly from a Gaussian distribution with standard deviation equal to the square root of the expectation value.

Another technique of assessing the polarization dependence of our data was applied to certain decays measured at high excess vibrational energy whose temporal evolution was quasi-biexponential in nature. In such cases, individual decays were fit to a biexponential decay law using a nonlinear least squares fitting algorithm and accounting for convolution with the measured response function[6]. The behavior at early time of these decays is well characterized by the fast lifetime and fast-to-slow amplitude ratio obtained as parameters from such a fit. Measurements of fluorescencepolarized parallel, perpendicular, and at 54.7° (magic angle) to the excitation polarization were compared on the basis of their respective fit parameters to determine the effect, if any, of polarization anisotropy transients on this early time evolution.

In Section II B of Chapter 5, we discuss calculations of the binding potentials of *t*-stilbene–rare gas van der Waals complexes. These calculations consisted of summing simple isotropic atom–atom potentials representing the interaction of each rare gas atom with all other atoms of the complex, including other rare gas atoms in the higher complexes. The structure of the parent molecule was assumed fixed. The two-body potentials were of the form

$$V(r) = -A\left[\frac{1}{r^6} - \frac{1}{2}\frac{\sigma^6}{r^{12}}\right] \tag{9}$$

where r is the separation of the two atoms. This potential has a minimum energy $\epsilon = -A/(2\sigma^6)$ at separation σ. The parameters A and σ are functions of the species of the two atoms. Values of A and σ for homoatomic interactions of carbon, hydrogen and rare gas atoms have been derived from experimental data of various types.[7,8,9,10] Those values which are pertinent to our calculations are given in Table I, along with the corresponding well depths.

The combining rules proposed in Ref. 8

$$A_{IJ} = \sqrt{A_{II}A_{JJ}} \qquad \text{and} \qquad \sigma_{IJ} = \frac{\sigma_{II} + \sigma_{JJ}}{2} \tag{10}$$

may be applied to the data of Table I to obtain parameters for C–RG and H–RG interactions. C–RG parameters derived in this manner from the data of Ref. 7 were used in the calculation of tetracene–rare gas van der Waals potentials by Ondrechen et al.[11] These derived parameters, and H–RG parameters used in the same calculations, are given at the top of Table II. Our initial potential calculations were based on these parameters, as explained in Chapter 5. Also given in Table II are parameters used in later calculations which are based on Eq. (10), the C–C and H–H values of Ref. 10, and the rare gas data of References 7 and 9. Since these latter two references are reasonably consistent on the neon and argon data, the values of Ref. 7 were used throughout. We note that the upper and lower sets of H–RG parameters differ substantially. Data from Ref. 8 were cited in Ref. 11 as the basis for the upper values, but these data could not be found. In any case, the results of our calculations were not qualitatively affected by the choice of H–RG parameters.

References

1. P. M. Felker and A. H. Zewail, J. Chem. Phys. **86**, 2460 (1987).
2. G. Herzberg, *Molecular Spectra and Molecular Structure* (Van Nostrand Reinhold, New York, 1966), Vol. III, p. 208.
3. D. K. Negus, D. S. Green, and R. M. Hochstrasser, Chem. Phys. Lett. **117**, 409 (1985).
4. P. L. Meyer, *Introductory Probability and Statistical Applications* (Addison-Wesley, Reading, Massachusetts, 1970), p. 139.
5. D. E. Knuth *Seminumerical Algorithms: the Art of Computer Programming* (Addison-Wesley, Reading, Massachusetts, 1969), Vol. 2.
6. P. R. Bevington, *Data Reduction and Error Analysis for the Physical Sciences* (McGraw-Hill, New York, 1969).
7. A. D. Crowell and R. B. Steele, J. Chem. Phys. **34**, 1347 (1961).
8. J. O. Hirshfelder, C. F. Curtiss, and R. B. Bird, *Molecular Theory of Gases and Liquids* (Wiley, New York, 1954) p. 168.
9. A. L. Burgmans, J. M. Farrar, and Y. T. Lee, J. Chem. Phys. **64**, 1345 (1976).
10. G. Némethy, M. S. Pottle, and H. A. Scheraga, J. Phys. Chem. **87**, 1883 (1983), and references therein.
11. M. J. Ondrechen, Z. Berkovitch-Yellin, and J. Jortner, J. Am. Chem. Soc. **103**, 6586 (1981).

Table I. Homoatomic 6–12 potential parameters

	A (Kcal Å^6/mol)	σ (Å)	$\|\epsilon\|$ (cm^{-1})
Ref. 7			
C–C	344.0	3.81	19.6
Ne–Ne	143.9	3.16	25.2
Ar–Ar	1598	3.87	83.2
Ref. 9			
He–He	28.6	2.97	7.31
Ne–Ne	153.6	3.11	29.7
Ar–Ar	1580.6	3.76	97.8
Ref. 10			
C–C (Aliphatic)	370.4	4.12	13.3
C–C (Aromatic)	509.4	3.70	34.6
H–H	45.5	2.93	12.6

Table II. Heteroatomic potential parameters derived from homoatomic parameters by the combining rules of Eq. (10)

	A (Kcal Å^6/mol)	σ (Å)	$\|\epsilon\|$ (cm^{-1})
Parameters used by Ondrechen et al. (Ref. 11)			
C–Ne	222	3.49	21.7
C–Ar	741	3.84	40.4
H–Ne	168	3.24	25.4
H–Ar	560	3.60	45.0
Alternate parameters			
C(Aliphatic)-He	102.9	3.54	9.1
C(Aromatic)–He	120.7	3.34	15.3
C(Aliphatic)-Ne	230.9	3.64	17.4
C(Aromatic)–Ne	270.8	3.43	29.1
C(Aliphatic)-Ar	769.1	4.00	33.1
C(Aromatic)–Ar	901.9	3.78	53.6
H–He	36.1	2.95	9.6
H–Ne	80.9	3.04	17.8
H–Ar	269.6	3.40	30.6

Figure Captions

1. Example of a parallel fluorescence measurement used in the determination of the PRC recurrence period of *t*-stilbene. The data are shown as measured and after suppression of the fluorescence decay. (Deviations from exponential decay at long times, due presumably to ion feedback in the microchannel plate detector, have also been compensated for in the flattened data.)
2. Experimental fluorescence anisotropies ($R(t)$) as a function of the temporal alignment parameter t' described in the text. Temporal resolution for the measured decays was 8 ps per data point. Fluorescence intensities at times intermediate to the measured data values are approximated by linear interpolation. $t = 0$ marks the position of the initial rise of fluorescence intensities above background level. The maximum value of $R(t)$ is indicated at left for each curve.

Figure 1

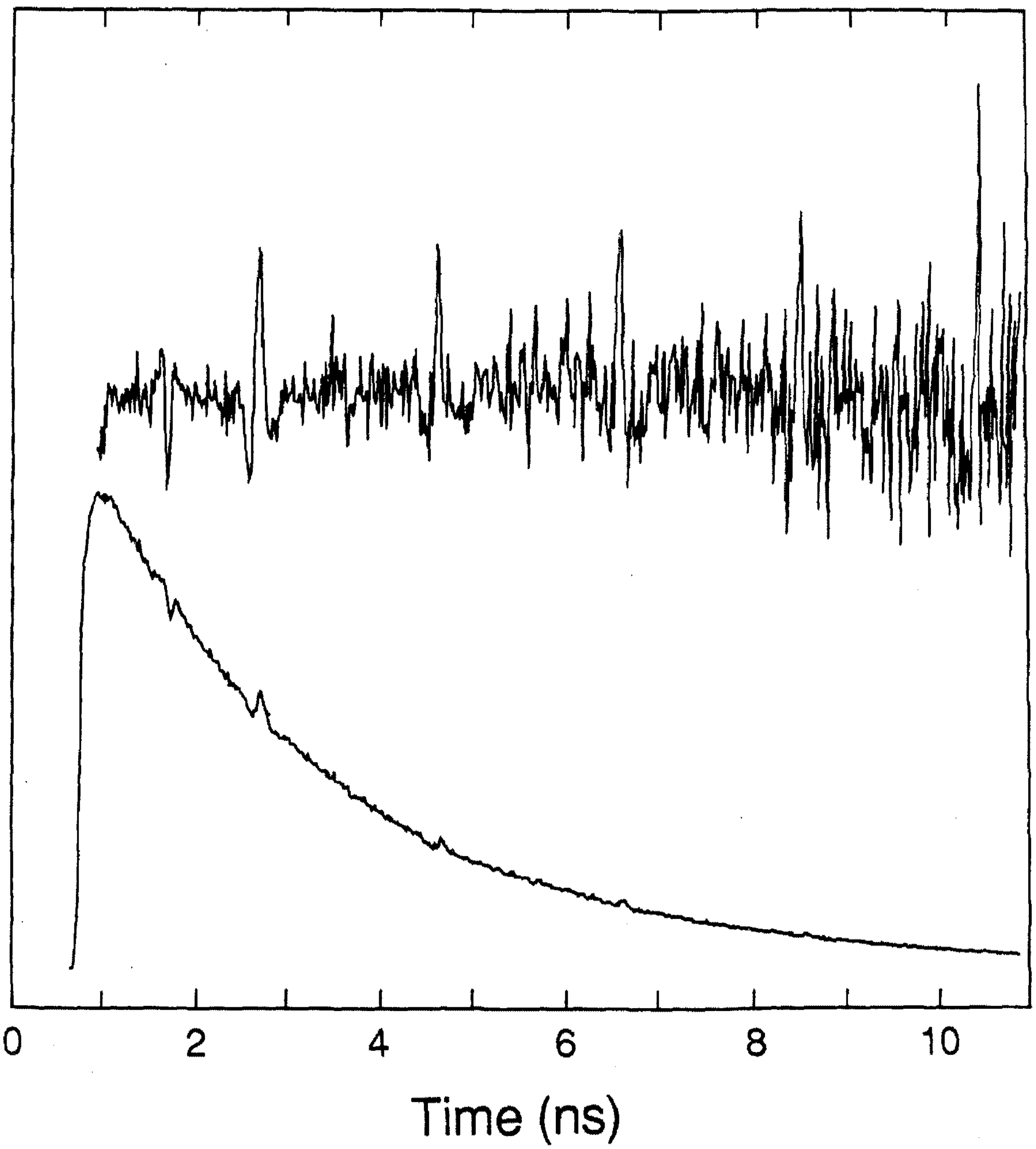

Figure 2

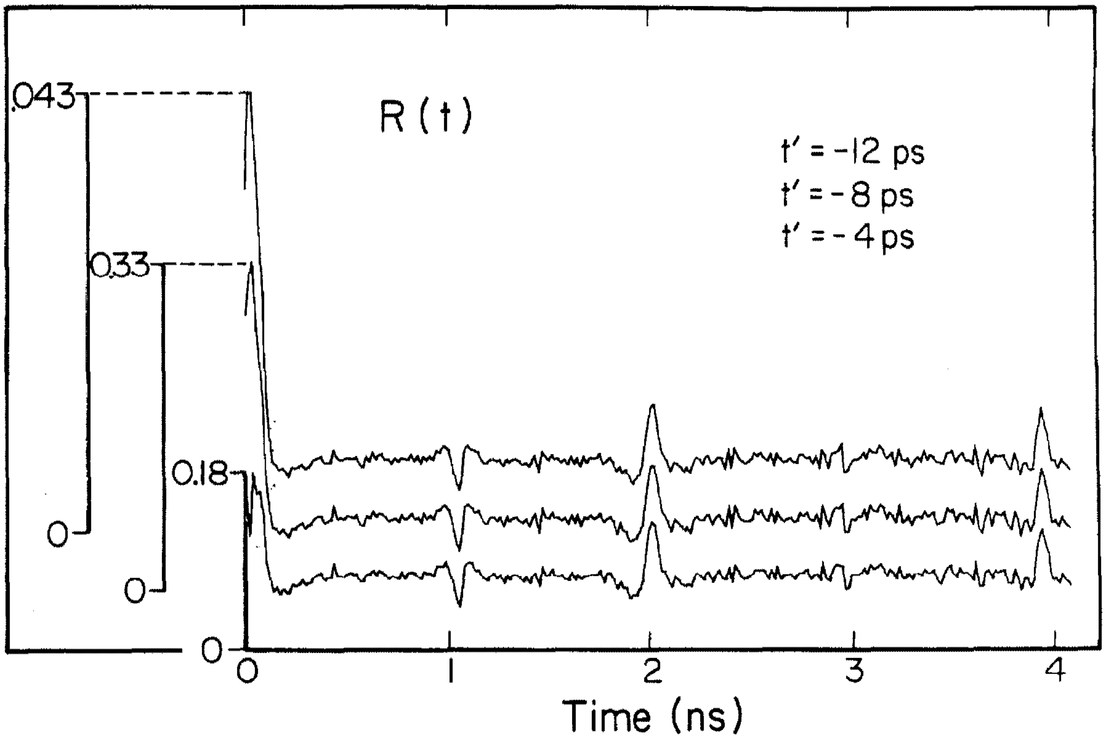

Chapter 5

Rotational Coherence Measurements and Comparisons with Theory

Portions of this chapter are taken from the following published articles:

"Purely Rotational Coherence Effect and Time-resolved Sub-Doppler Spectroscopy of Large Molecules. II. Experimental," by J. S. Baskin, P. M. Felker, and A. H. Zewail.

Reprinted with permission from The Journal of Chemical Physics, Volume 86, p. 2483. Copyright 1987 American Institute of Physics.

and

"Determination of Excited-State Rotational Constants and Structures by Doppler-Free Picosecond Spectroscopy," by J. S. Baskin and A. H. Zewail.

Reprinted with permission from The Journal of Physical Chemistry, Volume 93, p. 5701. Copyright 1989 American Chemical Society.

I. Introduction

In this chapter are presented experimental observations of the manifestations of rotational coherence in a variety of molecules and under a variety of conditions. The apparatus and procedures employed in the measurement and analysis of all data presented in Sections II, III, and IV A were fully described in Chapters 3 and 4 of this thesis. All measurements in these sections were on samples cooled by supersonic expansion. In Section IV B, measurements from another laboratory are compared with predictions of the theory developed in Chapter 2.

The goal of Section II is to demonstrate the practical capabilities of picosecond time-resolved fluorescence measurement for the extraction of precise molecular parameters of excited electronic states of polyatomic molecules. In each of subsections A through D, we present detailed analyses of purely rotational coherence (PRC) measurements on a different molecule (or related group of molecules). Special features of each case permit us to explore many different aspects of the PRC phenomenon, such as the influence of molecular asymmetry and arbitrary transition dipole directions. New information is derived about the rotational constants and structures of six of the eight molecules studied. In figures accompanying these discussions, the characteristic decay of fluorescence intensities will in some cases be suppressed (by multiplying the data by $e^{t/\tau}$, where τ is the measured lifetime) in order to facilitate the visual comparison of those features relevant to PRC.

Section III explores the interaction of vibrational motion and rotational coherence in *t*-stilbene and anthracene. Polarization-analyzed measurements permit contributions to the time-dependence of fluorescence due to intramolecular vibrational energy redistribution to be separated from those due to evolving ensemble orientation. Experimental results are compared with a model in which strict separability of vibrational and rotational motion is assumed, relying on the knowledge of PRC in these two molecules that was gained in the studies of

Section II.

Observations of rotational coherence in *t*-stilbene following the photodissociation of the jet-cooled van der Waals complex *t*-stilbene-He are discussed and analyzed in Section IV. Again, the PRC studies of both *t*-stilbene and *t*-stilbene-He in Section II provide a point of reference for the interpretation of our data.

II. Determination of Rotational Constants and Structures

A. *t*-Stilbene 0^0_0

The experiments presented in this subsection were carried out exciting *t*-stilbene to its S_1 vibrationless level[1] at 3101.4Å (32234 cm^{-1}). Stilbene is a highly favorable choice for the study of purely rotational coherence due to its intermediate size, its geometry (near-symmetric top), and the direction of the transition dipole involved (approximately parallel to the long axis[2,3]). These factors lead to polarization anisotropies that are readily observable, as we first illustrate by a selection of measured fluorescence decays and simulations in Figures 1 through 7. Experimental conditions and simulation parameters are given in the accompanying captions.

The results displayed in Figures 1, 3, and 4 were obtained detecting polarization-analyzed fluorescence to the S_0 vibrational ground state. The noteworthy feature of all these decays is the presence of periodic transients, or recurrences, which are detection polarization dependent. As can be seen in Fig. 1, these recurrences have opposite phase in the parallel and perpendicular decays while they are absent entirely for magic angle detection. This last fact indicates that the transients for parallel detection have twice the absolute amplitude of those for perpendicular detection (since $I_{54.7} \propto I_{\parallel} + 2I_{\perp}$, as discussed in chapter 2). For this reason only parallel decays are shown in the following Figures.

In Fig. 2 are displayed simulations employing parameters chosen to closely reproduce measurements under our standard expansion conditions (see below). A detailed comparison of experiment and simulation in order to derive accurate parameters for the *t*-stilbene S_1 state will be undertaken later in this section. For now, we need only note that the qualitative agreement of these decays with those experimentally observed at the *t*-stilbene origin (Fig. 1) is excellent.

Figure 3 attests to the persistence of polarization-dependent recurrences in *t*-stilbene fluorescence out to times of at least 14 nanoseconds (greater than five fluorescence lifetimes). Here also the strict periodicity of the transients (to within experimental uncertainties) and their alternating pattern is clearly observed. In order to achieve the signal-to-noise needed to reveal the later recurrences, several independently measured decays were added to produce the data in this figure.

An example of the influence of carrier gas pressure on our observations is shown next in Fig. 4. Two atmospheres and six atmospheres were the backing pressures employed for the top and bottom decays, respectively. The carrier gas was neon in both instances. All other conditions were identical. As the comparison reveals, the higher backing pressure produced a significant enhancement of the recurrence amplitudes. At a given pressure, the use of neon rather than helium as carrier gas also appeared to provide a noticeable though lesser enhancement of the recurrences. Based on these observations, six atmospheres of neon was established as the expansion regime employed whenever possible for the experiments described in this chapter. Measurements at yet higher backing pressures of both neon and helium have been carried out, but the results have not differed substantially from those produced at six atmospheres.

For the simulations of Fig. 2, a rotational temperature of 2K was assumed. In Fig. 5 an expanded view of the $T_{ROT} = 2$ K simulation is compared to one for which $T_{ROT} = 10$ K, all else remaining unchanged. The effect of increasing temperature is in good agreement with the trend in Fig. 4, in which lower backing pressure, which is known to provide less effective rotational cooling,[4] was seen to produce less prominent recurrences. This effect is easily understood within the framework of rotational coherence.[5] As higher ground state rotational levels are populated, more beat patterns with higher modulation frequencies contribute to the thermal average. The result is increasingly fast dephasing of the recurrences.[5] Convolution of these sharper recurrences with the detection response leads in turn to smaller apparent amplitudes, as observed here in both experiment and simulation.

Figure 6 presents a selection of decays recorded once more for 0^0_0 excitation, but now detecting other than resonance fluorescence. The first and second decays result from detection of spectrally resolved emission bands at -204 and -218 cm^{-1}, respectively; for the third, spectral resolution is low and a number of bands contribute. Details of the detection conditions are given in the caption. In all cases the basic character of the polarization anisotropy remains unaltered from that displayed for resonance detection. Similar recurrences have also been seen in the region of totally unresolved fluorescence 10000 cm^{-1} below the excitation energy. There is at most a slight loss in recurrence amplitude in decays measured for detection of broad band fluorescence to distinguish them from spectrally resolved decays. Even this difference has not been conclusively established, in light of the many variables which may contribute to such an effect.

Rotational coherence depends on the transition dipole direction but is otherwise independent of vibronic transition as long as the separation of rotational and vibronic wavefunctions is valid. This separation is assumed for all simulations presented in this thesis and, in particular, dictates that simulations for all parallel transitions in the 0^0_0 dispersed fluorescence spectrum of *t*-stilbene would be identical to those of Fig. 2. That no detection wavelength dependence is seen experimentally is therefore consistent with (and lends strong support for) both separability of rotational and vibrational motion at the energies in question and the assignment of all detected bands as essentially parallel-type. Note, however, that since the frequencies of rotational beat components are determined solely by the rotational energy levels in S_1, the *period* of recurrences is always rigorously independent of detection band in the symmetric top limit. (For asymmetric tops, changes in recurrence period as a function of detection could conceivably arise through a modification of the averaging that determines the asymmetry correction, as discussed in section 2. III. Such changes are expected by their nature to be exceedingly small.)

To complete the qualitative comparison of theory and experiment, we present in Fig. 7 polarization anisotropies formed (as described in Chapter 4) from the data of Fig. 1 and the simulations of Fig. 2, respectively. Several noteworthy features of rotational coherence, which are not apparent upon examination of the decays themselves, may be readily observed in this figure. An example is the prominent early time anisotropy which is largely concealed in the rise of the fluorescence intensities. For a perfect symmetric top undergoing parallel transitions, our considerations have shown that the manifestations of rotational coherence are strictly periodic with period $1/(2B')$. The full calculation indicates that the true molecular anisotropy due to rotational coherence is equal to 0.4 at times $n/(2B')$, $n = 0,1,2,\ldots$. The $R(t)$ values seen at early times in Fig. 7 are close to this value. That subsequent peaks are much smaller is due both to limited temporal response and asymmetry. Even when $r(t)$ is strictly periodic, returning to 0.4 at regular intervals, $R(t)$ away from $t = 0$ will not return to its initial value. This is a consequence of the existence of a discontinuity in the probability of emission at the instant of excitation which is not found at the recurrences. Asymmetry results in a further reduction of recurrence amplitudes, as discussed in Section III of Chapter 2. In Fig. 7 this damping is most evident for the out-of-phase recurrences and, as seen, is well accounted for by the simulation.

Also evident in Fig. 7 is the non-zero baseline value of $R(t)$. (The time axis defines $R = 0$ for the experimental anisotropy.) This is equal to the steady state branch-averaged anisotropy as discussed further in Chapter 2. Values of the residual anisotropy have been calculated elsewhere[6] for both symmetric and asymmetric tops. From the rotational coherence simulation in Fig. 7, we find a residual anisotropy of 0.075. This is identical to the value derived from Fig. 1 of ref. 6a for a symmetric top with a ratio of rotational constants of 10.4, corresponding to the assumed $A' / \frac{1}{2}(B' + C')$ of our simulation. An independent determination of the residual anisotropy was not made experimentally.

The preceeding comparisons have firmly established the correspondence between our experimental observations and the theoretically predicted manifestations of purely rotational coherence.[5] The basic structure of the observed transients and their polarization and temperature dependence are seen to be in good accord with theory. Our purpose now is to use the information contained in these measurements to improve our knowledge of the *t*-stilbene S_1 electronic state to the fullest extent possible. Specifically, we 1) account for the influence of asymmetry and possible nonlinearity of the measurement system time base in deriving a value of $B' + C'$, and 2) fit measurements to PRC simulations in an effort to establish values for all three excited state rotational constants. Since the results of these fits are found to be inconsistent with any reasonable *t*-stilbene structure when an *a*-axis polarized transition is assumed, the consequence of varying the direction of the transition moment in the simulations is investigated.

For the precise determination of the recurrence period τ_1 of the $S_1 0^0$ level of *t*-stilbene, we consider only fluorescence decays following $S_1 0^0_0$ excitation that were measured on a directly calibrated time scale and also display four or more distinct recurrences. Eleven such experiments were carried out over the course of a year. Calibration of the time scale, as described in Section II of Chapter 3, was performed the same day for the majority of these measurements, and within five days for all others. A daily calibration was not deemed necessary for the latter since no variation in the time base was detected between successive calibrations over an extended period. A weighted average of data from all 11 decays served as the basis for the recurrence period of 1948.4 ps reported in ref. 7.

Although an uncertainty (90% confidence limit) of from around 4 to 11 ps is estimated for the period derived from each single decay considered above, including the uncertainty associated with the time calibration, all 11 values lie between 1942 and 1952 ps, and only three are outside the range 1947.7 ± 1.6 ps. The small scatter of these values demonstrates the precision of the measurement procedure and suggests that the unavoidably subjective uncertainty estimates are in most cases conservative, as intended. Additional evidence of this precision is found in seven decays of comparable quality to those above, but which were measured on a time scale that could not be directly calibrated. The recurrence periods derived from them (now ignoring the substantial uncertainty in the absolute calibration) also fall within a ± 5 ps range, with the scatter about the mean again typically less than half of the estimated uncertainties. These observations appear to amply justify the 90% confidence limit of 2.5 ps quoted in ref. 7 for the *t*-stilbene recurrence period.

The value of τ_1 given above was derived with no consideration given to possible nonlinearity of the measurement time base. In fact, our data do suggest a correlation between measurement range and measured period which is consistent with other indications of a slight systematic nonlinearity as discussed in Section II of Chapter 3; that is, measurements over earlier portions of the calibration range tend to yield longer periods. Even if this trend is real, its effect is at the limits of our measurement precision and can therefore introduce no great error. Nevertheless, it is preferable in general to minimize any possible bias that such a nonlinearity might produce by ignoring measurements centered far from the center of the full calibration range. When this is done in the present case, the derived recurrence period is shortened by about 1 ps, the exact amount depending on the particular restricted set of measurements used. The weighted averaged of one such set results in a value of τ_1 of 1947.7 ± 2.5 ps, which we take as the final experimental recurrence period of *t*-stilbene. As before, the quoted uncertainty is justified by the small variation among many measurements, including those over only part of the calibration range.

To derive an accurate value of $B' + C'$ from this period, the effect of asymmetry must be considered. This was not taken into account in earlier treatments.[7] As the following discussion will indicate, 2.6 GHz and -0.0054 may be taken as reasonable values for A' and b. Based on these values, both application of Eq. (3.13) of Chapter 2 (with $a = 3$) and analysis of PRC simulations show that the asymmetry correction combined with the above value of τ_1 results in a $B' + C'$ near 0.5132 GHz. The additional uncertainty in $B' + C'$ arising from the uncertainty in this correction is no more than 0.0001 GHz, giving a final value of $B' + C'$ of 0.5132 ± 0.0008 GHz. This value applies to $^{12}C_{14}H_{12}$ and is uneffected by the presence of ^{13}C isotopes (see below).

The preliminary values of the individual rotational constants of S_1

t-stilbene used in the simulations of Figs. 2 through 7 were deduced by visual comparisons of the widths and amplitudes of recurrences. In this process the transition dipoles were held fixed along the *a* inertial axis. Note that A′ was left fixed for these simulations at a value (2.676 GHz) calculated from an experimental ground state structure,[8] while the geometric constraint,

$$A^{-1} \geq C^{-1} - B^{-1} \tag{2.1}$$

actually requires that A′ be less than 2 GHz to be consistent with the proposed B′ and C′ of 0.273 GHz and 0.240 GHz. Or, from the opposite perspective, the proposed B′ and C′ are too widely separated for the assumed A′.

Fits of data to PRC simulations assuming an *a* axis dipole have now been carried out and are in basic accord with the above values, i.e., a relatively large separation of B′ and C′ is needed to reproduce the measurements. For example, we show in Fig. 8 a measurement of the first out-of-phase and first in-phase recurrence in the parallel component of stilbene fluorescence (with the fluorescence decay suppressed) and the corresponding best fit, planar molecule, *a* axis polarized PRC simulation. The weighted residual is shown above the data; the reduced chi-square value of 1.04 indicates the generally satisfactory quality of the fit. The resulting parameters are T = 2.8 K, A′ = 2.182 GHz, B′ = 0.2716 GHz, and C′ = 0.2416 GHz. (The short time-scale of this experiment was not calibrated directly but determined by setting B′ + C′ = 0.5132 GHz.) When the constants were not constrained by planarity, a slightly better fit was found by further separation of B′ and C′ to 0.2730 GHz and 0.2402 GHz without reducing A′. This latter is again a physically unrealizable set of constants, as seen from relation (2.1).

The fit of Fig. 8, as others in this thesis, was carried out using the constants for a single isotopic species, in this case $^{12}C_{14}H_{12}$. Since the seven distinct species of $^{12}C_{13}{}^{13}CH_{12}$ comprise 13.3% of the total sample, have recurrence periods ranging up to ~ 22 ps longer than that of the principal isotope, and may have small enough spectral shifts to contribuate to the observed signal, their effect must be considered. (Multiply substituted isotopes make up only 1% of the total and can be ignored.) At long times, accumulated phase differences will disperse the recurrences of the minor isotopes and the observed recurrences should have amplitudes approaching ~ 86% of those of a single species. Simulations confirm that this limit is reached after five or six periods but also show that the isotope effect on the fluorescence intensity over the time range shown in Fig. 8 is negligible. This justifies the fitting procedure used. The shifts in recurrence peaks (< 2 ps at all times) induced by the inclusion of minor isotope fluorescence in the simulations results in an inconsequential change (< 0.1 ps) in the apparent recurrence period from that of $^{12}C_{14}H_{12}$.

Despite reasonable success in reproducing the measurements with simulations based on the assumption of an *a* axis transition moment, one serious deficiency becomes evident upon closer scrutiny: the derived rotational constants are incompatible with the basic chemical structure of stilbene (α,β-diphenyl-ethylene). This fact is most easily appreciated through consideration of Fig. 9, which shows the general structure of *t*-stilbene. (Figure 9 is specifically the planar geometry of S_1 *t*-stilbene as calculated by Warshel[9] but with regular hexagons substituted for slightly distorted phenyl rings.) The in-plane inertial axes are indicated. It should be clear that, regardless of the particular bond angles chosen, the *a* axis must pass approximately through the centers of mass of the phenyl rings. This is true because the rings constitute the bulk of the molecule's mass, and the parallel axis theorem indicates that the rings' contribution to the moment of inertia is minimum for such an axis. In consequence, as long as the molecule is planar (see below), the A rotational constant will be determined principally by a single quantity, the lateral dimension of the rings, represented by L in the figure. (The ethylene carbons can never be far enough from this axis to make a large contribution to I_a.) For the pictured structure, with ring carbon bond lengths of 1.419Å, A′ is approximately 2.6 GHz. Values in the literature for phenyl C-C bonds[10] do not vary by more than 2% from the given value for either ground or excited electronic states. Thus to produce an A′ from a planar structure that is more than 5% smaller than 2.6 GHz requires increases in either bond lengths or bond angles which are completely unreasonable. *Therefore, A′ cannot reasonably be smaller than ~ 2.5 GHz and, from relation (2.1), B′* and *C′ cannot differ as much as suggested by the a axis fits of PRC data.* (A′ will also be reduced by a nonplanar geometry which results in an angle between the *a* axis and the plane of one or both rings, but this will generally reduce the difference in B′ and C′ rather than increase it as required. Also, recent spectroscopic studies[11,12] strongly support a planar structure of *t*-stilbene in both S_0 and S_1).

From the detailed analysis of PRC measurements, coupled with geometric constraints on the rotational constants of *t*-stilbene, we have concluded that the experimental results are not adequately reproduced by the *a* axis treatment so far attempted. The problem, simply stated, is that measurements of *t*-stilbene PRC recurrences are consistently smaller, at a given width, than can be produced by simulations based on a reasonable stilbene structure. From measurements such as that of Fig. 3, it may be seen that there is no substantial decrease in recurrence amplitude over at least four or five recurrence periods. This suggests that the inconsistency is due not to the action of some unforeseen damping of recurrences with time but to an effect which contributes more or less uniformly at all times.

Further support for this conclusion may be found in the behavior of the stilbene PRC signal at early times. No potential causes of recurrence damping (such as asymmetry or collisions) will have any effect on the initial anisotropy decay so that anomalous behavior at this time must be attributed to the influence of other factors. For experiments with a measured response of 40 ps, the manifestations of the initial decay in stilbene are sufficiently apparent to be used for this purpose. Since it is found that, even at early time, the *a* axis dipole simulations predict a more prominent PRC effect than actually observed, the discrepancy cannot be totally accounted for by any damping mechanism. (Ionization experiments with improved temporal response[13] permit an even better comparison of early time behavior. The large discrepancy between the observed and simulated initial decays in those experiments appears to strengthen the conclusions reached above; however, the fact that the excitation and probe transitions are different introduces additional degrees of freedom that make a direct comparison impossible.)

Two possible experimental causes of an apparent uniform reduction in recurrence amplitudes are incomplete polarization analysis and an unstable or inaccurately characterized response. Since each will necessarily play some role, a perfect agreement with the simulations should not be expected. However, attempts to determine the magnitudes of these effects have led us to conclude that they are not large enough to totally account for the differences between experiment and simulation in *t*-stilbene. The fact that no similar discrepancies have been encountered in fitting fluorene-argon and anthracene measurements provides additional evidence for this conclusion.

Since the *a* axis is not a symmetry axis of stilbene, another possible cause of the observed discrepancy is a transition dipole with a significant component perpendicular to that axis. The dipole is at most restricted to the *ab* plane in the likely case that the *c* inertial axis is a C_2 axis.[12] Even if the transition is very nearly *a* axis polarized in zeroth order, a hybrid band could result from mixing of the S_1 state with another low lying excited state, of which there are many.[3] It is pertinent, therefore, to consider the effect of an off-axis dipole on the simulations and determine if such a dipole may succeed in reconciling theory with experiment.

An obvious consequence of an off-axis dipole is a transfer of intensity from the parallel-type recurrence pattern associated with the *a* axis to a perpendicular-type pattern which consists, in general, of low amplitude features, as will be seen in the case of anthracene. In addition, beat patterns unique to the off- axis dipole case will result from interference between levels reached via transitions induced by different dipole components. In any case, the relative amplitudes of the nutation recurrences will surely be reduced and, importantly, this effect will be felt fairly uniformly in time beginning at $t = 0^+$, in qualitative agreement with the experimental indications.

To determine if this qualitative agreement with the experimental evidence will translate into quantitative agreement as well, simulations were carried out using rotational constants $A' = 2.6$ GHz, $B' = 0.269$ GHz, and $C' = 0.244$ GHz, which were derived from the structure of Fig. 9. This structure serves as our best estimate of the structure of stilbene in its S_1 state for the following reasons: 1) it differs only slightly from the theoretical structure of Ref. 9; 2) it comes quite close to reproducing the measured $B' + C'$ (which the exact S_1 structure of Ref. 9 does not); and 3) its asymmetry is close to the maximum reasonable value, which the fits of PRC recurrence lineshapes strongly favor. This last point, which requires the choice of a planar structure, conforms with the spectroscopic evidence of planarity[11,12] and is supported by PRC measurements on the stilbene-Ne_1 van der Waals complex (see Section I.

B.ii of this chapter). The simulations based on this structure confirm the expected reduction in recurrence amplitude as the angle θ between the transition dipole and *a* axis is increased. Even at $\theta = 30°$, at which value the nutation recurrences retain little more than half of their original amplitudes, the new polarization dependent structure which appears remains far too small to be observed at the signal-to-noise of the present experiments. Furthermore, at temperatures of 2 to 3K, the ratio of amplitudes of the first in-phase recurrence to the first out-of-phase recurrence varies only slightly as θ ranges from 0 to 30°. Thus parameters which reproduce the experimentally determined amplitudes of both of these recurrences may easily be found by the following procedure: first, the temperature corresponding to the measured recurrence ratio is found; then θ is adjusted to yield the desired absolute recurrence amplitudes.

When this procedure is applied to the stilbene PRC measurement of Fig. 8, a temperature of 2.3K and a value of $\theta = 21°$ are obtained. In Fig.10, a simulation produced using these parameters is compared with the data of Fig. 8. Though optimization of all degrees of freedom has not been carried out due to the time intensive nature of the computations, the satisfactory agreement is evident. To appreciate the improvement which this simulation represents over that of Fig. 8, it must be recalled that the rotational constants used for the latter are not compatible with the structure of stilbene. Even then, the simulation overshoots the positive recurrence peak by an amount (3.6 σ) that is expected to occur in random noise only once in about 6300 data points. By contrast, the largest residual of the 300 point fit in Fig. 10 (-2.63 σ) is expected once in 233 points.

By applying the above procedure to other sets of data, both larger and considerably smaller values than 21° are indicated for the angle θ. These results may be explained in part by noise, but it is also likely that variable experimental factors at times play a significant role in reducing recurrence amplitudes. Therefore, the value of 21° derived in the example above should be considered an upper limit rather than an accurate estimate of θ.

One question which remains to be answered is whether the hypothesis that the stilbene dipole deviates significantly from the *a* axis is compatible with other experimental evidence. The polarization of the $S_1 \leftarrow S_0$ transition of stilbene in dilute mixed crystal has been studied.[2] In these experiments, high resolution absorption and fluorescence spectra were recorded for stilbene in a crystalline solution of dibenzyl, whose crystal structure is known.[14] Stilbene absorption was detected for a single direction of polarization in the *ac* plane of the dibenzyl crystal, parallel to the long axis of the dibenzyl molecules. Without knowing both the sensitivity of these experiments and the exact orientation of the stilbene molecules in the dibenzyl crystal, the bounds that this result places on the dipole direction cannot be determined. However, by assuming the same orientation of the phenyl rings for both stilbene and diphenyl in the diphenyl crystal, an estimate can be made of the sensitivity required to detect a *b* inertial axis component of a given magnitude. Using the data from Ref. 14 and the stilbene structure of Fig. 9, the projections of the stilbene molecule and its inertial axes on the *ac* crystal plane can be found. With the foreshortening of the *b* axis in projection, the sensitivity in absorption to a dipole component along that axis is reduced by about a factor of four. Thus a dipole at an angle of 11° to *a* in the *ab* inertial plane (not to be confused with the *ab* crystal plane) would show a 100 to 1 absorption ratio for polarizations parallel and perpendicular to the *a* axis projection. For an angle of 21° the ratio drops to 25 to 1. It seems reasonable to assume then, that these experiments are not incompatible with a value for theta of the order of 10°.

In summary, the small amplitudes of PRC recurrences observed in the polarization-analyzed fluorescence of *t*-stilbene cannot be reproduced by simulations based on both a reasonable excited state molecular structure and an *a* axis polarized $S_1 \leftarrow S_0$ transition. In addition, it has been shown that, at least qualitatively, the observations may be accounted for within the limitations of the present treatment by an off-axis direction for the transition dipole. However, considering the variability among measurements and recognizing that experimental factors will in general cause an overestimation of θ, these results make it possible only to set an upper limit on the actual value of θ and do not exclude the possibility that all or part of the amplitude reduction is due to other causes. For example, deviations from the conditions underlying any or all of the assumptions listed in Chapter 4 have not been considered here at all and remain possible contributors. Also, evidence obtained recently through high resolution fluorescence excitation studies of *t*-stilbene[15] does not appear to support the hypothesis of a hybrid band, but does show anomalies consistent with our own observations. In particular, the investigators report that they are unable to assign a series of lines seen in the partially resolved rotational structure of these spectra to a normal perpendicular transition. This was interpreted as evidence for the operation of unusual rotational selection rules. On the other hand, theoretical treatments indicate that a weak perpendicular band is expected to lie very close to the $S_1 \leftarrow S_0$ transition,[3] and this could be the source of the observed anomolous lines. Whatever the origin, the additional intensity associated with those lines provides a possible explanation for the reduced amplitudes of PRC recurrences. PRC measurements with improved signal-to-noise and more precise characterization of experimental influences may be important for distinguishing such possibilities. A precise measurement of the steady-state fluorescence anisotropy could also help to resolve the question of dipole direction, since the ratio of parallel to perpendicular fluorescence intensity changes by six % as θ varies from 0 to 20° for the assumed rotational constants.

In concluding the discussion of PRC measurements on stilbene, it is appropriate to comment on one aspect of the PRC technique which is highlighted by the high resolution stilbene spectra of Ref. 15. Despite a resolution far greater than the natural linewidth of stilbene, these spectra could not be assigned due to their complex structure and congestion. How then, can PRC measurements permit a precise determination of $B' + C'$? Two separate factors may be cited as important contributors to this result. First, PRC probes *only the excited state level structure*, while spectra show transition frequencies which depend on both ground and excited state rotational constants and may be greatly complicated when the two differ. Secondly, as argued in Section III of Chapter 2, and confirmed by simulations, PRC recurrences in asymmetric tops are largely immune to interference from the $K = 0$ and $K = 1$ manifolds, which are strongly perturbed by asymmetry. This is by no means true for spectra of cold prolate top molecules, for which a large fraction of the signal originates from molecules in these manifolds in the ground state (~ 23% for stilbene at 2K). Thus PRC provides a Doppler-free view, not simply of the frequency domain spectrum, but of a simplified spectrum from which ground state interference and the most irregular lines have been effectively eliminated. Moreover, through the coherent excitation process, PRC automatically associates or "assigns" sets of lines on the basis of ground state of provenance. In this way a simple pattern of commensurate frequencies which is present but hidden in the frequency domain stilbene spectra is revealed in the PRC measurements. Of course, if the spectra can be analyzed, they will necessarily provide more information than can be obtained from PRC.

B. t-Stilbene-rare gas van der Waals complexes

Van der Waals complexes, as prototypical weakly bound systems, have been the subject of studies in many areas of chemical dynamics in the past decade. Rare gas atoms bound to aromatic molecules form one such group of complexes. Interest in the structures of these complexes has prompted efforts to resolve the rotational structure of electronic transitions of a number of different systems. This has been accomplished for smaller aromatics such as benzene[16] and *s*-tetrazene,[17] using conventional supersonic expansions, and for fluorene-h_{10}[18] and -d_{10}[19] using a strongly collimated expansion to lower the Doppler width to 15 MHz. Previously reported observations of PRC recurrences in the polarization-analyzed fluorescence of stilbene-argon[20] and stilbene-helium[21] have shown that structural information about the excited states of large complexes may readily be obtained from time domain measurements. In the following, the application of this alternative technique to elucidate the structure of these and other stilbene-rare gas complexes will be discussed.

In keeping with the relatively small masses of the added rare gas atoms, PRC in each of the stilbene complexes is expected to closely resemble that in stilbene. Measurements confirm this expectation, revealing periodic nutation-like recurrences in each case. Thus $B' + C'$ for each complex is given to very good approximation by the reciprocal of its measured recurrence period.

To establish the structure of a complex, the measured $B' + C'$ is compared to $B' + C'$ values calculated for possible configurations of rare gas atoms around stilbene. For this purpose, it is assumed that the structure of stilbene within the complex is that of Fig. 9, which was shown to be a good approximation for the bare molecule. The choice of possible positions for the rare gas atoms is guided by consideration of previous experimental results. From each of the spectral studies of aromatic-rare gas complexes cited above, as well as from partially resolved spectra of several aniline-rare gas complexes,[22] positions of the rare gas atoms relative to the aromatic molecule have been determined. In all cases the atoms were found to be above the plane of the rings, at a distance of from 3.2 to 3.65 Å. The variation of heights was much smaller among the argon complexes, falling between 3.4 and 3.44 Å. Also, laser excitation studies of jet-cooled stilbene under varying helium stagnation pressures[23] suggest that, for helium at least, there are four and only four equivalent rare gas bonding sites on stilbene. These findings lead us to assume as tentative complex structures ones in which the rare gas atoms are situated above or below the phenyl rings at heights falling within the ranges indicated above.

The criterion imposed by the measured $B' + C'$ value, when coupled with the restrictions described above, is alone very effective in pointing the way to a probable complex structure. Further information about the rotational constants, and hence structure, of the complex is afforded by the analysis of recurrence lineshapes. Comparisons of measured recurrences with PRC simulations are particularly helpful in assessing the degree of asymmetry of the molecule.

Calculations have also been carried out using Lennard-Jones two-body potentials to model the interaction of the rare gas atoms with each atom of the stilbene molecule as described in Chapter 4. Calculations of this type have been used frequently to assist in the interpretation of the spectroscopy of van der Waals molecules, providing information about structures, binding energies, and numbers of stable isomers.[24,25,17] In the present case, the experimentally derived stilbene complex structures, which reflect the vibrationally averaged positions of the rare gas atoms, provide a means to critically assess the accuracy of the calculated potentials. For meaningful comparison of calculation and experiment, it must be taken into account that large amplitude zero point motions of the weakly bound rare gas atoms may cause equilibrium and average structures to differ substantially.

PRC recurrence periods have been measured for five different complex absorptions to the red of the stilbene origin. These are listed in Table I with the stilbene value for comparison. Also listed in Table I are values of $B' + C'$ based on Eq.(3.13) of Chapter 2. The approximate asymmetry corrections were calculated using rotational constants indicated by the analyses to follow and were in all cases much smaller than the quoted uncertainties. The measurements at each complex absorption are discussed below, under separate headings for each rare gas species.

i. **Argon.** Two absorption bands have been studied which appear to the red of the stilbene 0^0_0 excitation energy only when low concentrations of argon are mixed into the backing gas. These absorptions, at $-40\ \text{cm}^{-1}$ and $-63\ \text{cm}^{-1}$ relative to the stilbene origin,[23,15] have been attributed to the stilbene-Ar_1 complex by means of mass-resolved two-photon ionization[26] and earlier measurements of PRC recurrence periods.[20] The greatly improved values given in Table I were derived from new measurements. These not only support the assignment of both absorptions to a single stoichiometry but also place strict limits on the difference in vibrationally averaged molecular structures. This has an important bearing on the determination of the nature of the $23\ \text{cm}^{-1}$ vibration, since a long axis van der Waals bend may change the effective constants considerably. Finally, we note that the value of $B' + C'$ derived from the PRC measurements has recently been corroborated by analysis of the high resolution spectrum of the -63 cm^{-1} band[15] from which a value of 0.413 ± 0.002 GHz was obtained.

Our goal now is to use the information gained from these measurements and the *t*-stilbene analysis in the previous section to deduce the structure of the complex. To begin, we tentatively assume the validity of the classical picture of molecule + localized atom and consider the consequence of the placement of a single argon atom at 3.4 Å above and on the axis of a stilbene phenyl ring. The resulting structure has rotational constants B and C whose sum is approximately 5% smaller than the value derived from the PRC recurrence period of the -40 or -63 cm^{-1} bands. To produce a calculated $B' + C'$ consistent with the measured value while keeping the argon on the ring axis, one must reduce the separation of the argon atom and the ring plane to about 2.5 Å. On the other hand, a structure having the required $B' + C'$ may also be obtained by maintaining the argon atom at ~ 3.4 Å above the ring and displacing it ~ 0.5 Å parallel to the molecular plane in the direction of the ethylene. The consistent nature of the derived argon-aromatic separations in other van der Waals complexes strongly favors this latter alternative, which is shown in Fig. 11. Though the height of the argon atom may deviate somewhat from the characteristic value, because repulsion between the argon and carbon atoms makes a substantially smaller separation energetically untenable, the measured recurrence period is sufficient to establish that the argon is on average closer to the center of the molecule then the ring axis. (This same conclusion would also be reached starting from any other reasonable stilbene structure that is planar.)

From the preceeding considerations, we conclude that the argon position in Fig. 11 is the average position of the argon atom for both of the studied stilbene-Ar_1 excitations. This position, proposed on the basis of experimental evidence, also seems quite plausible when considered on physical grounds alone. The location of a binding site for rare gas atoms on the axis of an isolated aromatic ring is well established.[16,17] A rare gas atom above a phenyl ring of stilbene will feel not only the potential of the adjacent ring but also the long range attraction of the remainder of the molecule. These two contributions give rise to a resultant potential whose minimum is displaced from the ring axis toward the ethylene and opposite phenyl ring, consistent with the argon displacement in the proposed structure. The size of the displacement provides an indication of the relative strengths of the short and long range forces.

The probable average position of the argon atom established above can now be used to evaluate the accuracy of potential surface calculations using the 6-12 atom-atom potential function described in Ref. 24. Potential parameters also taken from Ref. 24 and based on earlier work[27] were used initially, with all carbons treated equally. In Fig. 12 a portion of the resulting potential is represented by a plot of the minima of energy with respect to height above each point of the molecular plane. Grid lines are at 0.5 Å separations. The heights at which the plotted energy values occur vary from near 3.4 Å directly over the molecule to near zero (i.e., the energy minima are located in the molecular plane) at the edges of the plot. The energies in the figure range from -475 to $-102\ \mathrm{cm}^{-1}$.

The global energy minimum of $-475\ \mathrm{cm}^{-1}$ is reached when the argon is situated 3.4Å above point A, or at one of three other equivalent, symmetrically placed points in the plane bisecting the ethylene bond. This minimum energy configuration is immediately disqualified as a candidate for the correct complex structure, however, by a resulting rotational constant sum which is more than 10% higher than the measured $B' + C'$. Interestingly, the calculated potential also has a local minimum above point B at almost precisely the position of the argon deduced from the PRC measurement. The height of the argon at this minimum is 3.46 Å, the energy is $-454\ \mathrm{cm}^{-1}$, and the corresponding $B' + C'$ is 0.414 GHz. The energy barrier between this minimum and the global minimum is less than 1 cm^{-1}, however, so localization of the argon at this position is not consistent with the model calculation. Indeed, due to its flatness, it is unclear whether the ground state of the calculated potential would even be localized above point A, or would instead correspond to a large amplitude motion extending across both rings of the molecule. This is illustrated by Fig. 13 which shows the cross sections of the potential surface of Fig. 12 which pass parallel to the long axis of the molecule through the two local minima (above points A and B). The total zero point energy associated with the three degrees of freedom of the van der Waals bond is typically 30 to 40 cm^{-1}, with about 20 cm^{-1} of that due to the out-of-plane stretch.[28,29] The extent of the ground state wave function along the long axis of the molecule is certainly limited by this energy. One can see that the classical turning points of motion on the potential surface lie near the centers of the two rings (whose positions at ± 3.3Å are indicated on the axis in the figure) for an energy of 30 cm^{-1}.

In the approximation of separability of the potential in principal axis coordinates, only the estimated 5 to 10 cm^{-1} of zero point energy associated with the long axis motion itself would be pertinent to the problem of determining the localization of the ground state along that axis. Calculations[28] for pentacene-R (R = Ne, Ar and Kr) suggest that the one dimensional treatment is a satisfactory approximation to the three dimensional problem near the bottom of a deep well. In that case the argon atom would be very well localized near A, and the corresponding rotational constants would be completely incompatible with the measurements.

On the other hand, to determine if a large amplitude zero point motion which would result from a higher zero point energy in this potential is consistent with the experimental observations, an estimate is required of the average rotational constants to be expected from it. As a simple approximation, we take a classical particle traveling at constant velocity and constant height between the two 30 cm^{-1} turning points above the *a* inertial axis of stilbene. The average of $B' + C'$ calculated relative to axes parallel to the stilbene inertial axes is found to be about 7% higher than measured. This value decreases by only about 0.7% for each 10 cm^{-1} of additional energy in the van der Waals bond. Since the probability amplitude of any ground vibrational state is, in fact, concentrated toward the center of the potential well rather than uniformly distributed as presumed above, an improved estimate would yield still larger rotational constants. This comparison leads us to conclude that the potential surface of Fig. 12 is a very poor approximation to the actual stilbene-Ar_1 potential.

Using data from other sources[30] and combining rules relating the 6-12 parameters of hetero-atomic and homo-atomic interactions,[31] alternative parameters may be derived to describe the carbon-argon and hydrogen-argon interactions. Calculations of the stilbene-argon potential using these variants also give long flat potential valleys with global minima on the ethylene, as long as the same parameters are applied for all carbon atoms.

One possible cause for the failure of the above calculations is the equivalent treatment of the ethylene and phenyl carbons. A distinction is drawn in Ref. 30 between the potential parameters of aromatic and tetrahedral aliphatic carbons; consequently, the derived carbon-argon paramters may also be so distinguished. The stilbene-argon potential surface calculated applying the aromatic and aliphatic parameters to the phenyl and ethylene carbons, respectively, is qualitatively different from those of the previous calculations. Now minima are found only above (and below) the rings, separated by a substantial barrier over the ethylene. The minimum energy is $-458\ \mathrm{cm}^{-1}$ for an argon located at a height of 3.45Å and displaced 0.3Å inward from a ring axis. Cross sections of this surface are shown in Fig. 14 for comparison with those of Fig. 13. Again, the energies are minimized with respect to height above the molecular plane and the abscissa represents distance along the stilbene a axis.

While the equilibria of this potential are situated closer to the ring axes than is the argon position derived from the measured $B' + C'$, it is clear from the figure that vibrational averaging will result in an effective argon position displaced from the equilibrium toward the center of the molecule. In fact, the average $B' + C'$ estimated using the $30\ \mathrm{cm}^{-1}$ turning points for this potential, in the same approximation as that employed for the potential of Fig. 13 (but with appropriately rotated inertial axes), agrees very well with the measured $B' + C'$. The difference between this rough estimate and a precise calculation should also be relatively minor in the present situation since the argon atom does not approach any of the inertial axes. Without attributing undue importance to this quantitative agreement, it remains evident that this potential is much more satisfactory than those in which no distinction between carbon atoms was made. Nevertheless, because the justification for the particular choice of potential parameters is strictly empirical, this potential, and any quantities derived from it (well depth, barrier height, etc.) must be accepted with a great deal of caution. It will be shown below that the well depths derived from similar treatments of other stilbene complexes are, in fact, fairly inaccurate.

ii. Neon. The absorption lying 16 cm^{-1} to the red of the stilbene origin appears only in the presence of neon and has been assigned as the origin of the stilbene-Ne_1 complex.[32] The measured PRC recurrence period, midway between those of stilbene and stilbene-Ar_1, is supportive of this assignment when the neon atom is assumed to sit on one of the phenyl rings. As in the case of the argon 1:1 complex, to achieve precise agreement of the measured and calculated values of $B' + C'$, the rare gas atom must be either displaced off the ring axis toward the center of the molecule or lowered to a height of, again, about 2.5 Å from the ring plane. Though a consistent behavior of neon in rare gas-aromatic complexes has not been established, all available data support a distance of the neon atom from the ring plane of at least 3Å. Thus the PRC measurement again implies an off-center position of the rare gas atom on the phenyl ring. The required displacement of the neon from the ring axis depends, of course, on its distance from the ring plane. With a van der Waals radius ~ 0.3Å smaller than that of argon,[27,31] neon can be expected to be situated near 3.1Å above the ring, leading to a displacement toward the ethylene of about 0.25Å.

One noteworthy aspect of the stilbene-Ne_1 PRC measurements is the clear indication that the asymmetry of the complex is much smaller than that of bare stilbene. The most obvious consequence of reduced asymmetry is an enhancement of recurrence amplitudes, and the recurrences in stilbene-Ne_1 have been the largest seen in any of the molecules studied to date. Further evidence of the low asymmetry of the complex is provided by the exceptional prominence of the later out-of-phase recurrences which would be strongly damped if the asymmetry were larger. Based on the neon position deduced from an assumed neon-ring separation of 3.1Å, the following rotational constants may be calculated for stilbene-Ne_1: $A' = 1.43$ GHz, $B' = 0.228$ GHz, and $C' = 0.225$ GHz. The value of *b* which these constants yield is about one quarter that of bare stilbene. By contrast, *b* for the derived stilbene-Ar structure is slightly larger than that of stilbene and the recurrences seen in the two molecules are comparable in appearance.

A quantitative assessement of the proposed stilbene-Ne rotational constants is provided by comparison of the measured recurrence lineshapes with the results of PRC simulations. Simulations for both stilbene-Ne and stilbene were carried out assuming transition moments along the stilbene *a* axis in each case. (This assumption leads to a small dipole component in the stilbene-Ne *c* axis since its *a* inertial axis is rotated slightly (5.2°) out of the stilbene plane). While the absolute recurrence amplitudes in these simulations are larger than the measured amplitudes for both molecules, the enhancement of recurrences in stilbene-Ne relative to those in stilbene (~ 40%) is in rough agreement in simulation and experiment. The reduction in recurrence widths of 15 to 20 ps in the complex is also reproduced very well by the simulations. These comparisons provide strong evidence of a large difference in the asymmetries of stilbene and stilbene-Ne, and in so doing strongly corroborate not only the position of the neon atom in the complex, but also the underlying stilbene structure. For example, electron diffraction data[8] and early spectroscopic analysis[1] suggested a non-planar stilbene structure in which the phenyl rings are rotated ~ 30° in opposite sense. Such a structure would decrease the asymmetry of stilbene while increasing that of stilbene-Ne, thereby quickly reducing the difference between them. For a twist of the phenyls of 30° or more, stilbene-Ne would be more asymmetric than stilbene, a clear contradiction to the observations.

Results of potential calculations for the *t*-stilbene-Ne_1 complex are very similar to those obtained for the argon 1:1 complex when all carbon atoms are treated equally. Thus two types of minima are found, with the ethylene minima slightly deeper than those on the phenyl rings. Using the potential parameters of Ref. 24, the minima are at -231 cm^{-1} and -222 cm^{-1}, respectively, and are separated by a barrier of less than 8 cm^{-1}. Though the phenyl minima again coincide with the experimentally determined rare gas position, the form of the potential is inconsistent with the measurements, just as it was in the argon case.

Separate parameters for ethylene carbon and ring carbon interactions with neon may also be derived, as described for argon. These again provide better agreement with the PRC measurements than a single set of carbon parameters, for the resulting potential has global minima, of -235 cm^{-1}, situated above and below the phenyl rings. Although the ethylene minima do not disappear entirely in this case, surviving as very shallow secondary minima 25 cm^{-1} up the sides of the phenyl ring potential wells, the wells over different rings are distinctly separated by a 56 cm^{-1} barrier, insuring localization of the neon atom on one half of the molecule.

While the above potential qualitatively satisfies the criterion of the PRC measurements, it fails to meet a quantitative test of the stilbene-Ne potential provided by dissociation studies.[33] These show an upper limit to the dissociation energy of 150 cm^{-1}, so that a well depth of more than 190 cm^{-1} is very unlikely. The error of 20% or more in the calculated well depth may be taken as an indication of the approximate nature of the calculations.

iii. Helium. The assignment of the four helium complex absorptions to the red of the stilbene origin has been made on the basis of order of appearance with increasing stagnation pressure and spectral shift.[23] Results of PRC measurements on the assigned stilbene-He_1 band are summarized in Table I. These are consistent with one helium atom positioned above a phenyl ring. Because of the low mass of helium, displacements of the helium atom of up to an angstrom are needed to change the rotational constants significantly on the scale of the PRC measurement uncertainty. This fact, coupled with the relatively wide range of reported helium-aromatic vdW bond lengths,[16a,17,22] makes it possible to establish only fairly wide bounds on the actual location of the helium atom. Thus while the most probable value of $B' + C'$ would require an off-axis position for the helium atom at any height above 2.8 Å, the lower bound on $B' + C'$ is reproduced by an on-axis helium 3.3Å above the ring plane.

Potential parameters for stilbene-He potential calculations were derived using combining rules and He-He parameters (well depth and equilibrium separation) based on differential elastic scattering measurements.[34] Potential calculations for helium show results similar to those for the other rare gases. Again the use of separate ethylene/phenyl parameters is needed to localize the helium above a single ring, but the depth of the calculated potential well (122 cm^{-1}) is much higher than the probable value of 80 to 90 cm^{-1}, based on the measured D_0 of $\leq 47\ cm^{-1}$.[33,21]

The recurrence period measured for stilbene-He_2 is also consistent with helium positions on the phenyl rings. In this case, however, a displacement of the atoms off the ring axis toward the center of the molecule is strongly indicated. By assuming that the two heliums in the 1:2 complex and the single helium in the 1:1 complex occupy equivalent positions, more stringent bounds could be derived for the coordinates of that position. These bounds would still be relatively loose, however, so any further efforts to refine the structure of the helium complexes should begin with more precise recurrence measurements.

Three different isomers are expected to exist for stilbene-He_2, assuming negligible interaction of the two helium atoms. Calculations show that the recurrence periods of these isomers would differ by less than four picoseconds, making them indistinguishable at the resolution of the present experiments. Lineshapes of the first few recurrences would also be minimally affected by the superposition of signals from the different isomers, which is consistent with the prominent recurrences observed.

C. Fluorene and fluorene-argon.

The PRC spectra of fluorene ($C_{13}H_{10}$) and fluorene-argon, exciting their S_1 origins[18] at 2959.9 Å and 2963.7 Å, respectively, have also been measured in our laboratory. Though no new structural information about these molecules is obtained, the analysis of this data provides an excellent demonstration of the PRC technique for two reasons. The first is that the values of all S_0 and S_1 rotational constants of the two molecules have been determined from completely resolved rotational spectra of their $S_1 \leftarrow S_0$ 0^0_0 transitions.[18] The availability of these values offers the opportunity to test the accuracy of both experimental and theoretical aspects of the technique. The second reason that these molecules are of particular interest is their moderately large degree of asymmetry, with b for fluorene-Ar about 16 times the value for *t*-stilbene. The discussion of this section will emphasize the effects of asymmetry on PRC and the results will show that near-symmetry is not a requirement for practical application of the PRC technique.

The excited state rotational constants of fluorene and fluorene-Ar, as given in Ref. 18, are shown in Table II along with the corresponding value of the asymmetry parameter b. Both molecules are nearest the prolate case in the symmetric top limit. Since the transitions are a axis polarized in both molecules, they may be considered as parallel transitions in first approximation. The dipole directions are rigorous since the *a* axis is perpendicular to a plane of symmetry in each case.[18]

Time-resolved measurements of the parallel fluorescence of both fluorene and fluorene-argon display simple patterns of regular in-phase recurrences. Recurrence periods were determined as described previously from two carefully calibrated experiments for each molecule. These are 943.2 ± 3.8 ps for fluorene and 1138 ± 3 ps for fluorene-Ar_1. The reciprocals of the measured periods, which are found in column 6 of Table II, represent first approximations to $B' + C'$, in accord with the nature of the transitions and the discussion of Section III of Chapter 2. Of course, the observation of distinct, periodic recurrences alone also leaves open the possibility that the molecules are oblate, in which case $1/\tau \simeq A' + B'$ instead. The value of the third rotational constant can only be inferred from the recurrence lineshapes.

The asymmetry corrections to the first approximations of $B' + C'$ may be estimated by application of Eq.(3.13) of Chapter 2. However, because the corrections so calculated are large (of the order of one percent), they are subject to uncertainties which are larger than the measurement uncertainties. Therefore, in this case, more accurate determinations of the asymmetry corrections are warranted. These are provided by PRC simulations using the rotational constants of Ref. 18. By careful measurement of the positions of recurrence peaks in the simulated fluorescence (over the range which provided the experimental τ_1), asymmetry corrections of -0.49% for fluorene-Ar and -0.44% for fluorene are found. The uncertainty in each of these corrections is ~ 0.05%. Application of these corrections results in the final experimental $B' + C'$ values given in the last column of Table II. Their agreement with the values in column 4 is a reassuring confirmation of the PRC experiments, calibration, and analysis. In determining these values no provision was made for the suspected nonlinearity of our measurement system. The small displacement to lower frequency of our results from those of Ref. 18 is consistent with the effect which such a nonlinearity would produce. Because the asymmetry correction, and thus the derived $B' + C'$, depends on the parameters used in the simulation, the error bars on the experimental value would be somewhat larger if the rotational constants were not well-known in advance. By contrast, the correction appears quite insensitive to changes in temperature so that uncertainty in the sample temperature entails no additional uncertainty in the derived $B' + C'$

The rotational coherence of fluorene has also been observed in picosecond fluorescence depletion measurements in a rotationally warm (20-25 K) molecular beam.[35] Characteristic recurrence behavior was seen for excitation of several different vibronic bands in S_1. For excitation at an excess vibrational energy of 927 cm^{-1}, the interval between the time zero peak and the first in-phase recurrence was measured and reported to be 928 ps. This value differs by almost 2% from the high resolution value of $(B' + C')^{-1} = 946$ ps at the origin. While no error bar is given for the interval measurement, the authors indicate that the discrepancy is significant and suggest centrifugal distortion as the cause. We now know that at least part of the discrepancy can be attributed simply to asymmetry. For example, in a fluorene PRC simulation at 3 K, the interval preceeding the first recurrence was found to be 0.85% shorter than $(B' + C')^{-1}$.

Neither centrifugal distortion nor vibrational effects in this relatively rigid molecule appear likely causes of an actual change in rotational constants of the size and direction needed to account for the remaining difference of 1% or 10 ps. In particular, if centrifugal distortion did occur at the low angular momenta of the sample molecules, it would be expected to increase the recurrence period rather than decrease it. However, the short interval could very reasonably be explained by a substantial increase in the asymmetry correction with temperature. This possibility is suggested by the dependence of α in Eq. (3.13) of Chapter 2 on J^2, coupled with the strong thermal bias toward low K. An accurate PRC simulation at 25 K could settle this question.

The use of PRC measurements to obtain more than the value of $B' + C'$ requires a detailed analysis of recurrence lineshapes and comparison with simulations. With the dipole directions fixed by symmetry for the case at hand, there remain four parameters to specify for the simulations: A', B', C', and T. In the following paragraphs the influence of these parameters is described and illustrated by means of simulations for the case of fluorene-argon. Best-fit parameters are also determined for a specific set of experimental data. The response used in the simulations of this sub-section has a full-width at half maximum of approximately 57 ps, while those of responses measured with the data ranged from 56 to 60 ps. Since fluorene-argon has no symmetry axis, its rotational symmetry species all have equal nuclear statistical weights.

The first parameter to consider is T, the rotational temperature of the sample. In Fig. 15 simulations of the first positive recurrence of fluorene-argon at two different temperatures are compared with experimental data. All three rotational constants were set equal to 0.4393 GHz for these calculations, which would be a reasonable starting point if the only available information about the structure of the molecule were the measured recurrence period. While both recurrence amplitudes and widths vary in the simulations, it is the widths which provide the most effective gauge of temperature, since they are less sensitive to other parameters. Therefore, in Fig. 15 the three recurrence peaks are shown with equal amplitudes rather than in true relative scale, permitting a direct comparison of their widths. From this comparison, the measured recurrence is seen to be broader than the 5K simulation and narrower than that at 1K. This yields a first estimate of the temperature characteristic of the experimental data of (3 ± 1)K, a value typical of such supersonic expansions. While further refinement of a preliminary temperature estimate of this sort may in general be required after other simulation parameters are adjusted, in the present case the recurrence widths will be seen to depend almost exclusively on temperature within the range of parameters considered.

With the rotational temperature obtained, the effect of the choice of rotational constants on recurrence amplitudes may be examined. An example of this dependence is shown in Fig. 16, in which three simulations with fixed A′ and increasing separation of B′ and C′ are each compared with the same set of experimental data. The temperature is fixed at 3K, A′ is set equal to 0.8097 GHz, and $b = -0.04$, -0.0855, and -0.13 for the three simulations. The corresponding values of B′ and C′ are given in the caption. The vertical scale is graduated in units of percent deviation from the baseline fluorescence intensity of the simulations. The measured data appear to be in closest agreement with the second of the three simulations, which is based on the rotational constants from Ref. 18. The distinctions must be drawn mainly from the systematic nature of the deviations at the recurrences and are admittedly subtle. What should be clear from the simulations in the figure, however, is that PRC does depend markedly on the degree of asymmetry of the molecule and thus can serve as a useful probe of that asymmetry given measurements of sufficient signal-to-noise.

Several additional points about Fig. 16 are worth noting. One concerns the damping of recurrence amplitudes with time. Both the first and second positive recurrences are shown to illustrate this damping in simulation and experiment. Similarly, increasing asymmetry can be seen to result in the virtual disappearance of the out-of-phase recurrences which were seen clearly in stilbene and are still quite evident in the top simulation of Fig. 16. Both characteristics offer positive evidence of asymmetry and are therefore useful for distinguishing between asymmetry-induced amplitude changes and those resulting from changes in A′ or T alone. Also evident in Fig. 16 is the difference in recurrence separations among the three simulations, although the same value of B′ + C′ was used for each. This illustrates graphically the importance of the asymmetry correction in Eq.(3.13) of Chapter 2, reiterating the fact that the precise determination of B′ + C′ from a PRC recurrence period is possible only when at least rough approximations of the individual rotational constants are available.

The value of A′ was held fixed for the simulations of Fig. 16. If, instead, A′ were varied and B′ and C′ held fixed, similar changes in recurrence amplitudes would result. Thus a different estimate of A′ would shift the value of B′ - C′ at which the most satisfactory agreement with experiment was produced. Similarly, a change in the temperature estimate of even 1K would alter the simulated recurrence amplitudes enough to substantially influence values derived for other parameters. For these reasons, error bars on the experimental value of B′ - C′ cannot be estimated from simulations like those in Fig. 16 alone.

When all simulation parameters are simultaneously optimized to reproduce the fluorene-Ar data of Fig. 16, best fit parameters of A′ = 0.76 GHz, B′ = 0.471 GHZ, C′ = 0.402 GHz, and τ = 2.6 K are obtained. The simulation calculated from these parameters is shown in Fig. 17. The differences between this simulation and the middle simulation in Fig. 16

appear very minor and, indeed, the reduced chi-square values indicate that both simulations are very acceptable approximations to the data.

Based on the statistics of the fit of the entire data set, only rather broad bounds may be placed on the rotational constants. Uncertainties are difficult to determine due to the interaction of the parameters, but 90% confidence limits of the order of three percent are estimated for B′ and C′ separately. The value of A′ is much less precisely determined. Even when B′ and C′ are not optimized as A′ is varied, no value of A′ from 0.62 GHz up to the upper limit imposed by relation (2.1) of ~ 2.8 GHz can be rejected at a 90% confidence level based on the chi-square test. Excellent fits are obtained for all values between 0.65 GHz and 1.0 GHz.

One factor contributing to the breadth of the chi-square minimum and the consequent poor discrimination in the values of the rotational constants is the choice of the data set. The nature of PRC for a parallel transition is such that the readily accessible information is highly concentrated in the recurrences. Thus the great majority of data points in the range of Fig. 16 are equally well fit by all three of the simulations shown, and many others as well. The low contributions of these background points to the chi-square sum tend to dilute the significant information supplied by the fit of the recurrences and can lead to acceptable chi-square values for simulations which clearly fail to reproduce the recurrence behavior. A fit in which were included only the points in the immediate vicinity of a recurrence, such as the range shown in Fig. 15 would therefore help to establish tighter limits on the rotational constants. A fit of a single recurrence is not of itself sufficient to distinguish differences in asymmetry, however, and should be used only in conjunction with fits of other recurrences or of a wider range of data.

D. Anthracene

The preceding has shown the manner in which temperature and molecular structure interact to determine the characteristics of PRC for a parallel-type transition. For a transition polarized perpendicular to the near symmetry axis of the molecule, the appearance of a second recurrence period introduces some additional features to the analysis. An example is the $S_1 \leftarrow S_0$ 0^0_0 transition of anthracene (λ_{ex} = 3610.8 Å). In Ref. 7 it was shown that in this case the manifestations of PRC are expected to be very subtle. (See also Section III of this chapter for discussion of this point.) No *polarization-dependent* structure was observed in the fluorescence measurements reported there, so no information about S_1 molecular parameters was obtained. Experiments have now been performed at lower rotational temperatures (achieved via increased laser-to-nozzle distance) and improved signal-to-noise. In these, reproducible, polarization-dependent transients characteristic of PRC have been detected. These transients are in evidence in the data of Fig. 18 which is displayed in the form of R(t), the experimental polarization anisotropy, formed from measurements of each of the two principal orthogonal polarization components of fluorescence as described in Chapter 4. The use of R(t) is advantageous because it reveals much more clearly the early time effects associated with PRC, and largely eliminates the influence of the polarization-independent fluorescence decay, even when it is non-exponential.[7]

By comparison with the standard deviation (σ) of the R(t) values (shown in the figure), it can be seen that many of the features have amplitudes well above the level of noise. Note, however, that the corresponding features in the fluorescence decays are of very low amplitude, with typical modulations depths of about 1%. For this reason, and because the fluorescence lifetime is moderately long (~ 21 ns), the level of noise remains fairly constant for all data points in Fig. 18. Most of the initial decay of R(t) falls outside the scale of the figure, which was chosen to show the later transients in greater relief.

To begin to appreciate the behavior of the measured anthracene R(t), it is useful to consider first the anisotropy resulting from PRC in the near equivalent symmetric top. This is shown in Fig. 19. The parameters used for this simulation were chosen for illustrative purposes only. In this symmetric top anisotropy, it is an easy matter to distinguish the existence of the two separate recurrence periods despite their strong interaction at times. These periods are given exactly by the relations $\tau_2 = 1/[4(A'-B')] = 139$ ps and $\tau_1 = 1 / (2 B') = 1.22$ ns. Bearing in mind that asymmetry will reduce recurrence amplitudes and introduce further irregularities, one may recognize in the R(t) of Fig. 18 features analogous to those of Fig. 19. In particular, the first, third, and fourth positive nutation recurrences are distinctly visible and it is from these that a value of 1.220 ± 0.013 ns has been derived for τ_1. The first out-of-phase nutation recurrence is also clearly distinguished. No prominent feature is visible at the expected position of the second positive recurrence in Fig. 18 but, as the simulation of Fig. 19 illustrates, such a "missing" recurrence may easily result when the two types of recurrence interfere. As was the case for a parallel transition, $1/\tau_1$ serves as a good first estimate to the sum $B'+C'$. An accurate value for τ_2 is much more difficult to obtain, however, since the smaller amplitudes of the rotation recurrences are strongly perturbed by asymmetry and easily distorted by noise. A period of anywhere from 110 ps to 145 ps is suggested by the behavior of R(t) between the first out-of-phase and first in-phase nutation recurrence. Simulations will confirm that the spacing of rotation recurrences becomes very irregular in the asymmetric top, making a practical measurement of τ_2 very difficult.

Though an accurate value of τ_2 is difficult to determine in general, it is worth noting at this point the utility of this second period in fixing the values of all three rotational constants. Specifically, as one can see from the near-symmetric top relations, equations (3.1) and (3.2) of Chapter 2, the (approximate) value of A′ (or C′ in the oblate case) is uniquely determined by a knowledge of both periods. Thus the constant whose precise value is most difficult to establish for a near parallel transition could potentially be found for a perpendicular transition without even fitting the data. Furthermore, since the three constants are constrained by relation (2.1), a knowledge of A′ places an upper limit on the difference between B′ and C′ which may be useful in the determination of their values. In fact, if the molecule is known to be planar, relation (2.1) becomes an equality (neglecting contributions from out-of-plane vibrational motion) and the values of A′, B′, and C′ are completely specified by the following equations in τ_1 and τ_2 (subject to corrections for the influence of asymmetry):

$$A' = \frac{1}{2\tau_1} + \frac{1}{4\tau_2}$$

$$B' = \left(\frac{1}{2\tau_1^2} + \frac{1}{4\tau_2\tau_1} + \frac{1}{16\tau_2^2} \right)^{\frac{1}{2}} - \frac{1}{4\tau_2}$$

$$C' = \frac{1}{\tau_1} - B' . \qquad (2.2)$$

Guided by the above relationships, the measured periods, and rotational constants calculated from data on the ground state structure of anthracene[36] a range of possible values for each of the excited state rotational constants was determined. A fit of the data over the central 5.5 ns of the time range shown in Fig. 18 was then carried out. The nuclear statistical weights used for the four rotational symmetry species of anthracene were[37] 288, 240, 240, and 256 for + +, + −, − +, and − −, respectively. No substantial differences were seen using these correct weights vs. using equal weights for the four species, however.

The detailed structure of the PRC signal was found to change substantially with changes of B′ or C′ of less than 0.5 MHz. The fast alteration of the total PRC pattern with changing constants due to interference between nutation and rotation beats makes it very important to start the fitting process close to the correct values. This increased difficulty of the fit entails with it, of course, the ample compensation of producing more precise values for the rotational constants.

In Fig. 20 is presented the simulated R(t) resulting from the best fit parameters. The excited state rotational constants determined from the fit are given in Table III, along with ground state constants calculated from the crystal structure of Ref. 36a. Uncertainties for the values in Table III will be explained below. The derived excited state constants do not satisfy relation (2.1) but the discrepancy, or inertial defect, amounts to only ~ 1.1 amu- Å^2, while the uncertainty in this value is about 2.2 amu- Å^2, as calculated from the correlated uncertainties in the constants. The rotational temperature was determined to be 1.6 K for these measurements in which laser excitation occured 5 mm from the 60 μ nozzle ($x/D \simeq 80$).

All features of the experimental R(t) are satisfactorily reproduced by the simulation. Note in particular the missing second and the shapes and widths of the third and fourth nutation recurrences, all of which are quite sensitive to the simulation constants. Figure 21 shows a detailed comparison of simulation and data over a portion of the time range of Figs. 18 and 20, including the third and fourth recurrence peaks just mentioned. Despite transients of up to 7σ in amplitude, deviations exceed 2σ at only 2 points. It may be seen in Figs. 20 and 21 that no well defined succession of rotation recurrences appears in the simulated R(t). This suggests that the period τ_2 will be clearly seen only if the asymmetry is much smaller than that of anthracene for which $b \simeq -0.02$.

The simulations also reveal a much greater irregularity in the apparent separation of nutation recurrences in this case than in the parallel dipole case. This is presumably due to the interference of the rotation structure which is absent for a parallel transition. The wide variation in recurrence shapes and widths seen in the figures offers a clear indication of this interference. As a result it is found that values of $B' + C'$ derived using measured values of τ_1 are less accurate in the perpendicular than in the parallel transition case.

The uncertainties given in Table III for the excited state rotational constants were established on the basis of the 90% confidence level of 1.1 for the value of the reduced chi-square statistic (χ^2) when fitting 342 data points with six adjustable parameters. This process is illustrated graphically in Fig. 22 where χ^2 is plotted against changes in the rotational constants around the best fit values. In plots numbered 2, 3, and 4, the individual rotational constants B', A', and C', respectively, are varied. The remaining plot (number 1) was obtained by changing all three constants simultaneously. This last is equivalent to a change in the time scale only, so that the PRC signal is stretched or compressed but remains unchanged in appearance. The temperature was optimized for each point on this curve, falling in all instances between 1.5 and 1.7 K. Of course, the conclusions drawn from these plots are valid only in the absence of systematic errors. For example, fitting without using the complete distribution of natural isotopic abundances could have a small effect on the results.

The plots show that the PRC interference pattern is sensitive to changes of the individual constants of about 0.2% at the signal-to-noise of these experiments. The error bars of 0.6% given in Table III reflect not only the larger changes which are possible when all three constants change simultaneously, but also the uncertainty in the time scale of the experiments, which is rather large (0.25%) due to the indirect calibration needed at this short time range. Since these factors may raise or lower the values of the constants only in a correlated fashion, the ratios of pairs of constants may be given with considerably greater accuracy (~ ± 0.2%) than can the constants individually.

The measured S_1 rotational constants may be compared with calculated ground state constants given in Table III to draw some conclusions about the effect of electronic excitation on the structure of anthracene. The uncertainties in the ground state constants are based on the quoted standard deviations of the seven structural parameters of ref. 35a. It is found that the rotational constants have a roughly linear, equal, and additive dependence on variations in each parameter when those variations are scaled to the standard deviations. Thus, for example, if the change in rotational constant B caused by the variation of any parameter by one standard deviation is ΔB, the amplitude of the maximum change in B which may be produced by simultaneously varying all parameters by one standard deviation is $\Delta B_{max} = 7 \cdot | \Delta B |$. If it is assumed that measurement errors in the seven parameters are independent and normally distributed, the standard deviation of the derived constant B is then

$$\sigma_B = \left(\sum_{i=1}^{7} \Delta B^2 \right)^{1/2} = \frac{\Delta B_{max}}{(7)^{1/2}} .$$

The values given in Table III are 90% confidence limits of 1.645 σ, or 0.622

ΔB_{max} under the same assumptions. A more sophisticated error analysis would have to account for any correlation of the measured parameter values resulting from the fact that they were derived from the same x-ray data. At worst the errors could be a factor of $(7)^{1/2}$ larger than given, but they could also be reduced by the correlations.

Comparing the constants for the two electronic states, one finds changes upon excitation are of the order of $(+\ 0.3 \pm 1)\%$ for A and $(-2 \pm 1)\%$ for B and C. This may be compared with an estimate of a change of -1% for all three constants derived from rotational band contour measurements and simulations.[37] The decrease in B indicates a 0.5 to 1.5 % stretch of the molecule in the direction of its long axis. The uncertainty in the change in A leaves open a wide range of possible changes in the short axis of anthracene. It could also expand, or it could contract enough to partially compensate for the stretch of the long axis, resulting in minimal changes in C-C bond lengths.

Anthracene bond length changes from S_0 to S_1 were calculated in a recent theoretical treatment by Zerbetto and Zgierski.[38] These are inconsistent with the above experimental results. They correspond to changes in both B and C of -0.5% only, when it is assumed that bond angles, which were not reported, do not change significantly. If instead one considers only the absolute values of the S_1 constants, one finds that the theoretical B′ and C′ are in reasonable agreement with the PRC results, while the theoretical A′ is a full 2½% lower than its experimental value.

III. Excess vibrational energy dependence of rotational coherence in *t*-stilbene and anthracene

A. Results

i. *t*-Stilbene

The characteristics of purely rotational coherence in *t*-stilbene were clearly established by the experiments discussed in Section II A. We now turn to an examination of rotational coherence in the vibrationally excited molecule. The time evolution of fluorescence in *t*-stilbene at excitation energies below S_1+1300 cm^{-1} has been extensively investigated in previous picosecond studies.[39] The manifestations of intramolecular vibrational energy redistribution (IVR) in the form of both periodic energy transfer (vibrational quantum beats), and dissipative redistribution are observed. Our objective in carrying out polarization-analyzed fluorescence measurements on these vibrationally-evolving states was two-fold: 1) to determine if the observed rotational coherence depends in any fashion on the excess vibrational energy, and 2) to distinguish between the influence of rotational coherence and that of vibrational dynamics, for those cases in which both may contribute significantly to the time evolution of fluorescence. Results are presented below for excitations in each of the energy regimes classified by Felker et al.[39] on the basis of the type of IVR exhibited: no IVR (below 752 cm^{-1}), restricted IVR (789 - 1170 cm^{-1}) and dissipative IVR (above 1230 cm^{-1}).

Measurements at three different excitations in the low energy region produced the three parallel decays of Fig. 23. These are virtually identical to those observed for excitation of the S_1 origin, with the familiar pattern of recurrences clearly in evidence. Variations in the decay rates may be discerned, but these are very slight (a few percent at most). Various detection wavelengths and bandwidths were employed for these measurements; again no apparent dependence on detection band is observed. Expansion conditions for these decays differed from the standard, as described in the caption. Measured recurrence periods remain within measurement uncertainties ($\sim$ 10 ps) of the origin (zero excess energy) value of 1948 ps. (The possibility of a slight change is suggested, however, by a measured recurrence period of 1942 ± 6 ps at 83 cm^{-1}.)

Contrasting sharply with the low energy behavior are the results presented in Figures 24 and 25, obtained for excitation to intermediate (789 cm^{-1}) and high (1249 cm^{-1}) excess vibrational energy, respectively. Parallel and perpendicular fluorescence for the same excitation and otherwise identical detection are compared in each figure. The spectrally resolved fluorescence band detected is in each case assignable as emission from the optically prepared superposition state.[4] The nature of the temporal evolution observed substantiates this assignment.[39]

The decays displayed in Fig. 24 for 789 cm^{-1} excitation are strongly dominated by a polarization-independent modulation. This modulation is attributable to a cyclic transfer of energy between two coupled zeroth-order vibrations (restricted IVR). In the presence of such strong modulations, the manifestations of rotational coherence may easily go unnoticed. Only at very high signal-to-noise may recurrences be seen, most prominently in the third trough and on the sixth peak of the vibrational oscillation. A detailed comparison of these recurrences with those observed at the stilbene origin is presented in the discussion section.

In the decays of Fig. 25 (1249 cm^{-1} excitation) the influence of detection polarization is much more visible than in the preceding figure. The polarization anisotropy makes itself most evident here at a time—immediately after excitation—when it is scarcely detectible in the decays previously considered. As we will show in the discussion, such an effect is expected as a consequence of the relation of our temporal response to the different time scales of evolution involved and is not necessarily an indication of a change in the nature of the rotational dynamics. The very fast initial decay seen here represents the irreversible flow of vibrational energy out of the initially excited mode into the many equi-energetic bath modes of the molecule (dissipative IVR).[39] It is important to emphasize that detection for these decays was not at the laser wavelength and that careful checks were made to ensure that the observed fast components were completely free of scattered light.

In addition to the unrelaxed emission represented in Fig. 25, polarization-analyzed fluorescence in the vibrationally relaxed emission region for 1249 cm^{-1} excitation was also detected (Fig. 26). As for the preceding figures, both parallel and perpendicular fluorescence is shown. These decays resume the form observed for low energy excitations of a single exponential with the regular structure of polarization-dependent recurrences superimposed. That the recurrences appear less well-defined in these decays than in others presented cannot be considered significant. The measured recurrence period is unchanged (1943 ± 15 ps). The only discernible difference between the decays of Fig. 26 and those obtained at low energy excitation is their shorter lifetime. (2 ns vs. 2.7 ns at low energies. A very short rise-time may also be present but is unnoticeable here.)

ii. Anthracene

Time-resolved fluorescence studies[40] on the $S_1 \leftarrow S_0$ electronic transition of anthracene have revealed each of the three quasi-distinct categories of temporal evolution already described in reference to stilbene. Once again, each is found to occur at excitations within a particular range of excess vibrational energy in the S_1 state. To investigate the possibility of rotational coherence contribution to the observed fluorescence evolution, polarization-analyzed experiments analogous to, though less extensive than, those on stilbene were carried out on anthracene at excitations in these energy ranges.

Under experimental conditions comparable to those of Ref. 40, no polarization dependence of anthracene fluorescence was detected at any of the bands studied (252, 1380, 1409, 1420, and 1792 cm^{-1}). It should be noted that the signal-to-noise achieved in these measurements was in no case comparable to that of the data of Section II D which revealed purely rotational coherence at the anthracene origin. However, experiments at two excitations [in the regions of restricted (1409 cm^{-1}) and dissipative (1792 cm^{-1}) IVR] demonstrated the absence of distinct polarization dependence even when the signal-to-noise and conditions were such that polarization effects are easily seen in stilbene. A particularly interesting example of the effective polarization independence of anthracene fluorescence is seen in the data collected for high energy excitation (1792 cm^{-1}), shown in Fig. 27. The fluorescence band detected to produce these decays is spectrally resolved despite the very wide detection bandwidth employed. Measurements under identical conditions, but in the absence of anthracene, confirmed that laser scatter gave no contribution to the observed fast component. This data will be considered more closely in the discussion section.

On the basis of our measurements, it may be concluded that rotational coherence has a negligible effect on the evolution of anthracene fluorescence as observed under experimental conditions similar to those employed here, regardless of the polarization properties of the light involved in excitation or detection. The evolution that *is* observed, such as the transients of Fig. 27 and other quantum coherence effects reported in Ref. 40, may therefore be attributed exclusively to true intramolecular energy redistribution without contribution from the evolving ensemble-averaged orientation of the excited molecules that purely rotational coherence reflects.

B. Discussion

When strict separation of rotational and vibrational motion is assumed, rotational coherence is independent of the vibrational levels reached either in absorption or emission.[5] In this case, the intensity of polarization-analyzed fluorescence evolves as the product of a polarization independent envelope reflecting vibronic evolution, which we shall call $V(t)$, and the purely rotational coherence function appropriate to the given detection polarization ($C_\alpha(t)$ where α identifies the direction of detection polarization). That is,

$$I_\alpha(t) = V(t)\, C_\alpha(t)\ . \qquad (2.3)$$

In the following, experimental results are compared with simulations which have been based on this approximation and the $C_{\parallel}(t)$ and $C_{\perp}(t)$ used to produce Fig. 2, 5, and 7 of Section II A. The fact that these functions give a satisfactory reproduction of the observed purely rotational coherence at the t-stilbene origin makes them wholly adequate for this purpose.

It follows immediately from Eq. (2.3) above that the molecular anisotropy is independent of $V(t)$:

$$r(t) = \frac{I_{\parallel}(t) - I_{\perp}(t)}{I_{\parallel}(t) + 2I_{\perp}(t)} = \frac{C_{\parallel}(t) - C_{\perp}(t)}{C_{\parallel}(t) + 2C_{\perp}(t)} \; . \tag{2.4}$$

For comparison of simulations with anisotropies calculated (as described in Chapter 4) from measured signals, however, one must account for convolution with the detection response $S(t)$:

$$\begin{aligned} R(t) &= \frac{\int\limits_{-\infty}^{+\infty} I_{\parallel}(t')S(t-t')\,dt' - \int\limits_{-\infty}^{+\infty} I_{\perp}(t')S(t-t')\,dt'}{\int\limits_{-\infty}^{+\infty} I_{\parallel}(t')S(t-t')\,dt' + 2\int\limits_{-\infty}^{+\infty} I_{\perp}(t')S(t-t')\,dt'} \\ &= \frac{\int\limits_{-\infty}^{+\infty}\Big[C_{\parallel}(t') - C_{\perp}(t')\Big]V(t')S(t-t')\,dt'}{\int\limits_{-\infty}^{+\infty}\Big[C_{\parallel}(t') + 2C_{\perp}(t')\Big]V(t')S(t-t')\,dt'} \; . \end{aligned} \tag{2.5}$$

Thus the vibronic component does not simply divide out and $R(t)$ will depend on the form of $V(t)$, even when, as we shall assume here, $r(t)$ does not. In practice, this dependence is very slight unless $V(t)$ shows significant variation on the timescale of $S(t)$. The possibility that differences in $R(t)$ may be traceable to differences in $V(t)$ only should be kept in mind, however. Simulated anisotropies will prove useful in separating such convolution effects from the effect of real variations in $r(t)$.

$R(t)$ provides an effective means to evaluate the contribution of rotational coherence to measured decays displaying complicated and diverse temporal evolution, such as those in Fig. 24 and Fig. 25. The procedure will be to calculate the experimental $R(t)$ from the data and compare this with $R(t)$ derived from Eq. (2.5) with an appropriate choice of $V(t)$.

i. *t*-Stilbene

a. Low energy excitation

Polarization-analyzed measurements for low energy excitations have shown no significant difference from those for 0_0^0 excitation. For a closer comparison of the data, we present in Fig. 28 anisotropies for 83 cm^{-1} and 0 cm^{-1} excitation. The very close agreement of these traces is apparent. Thus rotational coherence is essentially unaffected by vibrational excitation in the low energy regime. The match of recurrence periods also imposes a limit on the changes in rotational constants which may result as a consequence of vibrational motion. One may conclude therefore that the assumption of separability of vibration and rotation is well satisfied at these energies.

b. Intermediate energy

In the case of 789 cm^{-1} excitation and -610 cm^{-1} detection (Fig. 24), $V(t)$ can be very well approximated by $V(t) \propto \left(1 + \alpha e^{-\gamma' t} \cos(\omega t)\right) e^{-\gamma t}$, with appropriate choices of α, γ', and γ. In Fig. 29 are presented a simulated parallel decay and simulated $R(t)$ using this $V(t)$, and the experimental $R(t)$ calculated from the 789 cm^{-1} decays of Fig. 24. In the experimental $R(t)$ of Fig. 29, the basic features seen in previous $R(t)$'s are again present. The recurrence period is also the same (1948 ± 15 ps). However, there appears to be a new feature here, as well, in the form of a weak periodic ondulation of the normally flat baseline or residual value. This feature has been reproduced several times; we feel it is therefore unlikely that undetected changes in experimental conditions between parallel and perpendicular decay collection are responsible. In particular, a shift of the time origin does not account for this effect, as shown by variation of the parameter t' in the $R(t)$ calculation (see Chapter 4).

Since the period of the observed ondulation is, at least approximately, that of the vibrational envelope, another possible cause which must be considered is the convolution effect alluded to earlier. The considerable disparity between the vibrational period and the measured response width (790 ps vs. 55 to 65 ps for the experiments in question) precludes this as the source of any change in $R(t)$ as large as that observed. This is confirmed by the simulated $R(t)$ of Fig. 29 which shows no comparable influence of $V(t)$. Comparing this simulation with others reveals that, in fact, the oscillations in this $V(t)$ have no visible effect on $R(t)$ at all. Anisotropies have also been calculated from measurements of fluorescence from the out-of-phase vibrational state ($\bar{\nu}_\mathrm{d} = -700\ \mathrm{cm}^{-1}$).[39] Although these anisotropies are of lower signal-to-noise than that of Fig. 29, they also appear modulated, and the apparent modulation is of opposite phase from that for $-600\ \mathrm{cm}^{-1}$ detection. These results strongly suggest that there are contributions to the fluorescence anisotropy other than those from purely rotational coherence, and that these contributions reflect a dependence of rotational motion on the nature of the vibrational motion being executed by the molecule. The mechanism of this dependence is open to speculation, but changes in vibrationally averaged rotational constants and Coriolis coupling are two possible factors to be considered.

c. *High energy*

For 1249 cm^{-1} excitation two different forms of decay were observed. For relaxed emission $V(t)$ is again single exponential. Though the lifetime is somewhat shorter than at the origin, this difference has negligible effect on $R(t)$ due to the vastly different timescale of $S(t)$. Thus $R(t)$ measured at the origin and $R(t)$ constructed from the decays of Fig. 26 should differ only if the vibrational evolution of the molecules significantly disrupts their rotational motion. The agreement of the traces of Fig. 30 indicates that rotation remains very regular. Furthermore, an absence of significant vibrational influence on $B' + C'$ is once again revealed by the measured recurrence period of 1943 ± 13 ps.

The $V(t)$ which corresponds to the unrelaxed emission of Fig. 25 is, on the other hand, a highly complicated function. A direct measurement of this function, subject to the limitation of our detection response, may be carried out by detection of magic angle fluorescence. (This is possible since $C_{54.7^\circ}(t)$ is simply a constant for $t > 0$, as discussed in Chapter 2.) In Fig. 31 is presented the result of such a measurement. The structure is roughly biexponential, with irregular partial recurrences at long times, as observed before[39]. Since it must in general be true that $I_{54.7^\circ}(t) \propto I_{\|}(t) + 2I_{\perp}(t)$, parameters for $V(t)$ may also be obtained from a complete knowledge of $I_{\|}(t)$ and $I_{\perp}(t)$, including their relative intensities. This relation is purely geometric and independent of the source of observed anisotropy. In practice this has been used to check the self-consistency of our data, which depends upon the theoretically determined normalization of parallel and perpendicular decays and the maintenance of uniform experimental conditions throughout a series of polarization-analyzed measurements (see below).

In order to simulate decays for comparison with those of Fig. 25, we shall adopt as a simple though useful approximation a biexponential $V(t)$. Parameters for the description of $V(t)$ in this approximation were determined by biexponential fits of magic angle decays. An example is plotted against the data of Fig. 31. The fit is seen to reproduce the early time behavior very satisfactorily. For $V(t)$ given by

$$V(t) \propto f e^{-t/\tau_1} + e^{-t/\tau_2} \ , \tag{2.6}$$

the parameters obtained are $\tau_1 = 44$ ps, $\tau_2 = 2.1$ ns, and $f = 10$ with uncertainties of about 10%. A biexponential fit of $I_{\|}(t) + 2I_{\perp}(t)$ formed from the decays of Fig. 25 yields parameters in good agreement with these. It must be noted that these parameters are quite sensitive to the response used in the fitting procedure; the large relative uncertainties directly reflect the uncertainty in the response.

With the parameters for $V(t)$ in hand, the simulations of Fig. 32 are readily calculated. A single measured response (55 ps FWHM) has been used in these simulations and in fitting all biexponential decays. One sees that rotational coherence does significantly influence the amplitude of the initial fluorescence spike, producing a polarization dependence similar to, though less pronounced than that displayed in Fig. 25. The quantitative agreement with experiment can be tested by comparison of parameters obtained from biexponential fits of corresponding sets of data. The results are given in Table IV. In addition to fit parameters for the simulations of Fig. 32, for which the assumed rotational temperature was 2 K, parameters are also given for simulations assuming a temperature of $\frac{1}{2}$ K.

It is seen from these values that rotational temperature strongly affects the apparent decay parameters and that $T_{ROT} = \frac{1}{2}$ K gives much better agreement with the measured parameters than $T_{ROT} = 2$ K. This despite the fact that our measurements of recurrences for 0_0^0 excitation under identical expansion conditions point strongly to a temperature of 2 K or greater. Thus the data again appear to contradict the assumption that rotational motion is adequately described by PRC in the vibrationally excited molecule. This contradiction is somewhat magnified by the evidence of Section II A, which indicates that simulations for which an *a* axis polarized transition is assumed, such as those of Fig. 32, predict more prominent transients at early time than are actually present in stilbene PRC. Further consideration is given to possible reasons for this discrepancy later in this section.

It is clear from the differences between parameters describing parallel, perpendicular, and magic angle data, whether measured or simulated, that the evolution of fluorescence may be significantly affected by rotational coherence. This fact should be borne in mind in the design and interpretation of time-resolved fluorescence experiments. In particular, in the study of vibrational dynamics, where $V(t)$ is sought, detection of other than magic angle fluorescence has the potential, at least, to be misleading. The importance of the effect, however, will depend not only on the particular molecule and excitation and detection arrangement, but also on the sample temperature. Thus previously reported parameters for $V(t)$ of the emission band currently under discussion[39] differ from those reported here in part because perpendicular fluorescence was detected. They also differ from the experimental perpendicular detection parameters in Table IV due to the lower rotational temperature obtained under the expansion conditions employed in the present study.

In addition to the highly visible anisotropy of the initial fluorescence spike, unrelaxed emission is found to display rotational coherence recurrences as well. To demonstrate this, the calculation of $R(t)$ from the decays of Fig. 25 is shown in Fig. 33, along with $R(t)$ derived from the simulations of Fig. 32. Despite the low signal-to-noise of the experimental data, the positive recurrence is clearly observed. The measured period is 1932 ± 21 ps, still not conclusively different from the origin value. Note that the recurrence amplitudes and widths of the experimental $R(t)$ match quite well those of the simulation.

Careful examination of the simulated $R(t)$ of Fig. 33 at early time reveals certain irregularities not seen in the simulations of Fig. 7 or Fig. 29. This is further highlighted in Fig. 34. The upper trace is an expanded view of the simulation of Fig. 33, calculated using Eq. (2.5) and the $V(t)$ appropriate to 1249 cm^{-1} unrelaxed emission. The lower trace resulted from an identical calculation, changing only the form of $V(t)$. We see from this comparison that the biexponential $V(t)$ evolves sufficiently fast to exercise distinct influence on the form of $R(t)$ over a duration of 200 ps. An effect of this size would be very noticeable in measurements at a signal-to-noise ratio as high as that of Fig. 18, for example.

We may now consider in some detail the source of the evident difference between the data of Fig. 25 and the simulations of Fig. 32. It is reasonable to suspect that this discrepancy, like the evidence already seen at intermediate vibrational energies, indicates a breakdown of the assumed separability of vibrational and rotational motion underlying the simulations. The likelihood of such a breakdown is certainly greater at higher energies. There are, however, other possible contributing factors which should be borne in mind. For example, an exceptionally limited coherence width in excitation, associated with the use of an ultra-fine tuning etalon to spectrally resolve the 1249 cm^{-1} band, could account for the observations by favoring low J transitions, just as would a lower rotational temperature. Arguing against this possibility is the fact that the etalon has also been used for measurements at the origin and other low vibrational energies, and no changes in recurrence behavior related to the laser bandwidth have been detected at those excitations.

Another factor in the simulations which cannot be ruled out as the cause of the apparent discrepancy is the assumption of a biexponential $V(t)$. Use of a more realistic model for the vibrational envelope might substantially alter the form of the simulated decays. If this is the cause of the apparent differences at early time, recurrence behavior would not be affected. The signal-to-noise of the data in Fig. 33 is too low to permit a judgement on this point. However, the evidence supplied by Fig. 30 of very regular rotational motion of vibrationally relaxed molecules suggests that any disruption of rotational motion at early time cannot be severe.

ii. Anthracene

As seen in Section I D, PRC in anthracene is much different than in *t*-stilbene. The reasons for this are apparent from the theoretical description developed in Chapter 2. It was shown there, as in Ref. 5, that the observable characteristics of rotational coherence are determined by the transition dipole direction in the molecule and its rotational constants. The excited state rotational constants of anthracene determined from PRC experiments at the S_1 origin are $A' = 2.159$ GHz, $B' = 0.444$ GHz, and $C' = 0.368$ GHz. Two differences between these values and those for stilbene have a significant bearing on the expected nature of rotational coherence. First, the asymmetry of anthracene is considerably more pronounced than that of stilbene ($b \simeq -0.02$ vs. -0.005). This has the following effects: 1) the applicability of symmetric top selection rules is reduced so that the number of interfering channels significantly involved in the fluorescence increases, and 2) the energy levels are more strongly perturbed from the regular symmetric top spacing. Both of these effects diminish the commensurability of beat frequencies which is the source of macroscopic recurrences. Secondly, B' and C' are substantially larger for anthracene than for stilbene (reflecting its more compact structure). The modulation frequencies related to the nutation of individual molecules are thus proportionately higher as well, entailing faster dephasing of nutation recurrences. (The increase in ground state constants will result in fewer initial levels being populated, but higher frequencies will still be involved, despite the lower J's.)

Also greatly affecting the form taken by rotational coherence are the directions of the dipole moments for the transitions involved, both in absorption and emission. The relative amplitudes of beat components are highly dependent on these. In anthracene the $S_1 \leftarrow S_0$ transition is b axis polarized, thus constituting a perpendicular transition in the symmetric top limit. In this case, even for a symmetric top, many additional high frequency beat components are possible. In particular, when the emission dipole is perpendicular as well, full recurrences are not expected and initial dephasing occurs on a much shorter timescale.

These considerations account for the subtlety of anthracene PRC, as displayed in the data of Section I. The absence of obvious rotational coherence effects in the vibrationally excited molecule is, for the most part, similarly explained. Note, however, that certain bands in the anthracene excitation spectrum are due to b_{1g} vibrations and gain their strength through vibronic coupling to a low-lying B_{3u} excited electronic state.[37] The transition dipole moment is then parallel to the a axis as in stilbene, and the manifestations of PRC are expected to change accordingly. The identification of these bands from their rotational band contours is sometimes problematic. The 1409 cm^{-1} band is a case in point, having been previously identified as a probable a axis transition.[41] That the present PRC measurements showed no sign of nutation recurrences in fluorescence at this excitation supports its subsequent assignment as the first overtone of an a_g vibration.[37]

To compare our experimental results at high energy against the assumption of separable vibrational and rotational motion, we have produced simulated parallel and perpendicular fluorescence decays corresponding to this case. These are displayed in Fig. 35. A rotational temperature of 2 K and rotational constants as given in the caption were used to produce the PRC functions. A biexponential $V(t)$ was assumed. The parameters for $V(t)$ were determined from the experimental 1792 cm^{-1} decays and are indicated in the figure. The calculated intensities were convoluted with a response of 57 ps FWHM, corresponding to those measured in connection with the decays of Fig. 27.

Surprisingly, the early time behavior in Fig. 35 deviates noticeably from that observed experimentally. As in stilbene, the very fast initial IVR decay interacts with the rotational dephasing to amplify its effect. However, based on the measurements reported here, the possibility of a difference between polarization components of the 1792 cm^{-1} band of the magnitude displayed in Fig. 35 may be conclusively rejected. The hypothesis of separable motions again appears to fail the test of experiment. Of course, comments made in regard to the deviation of measurement and simulation for the high energy measurements in *t*-stilbene are also appropriate here. However, since the deviations in the two cases are of opposite sense, it seems unlikely that an artifact of the simulation procedure could be responsible for both.

The preceeding results in both stilbene and anthracene have suggested that effects of vibration-rotation coupling may be inferred from polarization-analyzed fluorescence measurements. To more fully characterize these systems, further experiments, possibly with improved time resolution, are clearly needed.

IV. Rotational Coherence and Alignment in Dissociation Reactions

The S_1 dissociation dynamics of *t*-stilbene–X (X=He, Ar, Ne) van der Waals complexes at low excess vibrational energies have been studied in our laboratory by picosecond time-resolved fluorescence detection.[42,33] We focus here on the complex stilbene–He_1 (S–He). The binding energy D_0 of S–He is found to be less than 49 cm^{-1} in the excited state. Since calculations based on the pair-wise additive 6–12 potential model discussed in Section II B yield well depths of around 120 cm^{-1}, it appears reasonable to assume that D_0 is not substantially lower than this experimental upper limit. The rise of stilbene product fluorescence reveals that the complex dissociates to form vibrationless stilbene in about 40 ps at excitation energies of 84 cm^{-1} and 96 cm^{-1} above the S_1 origin. (These vibrations in the complex are at slightly higher energies than the corresponding bare molecule vibrations of 83 cm^{-1} and 95 cm^{-1}.) The assignment of the product vibrational states has been made by comparison of the spectra of dispersed fluorescence following dissociation with the spectrum obtained for 0_0^0 excitation of bare stilbene. This comparison is demonstrated for the 84 cm^{-1} band by plots (A) and (B) at the top of Fig. 36. In (C) is shown the dispersed fluorescence arising on excitation of the stilbene vibrational state at 83 cm^{-1}. Since this vibration is homologous to the 84 cm^{-1} vibration in S–He, emission prior to dissociation of the 84 cm^{-1} complex should look much like (C). That such emission is weak or absent in (A) is attributable to the very short dissociation lifetime relative to the excited electronic state lifetime of 2.67 ns.

The energies E' which must appear as kinetic energy in the products, either in the form of stilbene rotation or of relative translation of stilbene and helium, is equal to the excess excitation energy (i.e., in excess of the 0_0^0 energy) minus D_0. Thus E' is greater than 35 cm^{-1} and greater than 47 cm^{-1}, respectively, for these two dissociation reactions. Since D_0 is expected to be close to its upper limit, E' is probably not much higher than the above values.

At an excitation energy of 198 cm^{-1}, a dissociation lifetime of 160 ps is measured. The vibrational energy of the stilbene product is not known since the vibrational state is not accessible from the ground state by one-photon absorption. Thus E' cannot be determined and may reasonably have any value from 0 to $\sim$ 80 cm^{-1}. The mode selectivity displayed in these rates has been interpreted in terms of energetics, mode character and momentum gap propensity rules. In the present discussion, we are concerned rather with the effect of dissociation on the dynamics of product rotation.

To investigate this effect, stilbene product emission at each of the above excitations was polarization-analyzed. The result for 84 cm^{-1} excitation is shown in the lower half of Fig. 36 in the form of the experimental polarization anisotropy $R(t)$. Shown also in the figure for comparison are anisotropies of parent stilbene for two excitation energies and of S–He excited to its S_1 origin. The recurrence behavior displayed by the three lower anisotropies have been discussed in Sections II and III of this chapter. Fig. 36 reiterates the fact that the recurrence period reflects the fundamental nutation period of the molecules and can therefore serve to identify the fluorescing species. Accordingly, the periods for the two excitations of stilbene agree very closely, while that of S–He fluorescence is distinctly longer. The average of $B' + C'$ derived from the recurrence period is shown for each of the three measurements.

With the three lower data sets serving as reference, we now examine the anisotropy of the dissociation product in (A′) of Fig. 36. Recurrences are clearly present, though they are distinctly weaker than in the three other cases. The reduction in amplitude appears particularly severe for the out-of-phase recurrences. The period of these recurrences is seen to match the stilbene nutation period rather than that of the initially excited complex, thereby confirming the indication of spectra (A) and (B) that the emitter is stilbene. Rotational coherence must then be preserved, to some degree, in the dissociation process. As an experimental verification that the emission, and particularly the recurrences, observed are due to stilbene produced by dissociation of the S–He complex and not to an underlying parent absorption, the pressure dependence of the signal was carefully checked. No variation in recurrence amplitudes were observed over a range of pressures which was shown to change the ratio of complex to parent populations in the beam by more than a factor of two.

Recurrences similar to those at 84 cm^{-1} were observed in fluorescence from the vibrationless stilbene product of the 96 cm^{-1} S–He excitation. Recurrences were also seen at 198 cm^{-1}, but these were much weaker than for the lower two energies. Due to their weakness and to the spectral congestion at the energy of the S–He 198 cm^{-1} band, the assignment of these recurrences to dissociation products cannot be made with the confidence possible in the other two cases.

Having observed the transfer of coherence from excited S–He to stilbene product, we must now ask ourselves what aspects of the dissociation process govern that transfer and what can be learned from such measurements. A natural first attempt at interpreting the observed behavior is to compare it with the expectations of a classical treatment. Due to its simplicity, the prompt, impulsive model developed in Chapter 2 is an attractive alternative for such a comparison if it can be used. The validity of the assumption of impulsive separation can only be assessed on the basis of a particular dynamic model. This we will do below. However, given our knowledge of the dissociation lifetime and the rotational temperature of the molecular beam, we can immediately judge how well the condition of promptness is met. At a rotational temperature of 2.5 K typical of our experimental conditions, the most probable value of J in the S–He population is 10. The fundamental nutation period of S–He is 2.01 ns, as given in Table I. Thus the nutation period of a typical molecule in the sample is $\sim$ 200 ps, or about five times as long as the dissociation lifetime. Nutation is the only motion with which we need be concerned because the dipole directions are both essentially parallel. The typical excited S-He molecule sweeps out a

72° arc of its cone of nutation before dissociating. Furthermore, many molecules have higher J's and/or survive more than a single lifetime before dissociating. Application of the prompt model under these circumstances must be regarded as a rough approximation only. With this caveat in mind, in the absence of a treatment accounting fully for nonzero t_d, it is still instructive to compare the classical predictions with the observed behavior.

To carry out this comparison, calculations employing Equations (2.12), (2.43) and (2.35) of Chapter 2 have been performed. The exact quantum frequencies are used for integral values of J. The equilibrium geometry of the complex and principal axis coordinate system used in these calculations are as shown in Fig. 37. The helium atom is known to be located above the phenyl ring from the PRC analysis and spectral evidence (see Section II B), but its coordinates are not well determined. The values used in the calculation are the minimum energy coordinates of the 6–12 potential energy surface with helium interaction parameters given in Table II of Chapter 4. These coordinates are $x \sim 0$, $y = 3.0$Å, and $z = 3.15$Å. The potential surface about this minimum is reasonably symmetric, as it is dominated by the phenyl ring. Thus, in the absence of vibrational or rotational effects, the helium will remain in the yz inertial plane of stilbene as the dissociation proceeds. In this case the torque applied to the molecule, and therefore the angular momentum imparted to the nascent stilbene, is directed solely along the x axis.

We first perform the calculation for dissociation from the single equilibrium geometry. A rotational temperature of 2.5 K, E' of 50 cm^{-1}, and a 60 ps FWHM system response are assumed. The product stilbene is assumed to undergo symmetric top motion following dissociation. In Fig. 38a are displayed the out-of-phase and in-phase recurrences of the polarization anisotropy resulting from this calculation. Because symmetric top motion is assumed, all such recurrences are equal. For comparison, the signal expected under comparable experimental conditions for direct excitation of stilbene is shown in Fig. 38b, plotted on the same vertical scale. Thus the dissociation does result in a reduction of the recurrence amplitude. When calculated for the in-phase recurrence in the parallel fluorescence decay, the reduction is about 30%, while that observed in the first in-phase recurrence of the experimental data was typically about 40%. In the simulation, the effect results from the fact that the impulse adds an angular momentum of $|\vec{\jmath}_t| \sim 10$ to each molecule. Although the addition is vectorial and therefore reduces the total angular momentum of some molecules while increasing that of others, the increases dominate and the effective rotational temperature of the sample is raised. The influence on the recurrences is similar to that displayed in Figures 4 and 6 and discussed in Section II A of this chapter.

For the assumed geometry and energetics, one may also calculate the duration of the interaction of helium and stilbene after the complex has made the transition from a bound to a repulsive potential surface. Again relying on the 6–12 model, one finds that the potential has climbed to $< \frac{1}{2}\%$ of the well depth by the time the helium atom is 10Å from the ring plane. At the asymptotic velocity, the time required to reach that separation is about 1 ps. This time is short enough that even molecules of the highest significantly occupied J states of the sample undergo no significant displacement along their nutation trajectories. However, one must also consider rotation about the figure axis in order to see if the separation can truly be considered repulsive. This is true because any relative change in orientaion will affect the interaction geometry, and hence the torque, whether the dipole moves or not. For S–He, the fundamental rotation frequency of $2(A' - B')$ is about eight times its fundamental nutation frequency. The pertinent rotation frequency for a given state is the fundamental frequency multiplied by K. The most probable value of K is much lower than J for a prolate top. Thus rotation about the figure axis is also sufficiently slow compared to the duration of interaction after dissociation that the impulsive assumption appears reasonable.

Although the comparison of Figures 36A′ and B′ and 38a and b show that the experimental reduction of the in-phase recurrence is similar to that predicted by the model calculation, the out-of-phase recurrences seem to be more severely damped in the measured anisotropies. A simple extension of the model to include a distribution of initial geometries was made to investigate the role of vibrational averaging and see if this might account for the above difference. A long axis displacement of the helium (i.e., an average over a distribution of z_A) has no great effect on the calculated anisotropy. A stretch of the van der Waals bond has no effect at all since the impulsive force is normal to the stilbene plane. If the force remains normal to the plane as the helium executes a lateral displacement or perpendicular bend, however, there will clearly be a qualitative change. The torque then has a z component and will produce a z axis, or k, component of angular momentum. Since we have assumed that stilbene is a symmetric top, this lateral displacement can be treated within the reference frame conventions established in Chapter 2, particularly with regard to the form of the unitary transformation matrix, by rotating the x and y axes as the helium moves. Fig. 38c shows the anisotropy for a Gaussian perpendicular bend distribution with a half width at 1/e of 1.2Å (about equal to the lateral extent of the carbon ring). The contributions from off-axis geometries do produce noticeably smaller out-of-phase recurrences, and this is reflected in the average. On the other hand, the in-phase recurrence is in this case only 25% smaller than that of directly excited stilbene.

The above simulations suggest the manner in which information about dissociation dynamics may be obtained from polarization anisotropy measurements. However, it is clear that the roles of a great many factors must be examined closely before any solid conclusions can be drawn in the case of stilbene–helium dissociation discussed here.

References

1. J. A. Syage, W. R. Lambert, P. M. Felker, A. H. Zewail, and R. M. Hochstrasser, Chem. Phys. Lett. **88**, 266 (1982); J. A. Syage, P. M. Felker, and A. H. Zewail, J. Chem. Phys. 81, 4685 (1984).
2. R. H. Dyck and D. S. McClure, J. Chem. Phys. **36**, 2326 (1962).
3. G. Hohlneicher and B. Dick, J. Photochem. **27**, 215 (1984).
4. B. W. Keelan and A. H. Zewail, J. Phys. Chem. **89**, 4939 (1985).
5. P. M. Felker and A. H. Zewail, J. Chem. Phys. **86**, 2460 (1987).
6. a. G. M. Nathanson and G. M. McClelland, J. Chem. Phys. **81**, 629 (1984); b. A. P. Blokhin and V. A. Tolkachev, Opt. Spectrosc. (USSR) **51**, 152 (1981); c. G. M. Nathanson and G. M. McClelland, J. Chem. Phys. **85**, 4311 (1986).
7. J. S. Baskin, P. M. Felker, and A. H. Zewail, J. Chem. Phys. **86**, 2483 (1987).
8. M. Traetteberg, E. B. Frantsen, F. C. Mijlhoff, and A. Hoekstra, J. Mol. Struct. **26**, 57 (1975).
9. A. Warshel, J. Chem. Phys. **62**, 214 (1975).
10. B. P. Stoichoff, Can. J. Phys. **32**, 337 (1954); E. G. Cox, D. W. J. Cruickshank, and J. A. Smith, Proc. Roy. Soc. **247**, 1 (1958); J. H. Callomon, T. M. Dunn and I. M. Mills, Phil. Trans. R. Soc. A **259**, 499 (1966); D. G. Lister and J. K. Taylor, Chem. Commun. 1966, p. 152; T. Cvitas, J. M. Hollis, and G. H. Kirby, Mol. Phys. **19**, 305 (1970).
11. T. Suzuki, N. Mikami, M. Ito, J. Phys. Chem. **90**, 6431 (1986).
12. L. H. Spangler, R. van Zee, and T. S. Zwier, J. Phys. Chem. **91**, 2782 (1987); L. H. Spangler, R. van Zee, S. C. Blankespoor, and T. S. Zwier, J. Phys. Chem. **91**, 6077 (1987).
13. N. F. Scherer, L. Khundkar, T. Rose, and A. H. Zewail, J. Phys. Chem. **91**, 6478 (1987).
14. J. M. Robertson, Proc. Roy. Soc. A **150**, 348 (1935).
15. W. M. van Herpen, Ph.D. Thesis, Katholieke Universiteit te Nijmegan,

1988.

16. a. S. M. Beck, M. G. Liverman, D. L. Monts, and R. E. Smalley, J. Chem. Phys. **70**, 232 (1979); b. K. H. Fung, H. L. Selzle, and E. W. Schlag, Z. Naturforsch. **36a**, 1338 (1981).
17. R. E. Smalley, L. Wharton, D. H. Levy, and D. W. Chandler, J. Chem. Phys. **68**, 2487 (1978); C. A. Hayman, D. V. Brumbaugh, and D. H. Levy, J. Chem. Phys. **80**, 2256 (1984).
18. W. L. Meerts, W. A. Majewski, and W. M. van Herpen, Can. J. Phys. **62**, 1293 (1984).
19. W. M. van Herpen and W. L. Meerts, Chem. Phys. Lett. **147**, 7 (1988).
20. J. S. Baskin, P. M. Felker, and A. H. Zewail, J. Chem. Phys. **84**, 4708 (1986), and Appendix I of this thesis.
21. J. S. Baskin, D. Semmes, and A. H. Zewail, J. Chem. Phys. **85**, 7488 (1986).
22. K. Yamanouchi, S. Isogai, S. Tsuchiya, and K. Kuchitsu, Chem. Phys. **116**, 123 (1987).
23. T. S. Zwier, E. Carrasquillo M., and D. H. Levy, J. Chem. Phys. **78**, 5493 (1983).
24. M. J. Ondrechen, Z. Berkovitch-Yellin, and J. Jortner, J. Am. Chem. Soc. **103**, 6586 (1981).
25. For example, see: a. W. E. Henke, W. Yu, H. L. Selzle, E. W. Schlag, D. Wutz, and S. H. Lin, Chem. Phys. **92**, 187 (1985); b. J. Wanna and E. R. Bernstein, J. Chem. Phys. **84**, 927 (1986), and references therein; c. M. M. Doxtader, I. M. Gulis, S. A. Schwartz, and M. R. Topp, Chem. Phys. Lett. **112**, 483 (1984).
26. D. Bahatt, U. Even, and J. Jortner, Chem. Phys. Lett. **117**, 527 (1985).
27. A. D. Crowell and R. B. Steele, J. Chem. Phys. **34**, 1347 (1961).
28. S. Leutwyler, A. Schmelzer, and R. Meyer, J. Chem. Phys. **79**, 4385 (1983).
29. J. J. Ramaekers, H. K. van Dijk, J. Langlaar, and R. P. H. Rettschnick, Faraday Discuss. Chem. Soc. **75**, 183 (1983); G. Brocks and T. Huygen,

J. Chem. Phys. **85**, 3411 (1986); P. M. Weber, J. T. Buontempo, F. Novak, S. A. Rice, J. Chem. Phys. **88**, 6082 (1988).

30. G. Néméthy, M. S. Pottle, and H. A. Scheraga, J. Phys. Chem. **87**, 1883 (1983).
31. J. O. Hirshfelder, C. F. Curtiss, and R. B. Bird, *Molecular Theory of Gases and Liquids* (Wiley, New York, 1954) p. 168.
32. C. A. Taatjes, W. B. Bosma, and T. S. Zwier, Chem. Phys. Lett. **128**, 127 (1986).
33. D. H. Semmes, J. S. Baskin, and A. H. Zewail, submitted for publication.
34. A. L. Burgmans, J. M. Farrar, and Y. T. Lee, J. Chem. Phys. **64**, 1345 (1976).
35. J. F. Kauffman, M. J. Côté, P. G. Smith, and J. D. McDonald, J. Chem. Phys. **90**, 2874 (1989).
36. a. D. W. J. Cruickshank and R. A. Sparks, Proc. Roy. Soc. A **258**, 270 (1960); b. A. Almenningen, O. Bastiansen, and F. Dyvik, Acta. Cryst. **14**, 1056 (1961).
37. B. W. Keelan and A. H. Zewail, J. Chem. Phys. **82**, 3011 (1985).
38. F. Zerbetto and M. Z. Zgierski, Chem. Phys. **127**, 17 (1988).
39. P. M. Felker and A. H. Zewail, J. Phys. Chem. **88**, 6106 (1984); P. M. Felker, W. R. Lambert, and A. H. Zewail, J. Chem. Phys. **82**, 3003 (1985).
40. W. R. Lambert, P. M. Felker, and A. H. Zewail, J. Chem. Phys. **75**, 5958 (1981); *ibid.* **81**, 2209 (1984); *ibid.* **81**, 2217 (1984); P. M. Felker and A. H. Zewail, J. Chem. Phys. **82**, 2975 (1985); *ibid.* **82**, 2994 (1985).
41. W. R. Lambert, P. M. Felker, J. A. Syage, and A. H. Zewail, J. Chem. Phys. **81**, 2195 (1984).
42. D. H. Semmes, J. S. Baskin, A. H. Zewail, J. Am. Chem. Soc. **109**, 4104 (1987).

TABLE I. PRC measurements of *t*-stilbene van der Waals complexes.

	Energy (cm^{-1})	τ_1 (ns)	$B' + C'$ (GHz)
t-stilbene	0 ($\equiv$32234 cm^{-1})	1.9477(25)	0.5132(8)
t-stilbene-He_1	−6	2.0084(76)	0.4978(19)
-He_2	−12	2.0529(140)	0.4870(33)
-Ne_1	−16	2.2085(35)	0.4528(8)
-Ar_1	−40	2.4124(160)	0.4144(27)
	−63	2.4140(120)	0.4141(20)

TABLE II. Rotational constants of fluorene and fluorene-argon.

	From Reference 18					This work	
	A′ (GHz)	B′ (GHz)	C′ (GHz)	B′+C′ (GHz)	b	$1/\tau_{exp}$ (GHz)	B′+C′ (GHz)
Fluorene	2.1098(33)	0.5932(1)	0.4640(1)	1.0572(1)	−0.0409	1.0602(43)	1.0556(46)
Fluorene-Ar	0.8097(29)	0.4700(1)	0.4065(1)	0.8766(3)	−0.0855	0.8787(23)	0.8745(27)

Table III. Anthracene rotational constants (GHz).

	A	B	C
Ground state*	2.151(13)	0.4538(23)	0.3747(18)
Excited state	2.159(13)	0.4445(26)	0.3683(22)

*based on x-ray crystal structure of Ref. 36a.

Table IV. Biexponential fit parameters for measured and simulated decays of *t*-stilbene $S_1 + 1249\ \text{cm}^{-1}$ unrelaxed fluorescence.

Detection polarization		Measured	Simulated 2 K	 $\frac{1}{2}$ K
	τ_1 (ps)	33	37	33
$\hat{\epsilon}_2 \parallel \hat{\epsilon}_1$	τ_2 (ns)	2.1	2.1	2.1
	f	17	13	16
	τ_1 (ps)	56	47	53
$\hat{\epsilon}_2 \perp \hat{\epsilon}_1$	τ_2 (ns)	2.2	2.1	2.1
	f	7.0	8.7	7.3

Figure Captions

1. Time-resolved and polarization-analyzed fluorescence for 0_0^0 excitation and detection of jet-cooled *t*-stilbene. The orientation of the detection polarization relative to that of excitation is indicated for each decay. Detection bandwidth ($\Delta\bar{\nu}$): 12 cm^{-1}. Measured response: 40 ps FWHM. Supersonic beam conditions for these and following measurements (unless otherwise noted): 6 atmospheres Ne, nozzle aperture diameter (D) $\simeq$ 65 μ, laser to nozzle distance (X) = 3 mm, reservoir temperature (T) $\simeq$ 160 C.

2. Numerically simulated time-resolved and polarization-analyzed fluorescence accounting for purely rotational coherence. The following parameters were used in the rotational coherence calculation. Transition dipole moment directions: ($\|,\|$); ground state rotational temperature (T_{ROT}): 2 K; rotational constants: $A' = 2.675$ GHz, $B' = 0.240$ GHz, $C' = 0.273$ GHz. A single exponential population decay of lifetime 2.7 ns is assumed. The calculated intensity has been convoluted with a measured temporal system response of 50 ps FWHM.

3. Experimental polarization-analyzed fluorescence decay for 0_0^0 excitation and detection of jet-cooled *t*-stilbene. Excitation and detection polarization vectors are parallel in this and following figures when not explicitly indicated. The results of several separate experimental runs have been aligned and added together to produce this decay. Detection bandwidths: < 4 cm^{-1}. The last 4.5 ns of the data have been expanded in the inset with vertical solid and dashed lines indicating the expected positions of in-phase and out-of-phase recurrences, respectively.

4. Backing pressure dependence of jet-cooled *t*-stilbene polarization-analyzed fluorescence decays. The carrier gas is neon at the pressures indicated. All other conditions are as for Fig. 1.

5. Simulated time-resolved and polarization-analyzed fluorescence accounting for purely rotational coherence: temperature dependence. The value of

T_{ROT} used in the calculation is indicated. All other parameters are as given in the caption of Fig. 2.

6. Polarization-analyzed fluorescence decays for 0^0_0 excitation of jet-cooled *t*-stilbene. Shifts from the excitation energy of the centers of spectral detection ($\bar{\nu}_d$) are given in the figure. $\Delta\bar{\nu}$: (from left to right) 4 cm^{-1}, 3 cm^{-1}, 64 cm^{-1}. A single fluorescence collection lens was used for the -1650 cm^{-1} decay.
7. Fluorescence polarization anisotropies formed from the decays of Fig. 1 (bottom) and Fig. 2 (top). The normalization of the experimental decays for the calculation of $R(t)$ for this figure was chosen to give a 'residual' $R(t)$ value of 0.075 to match that of the simulation.
8. Fit of the experimentally measured first out-of-phase and first in-phase recurrences of *t*-stilbene PRC using an a axis transition dipole ($\theta = 0°$). An instrument response of 52 ps FWHM was measured with the data and used in the fit. The rotational constants found are given in the text and are not compatible with any reasonable *t*-stilbene structure. The weighted residual is plotted above the data.
9. The structure of *t*-stilbene in S_1 based on calculations of Ref. 9. See text for details. The in-plane inertial axes are shown.
10. An example of the use of an off-axis dipole to simulate *t*-stilbene PRC. The angle θ is the angle between the dipole and the a axis, with the dipole remaining in the molecular plane. The rotational constants are those of the structure in Fig. 9 (adjusted slightly to give $B' + C' = 0.5132$ GHz). The weighted residual is plotted above the data.
11. Proposed vibrationally-averaged structure of *t*-stilbene–Ar$_1$ in S_1. The position of the argon atom is based on PRC measurements and an assumed height above the stilbene molecular plane of 3.42Å. The stilbene structure is that of Fig. 9.
12. Potential energy of the stilbene–Ar$_1$ van der Waals bond as a function

of the projection of the argon atom in the stilbene plane. The energies are minimized with respect to the height of the argon above the plane. Potential parameters of Ref. 24, given in Table II of Chapter 4, are used in the calculation. Minima in the potential are located above points A and B.

13. Cross-sections of the potential surface of Fig. 12 running parallel to the *a* axis of stilbene and passing through the two potential minima. The dotted line indicates an energy of 30 cm^{-1} above the deepest minimum. The carets on the horizontal axis mark the positions of the phenyl ring centers.
14. Cross-sections of a stilbene–Ar_1 potential energy surface calculated using different potential parameters for the ethylene carbons and ring carbons. These parameters are described in Chapter 4 and given in Table II of that chapter. The cross-sections are taken in the same direction and positions relative to the stilbene molecule as those of Fig. 13, though in this case there is only one set of equivalent minima. Again, the dotted line indicates an energy of 30 cm^{-1} above the potential minimum, and the carets on the horizontal axis mark the positions of the phenyl ring centers.
15. Temperature dependence of the first positive recurrence of fluorene–Ar_1 parallel fluorescence. Experimental data (circles) are compared with two simulations of different widths. The simulations are for a spherical top, $B' = 0.4393$ GHZ, at $T = 1$ K and $T = 5$ K. The vertical scales differ for the three sets of data.
16. Dependence of fluorene–Ar_1 PRC on asymmetry. One set of experimental data is compared with three simulations. The vertical scale is graduated in units of percent mo modulation relative to the baseline intensity. For all simulations $T = 3$ K, $A' = 0.8097$ GHz. Top: $B' = 0.4531$ GHz, $C' = 0.4234$ GHz. Middle: $B' = 0.4700$ GHz, $C' = 0.4065$ GHz. Bottom: $B' = 0.4865$ GHz, $C' = 0.3900$ GHz. The asymmetry parameter *b* is given in the figure for each simulation.
17. Comparison of a fluorene–Ar_1 parallel fluorescence measurement with its

best-fit PRC simulation (solid line). The data are the same as in Fig. 16. The simulation parameters are given in the text.

18. Experimental $R(t)$ of anthracene fluorescence for S_1 0^0_0 excitation and detection. The vertical error bar corresponds to roughly one standard deviation of the data values. The measured instrument response was 68 ps FWHM.

19. Simulated $R(t)$ for an "anthracene-like" symmetric top. $A' = 2.2027$ GHz, $B' = 0.4098$ GHz, $T = 1.6$ K.

20. Simulated asymmetric top $R(t)$ using the parameters yielding a best fit to the experimental anthracene $R(t)$ of Fig. 18. The rotational constants are given in Table III, and the temperature is 1.6 K.

21. Detailed comparison of data from Fig. 18 (dashed line and circles) and simulation from Fig. 20 (solid line) over a restricted time range.

22. Variation of the reduced chi-square statistic as a function of fit parameters for the anthracene PRC fit. For the plot labeled 1, the rotational constants are varied simultaneously, maintaining fixed ratios. For each of the three remaining plots, a single rotational constant is varied. These are B' in 2, A' in 3, and C' in 4. The dotted line represents the 90% confidence limit on the value of χ^2 for a chi-square distribution with 337 degrees of freedom.

23. Polarization-analyzed fluorescence decays of jet-cooled *t*-stilbene. Excitation energies above the S_1 origin are indicated. Detection energy shifts from the excitation ($\bar{\nu}_{\mathrm{d}}$) and detection bandwidths ($\Delta\bar{\nu}$) : (from left to right) -278 cm^{-1} and 24 cm^{-1}, -260 cm^{-1} and 9 cm^{-1}, -620 cm^{-1} and 3 cm^{-1}. Approximate backing pressures of helium: (from left to right) 38 atm., 22 atm., and 30 atm. For all three: D = 25 μ, X = 1.5 mm and T $\simeq$ 170 C.

24. Polarization-analyzed fluorescence decays for S_1+789 cm^{-1} excitation of jet-cooled *t*-stilbene. $\bar{\nu}_{\mathrm{d}} = -610$ cm^{-1}, $\Delta\bar{\nu} = 12$ cm^{-1}. Manifestations of both vibrational and rotational coherence are present.

25. Polarization-analyzed fluorescence decays for S_1+1249 cm^{-1} excitation of

jet-cooled *t*-stilbene. $\bar{\nu}_d = -205$ cm^{-1}, $\Delta\bar{\nu} = 32$ cm^{-1}. The -205 cm^{-1} band is isolated and spectrally resolved at this bandwidth (Ref. 39).

26. Polarization-analyzed fluorescence decays for S_1+1249 cm^{-1} excitation of jet-cooled *t*-stilbene. $\bar{\nu}_d = -1640$ cm^{-1}, $\Delta\bar{\nu} = 24$ cm^{-1}. Fluorescence in this spectral region is totally unresolved (Ref. 39).

27. Polarization-analyzed fluorescence decays for S_1+1792 cm^{-1} excitation of jet-cooled anthracene. $\bar{\nu}_d = -390$ cm^{-1}, $\Delta\bar{\nu} = 160$ cm^{-1}, X = 2 mm, T = 175 C. The detected band is spectrally resolved at this bandwidth (Ref. 40).

28. Experimental fluorescence polarization anisotropies for 0^0_0 excitation (lower) and 83 cm^{-1} excitation (upper) of jet-cooled *t*-stilbene. For the origin measurement: $\bar{\nu}_d = 0$ cm^{-1}, $\Delta\bar{\nu} = 2$ cm^{-1}. Conditions for the 83 cm^{-1} measurement are as given for the leftmost decay of Fig. 23. Response widths were in each case 60 ps FWHM.

29. Comparison of experimental and simulated fluorescence polarization anisotropies for S_1+789 cm^{-1} excitation of jet-cooled *t*-stilbene. The lower $R(t)$ was formed from the decays of Fig. 24; the upper from parallel and perpendicular fluorescence simulations, the first of which is shown in the figure. Simulation parameters for the calculation of purely rotational coherence $(C_\alpha(t))$ are as given in the caption of Fig. 2. The assumed vibrational envelope is given by $V(t) = [1+0.6\exp(-t/2.9\text{ns})\cos(2\pi t/0.79\text{ns})]\exp(-t/2.7\text{ns})$.

30. Experimental fluorescence polarization anisotropies for 0^0_0 excitation (lower) and 1249 cm^{-1} excitation (upper) of jet-cooled *t*-stilbene. The lower trace is a more detailed view of the lower $R(t)$ of Fig. 28. The 1249 cm^{-1} $R(t)$ was formed from the decays of Fig. 26. Response widths were in each case $\simeq$ 60 ps FWHM.

31. Polarization-analyzed fluorescence decay for S_1+1249 cm^{-1} excitation: magic angle detection. $\bar{\nu}_d = -205$ cm^{-1}, $\Delta\bar{\nu} = 32$ cm^{-1}. The solid trace is the best fit biexponential accounting for convolution with a measured response of 55 ps FWHM.

32. Simulated time-resolved and polarization-analyzed fluorescence accounting for purely rotational coherence. Parameters for $C_\alpha(t)$ are as for Fig. 2. $V(t)$ is given in the figure. Calculated intensities are convoluted with a 55 ps response.

33. Comparison of experimental and simulated fluorescence polarization anisotropies for S_1+1249 cm^{-1} excitation of jet-cooled *t*-stilbene. The experimental $R(t)$ was formed from the decays of Fig. 25; the simulated $R(t)$ from those of Fig. 32.

34. Simulated fluorescence polarization anisotropies showing the dependence on $V(t)$. The upper trace is an expanded view of the simulated $R(t)$ of Fig. 33. $V(t)$ used in the calculation of each $R(t)$ is indicated. Other aspects of the two calculations were identical.

35. Simulated time-resolved and polarization-analyzed fluorescence accounting for purely rotational coherence. The following parameters were used in the calculation of $C_\alpha(t)$. Transition dipole moment directions: $(\perp_B,\perp_B)$; T_{ROT}: 2 K; rotational constants: $A' = 2.134$ GHz, $B' = 0.446$ GHz, $C' = 0.371$ GHz. $V(t)$ is given in the figure, and approximates the decays of Fig. 27 for 1789 cm^{-1} excitation of anthracene. Calculated intensities are convoluted with a 57 ps response.

36. Time- and frequency-resolved spectra of stilbene and stilbene-He$_1$ complex. Excitation energies relative to the respective (complex or parent molecule) 0_0^0 transition energies are given at left. Excitation frequencies are marked by an asterisk in the upper spectra. Spectral resolutions for (A), (B), and (C) are 4, 1, and 5 cm^{-1}, respectively. The time-resolved data is presented in the form of polarization anisotropies. Temporal resolution was about 60 ps FWHM for all measurements. $\bar{B}$ is $\frac{1}{2}(B' + C')$ of the complex or parent stilbene. Typical beam conditions are 500 psig for the complex, $X/D \sim 60$, and sample reservoir temperature ~ 150°C. [Reprinted from J. S. Baskin, D. Semmes, and A. H. Zewail, J. Chem. Phys. **85**, 7488 (1986).]

37. Assumed equilibrium geometry of stilbene–helium in stilbene principal axis frame.

38. Classical polarization anisotopies of stilbene calculated for discretely distributed j and correct quantum mechanical frequencies. Stilbene is approximated as a symmetric top with $B' = .2566$, $A' = 2.6$. All three signals are calculated for an initial rotational temperature of 2.5 K and account for convolution with a system response of 60 ps FWHM. The full range of the vertical scale is in each case 0 to 0.174. In b), stilbene is dirctly excited ($\equiv$ PRC). In a) and c), stilbene is the product of dissociation of stilbene–helium. The dissociation impulse is normal to the stilbene plane in both cases. In a), the complex is fixed at the equilibium structure of Fig. 37. In c), the signal is averaged over a broad perpendicular bending trajectory as described in the text.

Figure 1

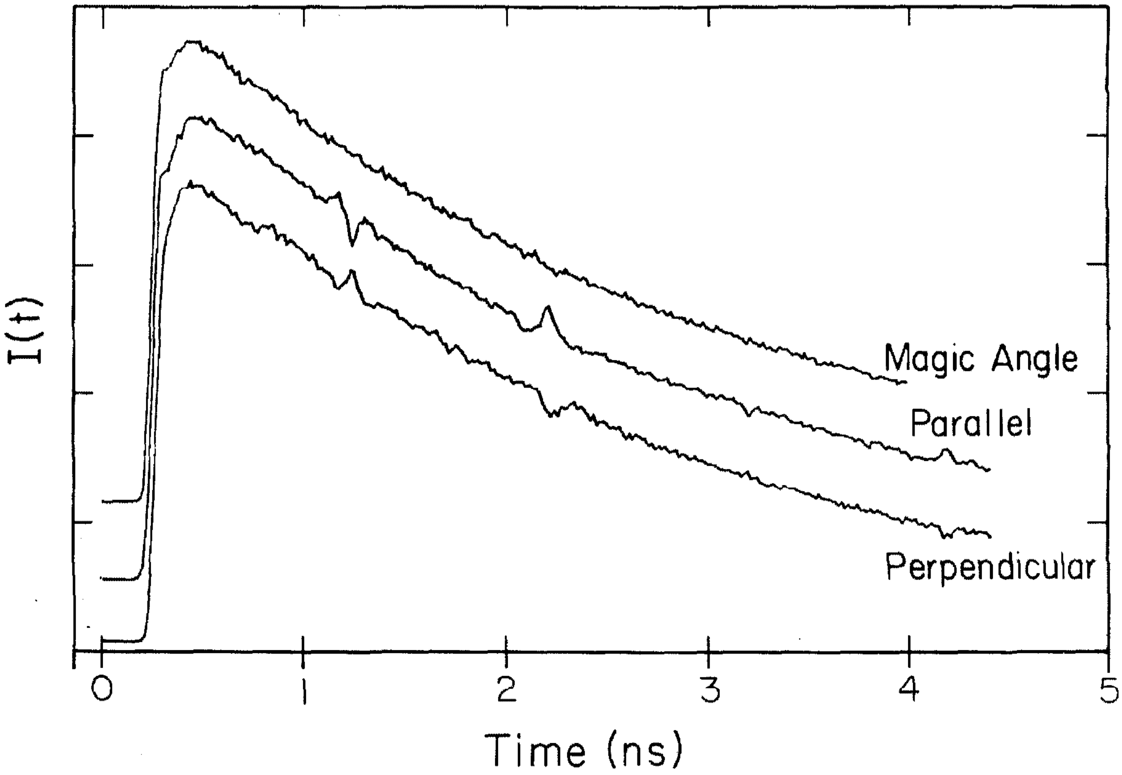

Figure 2

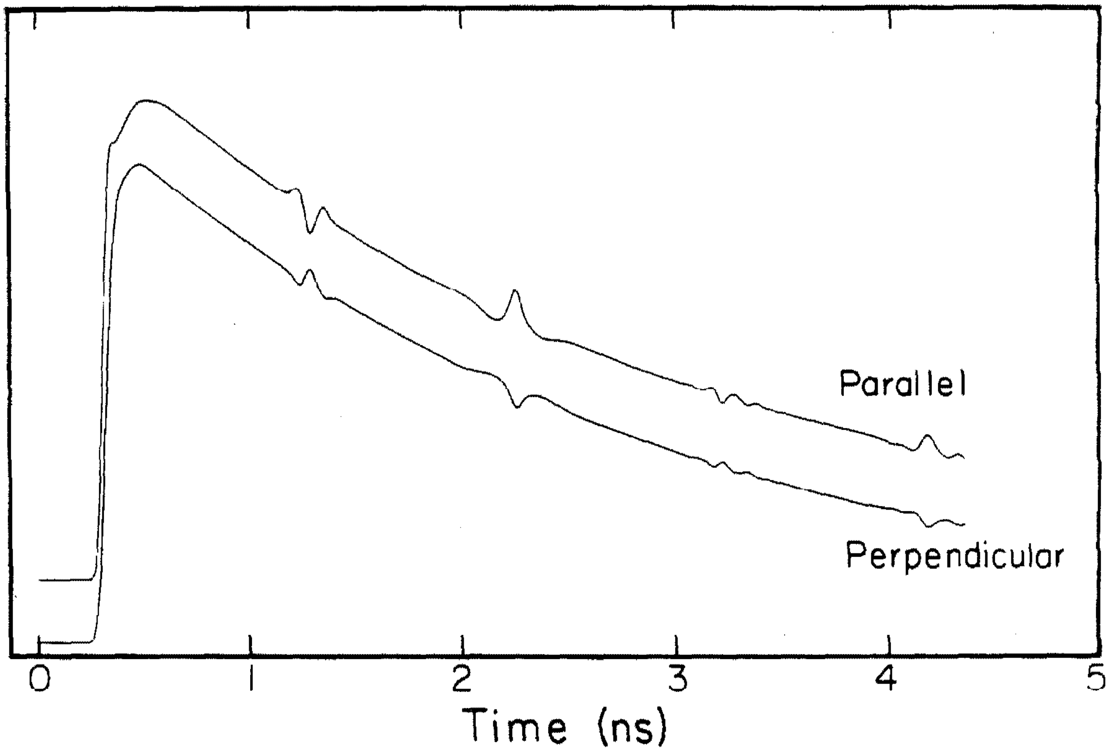

Figure 3

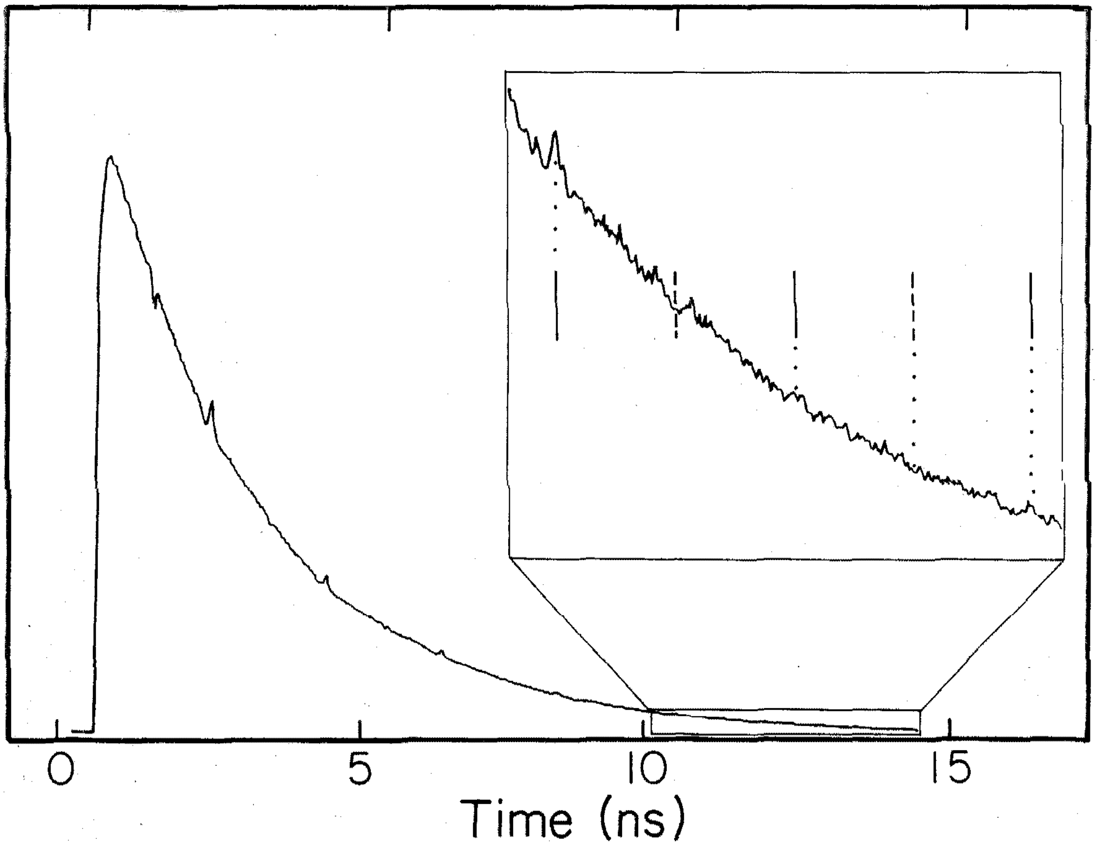

Figure 4

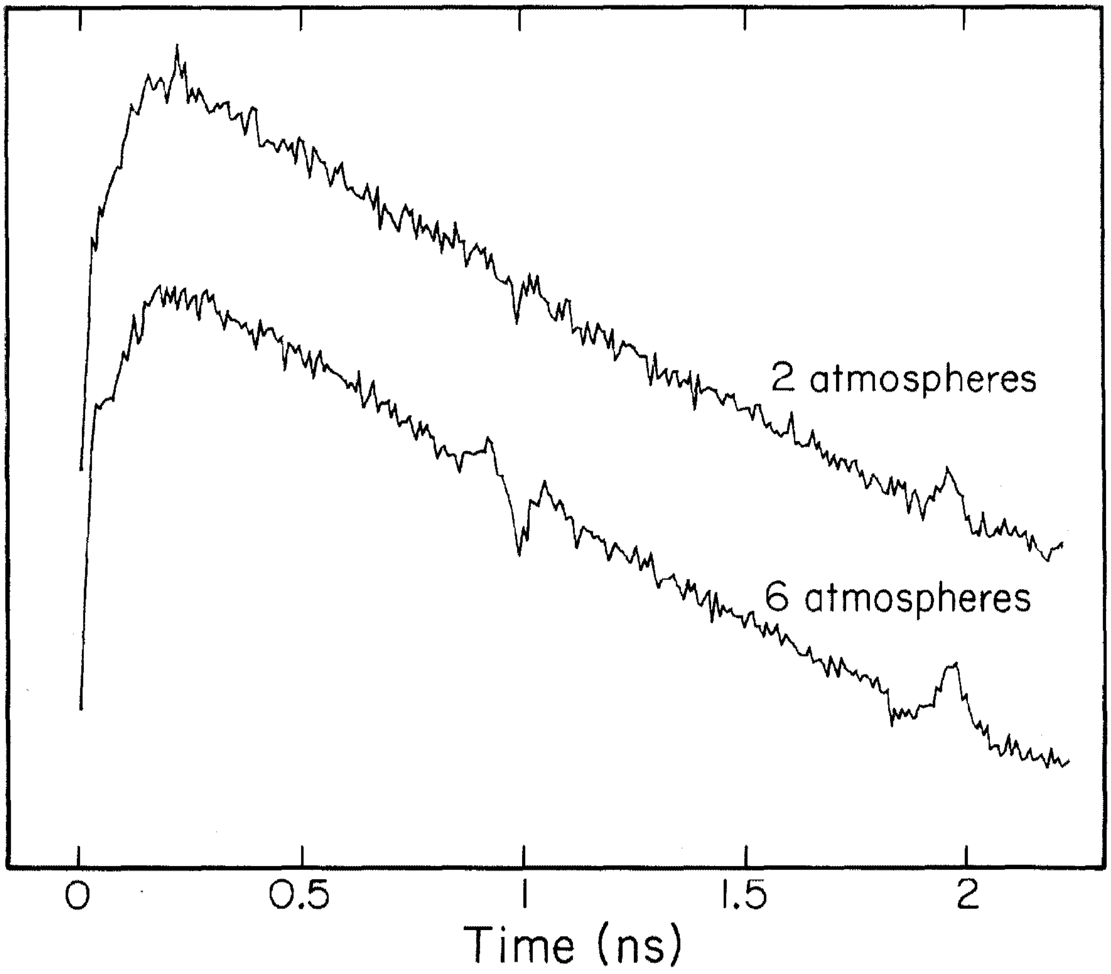

Figure 5

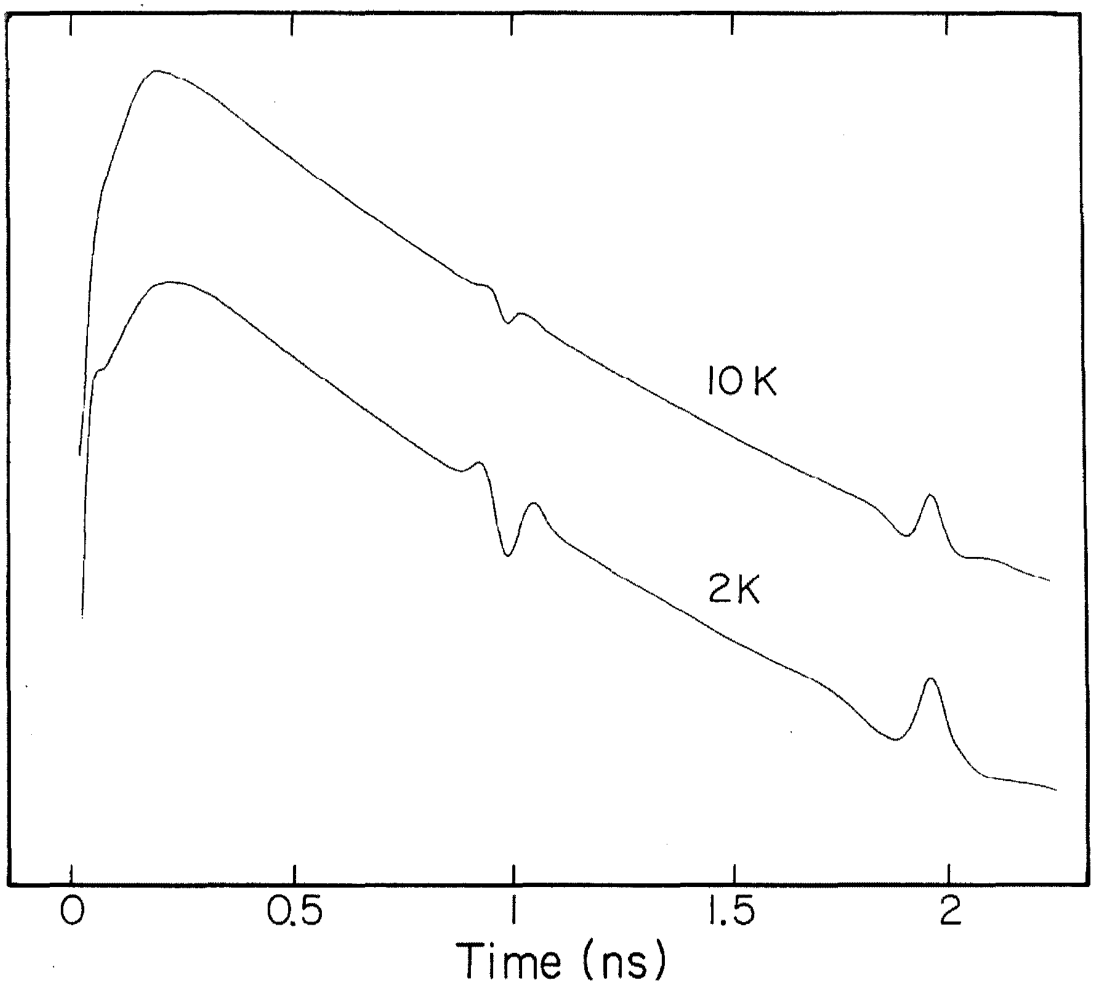

Figure 6

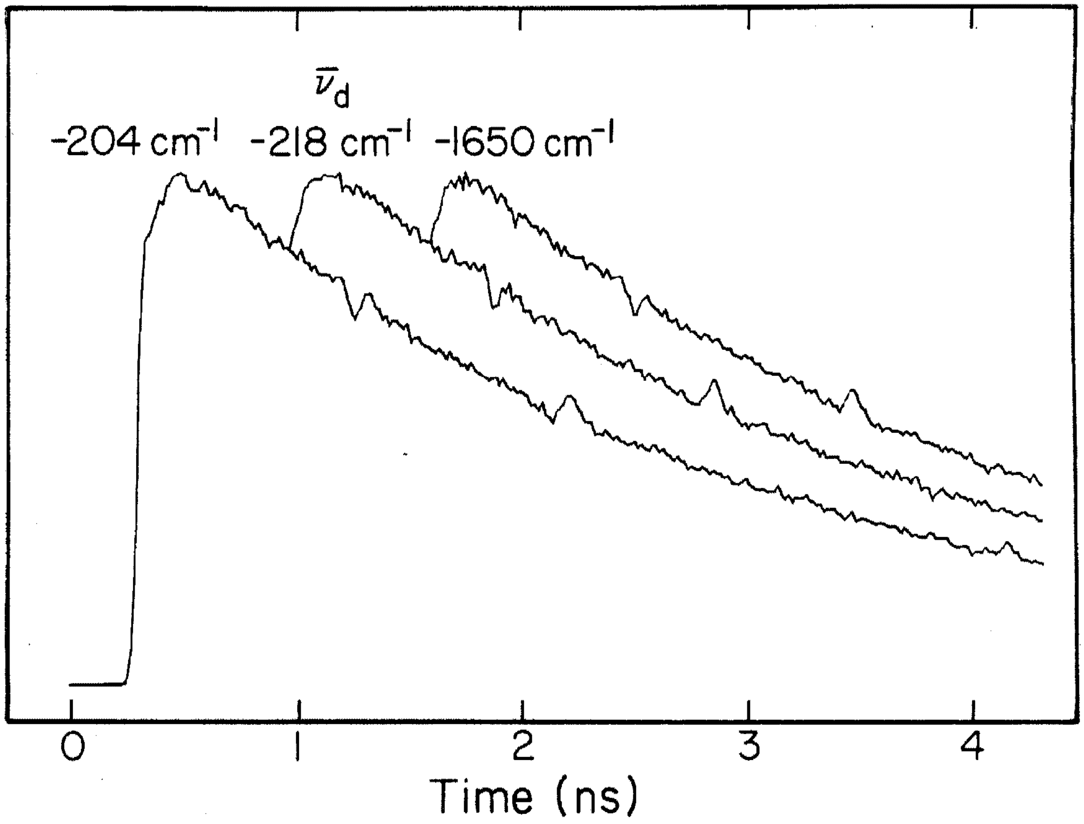

Figure 7

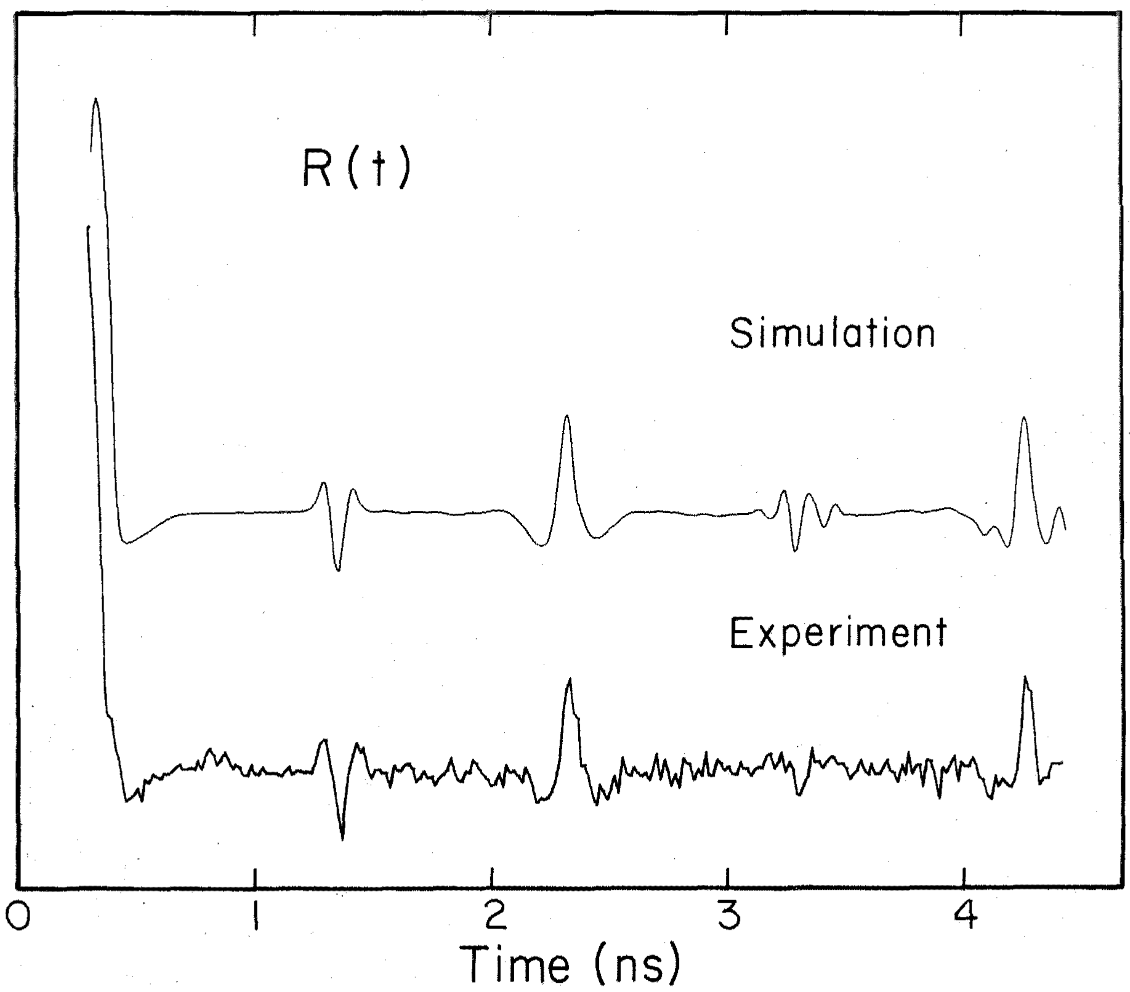

Figure 8

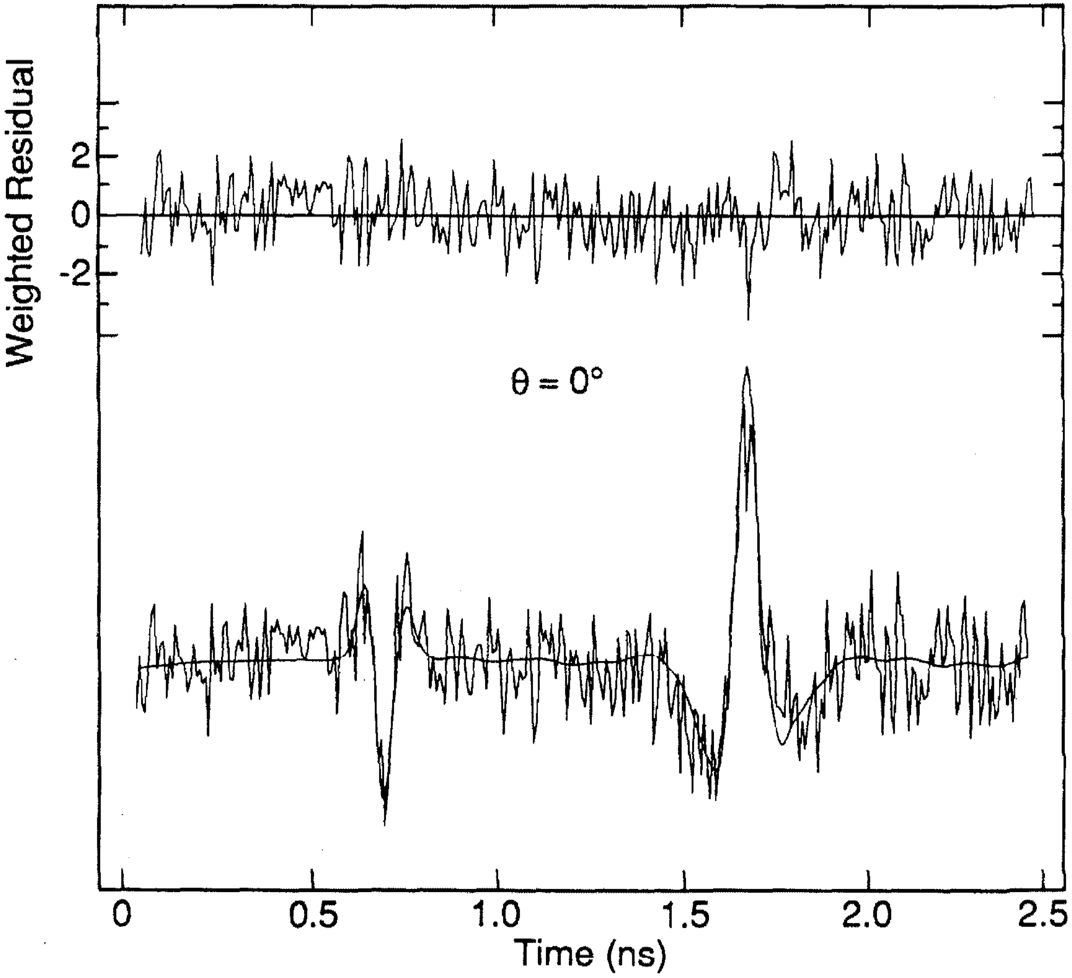

Figure 9

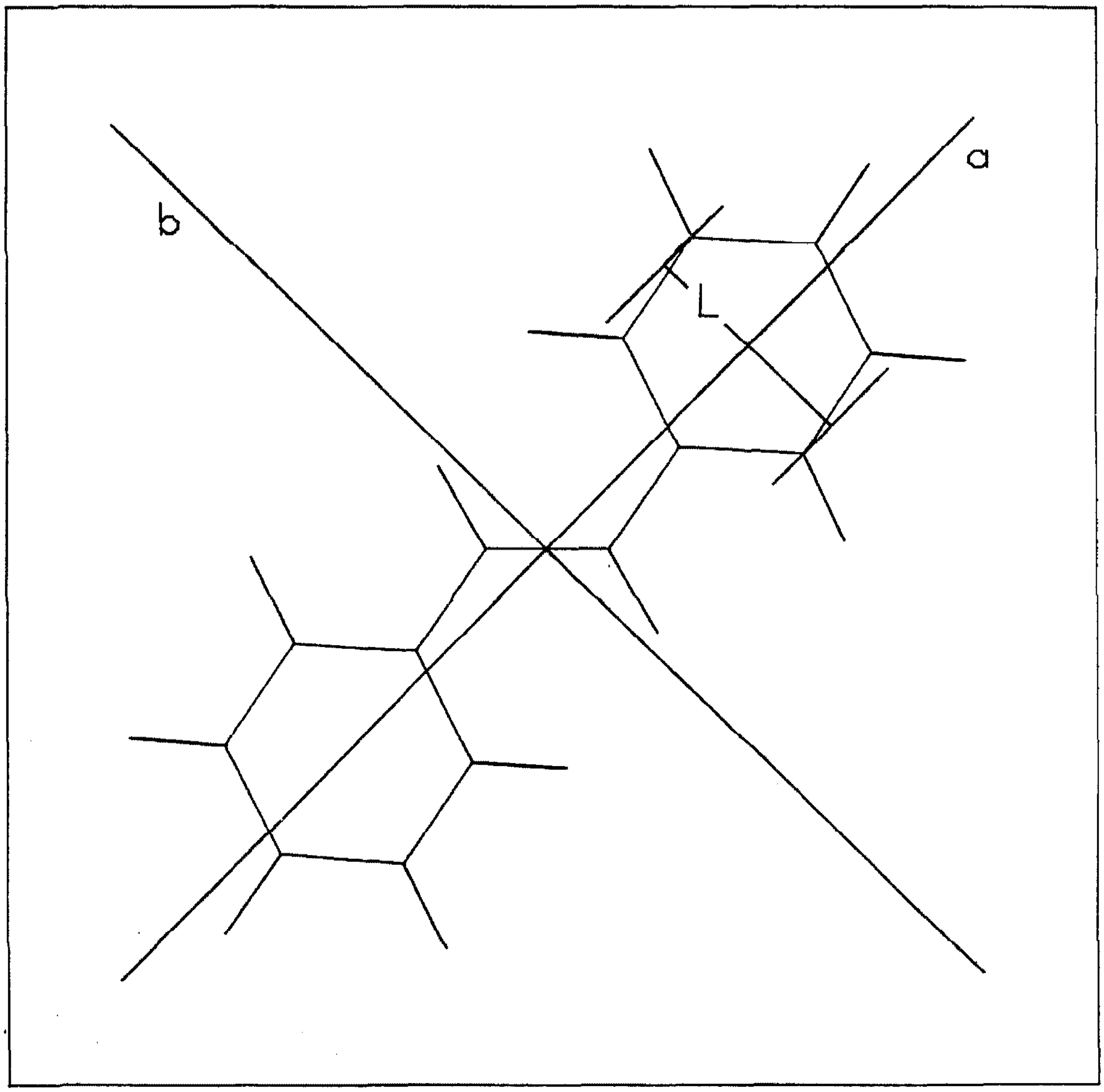

Figure 10

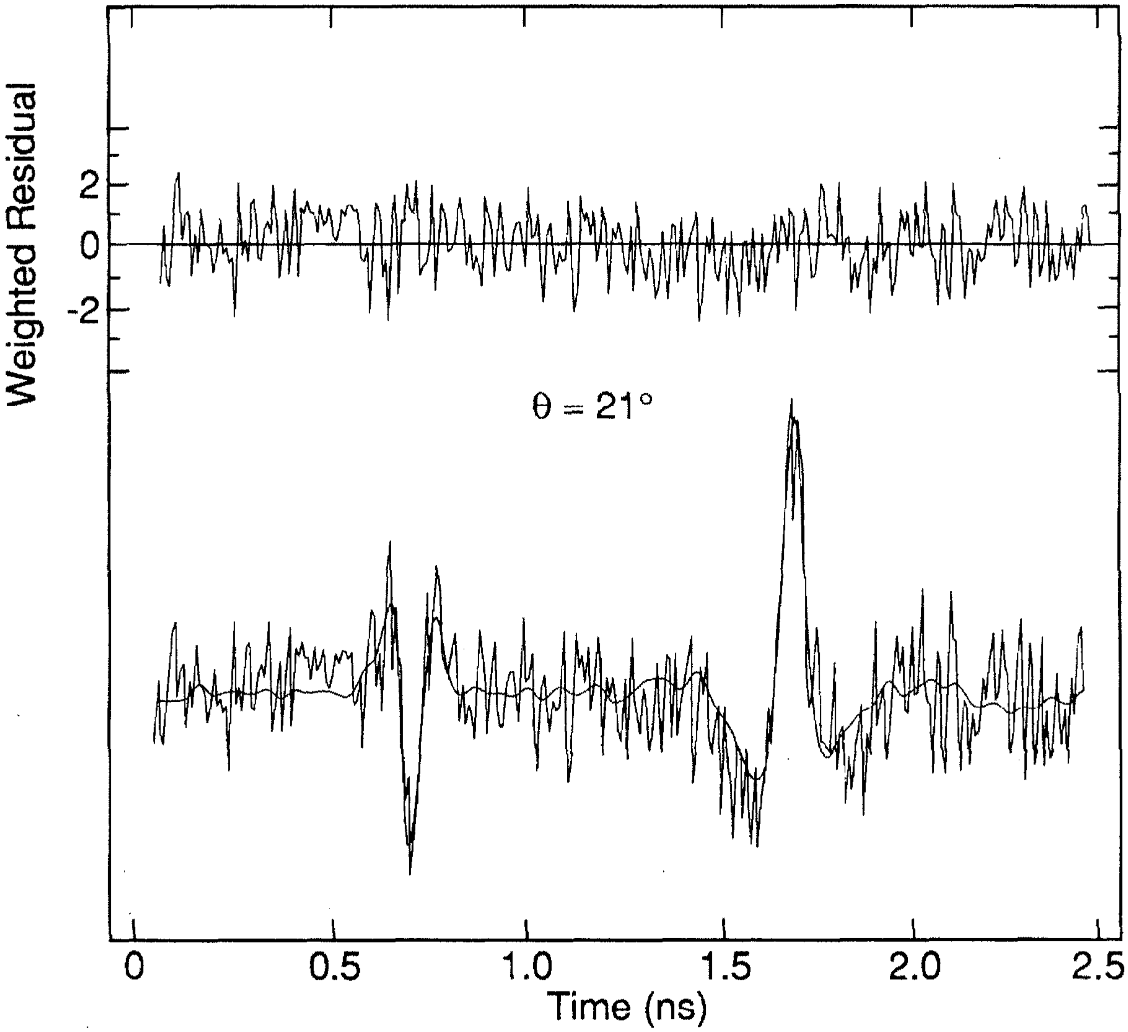

Figure 11

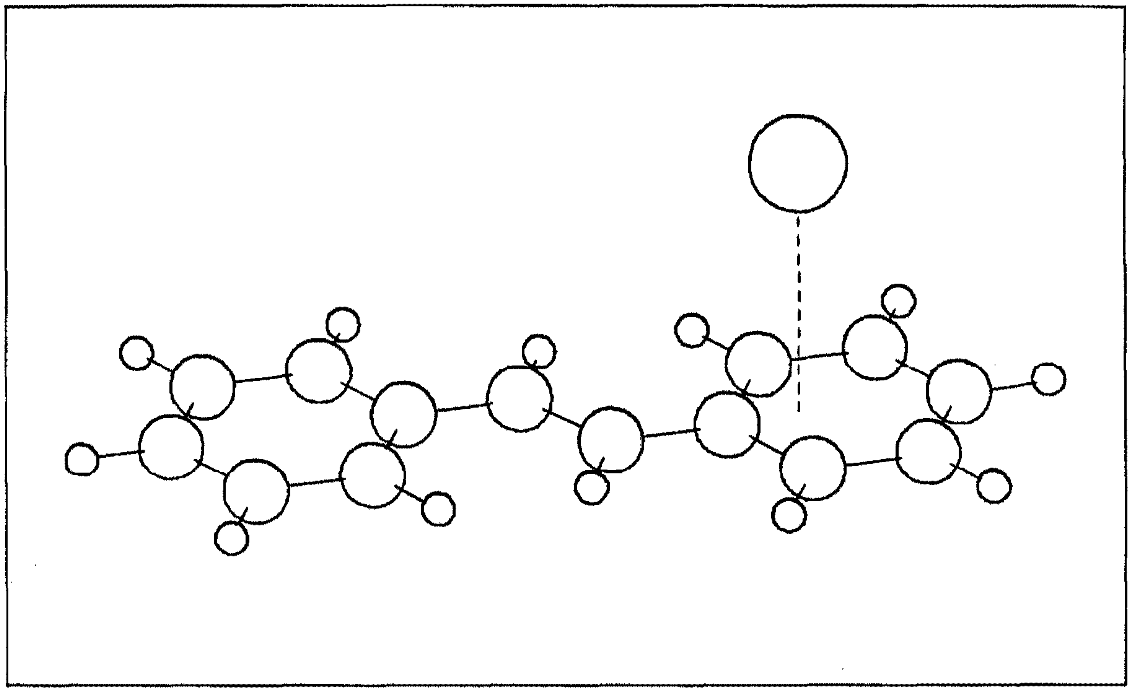

Figure 12

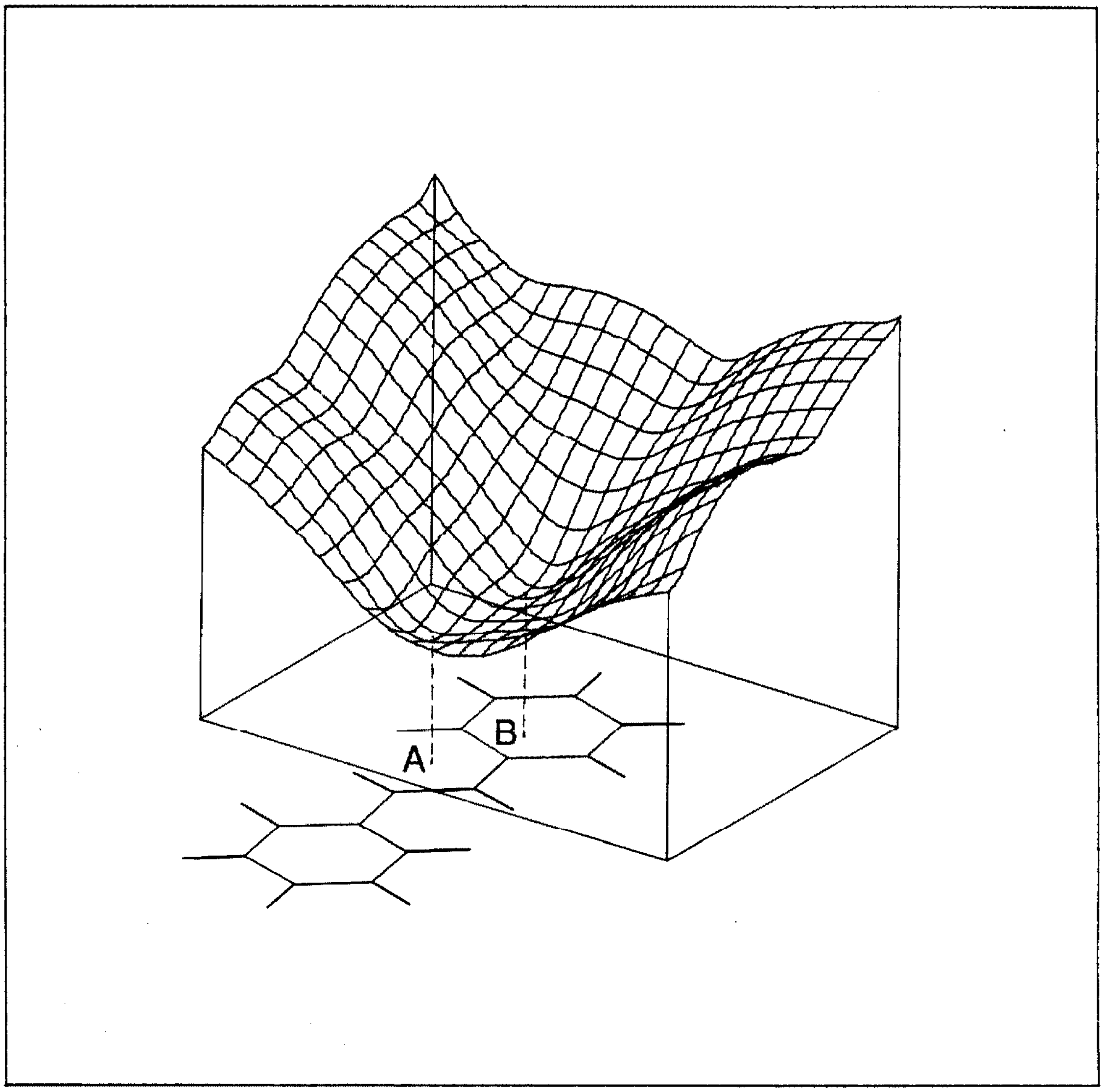

Figure 13

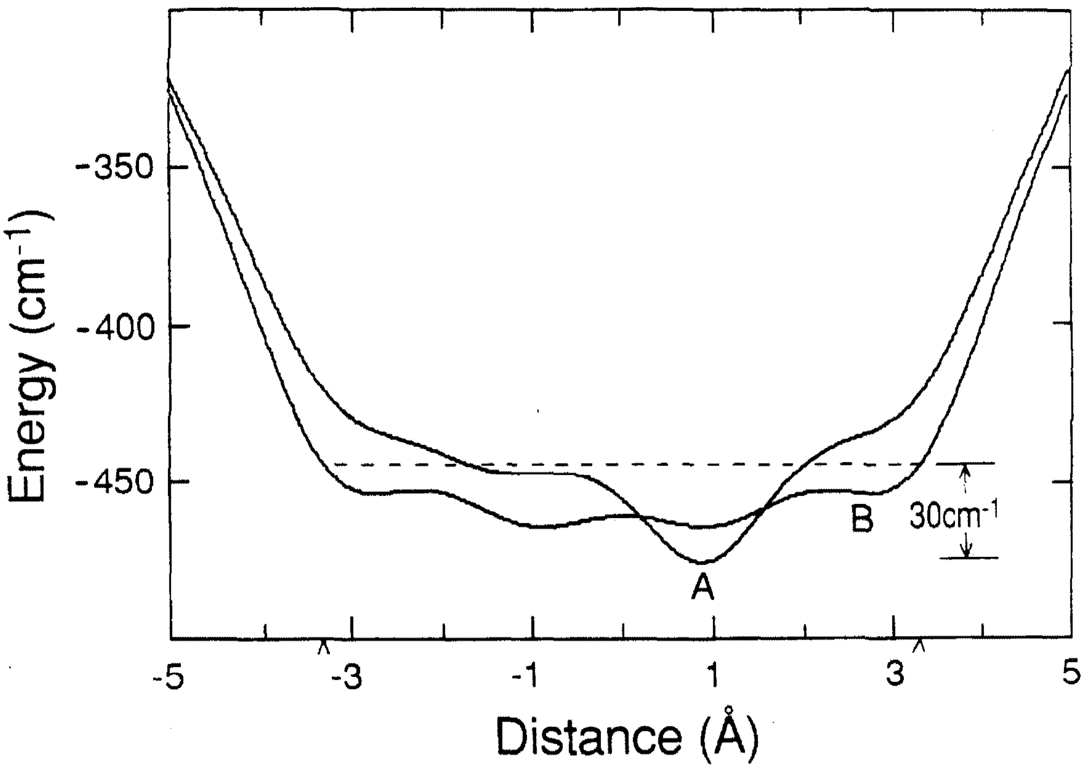

Figure 14

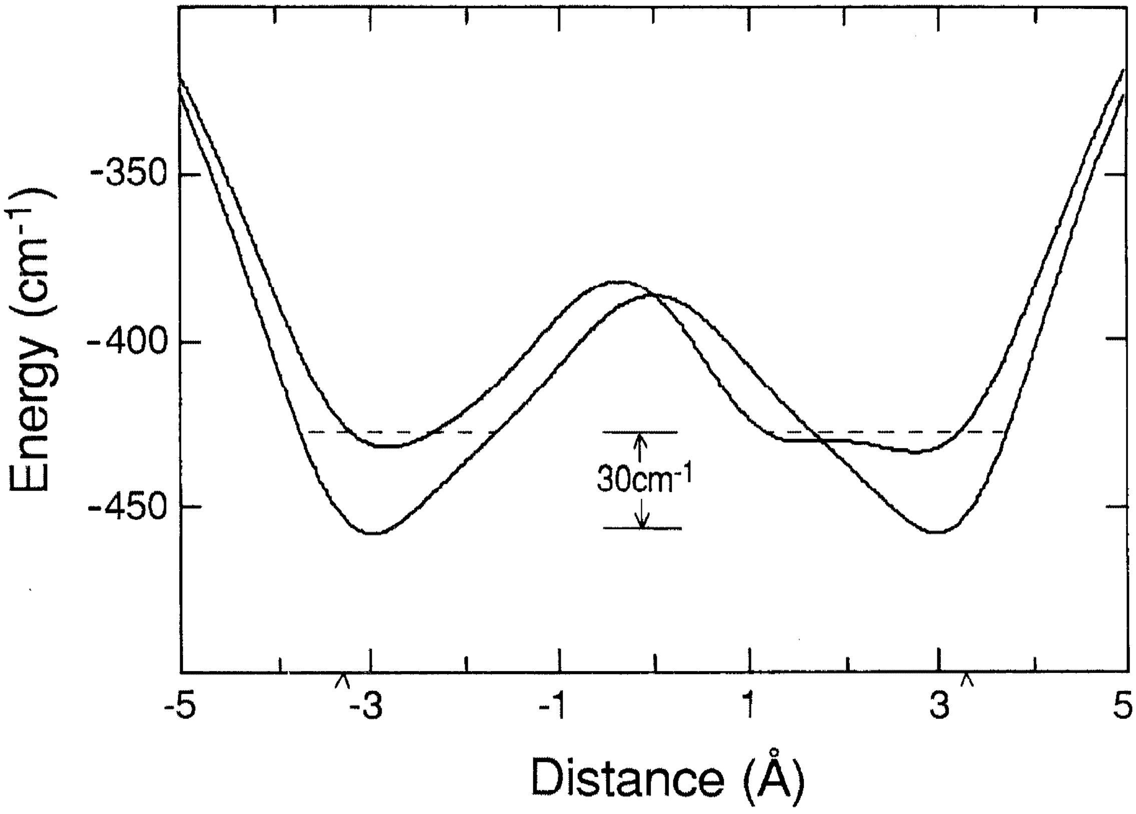

Figure 15

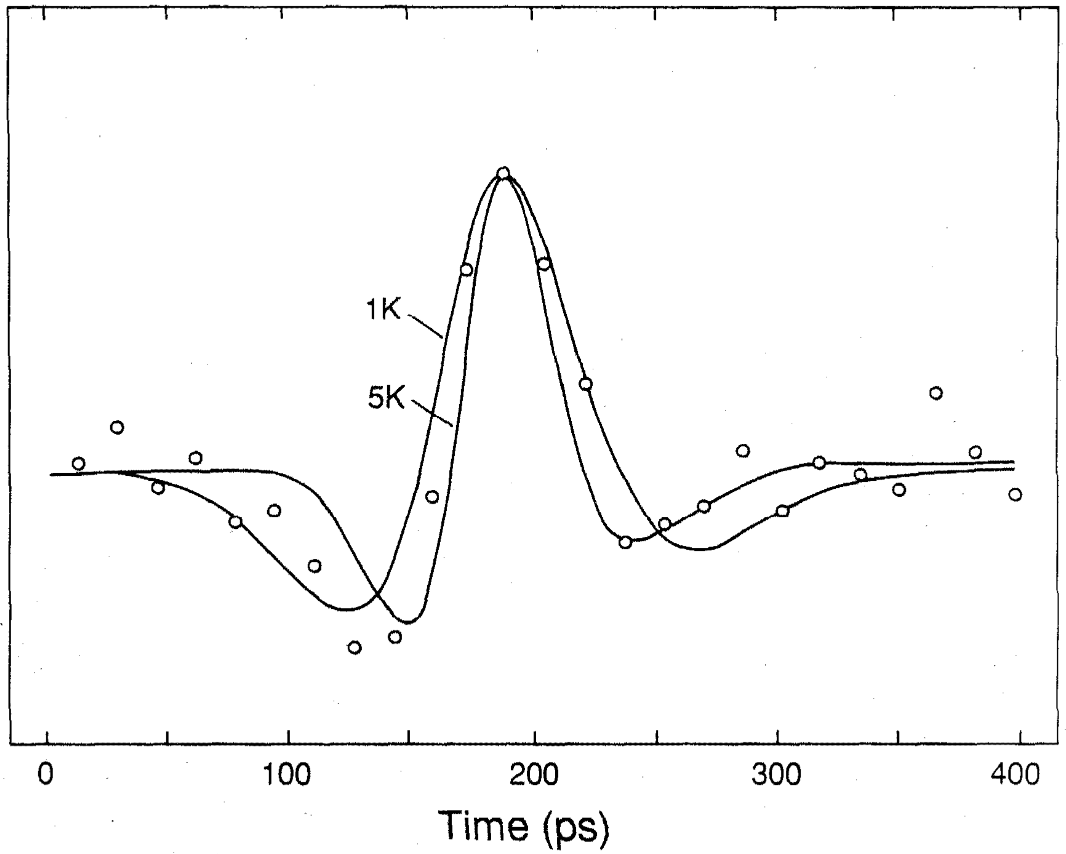

Figure 16

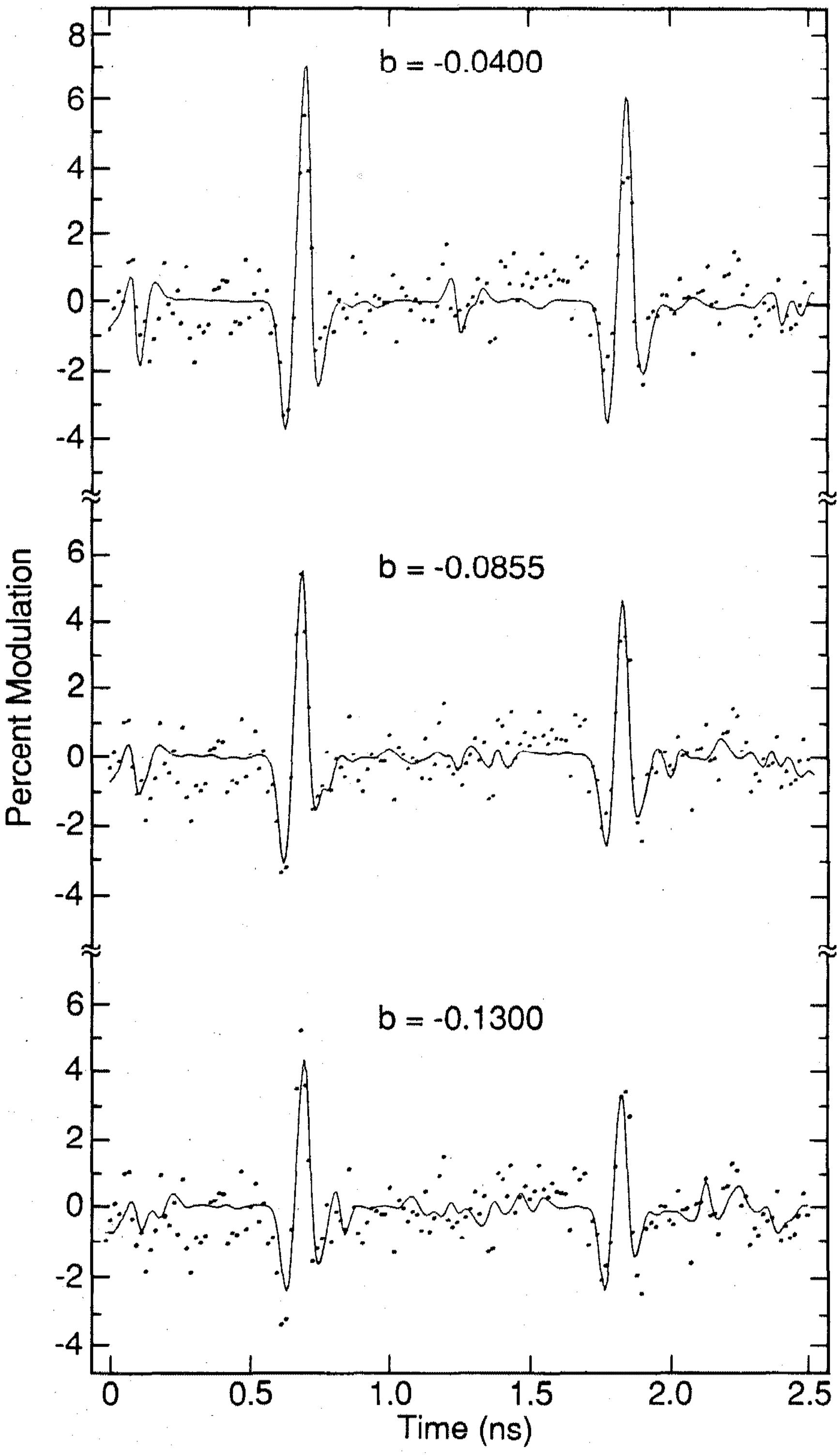
b = -0.0400
b = -0.0855
b = -0.1300
Percent Modulation
Time (ns)
8
6
4
2
0
-2
-4
6
4
2
0
-2
-4
6
4
2
0
-2
-4
0
0.5
1.0
1.5
2.0
2.5

Figure 17

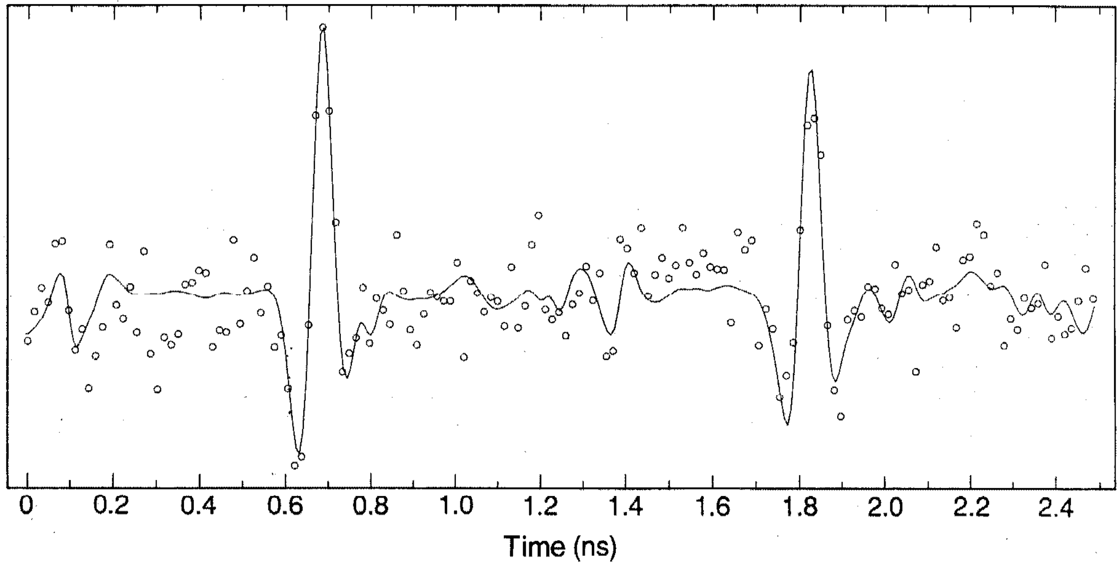

Figure 18

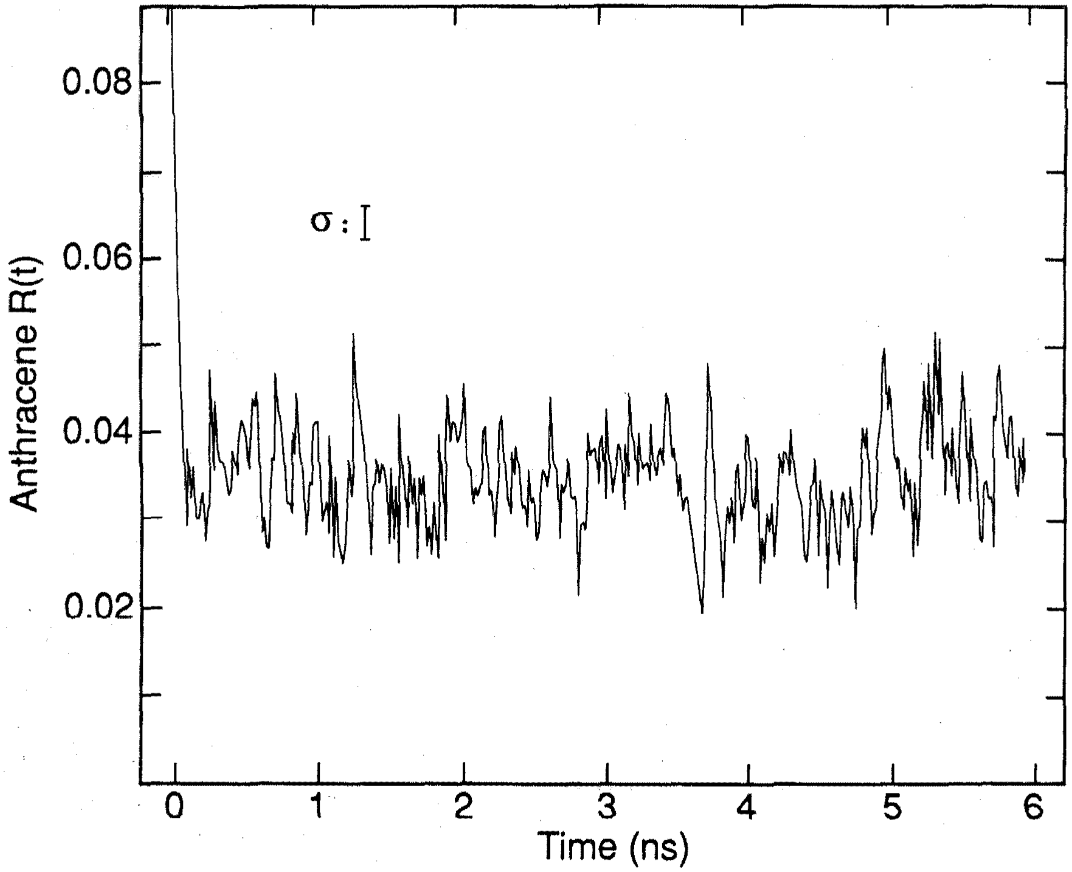

Figure 19

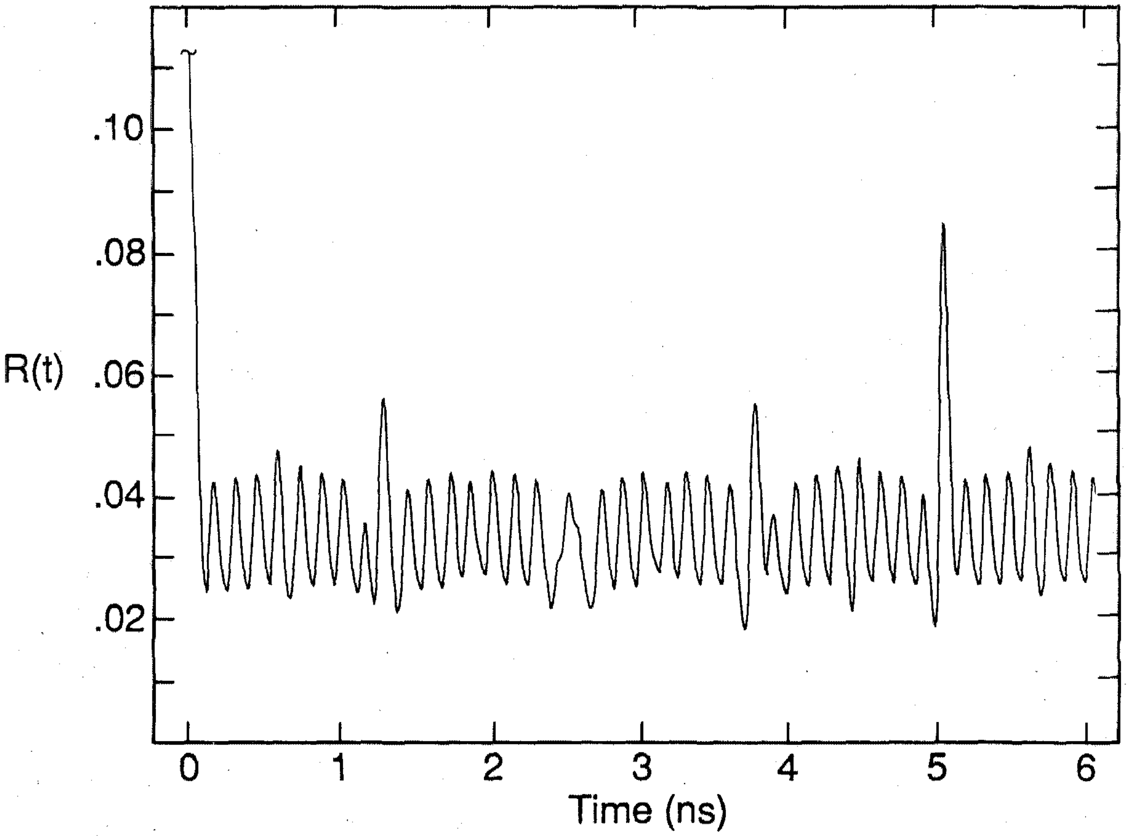

Figure 20

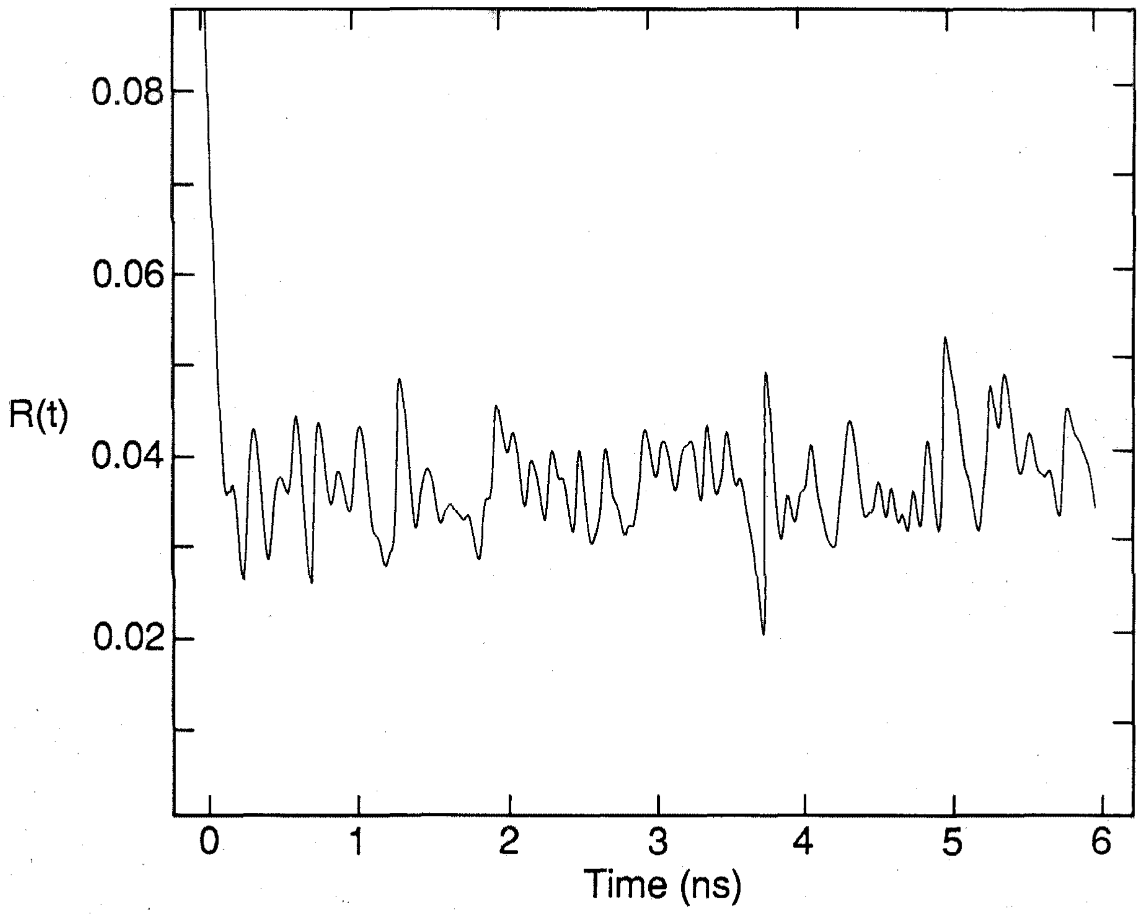

Figure 21

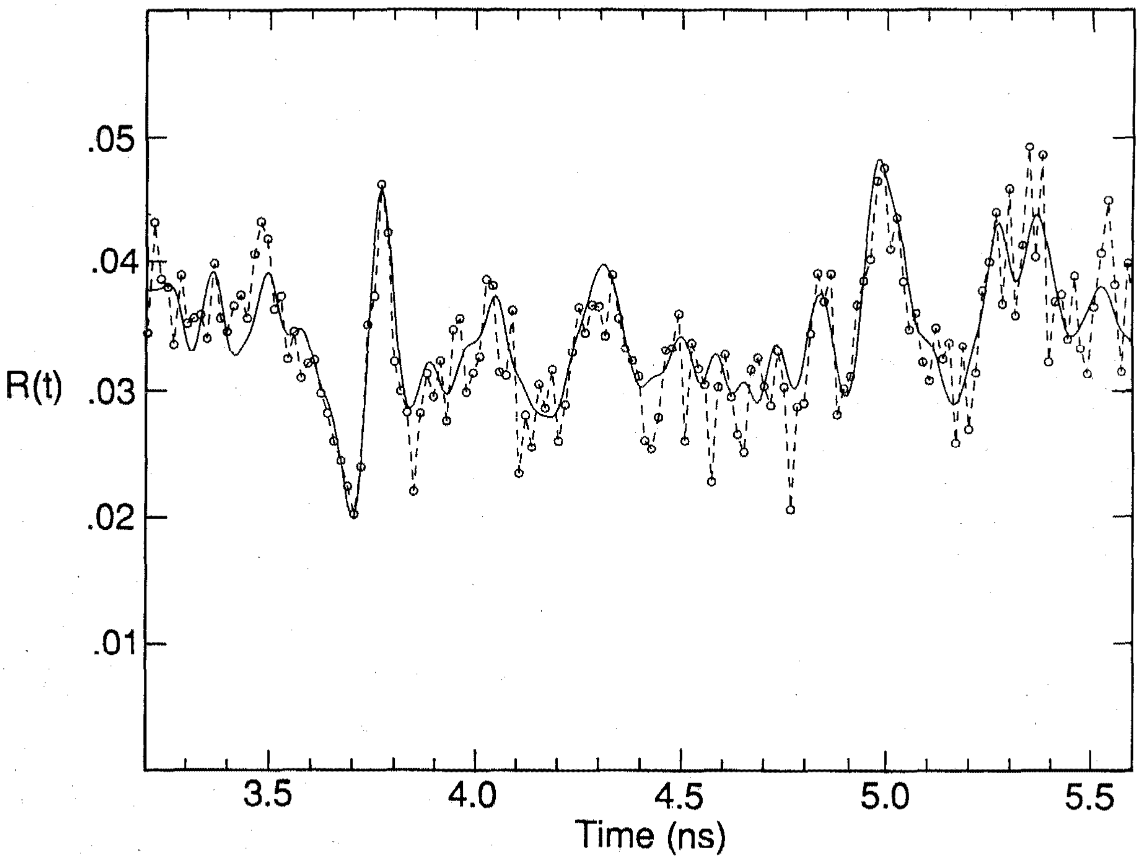

Figure 22

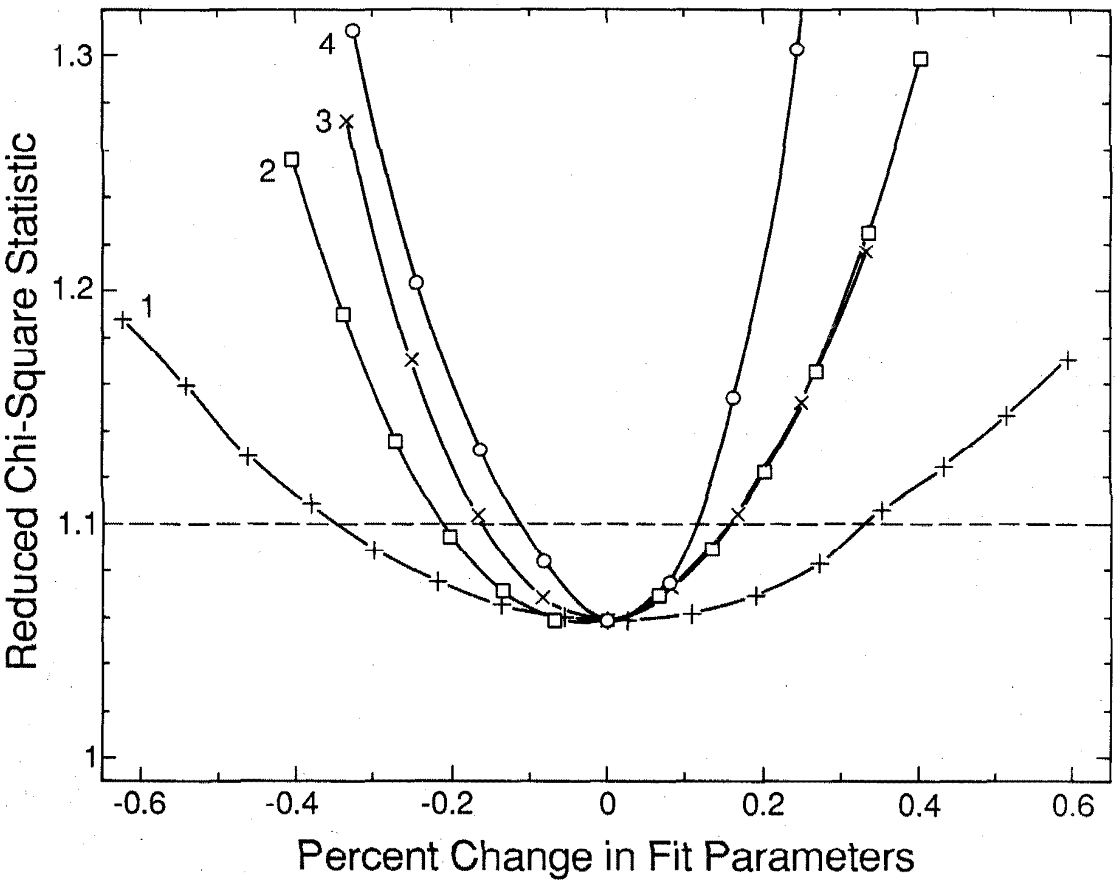
4
3
2
1
1.3
1.2
1.1
1
-0.6
-0.4
-0.2
0
0.2
0.4
0.6
Reduced Chi-Square Statistic
Percent Change in Fit Parameters

Figure 23

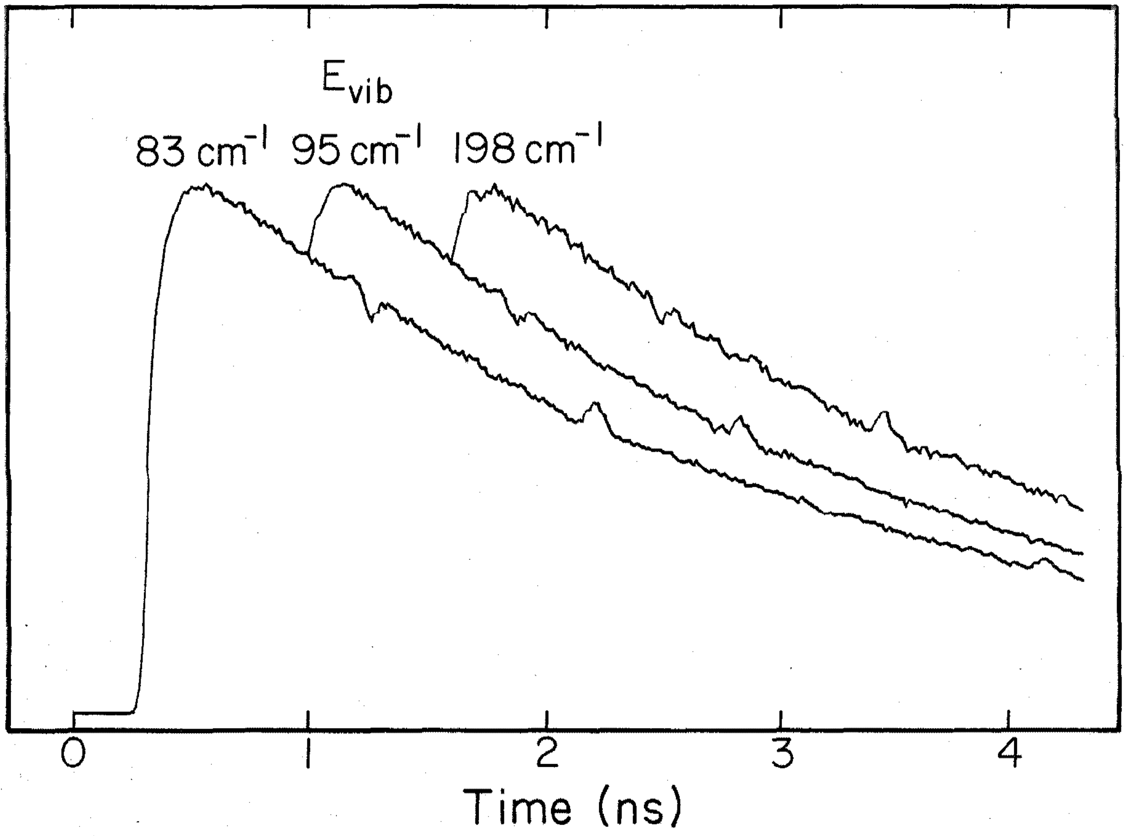

Figure 24

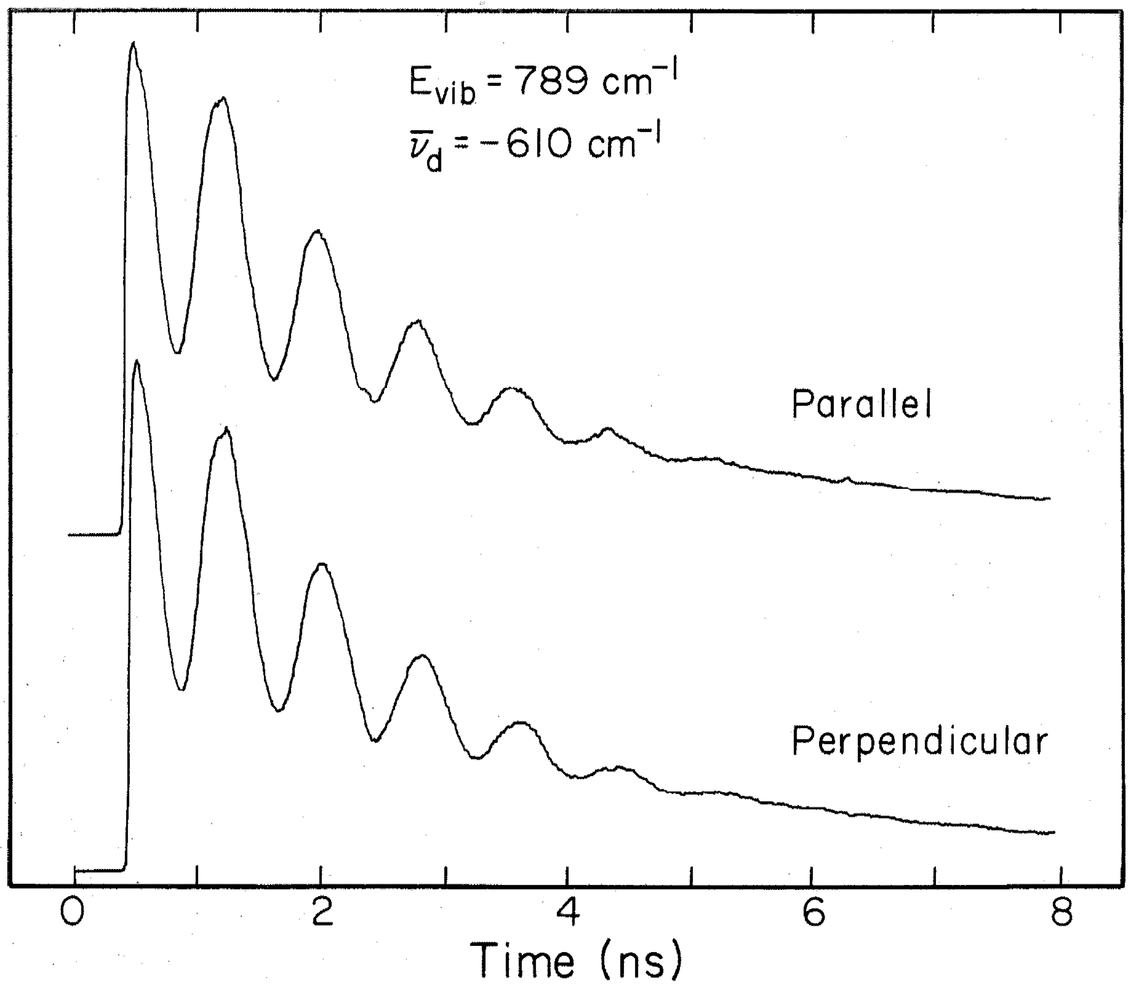
$E_{vib} = 789\ cm^{-1}$
$\bar{\nu}_d = -610\ cm^{-1}$
Parallel
Perpendicular
0
2
4
6
8
Time (ns)

Figure 25

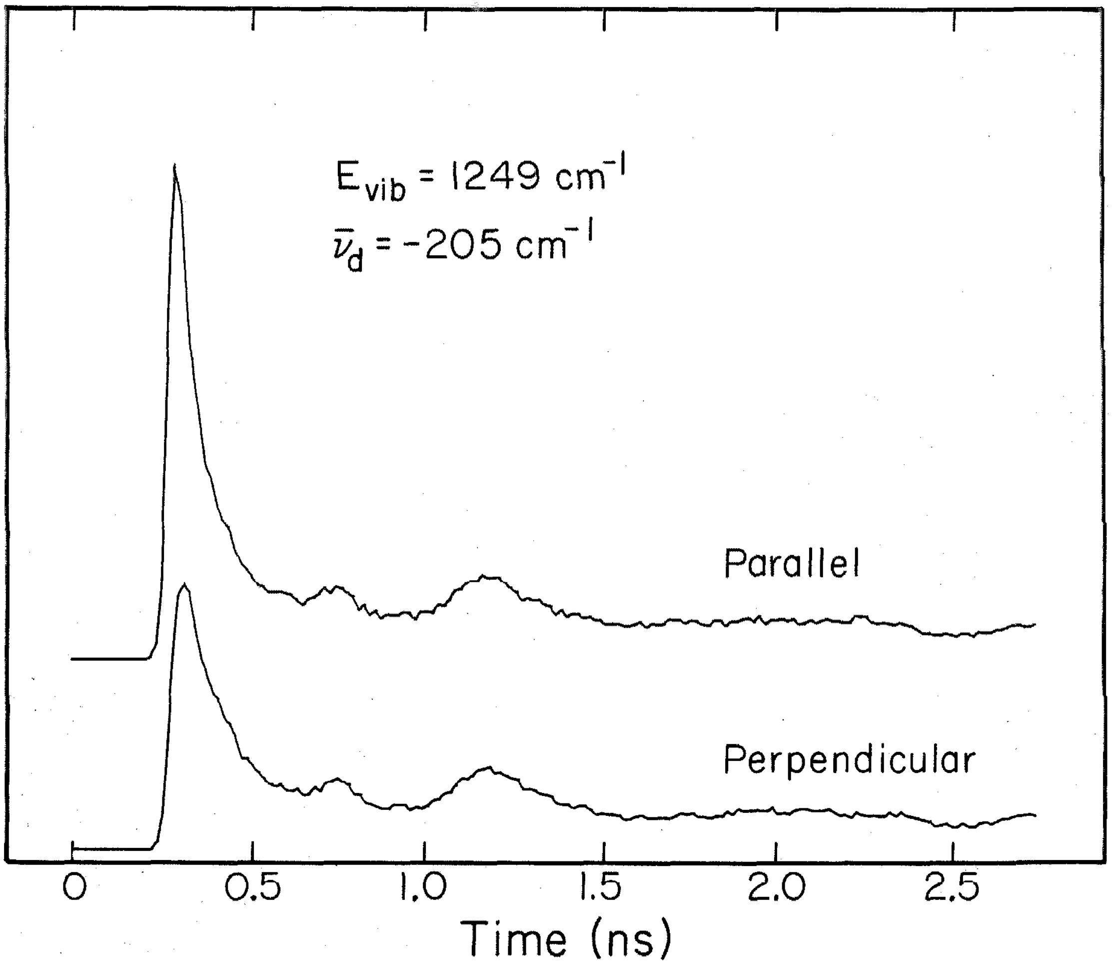
E_{vib} = 1249 cm^{-1}
$\bar{\nu}_d$ = -205 cm^{-1}
Parallel
Perpendicular
0
0.5
1.0
1.5
2.0
2.5
Time (ns)

Figure 26

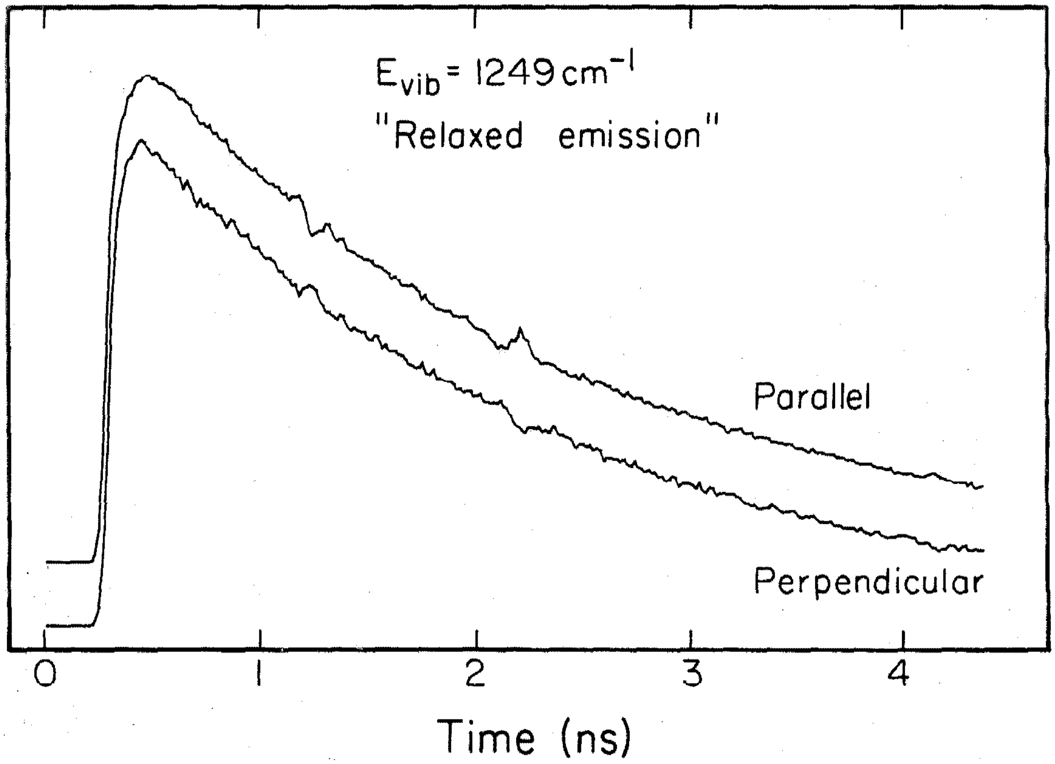
E_{vib} = 1249 cm^{-1}
"Relaxed emission"
Parallel
Perpendicular
0
1
2
3
4
Time (ns)

Figure 27

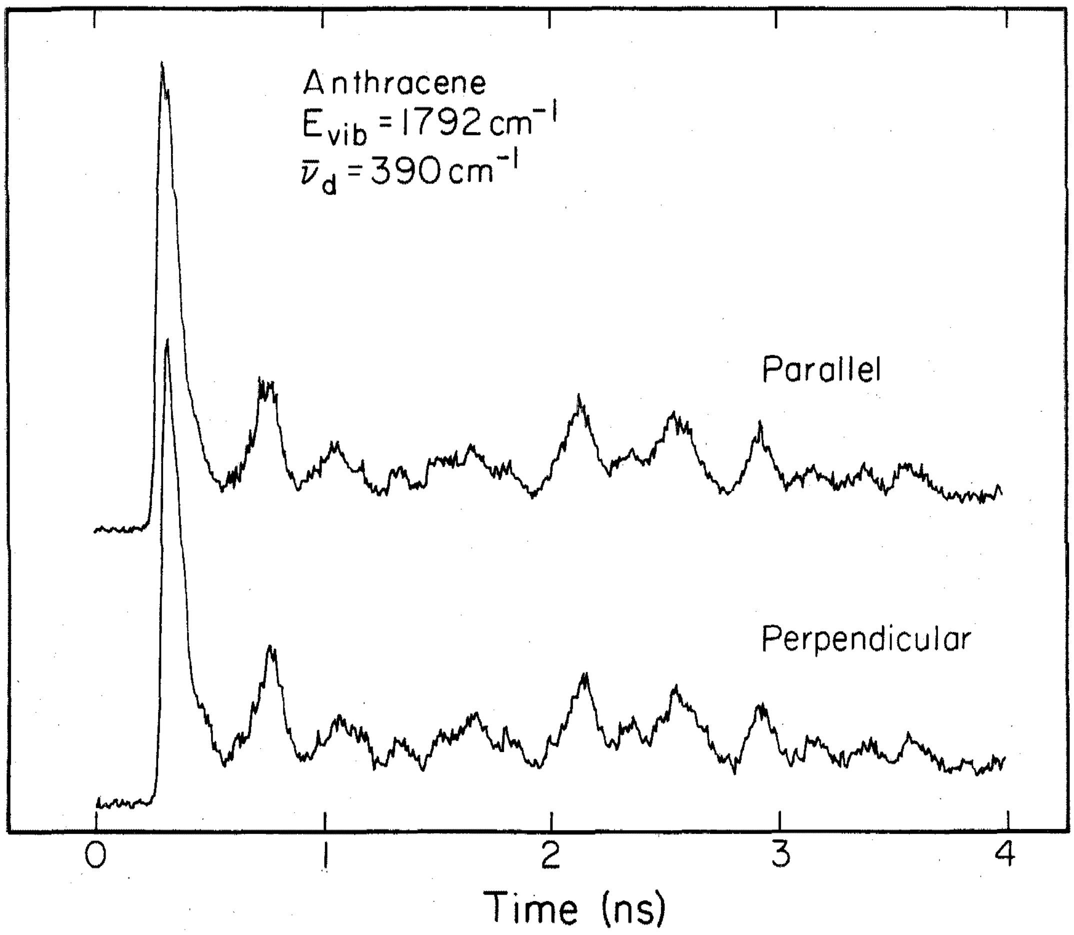
Anthracene
$E_{vib} = 1792\ cm^{-1}$
$\bar{\nu}_d = 390\ cm^{-1}$
Parallel
Perpendicular
0
1
2
3
4
Time (ns)

Figure 28

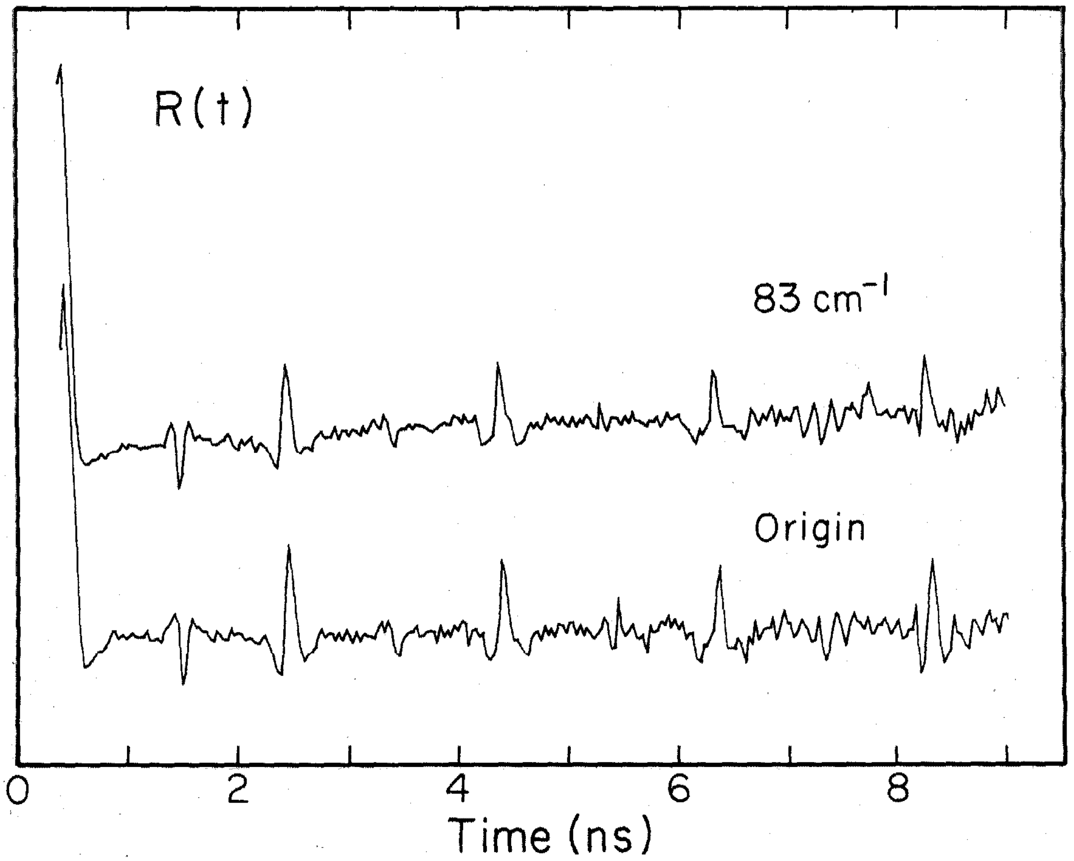

Figure 29

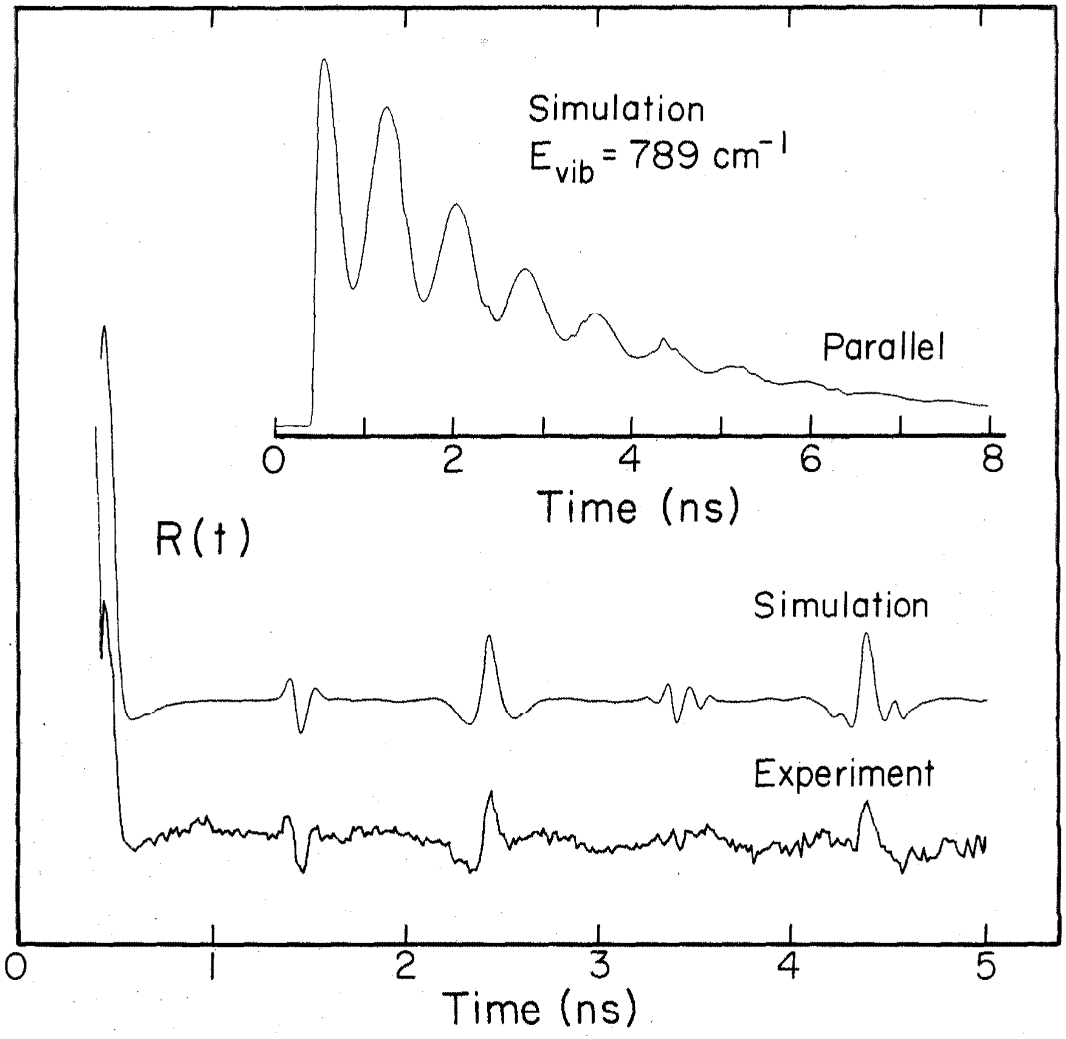
Simulation
$E_{vib} = 789\ cm^{-1}$
Parallel
0
2
4
6
8
Time (ns)
R(t)
Simulation
Experiment
0
1
2
3
4
5
Time (ns)

Figure 30

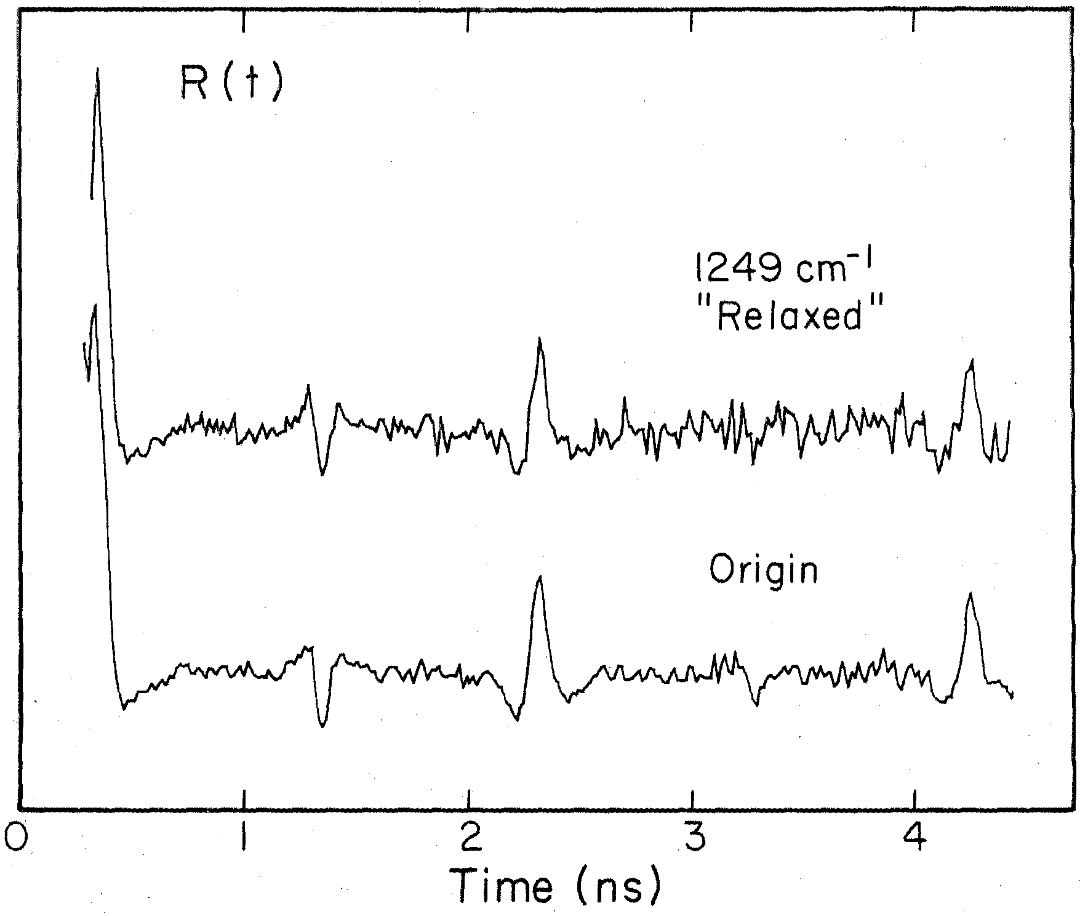

Figure 31

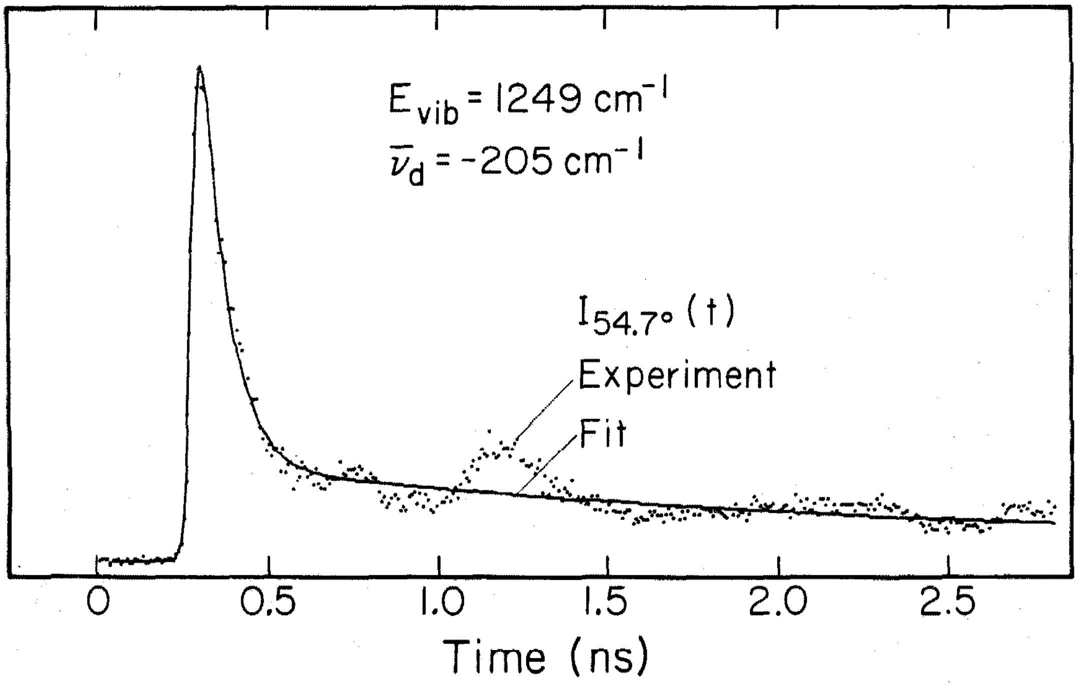
$E_{vib} = 1249\ cm^{-1}$
$\bar{\nu}_d = -205\ cm^{-1}$
$I_{54.7°}(t)$
Experiment
Fit
0
0.5
1.0
1.5
2.0
2.5
Time (ns)

Figure 32

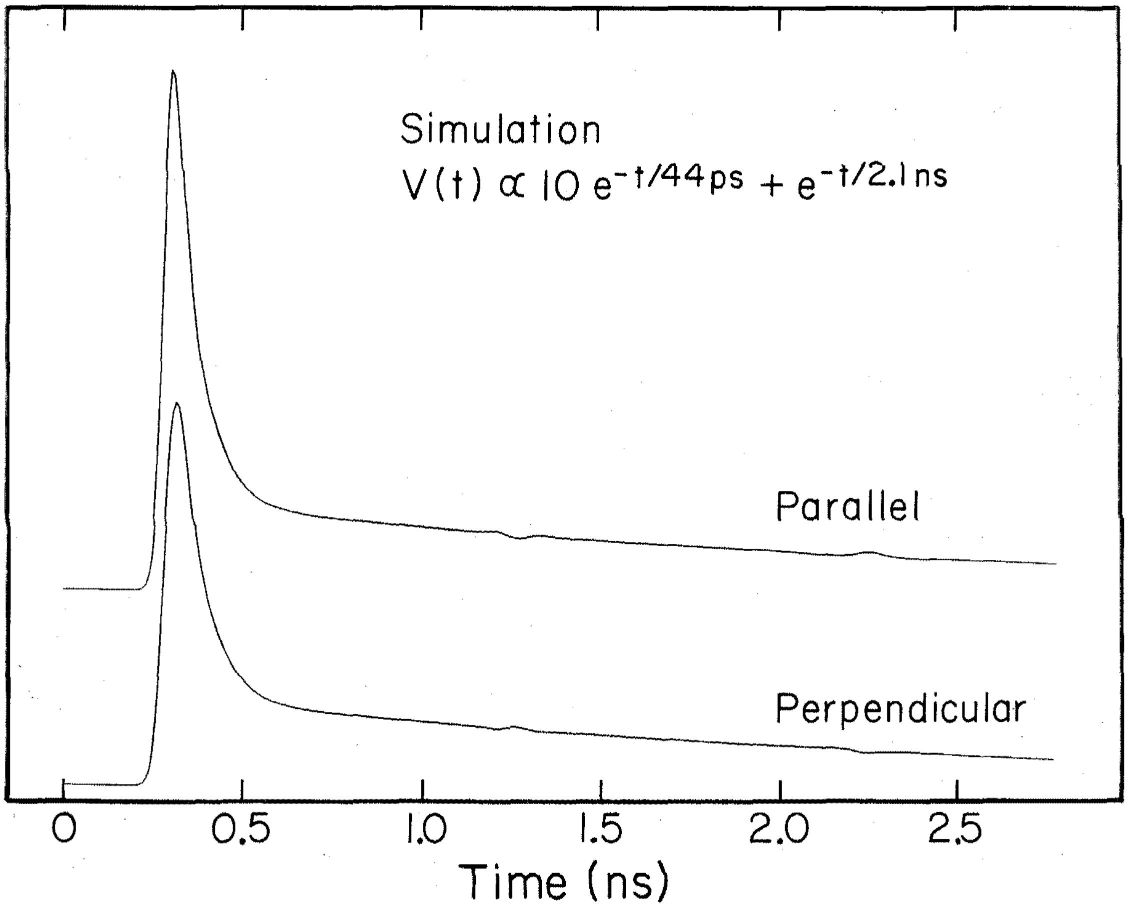
Simulation
$V(t) \propto 10\, e^{-t/44ps} + e^{-t/2.1ns}$
Parallel
Perpendicular
0
0.5
1.0
1.5
2.0
2.5
Time (ns)

Figure 33

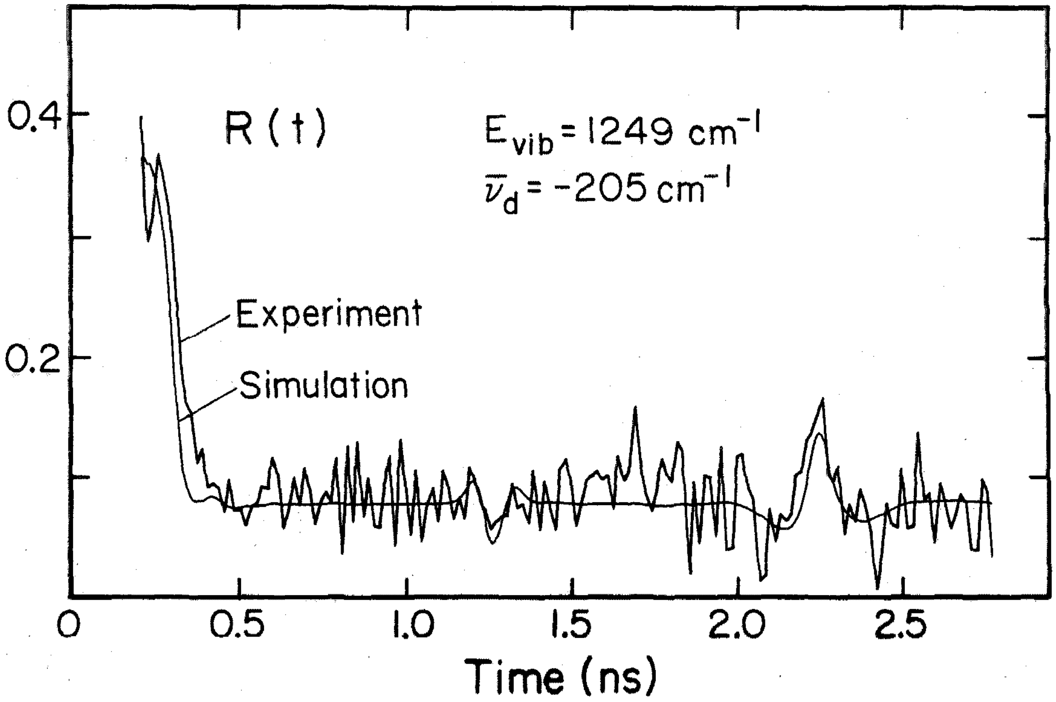

R (t)
$E_{vib} = 1249\ cm^{-1}$
$\bar{\nu}_d = -205\ cm^{-1}$
Experiment
Simulation
0.4
0.2
0
0.5
1.0
1.5
2.0
2.5
Time (ns)

Figure 34

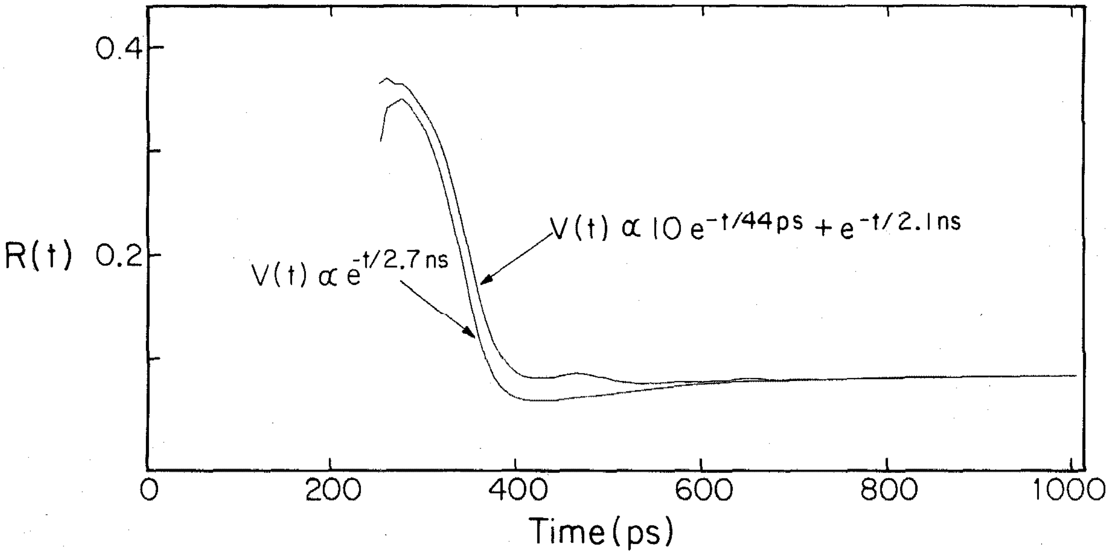
R(t)
0.4
0.2
V(t) ∝ 10 e^{-t/44ps} + e^{-t/2.1ns}
V(t) ∝ e^{-t/2.7ns}
0
200
400
600
800
1000
Time (ps)

Figure 35

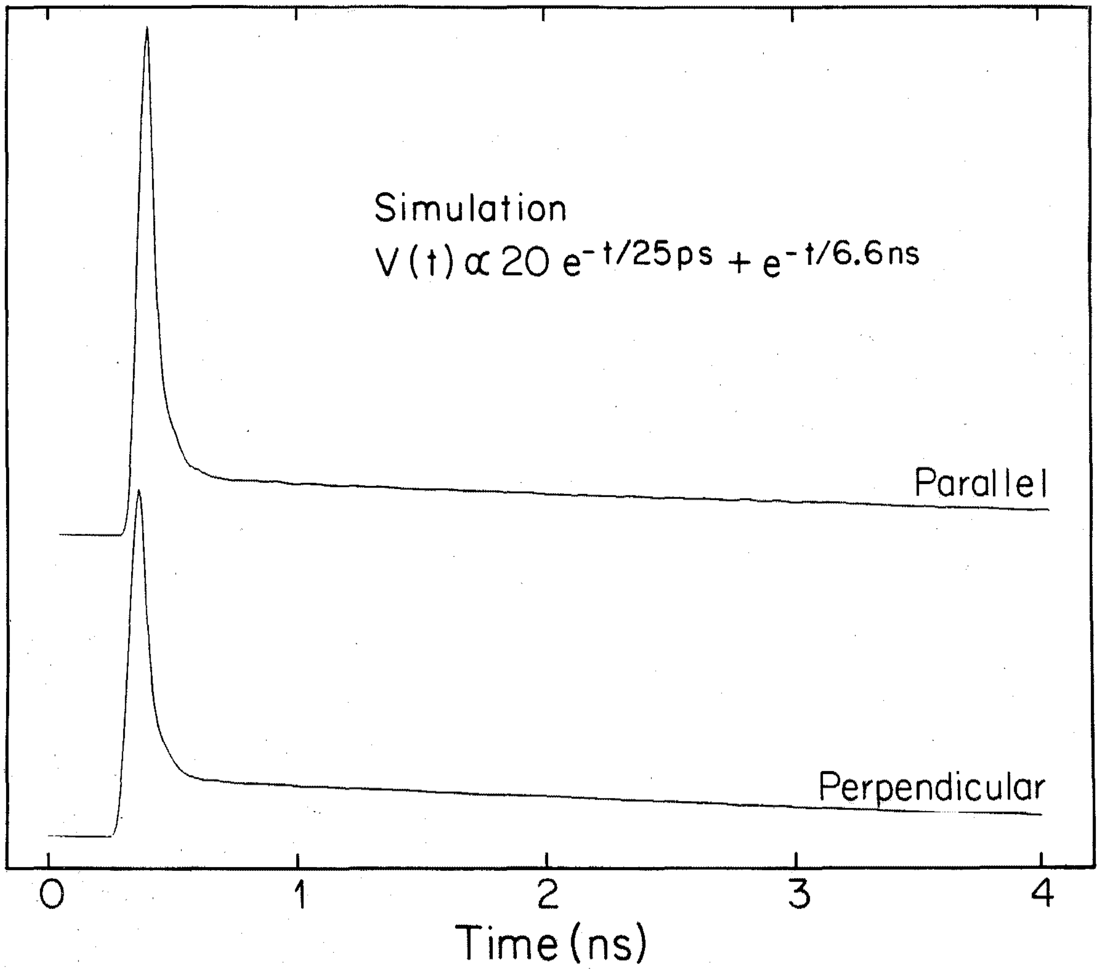
Simulation
$V(t) \propto 20\, e^{-t/25\mathrm{ps}} + e^{-t/6.6\mathrm{ns}}$
Parallel
Perpendicular
0
1
2
3
4
Time (ns)

Figure 36

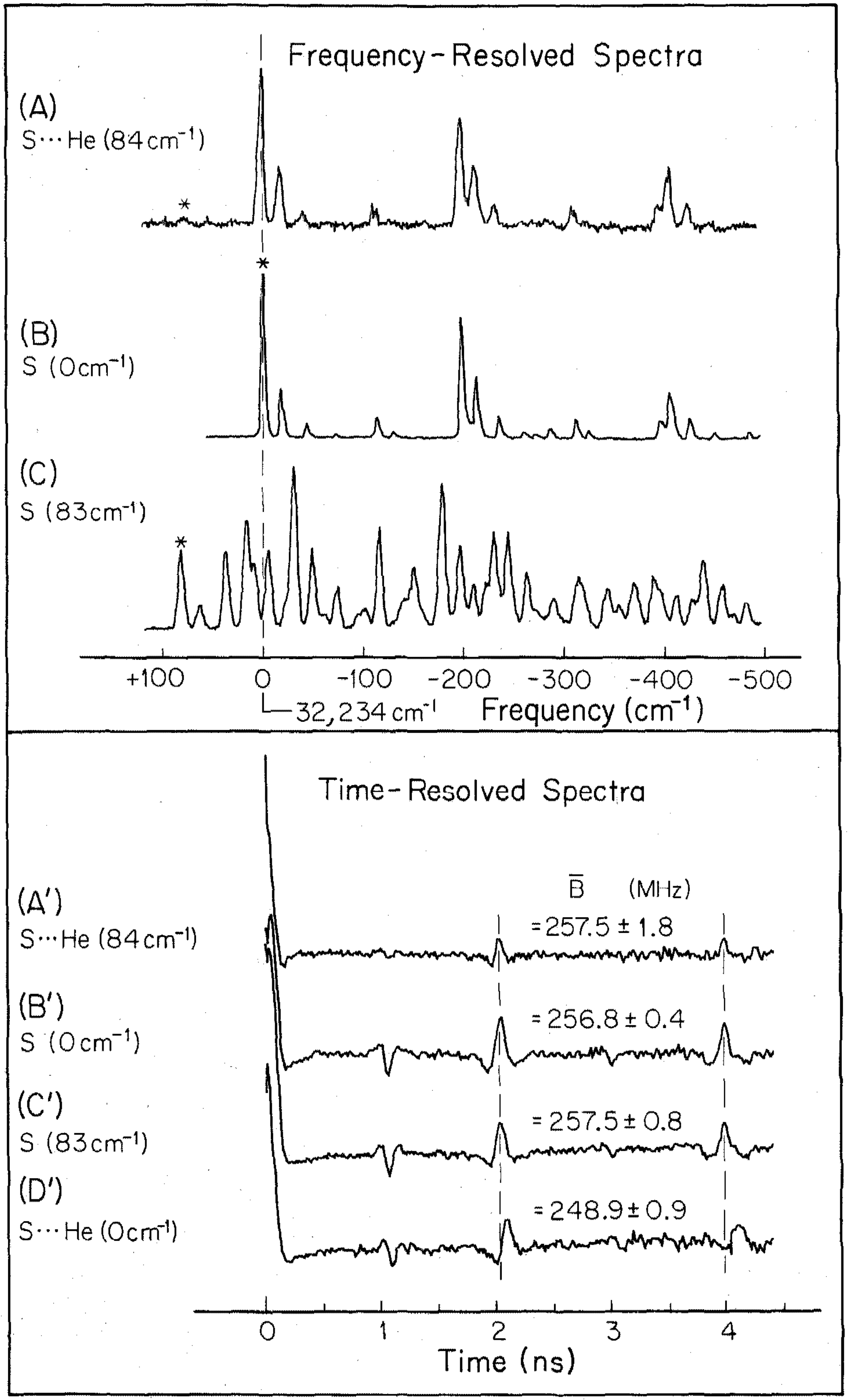
Frequency-Resolved Spectra
(A)
S···He (84cm⁻¹)
(B)
S (0cm⁻¹)
(C)
S (83cm⁻¹)
*
+100
0
-100
-200
-300
-400
-500
32,234 cm⁻¹
Frequency (cm⁻¹)
Time-Resolved Spectra
B̄ (MHz)
(A')
S···He (84cm⁻¹)
=257.5 ± 1.8
(B')
S (0cm⁻¹)
=256.8 ± 0.4
(C')
S (83cm⁻¹)
=257.5 ± 0.8
(D')
S···He (0cm⁻¹)
=248.9 ± 0.9
0
1
2
3
4
Time (ns)

Figure 37

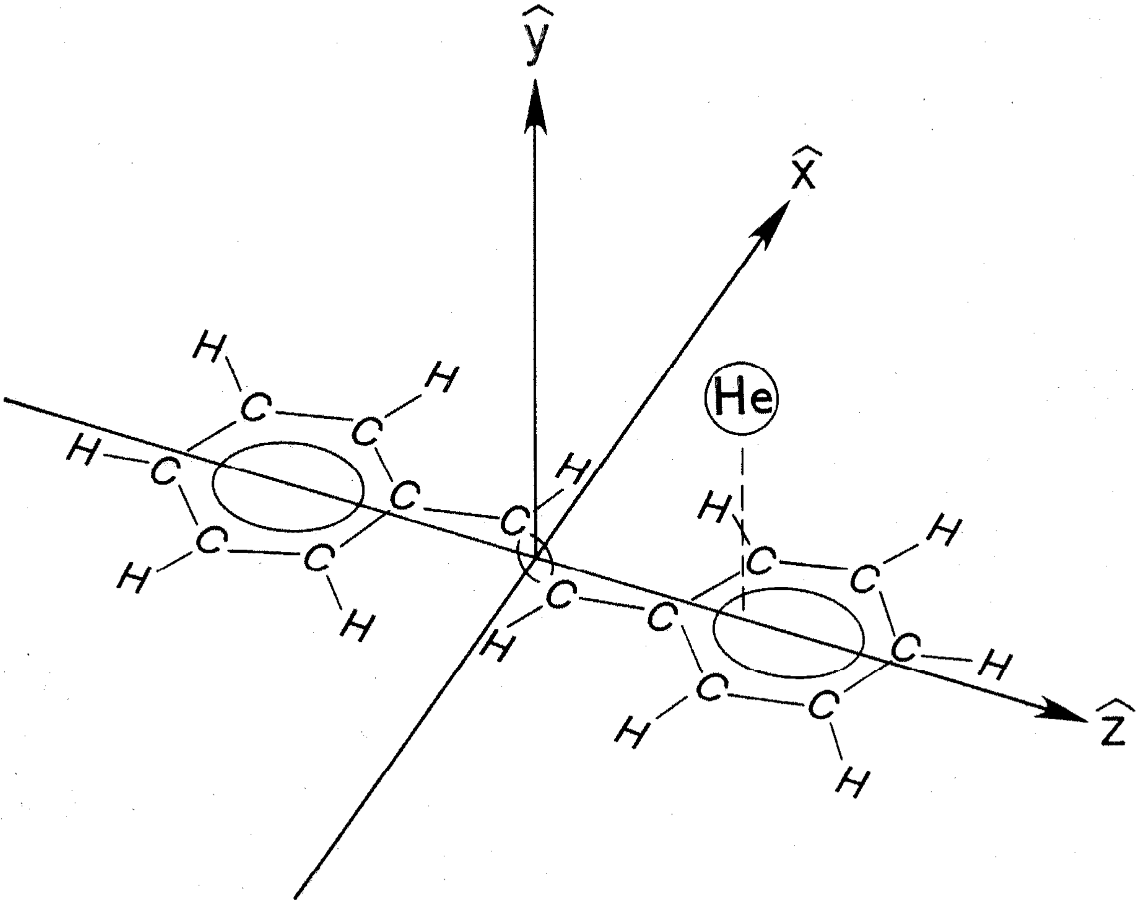

Figure 38

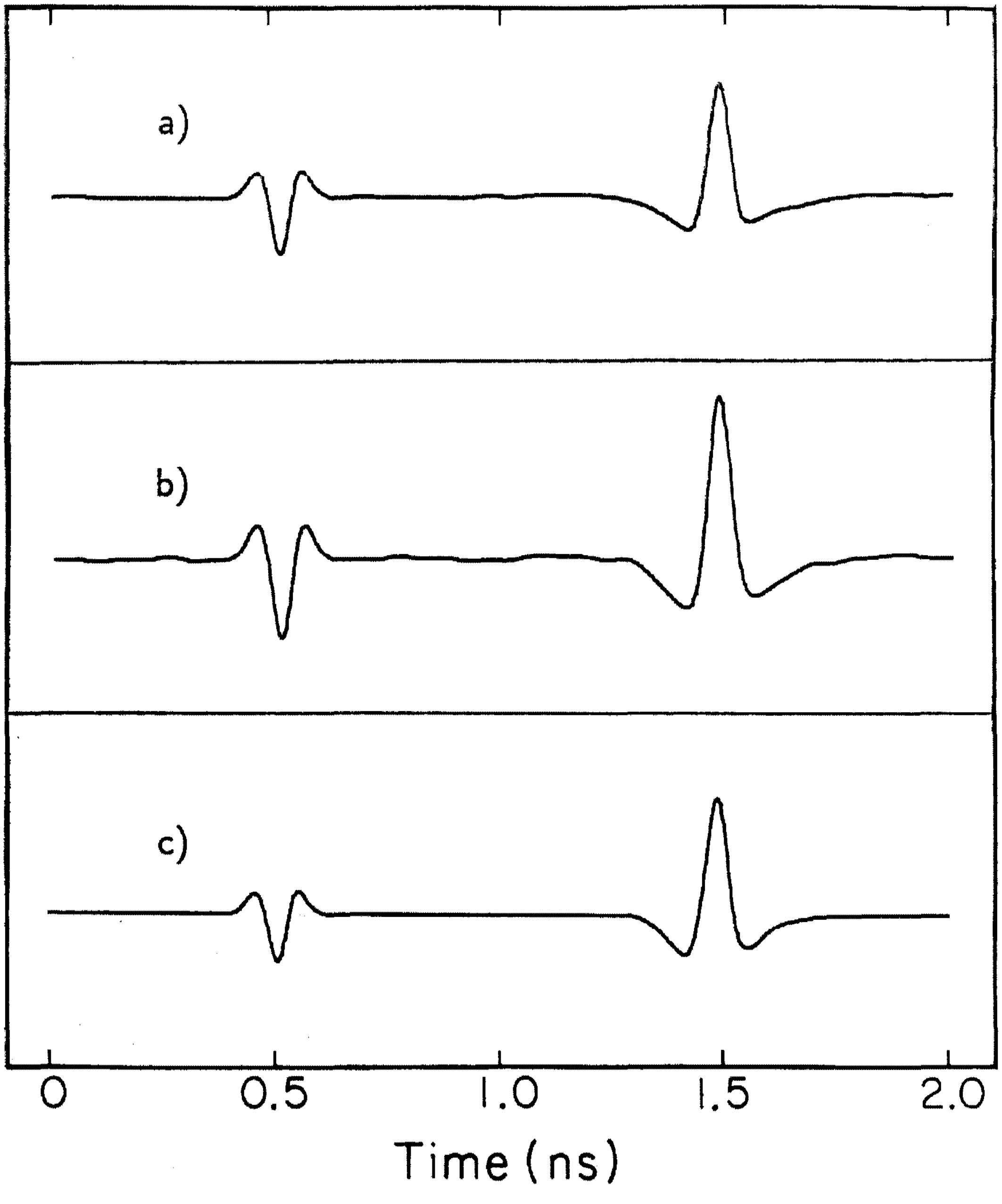

Appendix I

Doppler-free time-resolved polarization spectroscopy of large molecules: Measurement of excited state rotational constants

J. S. Baskin, P. M. Felker, and A. H. Zewail

Reprinted with permission from The Journal of Chemical Physics, Volume 84, p. 4708. Copyright 1986 American Institute of Physics.

Doppler-free time-resolved polarization spectroscopy of large molecules: Measurement of excited state rotational constants

J. S. Baskin,[a] P. M. Felker,[b] and A. H. Zewail
Arthur Amos Noyes Laboratory of Chemical Physics,[c] *California Institute of Technology, Pasadena, California 91125*

(Received 7 January 1986; accepted 6 February 1986)

Measurement of the rotational spectra and constants of molecules can be a powerful probe of excited state geometries and intramolecular dynamics. The conventional approach for obtaining rotationally resolved spectra is to use high-resolution (frequency domain, time-integrated) laser excitation. For medium-sized molecules, recent advances in these high-resolution techniques have made it possible to obtain Doppler-free spectra of benzene[1] (using two-photon excitation), and jet-cooled spectra of tetrazines,[2] pyrazine,[3] and others.[4] These results on *medium-sized* molecules have provided valuable information on geometries,[1,2] and on the dynamics of intramolecular singlet–triplet coupling[3,5] and the "channel 3" decay in benzene.[1] For large molecules, to obtain rotationally resolved spectra one needs stable, ultranarrow bandwidth lasers together with a scheme to reduce Doppler broadening to less than several megahertz.

In this Communication we report the first application of a *time-resolved polarization* technique to the study of the rotational constants and geometries of large molecules. The technique (1) is Doppler-free, or, more accurately, Doppler insensitive (one-photon excitation), (2) allows one to measure excited state rotational constants directly, (3) can provide information pertaining to absorption and emission transition dipole directions, and (4) can be readily applied to large molecules. Results are reported here for *t*-stilbene, *t*-stilbene-d_{12}, and *t*-stilbene–argon complexes. For each of these molecules (isolated by jet cooling[7]) we report values of the rotational constants $\frac{1}{2}(B+C)$ and compare these values with calculated ones. The results amply demonstrate the power of this probe of excited state rotational level structures.

The principle of the technique is as follows. A polarized picosecond pulse coherently prepares excited state S_1 rotational levels of individual molecules in the sample. This creates an initial alignment of excited molecules. By viewing the fluorescence with an analyzer one is able to time resolve the dephasing and rephasing of this alignment. Because the energy spacings of the coherently prepared rotational levels are *commensurate* [e.g., for parallel-type absorption in a symmetric top molecule, the spacings are $2BJ$, $2B(J+1)$, and $2B(2J+1)$], the rephasing, which results in a decrease or increase in the fluorescence intensity depending on the relative polarization of excitation and fluorescence detection, is manifested as transients at times determined by the rotational constants of the molecule. For parallel-type transitions in a symmetric top the recurrences occur at time intervals of $1/(2B)$. For parallel transitions in near prolate asymmetric tops, such as *t*-stilbene, they occur at intervals of $1/(B+C)$. Thus from these recurrences one can directly obtain rotational constants. The transients associated with the rotational motion can be suppressed by using magic angle (54.7°) detection, just as is done in liquids.[8]

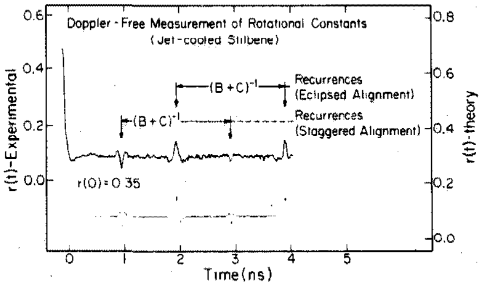

FIG. 1. Fluorescence anisotropy $r(t) \equiv [I_{\parallel}(t) - I_{\perp}(t)]/[I_{\parallel}(t) + 2I_{\perp}(t)]$ for the 0_0^0 absorption and fluorescence transition of *t*-stilbene. Top—experimental $r(t)$: expansion orifice 70 μm, 75 psig Ne backing pressure, laser-to-nozzle distance 3 mm, nozzle $T = 150$ °C. Bottom—simulated $r(t)$ calculated (Ref. 9) assuming rotational constants $A = 0.089\,267$, $B = 0.008\,767$, and $C = 0.008\,333$ cm^{-1}, fluorescence lifetime of 2.6 ns, [Ref. 7(a)] jet $T = 5$ K, and accounting for the finite temporal detection response. Transients occur at times when the alignment of the emission dipoles of molecules in the sample is "eclipsed" (i.e., along the direction of the excitation polarization) or when the alignment is "staggered" (biased toward 90° relative to the excitation polarization).

TABLE I. Recurrence times and rotational constants measured by the Doppler-free technique.

Molecule	Energy (cm^{-1})	Recurrence time (ns)	Rotational const. $\frac{B+C}{2}$ (cm^{-1}) Measured	Calculated
t-stilbene-h_{12}	0(≡32 234 cm^{-1})	1.951 ± 0.010	0.008 54 ± 0.000 04	0.008 42
t-stilbene-h_{12} (vib.)	+ 83	1.954 ± 0.020	0.008 53 ± 0.000 09	
t-stilbene-d_{12}	+ 93	2.140 ± 0.012	0.007 79 ± 0.000 05	0.007 70
t-stilbene-Ar:				
1)	− 40	2.384 ± 0.064	0.006 99 ± 0.000 20	0.006 67[a]
2)	− 63	2.410 ± 0.040	0.006 91 ± 0.000 12	

[a] The principal A axis of inertia is very close to that of t-stilbene (∼ 10°).

There are two unique features of the above scheme. First, the picosecond temporal resolution allows for observation of the transients, which can have widths on the order of 10 ps or less. Second, thermal effects (arising from the initial population of J, K levels in S_0) do not wash out these recurrences. This is because of the commensurability of beat frequencies for a symmetric top or near commensurability for an asymmetric top.[9,10]

Our experimental apparatus has been described in detail elsewhere.[11] Briefly, we measure the decay of spectrally resolved, polarization-analyzed fluorescence that emanates from a jet-cooled sample upon excitation with the linearly polarized, frequency-doubled output of a picosecond dye laser (synchronously pumped, cavity dumped). Decays and recurrences are measured using time-correlated single-photon counting. For this work the temporal response of the detection system was typically 45 ps.

Figure 1 shows experimental results corresponding to the excitation of the S_1–0_0^0 band[7(a)] of t-stilbene at 32 234 cm^{-1} and detection of the same fluorescence band. [Note that rotational structure[12] is not resolved by the excitation laser (bandwidth ∼ 5 cm^{-1}) nor by the detection monochromator.] The data are presented as the polarization anisotropy, $r(t)$, calculated directly from observed decays ($I_\parallel$ and $I_\perp$) *without deconvolution of the detection* response function. Also included in the figure is a simulation of the data calculated using known parameters for t-stilbene[12,13] and expressions for $I_\parallel$ and $I_\perp$.[9,10] In the figure one can see clearly the recurrences associated with thermally averaged rotational coherence. The spacings between recurrences in the experimental traces determine directly the average of the rotational constants B and C. The value so obtained for the 0^0 level of t-stilbene is given in Table I. It agrees well with the value calculated using the geometry of Ref. 14.

We have also made measurements on t-stilbene S_1 vibrational level at 83 cm^{-1},[7] t-stilbene-d_{12} S_1–0^0 level,[7(a)] and on the t-stilbene–argon van der Waals complex bands[7(c)] occurring at − 40 and − 63 cm^{-1} shifts with respect to the t-stilbene 0_0^0 band. The rotational constants derived from these measurements appear in Table I, and compare well with calculated values. The calculated value for the argon complexes was obtained by assuming the same t-stilbene geometry as above, with one argon atom placed 3.45 Å[15] above one of the phenyl groups and on the inner side of that moiety (the phenyl groups are tilted about 30° out of the plane defined by the ethylene group[14]). Notably, calculations based on the assumption of two argon atoms yield significantly lower $(B+C)/2$ values (∼0.0052 cm^{-1}) than those obtained from experiment.

In conclusion, we have presented results that demonstrate the usefulness of time-resolved, Doppler-free polarization techniques in studying the rotational level structures of large molecules. This technique should be applicable to a wide variety of problems associated with the spectra and dynamics of the excited states of large molecules.

---

[a] ARCS fellowship, Applied Physics Department, California Institute of Technology.

[b] Present address: Department of Chemistry, University of California, Los Angeles, California 90024.

[c] Contribution no. 7351. This work is supported by a grant from the National Science Foundation (DMR-8521191).

[1] E. Riedle, H. J. Neusser, and E. W. Schlag, J. Phys. Chem. 86, 4847 (1982); J. Chem. Phys. 80, 4686 (1984).

[2] C. A. Haynam, D. V. Brumbaugh, and D. H. Levy, J. Chem. Phys. 80, 2256 (1984); Y. D. Park and D. H. Levy, *ibid.* 81, 5527 (1984).

[3] (a) B. J. van der Meer, H. Th. Jonkman, and J. Kommandeur, Laser Chem. 2, 77 (1983); B. J. van der Meer, H. Th. Jonkman, J. Kommandeur, W. L. Meerts, and W. A. Majewski, Chem. Phys. Lett. 92, 565 (1982); G. Ter Horst, D. W. Pratt, and J. Kommandeur, J. Chem. Phys. 74, 3616 (1981); (b) P. M. Felker, W. R. Lambert, and A. H. Zewail, Chem. Phys. Lett. 89, 309 (1982). The time-resolved data of Ref. 3(b) agree with the frequency-resolved data of Ref. 3(a) when Fourier transformed.

[4] The high resolution spectra of indole has been obtained recently by L. Phillips and D. H. Levy (to be published). Earlier work by Majewski *et al.* gave the fully resolved rotational spectra of naphthalene and other molecules (see, for example, J. Mol. Spectrosc. 104, 271 (1984).

[5] Other studies using quantum beats on similar systems have provided similar important information about intramolecular couplings (see, e.g., Ref. 6). We will not concern ourselves here with such couplings. Nor are we concerned with the effect of picosecond energy redistribution [Refs. 16(a) and 16(b)] or singlet–triplet coupling [Ref. 16(c)] on $r(t)$.

[6] J. Chaiken, M. Gurnick, and J. D. McDonald, J. Chem. Phys. 74, 106, 117 (1981); M. Gurnick, J. Chaiken, J. D. McDonald, *ibid.* 74, 123 (1981); J. Mulbach, M. Dubs, H. Bitto, and J. R. Huber, Chem. Phys. Lett. 111, 288 (1984).

[7] (a) J. A. Syage, W. R. Lambert, P. M. Felker, A. H. Zewail, and R. M. Hochstrasser, Chem. Phys. Lett. 88, 266 (1982); J. A. Syage, P. M. Felker, and A. H. Zewail, J. Chem. Phys. 81, 4685 (1984); (b) A. Amirav and J. Jortner, Chem. Phys. Lett. 95, 295 (1983); (c) T. S. Zwier, E. Carrasquillo M., and D. H. Levy, J. Chem. Phys. 78, 5493 (1983).

[8] See, e.g., K. B. Eisenthal, Acc. Chem. Res. 8, 118 (1975). For details on the comparison between isolated molecules and molecules in solution see Ref. 9. For a discussion of steady-state fluorescence anisotropy arising from gaseous samples see Ref. 17.

[9] P. M. Felker and A. H. Zewail, J. Chem. Phys. (to be submitted).

[10] P. M. Felker, J. S. Baskin, and A. H. Zewail, J. Phys. Chem. 90, 724 (1986).

[11] W. R. Lambert, P. M. Felker, and A. H. Zewail, J. Chem. Phys. 75, 5958 (1981); P. M. Felker and A. H. Zewail, *ibid.* 82, 2975 (1985).

[12] B. W. Keelan and A. H. Zewail, J. Phys. Chem. 89, 4939 (1985); and references therein.

[13] R. H. Dyck and D. S. McClure, J. Chem. Phys. 36, 2326 (1962); G. Hohlneicher and B. Dick, J. Photochem. 27, 215 (1984).

[14] M. Traetteberg, E. B. Fraasten, F. C. Mijlhoff, and A. Hoestra, J. Mol. Struct. 26, 57 (1975).

[15] A. Amirav, U. Even, J. Jortner, and B. Dick, Mol. Phys. 49, 899 (1983); see also W. E. Henke, W. Yu, H. L. Selzle, E. W. Schlag, D. Wutz, and S. H. Lin, Chem. Phys. 92, 187 (1985).

[16] (a) J. W. Perry, N. F. Scherer, and A. H. Zewail, Chem. Phys. Lett. 103, 1 (1983); N. F. Scherer, J. F. Shepanski, and A. H. Zewail, J. Chem. Phys. 81, 2181 (1984); N. F. Scherer, J. W. Perry, F. E. Doany, and A. H. Zewail, J. Phys. Chem. 89, 894 (1985); (b) D. K. Negus, D. S. Green, and R. M. Hochstrasser, Chem. Phys. Lett. 117, 409 (1985); (c) Y. Matsumoto, L. H. Spangler, and D. W. Pratt, *ibid.* 95, 343 (1983); 98, 333 (1983).

[17] G. M. Nathanson and G. M. McClelland, J. Chem. Phys. 81, 629 (1985).

Appendix II

Fortran program ATDP1

The following program evaluates the theoretical expression for purely rotational coherence in asymmetric top molecules derived in "Purely rotational coherence effect and time-resolved sub-Doppler spectroscopy of large molecules. I. Theoretical," P. M. Felker and A. H. Zewail, J. Chem. Phys. **86**, 2460 (1987). The directions of the transition dipole moments in the molecular principal axis frame are unrestricted. This program is based on the program AT7 which is limited to calculations in which the transition dipoles lie along principal inertial axes. The initial asymmetric top PRC programs, including ATHALF, from which AT7 was developed, were written by Peter Felker. See Chapter 2, Section III for a discussion of the algorithm.

The program commonly used for off-axis dipole calculations was an alternate version of ATDP1 incorporating the near-symmetric treatment described in Chapter 4. An example of the implementation of this approximation is provided in the program ATFIT2 in Appendix III.

```
      PROGRAM ATDP1
C ----------  FOR ARBITRARY DIPOLE DIRECTIONS
C     TO CALCULATE BEATING DECAYS ARISING FROM THE COHERENT
C     PREPARATION OF ROTATIONAL LEVELS IN AN ASYMMETRIC TOP
C     MOLECULE - ONE TEMPERATURE, ONE FREQUENCY RESOLUTION,
C     ONE TEMPORAL RESOLUTION, PARALLEL AND
C     PERPENDICULAR DETECTION POLARIZATIONS.
C
C   INPUT FILES:
C     ATDPIN.DAT   -  NMAX IS MAX VALUE OF GROUND STATE TOTAL
C                          ROTATIONAL ANGULAR MOMENTUM Q. N. (NG).
C                          (LARGEST NMAX IS CURRENTLY 45)
C                     NSKIP IS NG INCREMENT.
C                     NPTS IS NUMBER OF DECAY POINTS TO BE
C                          CALCULATED
C                     NURES IS THE BEAT FREQUENCY RESOLUTION
C
C     ASYM/G/E.DAT -  CONTAIN ASYMMETRIC TOP ROTATIONAL ENERGIES
C                           AND EIGENFUNCTIONS, ARRANGED BY N
C                           AND SYMMETRY SPECIES
C                           (G: GROUND STATE,  E: EXCITED STATE)
C
      REAL NG,NI,NJ,KG,KIP,KJ,NU,NJFAC,NTNP1,  IKKSUMS
      REAL IDPA, IDPB, IF1, NURES, NUMAX, IFF, IKSJ, IKSI
      REAL   RQ2SUMLE2(-2:2), IQ2SUMLE2(-2:2), IF7PL, IF7PR, IF7
      DIMENSION  RF(3,3,24), IFF(3,3,24), IKMAX(0:46,4)
      DIMENSION  F6JPL(3,3,0:2), F6JPR(3,3,0:2)
      DIMENSION  EG(0:46,24,4), EIVECG(0:46,24,-46:46,4)
      DIMENSION  E(0:46,24,4), EIVEC(0:46,24,-46:46,4)
      DIMENSION  IJSYM(3,7,4), ISYMIJ(3), NKSYM(0:1,4)
      DIMENSION  KMAXG(4),KMAXJ(4),KMAXI(4),KFAC(3),DPSYM(3)
      DIMENSION   RDPA(3), IDPA(3), RDPB(3), IDPB(3)
      DIMENSION  DECAYPL(5000), DECAYPR(5000), NSYMK(0:1,4)
      DIMENSION FMDPL(50000)
      DIMENSION STATWT(4)
      DIMENSION T3J11(0:2, -1:1, -1:1, -2:2)
      COMMON /RJMS/  NI, NJ, LL, NG
C
      OPEN(UNIT=21, FILE='ATDPIN.DAT', STATUS='OLD')
      READ(21,9011) NMAX, NSKIP, NPTS, NURES, NUMAX
      READ(21,903) T
      READ(21,902) (STATWT(J), J=1,4)
      READ(21,902) A1
      READ(21,902) B1
      READ(21,902) C1
      READ(21,902) THETAA, PHIA
      READ(21,902) THETAB, PHIB
      READ(21,902) CT
      CLOSE(UNIT=21, DISP='SAVE')
9011  FORMAT(I3,2X,I3,2X,I4,2X,F8.6,2X,F8.2)
902   FORMAT( 4F10.5 )
903   FORMAT(F5.1)
```

```
C
      TWOPI = 6.28318
      RADCON = TWOPI/360.
      THETAA = THETAA*RADCON
      PHIA = PHIA*RADCON
      THETAB = THETAB*RADCON
      PHIB = PHIB*RADCON
C     WRITE(18,8876)  NUMAX
C8876 FORMAT( ' NUMAX = ', F12.6 )
      INUMAX = 0
C
      SQ2=SQRT(2.)
      DSQ2=1./SQ2
      RKA=(2.*B1-A1-C1)/(A1+C1)
C
C     SET EXCITED STATE SYMMETRIES FOR EACH A-TRANSITION MOMENT
C     COMPONENT AND GROUND STATE SYMMETRY USING THE ARRAY
C     IJSYM(I,II,JJ) WHERE I IS THE COMPONENT OF THE MOMENT
C     (1=A,2=B,3=C), II IS A CODE TO INDICATE WHICH COMPONENTS
C     ARE NONZERO ( 1=A only, 2=B only, 3=A and B, 4=C only,
C     5 = A and C, 6=B and C, 7=A,B, and C), AND JJ IS THE GROUND
C     STATE SYMMETRY (1=++, 2=-+, 3=--, 4=+- IN THE C,A NOTATION)
      DATA IJSYM/2,0,0, 0,3,0, 2,3,0, 0,0,4, 2,0,4, 0,3,4, 2,3,4,
     2           1,0,0, 0,4,0, 1,4,0, 0,0,3, 1,0,3, 0,4,3, 1,4,3,
     3           4,0,0, 0,1,0, 4,1,0, 0,0,2, 4,0,2, 0,1,2, 4,1,2,
     4           3,0,0, 0,2,0, 3,2,0, 0,0,1, 3,0,1, 0,2,1, 3,2,1/
C
      IF(RKA.GT.0.) GO TO 10
C
C   SET THE PROLATE CORRELATIONS BETWEEN BASIS SET (KGROUP) AND
C   ROTATIONAL SYMMETRY USING THE ARRAY NKSYM(II,JJ), WHERE II IS
C   THE INTEGER PARITY OF THE TOTAL ANGULAR MOMENTUM QUANTUM NUMBER
C   (II=0 STANDS FOR EVEN INTEGER, II=1 STANDS FOR ODD) AND JJ GIVES
C   THE BASIS SET "KGROUP" NUMBER (1=EVEN K AND SYMMETRIC
C   COMBINATION, 2=ODD K AND ANTISYMMETRIC COMBINATION,
C   3=ODD K AND SYMM. COMB., 4=EVEN AND ANTISYM.)
      NKSYM(0,1)=1
      NKSYM(1,1)=2
      NKSYM(0,2)=4
      NKSYM(1,2)=3
      NKSYM(0,3)=3
      NKSYM(1,3)=4
      NKSYM(0,4)=2
      NKSYM(1,4)=1
C
C   SET THE VALUES FOR PROLATE SYMMETRY TO "KGROUP" CONVERSION
C   USING THE ARRAY NSYMK(II,JJ), WHERE II IS THE INTEGER PARITY
C   (EVEN OR ODD) OF THE TOTAL ANGULAR MOMENTUM Q.N. AND JJ IS
```

```
C   THE SYMMETRY NUMBER (SEE ABOVE).
        NSYMK(0,1)=1
        NSYMK(1,1)=4
        NSYMK(0,2)=4
        NSYMK(1,2)=1
        NSYMK(0,3)=3
        NSYMK(1,3)=2
        NSYMK(0,4)=2
        NSYMK(1,4)=3
        GO TO 11
C
10      CONTINUE
C   OBLATE CORRELATIONS BETWEEN "KGROUP" AND SYMMETRY
        NKSYM(0,1)=1
        NKSYM(1,1)=4
        NKSYM(0,2)=2
        NKSYM(1,2)=3
        NKSYM(0,3)=3
        NKSYM(1,3)=2
        NKSYM(0,4)=4
        NKSYM(1,4)=1
C
        NSYMK(0,1)=1
        NSYMK(1,1)=4
        NSYMK(0,2)=2
        NSYMK(1,2)=3
        NSYMK(0,3)=3
        NSYMK(1,3)=2
        NSYMK(0,4)=4
        NSYMK(1,4)=1
C
11      CONTINUE
C
C   SET DIPOLE VALUES FOR THE TRANSITION DIRECTION.
C   THE "NEAR" TOP AXIS IS ALWAYS MADE THE Z AXIS, AND THE
C   INTERMEDIATE AXIS (B AXIS) IS ALWAYS X.
C
        IF(RKA) 1,1,5
C   PROLATE ROTORS
C    ABSORPTION MOMENTS FIRST
1       STH = SIN(THETAA)
C    Z-AXIS IS THE A-AXIS
        IDPA(2) = 0.
        RDPA(2) = COS(THETAA)
C    X-AXIS IS THE B-AXIS
        RDPA(1) = -DSQ2*STH*COS(PHIA)
        RDPA(3) = -RDPA(1)
C    Y-AXIS IS THE C-AXIS
        IDPA(1) = -DSQ2*STH*SIN(PHIA)
        IDPA(3) = IDPA(1)
```

```
C
        KFAC(1) = 0
        KFAC(2) = 1
        KFAC(3) = 1
        DPSYM(1) = 1.
        DPSYM(2) = -1.
        DPSYM(3) = 1.
        ITMA = 0
        IF( ABS( RDPA(2) )  .GT. .00001 )   ITMA = 1
        IF( ABS( RDPA(1) )  .GT. .00001 )   ITMA = ITMA + 2
        IF( ABS( IDPA(1) )  .GT. .00001 )   ITMA = ITMA + 4
C
C   PROLATE EMISSION MOMENTS
        STH = SIN(THETAB)
        IDPB(2)=0.
        RDPB(2) = COS(THETAB)
        RDPB(1) = -DSQ2*STH*COS(PHIB)
        RDPB(3) = -RDPB(1)
        IDPB(1) = -DSQ2*STH*SIN(PHIB)
        IDPB(3) = IDPB(1)
        GO TO 99
C
C   OBLATE ROTOR - THE SYMMETRY AXIS OF THE BASIS SET VECTORS IS C
5       CONTINUE
        STH = SIN(THETAA)
C    Y-AXIS IS THE A-AXIS
        IDPA(1) = -DSQ2*STH*SIN(PHIA)
        IDPA(3) = IDPA(1)
C    X-AXIS IS THE B-AXIS
        RDPA(1) = -DSQ2*STH*COS(PHIA)
        RDPA(3) = -RDPA(1)
C    Z-AXIS IS THE C-AXIS
        IDPA(2) = 0.
        RDPA(2) = COS(THETAA)
        KFAC(1) = 1
        KFAC(2) = 1
        KFAC(3) = 0
        DPSYM(1) = 1.
        DPSYM(2) = -1.
        DPSYM(3) = 1.
        ITMA = 0
        IF( ABS( RDPA(2) )  .GT. .00001 )   ITMA = 4
        IF( ABS( RDPA(1) )  .GT. .00001 )   ITMA = ITMA + 2
        IF( ABS( IDPA(1) )  .GT. .00001 )   ITMA = ITMA + 1
C
C    OBLATE EMISSION MOMENT
        STH = SIN(THETAB)
        IDPB(1) = -DSQ2*STH*SIN(PHIB)
        IDPB(3) = IDPB(1)
        RDPB(1) = -DSQ2*STH*COS(PHIB)
        RDPB(3) = -RDPB(1)
        IDPB(2)=0.
        RDPB(2) = COS(THETAB)
```

```
C
99      CONTINUE
C
C    CALCULATE THE NUMBER OF ROTATIONAL STATES FOR
C      ANY (N,KGRP) PAIR
        DO 5511 N = 0, NMAX + 1
           IKMAX(N,1) = INT(FLOAT(N)/2.) + 1
           IKMAX(N,2) = INT(FLOAT(N+1)/2.)
           IKMAX(N,3) = IKMAX(N,2)
           IKMAX(N,4) = IKMAX(N,1) - 1
5511    CONTINUE
C
C   INPUT EIGENVALUES AND EIGENVECTORS OF THE ASYMMETRIC TOP
C
C    GROUND STATE
        OPEN(UNIT=22,FILE='ASYMG.DAT',ACCESS='SEQUENTIAL',
     1   RECORDTYPE='SEGMENTED',EXTENDSIZE=200,FORM='UNFORMATTED',
     1   TYPE='OLD')
        DO 12 N = 0, NMAX + 1
        KGMX=4
        NN=N
        IF(N.EQ.0) KGMX=1
        IF(N.EQ.1) KGMX=3
        DO 12 KGRP=1,KGMX
        IKM=IKMAX(N,KGRP)
        READ(22) KKGRP, (EG(NN,ITAU,KKGRP), ITAU=1,IKM),
     1   ((EIVECG(NN,ITAU,IK,KKGRP), IK=1,IKM), ITAU=1,IKM)
        PM=-1.
        IF(KGRP.EQ.1.OR.KGRP.EQ.3) PM=1.
C
C   GET SYMMETRIC TOP COEFFICIENTS FROM + AND - COMBINATIONS
C   AND CONVERT THE IK INDEX TO SYMMETRIC TOP K VALUES
        DO 16 ITAU=1,IKM
        EIVECG(NN,ITAU,0,4)=0.
C       WRITE(16,41)  EG(NN,ITAU,KGRP)
        DO 16 IIK=1,IKM
        IK=IKM+1-IIK
        K=2*IK-1
        IF(KGRP.EQ.1) K=2*(IK-1)
        IF(KGRP.EQ.4) K=2*IK
        IF(KGRP.EQ.1.AND.IK.EQ.1)  GO TO 18
        GO TO 17
18      EIVECG(NN,ITAU,0,1)= EIVECG(NN,ITAU,1,1)
        EIVECG(NN,ITAU,1,1)=0.
        GO TO 16
17      EIVECG(NN,ITAU,-K,KGRP)=PM*DSQ2*EIVECG(NN,ITAU,IK,KGRP)
        EIVECG(NN,ITAU,K,KGRP)=DSQ2*EIVECG(NN,ITAU,IK,KGRP)
16      CONTINUE
12      CONTINUE
        CLOSE(UNIT=22, DISP='SAVE')
C
```

```
C   EXCITED STATE
        OPEN(UNIT=23,FILE='ASYME.DAT',ACCESS='SEQUENTIAL',
     1   RECORDTYPE='SEGMENTED',EXTENDSIZE=200,FORM='UNFORMATTED',
     1   TYPE='OLD')
        DO 22 N=0,NMAX+1
        KGMX=4
        NN=N
        IF(N.EQ.0) KGMX=1
        IF(N.EQ.1) KGMX=3
        DO 22 KGRP=1,KGMX
        IKM=IKMAX(N,KGRP)
        READ(23) KKGRP, (E(NN,ITAU,KKGRP), ITAU=1,IKM),
     1   ((EIVEC(NN,ITAU,IK,KKGRP), IK=1,IKM), ITAU=1,IKM)
        PM=-1.
        IF(KGRP.EQ.1.OR.KGRP.EQ.3) PM=1.
C
C   GET SYMMETRIC TOP COEFFICIENTS FROM + AND - COMBINATIONS
C   AND CONVERT THE IK INDEX TO SYMMETRIC TOP K VALUES
        DO 26 ITAU=1,IKM
        EIVEC(NN,ITAU,0,4)=0.
C       WRITE(16,41)  EG(NN,ITAU,KGRP)
        DO 26 IIK=1,IKM
        IK=IKM+1-IIK
        K=2*IK-1
        IF(KGRP.EQ.1) K=2*(IK-1)
        IF(KGRP.EQ.4) K=2*IK
        IF(KGRP.EQ.1.AND.IK.EQ.1)  GO TO 28
        GO TO 27
28      EIVEC(NN,ITAU,0,1)= EIVEC(NN,ITAU,1,1)
        EIVEC(NN,ITAU,1,1)=0.
        GO TO 26
27      EIVEC(NN,ITAU,-K,KGRP)=PM*DSQ2*EIVEC(NN,ITAU,IK,KGRP)
        EIVEC(NN,ITAU,K,KGRP)=DSQ2*EIVEC(NN,ITAU,IK,KGRP)
26      CONTINUE
22      CONTINUE
        CLOSE(UNIT=23, DISP='SAVE')
C
C   ZERO ELEMENTS OF UNDEFINED KGROUPS (NECESSARY?)
        DO 35 ITAU = 1, NMAX/2 + 1
        DO 35 K = -1*(NMAX + 1), NMAX + 1
        EIVECG(0,ITAU,K,2)=0.
        EIVECG(0,ITAU,K,3)=0.
        EIVECG(0,ITAU,K,4)=0.
        EIVECG(1,ITAU,K,4)=0.
        EIVEC(0,ITAU,K,2)=0.
        EIVEC(0,ITAU,K,3)=0.
        EIVEC(0,ITAU,K,4)=0.
35      EIVEC(1,ITAU,K,4)=0.
C
        DO 620 I=1,50000
620        FMDPL(I)=0.
        FMDPR1 = 0.
```

```
C
      DO 622 I=0,2,2
      DO 622 J = -1, 1
      DO 622 II = -1, 1
      DO 622 JJ=-2,2
622      T3J11(I,J,II,JJ) = 0.
C
      DSQ3 = 1./SQRT(3.)
      DNSQ10 = -1./SQRT(10.)
      DSQ30 = 1./SQRT(30.)
      T3J11(0,0,0,0)= -DSQ3
      T3J11(0,1,-1,0)= DSQ3
      T3J11(0,-1,1,0)= DSQ3
      T3J11(2,0,0,0) = DSQ30 + DSQ30
      T3J11(2,1,-1,0)= DSQ30
      T3J11(2,-1,1,0)= DSQ30
      T3J11(2,-1,0,1) = DNSQ10
      T3J11(2,0,-1,1) = DNSQ10
      T3J11(2,1,0,-1) = DNSQ10
      T3J11(2,0,1,-1) = DNSQ10
      T3J11(2,-1,-1,2)= 1./SQRT(5.)
      T3J11(2,1,1,-2) = 1./SQRT(5.)
C
      Q2SUMLE0 = 0.
      DO 655 MMP = -1, 1
        Q2SUMLE0 = Q2SUMLE0 + ( RDPB(2-MMP)*RDPB(2+MMP)
     1            - IDPB(2-MMP)*IDPB(2+MMP) )*T3J11(0,MMP,-MMP,0)
655   CONTINUE
C
      DO 304 IMU = -2, 2
      RQ2SUMLE2(IMU) = 0.
      IQ2SUMLE2(IMU) = 0.
      DO 304 MMP = -1, 1
         NNP = MMP + IMU
         IF( ABS(NNP) .GT. 1 )  GO TO 304
350      RQ2SUMLE2(IMU) = RQ2SUMLE2(IMU) + ( RDPB(2-MMP)
     1                *RDPB(2+NNP) - IDPB(2-MMP)*IDPB(2+NNP) )
     2                                        *T3J11(2,MMP,-NNP,IMU)
         IQ2SUMLE2(IMU) = IQ2SUMLE2(IMU) + ( RDPB(2-MMP)
     1                 *IDPB(2+NNP)+ IDPB(2-MMP)*RDPB(2+NNP) )
     2                                        *T3J11(2,MMP,-NNP,IMU)
304   CONTINUE
C
      EMAX = EG(NMAX+1,1,1)
C     WRITE(18,8875) EMAX
C8875 FORMAT( ' EMAX = ', F12.6 )
C
C     CYCLE THROUGH ALL GROUND STATE LEVELS AND THEIR TRANSITIONS
C
      DO 305 NNG=0,NMAX,NSKIP
C     WRITE(18,8879)  NNG
```

```
C8879  FORMAT( 'NNG = ', I4 )
       NMIN=NNG-1
       IF(NNG.EQ.0) NMIN=1
       NG=FLOAT(NNG)
       NGEO = JMOD(NNG,2)
C
C   SET HIGHEST K IN SYMMETRIC TOP EXPANSION OF GROUND
C     STATE EIGENFUNCTIONS
       KMAXG(1)= 2*IKMAX(NNG,4)
       KMAXG(2)= 2*(IKMAX(NNG,2)) - 1
       KMAXG(3)= KMAXG(2)
       KMAXG(4)= KMAXG(1)
       KKKMAX=4
       IF(NNG.EQ.1) KKKMAX=3
       IF(NNG.EQ.0) KKKMAX=1
C
C   DEFINE ALL CONSTANTS DEPENDING ON NG ONLY
       TWONG = NG + NG
       DEMFAC1 = 1. /
    1              SQRT( (TWONG + 3.)*( TWONG + 2.)*( TWONG + 1.) )
       T3J00A = SQ2*( NG + 1.)*DEMFAC1
       T3J01A = SQRT( ( NG + 2.)*( NG + 1.) )*DEMFAC1
       IF( NNG .EQ. 0 )  GO TO 391
       DEMFAC2 = 1. / SQRT( ( NG + 1.)*( TWONG + 1.)*NG  )
       DEMFAC3 = 1. / SQRT( ( TWONG + 1.)*NG*( TWONG - 1.) )
       T3J00B = NG*DEMFAC3
       T3J01B =  1. / SQRT( 4.*NG + 2.)
       T3J01C = DSQ2*SQRT( NG*( NG - 1.) )*DEMFAC3
C
391    DO 305 KGRPG=1,KKKMAX
C   GET THE SYMMETRY OF THE GROUND STATE LEVEL
       ISYMG= NKSYM(NGEO,KGRPG)
C
C   GET THE SYMMETRIES OF THE THREE POSSIBLE TRANSITION MOMENT-
C   ALLOWED EXCITED STATE LEVELS.
C   ( 0 MEANS TRANSITION IS DIPOLE FORBIDDEN )
       DO 50 I = 1, 3
         ISYMIJ(I) = IJSYM(I,ITMA,ISYMG)
50     CONTINUE
       EXPFAC1 = (-1)**(KMAXG(KGRPG))
C
       DO 308 ITAUG=1,IKMAX(NNG,KGRPG)
C
       ENRGY = EG(NNG,ITAUG,KGRPG)
C      WRITE(18,8878)  ENRGY
C8878  FORMAT(  ' GROUND STATE ENERGY: ', F12.6 )
       IF( ENRGY .GT. EMAX )  GO TO 308
       BOLT = STATWT(ISYMG)*EXP(-1.*ENRGY/(20.84*T))
    1                *(-1.)**NGEO*(2.*NG+1.)
C
```

```
C    FILL THE F6J, RF, AND IFF ARRAYS FOR THE CURRENT GROUND STATE
        DO 3040 NNJ = NMIN, NNG + 1
        INDEX = NNJ - NNG + 2
        NJ = FLOAT(NNJ)
C
C    THE FIRST INDEX OF F6J IS ALWAYS > OR = TO THE SECOND.
        DO 3333  NNI = NNJ, NNG + 1
           NI = FLOAT(NNI)
           INDEX2 = NNI - NNG + 2
           LMIN = 0
           IF( NNI .NE. NNJ )  LMIN = 2
           DO 3333  LL = LMIN, 2, 2
              F2 = (2.*FLOAT(LL)+1.)* T3J11(LL,0,0,0)*SIXJ(DDD)
              F6JPL(INDEX2,INDEX,LL) = F2*T3J11(LL,0,0,0)
              F6JPR(INDEX2,INDEX,LL) = F2*-1.*T3J11(LL,1,-1,0)
3333    CONTINUE
C
        FAC11=1.
        IF(NNJ.EQ.NNG) FAC11=-1.
        EXFAC1=(-1.)**(NNJ+KMAXG(KGRPG)+1)
C
C   IS NNJ EVEN OR ODD?
        NJEO = JMOD(NNJ,2)
C
C   CYCLE THROUGH KGROUPS CORRESPONDING TO ALLOWED IJ SYMMETRIES
C     AND THE VALUE FOR NNJ.
        DO 3040 I = 1, 3
        IF( ISYMIJ(I) .EQ. 0 )  GO TO 3040
        KGRPJ = NSYMK( NJEO,ISYMIJ(I) )
        IF(IKMAX(NNJ,KGRPJ) .EQ. 0) GO TO 3040
C
        KKFAC = KFAC(I)
C
        EXFAC2=(-1.)**(NNG+KMAXG(KGRPG)+KKFAC)
        EXFAC3=(-1.)*EXFAC2
C
        DO 3030 ITAUJ = 1, IKMAX(NNJ,KGRPJ)
C
        RF1 = 0.
        IF1 = 0.
C
        DO 303 KKG = KMAXG(KGRPG), 1, -2
C
        DO 303 KKJ = KKG - KKFAC, KKG + KKFAC, 2
        IF( ABS(KKJ) - NNJ )   710, 710, 303
710     KJ = FLOAT(KKJ)
        KG = FLOAT(KKG)
        IQ = KKJ - KKG
        FAC1=1.
C
        IF(IQ) 720,727,723
```

```
720     KJ = -KJ
        KG = -KG
        FAC1=FAC11
C
C     KJ = KG + 1
723     IF( NNG - NNJ ) 724,725,726
C       NJ > NG
724     T3JIG = EXFAC3*SQRT( (NG+KJ)*(NG+KJ+1) )*DEMFAC1
        GO TO 750
C       NJ = NG
725     T3JIG = FAC1* EXFAC3*SQRT( (NJ-KG)*(NJ+KG+1) )*DSQ2*DEMFAC2
        GO TO 750
C       NJ < NG
726     T3JIG = EXFAC1*SQRT( (NJ-KG)*(NJ-KG+1) )*DSQ2*DEMFAC3
        GO TO 750
C
C     FOR  KJ = KG  i.e. Q = 0 (ABSORPTION ALONG Z)
727     IF( NNG - NNJ )  728, 729, 730
C       NJ > NG
728     T3JIG = EXFAC3*SQRT( (NG-KJ+1)*(NG+KJ+1)*2.)*DEMFAC1
        GO TO 750
C       NJ = NG
729     T3JIG =  EXFAC2*KG*DEMFAC2
        GO TO 750
C       NJ < NG
730     T3JIG =  EXFAC1*SQRT( (NJ+KG+1)*(NJ-KG+1) )*DEMFAC3
C
750     F1 = T3JIG*
     1   EIVECG(NNG,ITAUG,KKG,KGRPG)*  EIVEC(NNJ,ITAUJ,KKJ,KGRPJ)
        IF1 = IDPA(2-IQ)*F1  + IF1
        RF1 = RDPA(2-IQ)*F1  + RF1
303     CONTINUE
        IF( I-2 )  751, 752, 751
751     IF( KKFAC )  9999, 752, 7511
C
7511    IF1 = IF1 + IF1
        RF1 = 0.
        GO TO 753
C
752     RF1 = RF1 + RF1
        IF1 = 0.
C
753     IF( KGRPG .NE. 1 )  GO TO 3020
C
C     KGRPG IS 1: ADD APPROPRIATE KG = 0 TERMS
        IF(KKFAC)  9999, 3010, 3015
C     KFAC IS 0, IDPA = 0  --->   ADD KJ = KG = 0 TERM
3010    IF( NNG - NNJ )  3011, 3020, 3012
C       NJ > NG
3011    T3JIG = EXFAC3*T3J00A
        GO TO 3013
C       NJ < NG
3012    T3JIG = EXFAC2*T3J00B
```

```
3013    RF1 = RF1 + RDPA(2)*T3JIG*EIVECG(NNG,ITAUG,0,1)*
     1                                   EIVEC(NNJ,ITAUJ,0,KGRPJ)
        GO TO 3020
C
C     KFAC IS 1  --->  ADD KJ = 1, KG = 0 TERM
3015    IF( NNG - NNJ )  3016, 3017, 3018
C       NJ > NG
3016    T3JIG = EXFAC3*T3J01A
        GO TO 3019
C       NJ = NG
3017    T3JIG = EXFAC3*T3J01B
        GO TO 3019
C       NJ < NG
3018    T3JIG = EXFAC3*T3J01C
C
3019    F1 = T3JIG*EIVECG(NNG,ITAUG,0,1)*EIVEC(NNJ,ITAUJ,1,KGRPJ)
        IF( I-2 )  754, 755, 754
754     IF1 = IF1 + 2.*IDPA(1)*F1
        GO TO 3020
C
755     RF1 = RF1 + 2.*RDPA(1)*F1
C
3020    RF(I,INDEX,ITAUJ) = RF1
        IFF(I,INDEX,ITAUJ) = IF1
3030    CONTINUE
3040    CONTINUE
C
C     START EXCITED STATE SUMS
        DO 302 NNJ=NMIN,NNG+1
        NDGJ = NNJ - NNG + 2
        NJ = FLOAT(NNJ)
C
        KMAXJ(1) = 2*IKMAX(NNJ,4)
        KMAXJ(2) = 2*( IKMAX(NNJ,2) ) - 1
        KMAXJ(3) = KMAXJ(2)
        KMAXJ(4) = KMAXJ(1)
C     IS NNJ EVEN OR ODD
        NJEO = JMOD(NNJ,2)
C
        NTNP1 = NJ*( NJ + 1.)
        TWONJ = NJ + NJ
        TWONJFAC = (TWONJ+4.)*(TWONJ+3.)*(TWONJ+2.)*(TWONJ+1.)
        DEMFAC4 = 1./( (TWONJ+5.)*TWONJFAC  )
        IF( NNJ .EQ. 0 ) GO TO 392
        DEMFAC5 = 1./( TWONJ*TWONJFAC )
        DEMFAC6 = SQRT( (TWONJ+4.)*DEMFAC5 / (TWONJ-1.) )
C
C   CYCLE THROUGH KGROUPS CORRESPONDING TO THE ALLOWED SYMMETRIES
C     AND THE VALUE FOR NNJ.
```

```
392     DO 302 I = 1, 3
        IF( ISYMIJ(I) .EQ. 0 )  GO TO 302
        KGRPJ = NSYMK( NJEO, ISYMIJ(I) )
        IF(IKMAX(NNJ,KGRPJ)  .EQ. 0) GO TO 302
        EXFAC7 = (-1)**( NNJ + KMAXJ(KGRPJ) )
        NJFAC = Q2SUMLE0*EXFAC7 / SQRT( TWONJ + 1.)
        F7LE0PL = F6JPL(NDGJ,NDGJ,0)*NJFAC
        F7LE0PR = F6JPR(NDGJ,NDGJ,0)*NJFAC
C
        DO 301 NNI=NNJ,NNG+1
C       WRITE(18,8877)  NNJ, NNI
C8877   FORMAT( ' NNJ = ', I4, ' NNI = ', I4 )
        NDGI = NNI - NNG + 2
        NI=FLOAT(NNI)
C       KMAXI(1) = 2*IKMAX(NNI,4)
        KMAXI(2) = 2*( IKMAX(NNI,2) ) - 1
        KMAXI(3) = KMAXI(2)
        KMAXI(4) = KMAXI(1)
C
        FAC33=1.
        IF(NNI.EQ.NNJ+1) FAC33=-1.
C
        F1 = FAC33*(2.*NI+1.)*(TWONJ+1.)
C
C   IS NNI EVEN OR ODD?
        NIEO = JMOD(NNI,2)
C   CYCLE THROUGH KGROUPS CORRESPONDING TO THE ALLOWED
C     IJ SYMMETRIES AND THE VALUE FOR NNI.
        IIMIN = 1
        IF( NNI .EQ. NNJ )  IIMIN = I
        DO 300 II = IIMIN, 3
        IF( ISYMIJ(II) .EQ. 0 )  GO TO 300
        KGRPI = NSYMK( NIEO, ISYMIJ(II) )
        IF(IKMAX(NNI,KGRPI)  .EQ. 0) GO TO 300
        EXFAC8 = (-1)**( NNJ + KMAXI(KGRPI) )
        MPMX2 = 1
        IF( KFAC(II) .EQ. KFAC(I) )  MPMX2 = 2
C
        DO 307 ITAUJ=1,IKMAX(NNJ,KGRPJ)
        ITAUIMIN=1
        IF(NNI .EQ. NNJ  .AND.  KGRPI .EQ. KGRPJ)  ITAUIMIN = ITAUJ
C
        DO 307 ITAUI=ITAUIMIN,IKMAX(NNI,KGRPI)
        NU = ABS( E(NNI,ITAUI,KGRPI) - E(NNJ,ITAUJ,KGRPJ) )
C       WRITE(18,8880)  NU
C8880   FORMAT( ' NU = ', F12.6 )
        IF( NU .GT. NUMAX) GO TO 307
C
```

```
645       RF7 = 0.
          IF7 = 0.
          RF7PL = 0.
          IF7PL = 0.
          RF7PR = 0.
          IF7PR = 0.
          FAC = 2.
C
          IF( NNJ + 1 - NNI ) 780, 770, 760
C
C     THIS SEGMENT IS FOR NI = NJ
760       IF( KGRPI .NE. KGRPJ  .OR. ITAUI .NE. ITAUJ )  GO TO 656
C
C     DIAGONAL TERM APPEARS ONCE IN SUMMATION
          FAC = 1.
C      L = 0
          RF7PL = F7LEOPL
          RF7PR = F7LEOPR
C
C      L = 2
656       IF(NNI+NNJ-2) 604, 793, 793
793       DO 404 KKJ=-KMAXJ(KGRPJ), KMAXJ(KGRPJ), 2
C
405       DO 504 KKIP= KKJ - MPMX2, KKJ + MPMX2, 2
          IF(ABS(KKIP)-NNI) 406,406,504
406       KIP=FLOAT(KKIP)
          IMU = KKIP - KKJ
C
          IF( IMU ) 764, 766, 765
764       KIP = -KIP
765       IF( ABS(IMU) .EQ. 1 ) GO TO 7666
C      KIP = KJ + 2
          T3JIJ = EXFAC7* SQRT( 6*(NJ+KIP-1)*(NJ+KIP)*
     1                          (NJ-KIP+1)*(NJ-KIP+2)  )*DEMFAC6
          GO TO 790
C      KIP = KJ + 1
7666      T3JIJ = EXFAC8*(1.-2.*KIP)*
     1                    SQRT( 6*(NJ-KIP+1.)*(NJ+KIP)  )*DEMFAC6
          GO TO 790
C      KIP = KJ
766       T3JIJ= EXFAC7*2.*( 3.*KIP*KIP - NTNP1 )*DEMFAC6
C
790       RF7 = RF7 + RQ2SUMLE2(IMU)*T3JIJ*EIVEC(NNI,ITAUI,KKIP,KGRPI)
     1                                   *EIVEC(NNJ,ITAUJ,KKJ,KGRPJ)
          IF7 = IF7 + IQ2SUMLE2(IMU)*T3JIJ*EIVEC(NNI,ITAUI,KKIP,KGRPI)
     1                                   *EIVEC(NNJ,ITAUJ,KKJ,KGRPJ)
504       CONTINUE
404       CONTINUE
          GO TO 800
C
C     THIS SEGMENT IS FOR NI = NJ + 1
770       IF(NNI+NNJ-2) 301, 7931, 7931
7931      DO 4041 KKJ=-KMAXJ(KGRPJ), KMAXJ(KGRPJ), 2
C
          DO 5041 KKIP= KKJ-MPMX2, KKJ+MPMX2, 2
          IF(ABS(KKIP)-NNI) 4061,4061,5041
4061      KIP=FLOAT(KKIP)
          IMU = KKIP - KKJ
          FAC3=1.
C
          IF( IMU ) 7641, 7661, 7651
7641      FAC3 = -1.
          KIP=-KIP
C
7651      IF( ABS(IMU) .EQ. 1 )  GO TO 7667
C      KIP = KJ + 2
          T3JIJ=FAC3*2.*EXFAC8*  SQRT( (NJ+KIP-1)*
     1                 (NJ+KIP)*(NJ+KIP+1)*  (NJ-KIP+2)*DEMFAC5 )
          GO TO 7901
C      KIP = KJ + 1
7667      T3JIJ = FAC3*(-2.)*EXFAC7*(NJ-2.*KIP+2.)*
     1                         SQRT( (NJ+KIP+1.)*(NJ+KIP)*DEMFAC5 )
          GO TO 7901
C      KIP = KJ
7661      T3JIJ= EXFAC8*(-2.)*KIP*
     1                       SQRT( 6*(NJ-KIP+1)*(NJ+KIP+1)*DEMFAC5 )
C
7901      RF7 = RF7 + RQ2SUMLE2(IMU)*T3JIJ*EIVEC(NNI,ITAUI,KKIP,KGRPI)
     1                                   *EIVEC(NNJ,ITAUJ,KKJ,KGRPJ)
          IF7 = IF7 + IQ2SUMLE2(IMU)*T3JIJ*EIVEC(NNI,ITAUI,KKIP,KGRPI)
     1                                   *EIVEC(NNJ,ITAUJ,KKJ,KGRPJ)
5041      CONTINUE
4041      CONTINUE
          GO TO 800
C
C     THIS SEGMENT IS FOR NI = NJ + 2
780       DO 4042 KKJ=-KMAXJ(KGRPJ), KMAXJ(KGRPJ), 2
C
          DO 5042 KKIP = KKJ-MPMX2, KKJ+MPMX2, 2
          KIP=FLOAT(KKIP)
          IMU = KKIP - KKJ
C
          IF( IMU ) 7642, 7662, 7652
7642      KIP = -KIP
7652      IF( ABS(IMU) .EQ. 1 )  GO TO 7668
C      KIP = KJ + 2
          T3JIJ = EXFAC8*SQRT( (NJ+KIP-1)*(NJ+KIP)*(NJ+KIP+1)*
     1                         (NJ+KIP+2)*DEMFAC4 )
          GO TO 7902
C      KIP = KJ + 1
7668      T3JIJ = 2.*EXFAC8*SQRT( (NJ-KIP+2.)*(NJ+KIP+2.)*(NJ+KIP+1.)
     1                                      *(NJ+KIP)*DEMFAC4 )
          GO TO 7902
C      KIP = KJ
7662      T3JIJ= EXFAC8* SQRT( 6*(NJ-KIP+2)*
     1                 (NJ-KIP+1)*(NJ+KIP+2)*(NJ+KIP+1)*DEMFAC4  )
```

```
C
7902    RF7 = RF7 + RQ2SUMLE2(IMU)*T3JIJ*EIVEC(NNI,ITAUI,KKIP,KGRPI)
     1                                  *EIVEC(NNJ,ITAUJ,KKJ,KGRPJ)
        IF7 = IF7 + IQ2SUMLE2(IMU)*T3JIJ*EIVEC(NNI,ITAUI,KKIP,KGRPI)
     1                                  *EIVEC(NNJ,ITAUJ,KKJ,KGRPJ)
5042    CONTINUE
4042    CONTINUE
C
800     RF7PL = RF7PL + F6JPL(NDGI,NDGJ,2)  * RF7
        IF7PL = IF7PL + F6JPL(NDGI,NDGJ,2)  * IF7
        RF7PR = RF7PR + F6JPR(NDGI,NDGJ,2)  * RF7
        IF7PR = IF7PR + F6JPR(NDGI,NDGJ,2)  * IF7
604     CONTINUE
C
        RKSJ = DPSYM(I)*RF(I,NDGJ,ITAUJ)
        IKSJ = IFF(I,NDGJ,ITAUJ)
        RKSI = RF(II,NDGI,ITAUI)
        IKSI = IFF(II,NDGI,ITAUI)
        RKKSUMS = RKSJ*RKSI - IKSJ*IKSI
        IKKSUMS = RKSJ*IKSI + RKSI*IKSJ
C
        INU = NINT( NU/NURES ) + 1
        IF(INU .GT. INUMAX)  INUMAX = INU
        RRR = EXPFAC1*F1*BOLT*FAC
        FMDPL(INU)= FMDPL(INU) +
     1                        RRR*( RKKSUMS*RF7PL - IKKSUMS*IF7PL )
        IF( INU .NE. 1 )  GO TO 307
        FMDPR1 = FNDPR1 + RRR*( RKKSUMS*RF7PR - IKKSUMS*IF7PR )
C
307     CONTINUE
300     CONTINUE
301     CONTINUE
302     CONTINUE
308     CONTINUE
305     CONTINUE
C
C   WE USE A FREQUENCY RESOLUTION OF (NURES) GHZ
C     AND A MAXIMUM OF (NUMAX) GHZ
        CONSTANT= TWOPI*CT*0.001*NURES
C
C   CALCULATE PARALLEL AND PERPENDICULAR DECAYS
        DO 621 I=1, NPTS
621        DECAYPL(I)=0.
C
        YMAX = 0.
        DO 602 J = 2, INUMAX
        IF( FMDPL(J) .EQ. 0. )  GO TO 602
        OMEGA = FLOAT( J - 1 )*CONSTANT
        DO 605 I = 1, NPTS
C       WRITE(18,8881)  OMEGA, I
C8881   FORMAT( 'OMEGA = ', F10.4, ' AT DECAY PT. ', I4 )
605     DECAYPL(I) = DECAYPL(I) + FMDPL(J)*COS( OMEGA*FLOAT(I-1) )
602     CONTINUE
C
        DO 706 I = 1, NPTS
           DECAYPR(I) = -0.5*DECAYPL(I) + FMDPR1
           DECAYPL(I) = DECAYPL(I) + FMDPL(1)
           IF(DECAYPL(I).GT.YMAX) YMAX = DECAYPL(I)
706     IF(DECAYPR(I).GT.YMAX) YMAX = DECAYPR(I)
        SCALE=5000./YMAX
C
        DO 707 I=1,NPTS
           DECAYPL(I)= DECAYPL(I)*SCALE
707        DECAYPR(I)= DECAYPR(I)*SCALE
C
        OPEN(UNIT=22, FILE='AT1PL.DAT', ACCESS='SEQUENTIAL',
     1   RECORDTYPE='SEGMENTED', FORM='UNFORMATTED', STATUS='NEW')
        WRITE(22) NMAX,T,A1,B1,C1,ITMA,ITMB,0,NPTS,CT,SCALE,
     1   (DECAYPL(I), I=1,NPTS)
        CLOSE(UNIT=22, DISP='SAVE')
C
999     OPEN(UNIT=22, FILE='AT1PR.DAT', ACCESS='SEQUENTIAL',
     1   RECORDTYPE='SEGMENTED', FORM='UNFORMATTED', STATUS='NEW')
        WRITE(22) NMAX,T,A1,B1,C1,ITMA,ITMB,1,NPTS,CT,SCALE,
     1   (DECAYPR(I), I=1,NPTS)
        CLOSE(UNIT=22, DISP='SAVE')
C
        STOP
C
C     THIS SEGMENT IS NOT REACHED UNLESS SOMETHING ISN'T WORKING.
9999    NMAX = 1
        GO TO 999
        END
C
C
        FUNCTION SIXJ(DDD)
```

[See the end of Appendix III for a copy of this subroutine.]

Appendix III

Fortran program ATFIT2

ATFIT2 is a general fitting program for purely rotational coherence in asymmetric top molecules. It searches the parameter space of A', B', C', T_{ROT}, and t_0 for the best fit of a simulated, principal-axis dipole PRC signal to a given input data file. The subroutine ATT3 calculates the simulation file for each trial set of rotational constants for up to three temperatures per call. ATEIG solves for the asymmetric top rotational energies and eigenfunctions by calling the IMSL Library routine EIGRS. CONVOL convolutes the calculated intensities with the given system response function. The parameter IPOL is set to 0 or 2 to indicate that the data to be fit is in the form of parallel fluorescence (with the decay due to the excited state lifetime removed) or of fluorescence anisotropy. The near-symmetric treatment may be chosen by setting the flag INEAR. Further details of the fitting procedure are discussed in Chapter 4.

```
      PROGRAM ATFIT2
C   TO DETERMINE THE ROTATIONAL COHERENCE PARAMETERS
C   RESULTING IN THE BEST FIT TO THE INPUT FILE ATFITD.DAT.
C   THE GROUND STATE STRUCTURE IS HELD FIXED AS GIVEN IN
C   THE FILE ASYMG.DAT.  THE CALCULATED BEATING DECAYS ARISE
C   FROM THE COHERENT PREPARATION OF ROTATIONAL LEVELS IN AN
C   AN ASYMMETRIC TOP MOLECULE.  ONE FREQUENCY RESOLUTION
C   AND ONE TEMPORAL RESOLUTION ARE USED.  DIPOLES ALONG
C   PRINCIPAL AXES ONLY.
C      GROUND STATES HAVING ENERGY GREATER THAN THE LOWEST
C    ENERGY OF THE N = NMAX + 1 MANIFOLD ARE NOT CONSIDERED.
C
C   INPUT FILES:
C      ATFITIN.DAT  - NMAX IS MAX VALUE OF GROUND STATE TOTAL
C                        ROTATIONAL ANGULAR MOMENTUM Q. N. (NG).
C                        (LARGEST NMAX IS CURRENTLY 45)
C                     NSKIP IS NG INCREMENT.
C                     NPTSD IS THE NUMBER OF DATA POINTS TO CONSIDER
C                     NURES IS THE BEAT FREQUENCY RESOLUTION
C                     TMIN IS THE INITIAL TEMPERATURE
C                     DELT IS THE TEMPERATURE STEP
C                     A0, etc. ARE INITIAL GUESSES AND A1 - A2, etc.
C                           ARE THE RANGES OF ROTATIONAL CONSTANTS
C                     IPOL INDICATES THE TYPE OF DATA TO BE FIT
C                     INEAR IS NON-ZERO FOR NEAR-SYMMETRIC TREATMENT
C                     TO IS TIME ZERO OF THE DATA
C                     DELCONST(I) IS THE STEP SIZE USED FOR
C                              THE Ith ROTATIONAL CONSTANT
C                              IN THE GRADIENT ESTIMATE
C
C      ASYMG.DAT    - GROUND STATE ENERGIES AND EIGENVALUES
C
C      ATFITDIN.DAT - DATA FILE TO BE FIT
C
C      ATFITRIN.DAT - RESPONSE FILE TO BE CONVOLUTED WITH
C                          THE SIMULATION. FIRST CHANNEL
C                          DETERMINES SIMULATION T = 0.
C
C         SIGIN.DAT - FILE OF DENOMINATORS USED IN
C                             CHI-SQUARE CALCULATION
C
C  OUTPUT FILES:
C      FOR018.DAT  - LISTS SETS OF PARAMETERS AND
C                          CORRESPONDING CHI-SQUARED
C
C SUBROUTINES:  ATT3( NT, A, B, C, T, TMIN, CHIMIN, ISHMIN )
C                     -  ATEIG, CONVOL
```

```
C
        REAL IDPA, IDPB, NURES, NUMAX
        DIMENSION  CHISQR1(6), STEP(3), T(3), BB(3)
        DIMENSION  AA(3), DIR(3), DELCONST(3)
        COMMON  T3J11(0:2,-1:1,-1:1,-2:2), KFAC, DPSYM, NMAX, NSKIP,
     1      NRP1, IKMAX(0:46,4), Q2SUMLE2(-2:2), Q2SUMLE0, CT001,
     2      TO, RWIDTH, SUMD, NPTSD, AINFIN, IPOL, ITMA, IJSYM(3,4),
     3      NKSYM(0:1,4), NSYMK(0:1,4), RDPA(3), IDPA(3), RDPB(3),
     4      IDPB(3), NURES, NUMAX, MPMN, MPMX, MPMX2, STATWT(4),
     5      IDEL(4,4), EG(0:46,24,4), EIVECG(0:46,24,-46:46,4)
        COMMON /CONVOL/  NR, R(500)
        COMMON /CHI/  D(5000), SIGDEM(5000)
C
        OPEN(UNIT=21, FILE='ATFITIN.DAT', STATUS='OLD')
        READ(21,9011) NMAX, NSKIP, NPTSD, NURES, NUMAX
        READ(21,903) TMIN, DELT
        READ(21,904) (STATWT(J), J=1,4)
        READ(21,902) A0
        READ(21,902) A1
        READ(21,902) A2
        READ(21,902) B0
        READ(21,902) B1
        READ(21,902) B2
        READ(21,902) C0
        READ(21,902) C1
        READ(21,902) C2
        READ(21,901) ITMA
        READ(21,901) ITMB
        READ(21,901) IPOL
        READ(21,901) INEAR
        READ(21,902) TO
        READ(21,904) DELCONST
        CLOSE(UNIT=21, DISP='SAVE')
9011    FORMAT(I3,2X,I3,2X,I4,2X,F8.6,2X,F8.2)
901     FORMAT(I3)
902     FORMAT(F10.5)
903     FORMAT( 2(2X, F6.2) )
904     FORMAT(4F10.5)
C
C   READ IN RESPONSE AND NORMALIZE
        OPEN(UNIT=22, FILE='ATFITRIN.DAT', ACCESS='SEQUENTIAL',
     1   RECORDTYPE='SEGMENTED', FORM='UNFORMATTED', STATUS='OLD')
        READ(22) NMAXX,TX,AX,BX,CX,ITHAX,ITHBX,IPOLX,NR,CT,
     1   (R(I), I=1,NR)
        CLOSE(UNIT=22, DISP='SAVE')
C
        CT001 = CT*.001
        SUM=0.
        DO 44 I = 1, NR
44        SUM = SUM + R(I)
C
        DO 55 I = 1, NR
55        R(I)=R(I)/SUM
```

```
C
C   READ IN DATA TO BE FIT
        OPEN(UNIT=22, FILE='ATFITDIN.DAT', ACCESS='SEQUENTIAL',
     1   RECORDTYPE='SEGMENTED', FORM='UNFORMATTED', STATUS='OLD')
        READ(22) NMAXX,TX,AX,BX,CX,ITMAX,ITMBX,IPOLX,NPTS,CT1,
     1   ( D(I), I = 1, NPTSD )
        CLOSE(UNIT=22, DISP='SAVE')
C
        IF( CT1 .EQ. CT )  GO TO 66
        WRITE(18,200)
200     FORMAT( ' The time resolutions do not agree. ' )
        STOP
C
66      OPEN(UNIT=27, NAME='SIGIN.dat', ACCESS='SEQUENTIAL',
     1   RECORDTYPE='SEGMENTED', FORM='UNFORMATTED', STATUS='OLD')
        read(27) NMAXX, TX, AX, BX, CX, ITMAX, ITMBX, IPOLX,
     1   NPTSX, CTX, ( SIGDEN(I), I = 1, NPTSX )
        CLOSE(UNIT=27, DISP='SAVE')
        IF( NPTSX .EQ. NPTSD )  GO TO 67
        WRITE(18,201)
201     FORMAT( ' Wrong time range for sigma file. ' )
        STOP
C
67      SUMD = 0.
        DO 6767 I = 1, NPTSD
6767      SUMD = SUMD + D(I)
C
        IF( IPOL .NE. 2 )  GO TO 77
        RINFIN = SUMD/NPTSD
        AINFIN = ( 1 + 2.*RINFIN )/( 1. - RINFIN )
C
77      SQ2=SQRT(2.)
        DSQ2=1./SQ2
C   ALL PARAMETER SETS WILL BE TREATED IN THE SAME BASIS
C     ( PROLATE OR OBLATE )
        RKA=( 2.*B0 - A0 - C0 )/( A0 + C0 )
C   SET EXCITED STATE SYMMETRIES FOR GIVEN A-TRANSITION
C     MOMENT DIRECTION AND GROUND STATE SYMMETRY USING
C     THE ARRAY IJSYM(II,JJ), WHERE II IS THE MOMENT
C     DIRECTION (1=A,2=B,3=C) AND JJ IS THE SYMMETRY
C     (1=++, 2=-+, 3=--, 4=+- IN THE C,A NOTATION)
        DATA IJSYM / 2,3,4,
     2   1,4,3,
     3   4,1,2,
     4   3,2,1/
C
C   UNRESTRICTIVE LIMITS ARE SET ON DELTA TAU FOR THE GENERAL CASE
        DATA IDEL / 30,30,30,30,
     2              30,30,30,30,
     3              30,30,30,30,
     4              30,30,30,30/
       IF(RKA.GT.0.) GO TO 10
```

```
C
        IF( INEAR .EQ. 0 )  GO TO 22
        WRITE(18,33)
33      FORMAT(' The near-symmetric approximation will be applied.')
C   SET NEAR-SYMMETRIC TOP PROLATE LIMITS ON DELTA TAU
C     AS A FUNCTION OF GROUND AND EXCITED KGROUP USING
C     THE ARRAY IDEL(KGRPG,KGRPJ).
        IDEL(1,1) = 0
        IDEL(1,2) = 1
        IDEL(1,3) = 1
        IDEL(1,4) = 1
        IDEL(2,1) = 1
        IDEL(2,2) = 0
        IDEL(2,3) = 0
        IDEL(2,4) = 1
        IDEL(3,1) = 1
        IDEL(3,2) = 0
        IDEL(3,3) = 0
        IDEL(3,4) = 1
        IDEL(4,1) = 1
        IDEL(4,2) = 1
        IDEL(4,3) = 1
        IDEL(4,4) = 0
C
C   SET THE PROLATE CORRELATIONS BETWEEN BASIS SET AND ROTATIONAL
C   SYMMETRY USING THE ARRAY NKSYM(II,JJ), WHERE II IS THE INTEGER
C   PARITY OF THE TOTAL ANGULAR MOMENTUM QUANTUM NUMBER (II=0
C   STANDS FOR EVEN INTEGER, II=1 STANDS FOR ODD) AND JJ GIVES THE
C   BASIS SET "KGROUP" NUMBER (1=EVEN K AND SYMMETRIC COMBINATION,
C   2=ODD K AND ANTISYMMETRIC COMBINATION, 3=ODD K AND SYMM. COMB.,
C   4=EVEN AND ANTISYM.)
22      NKSYM(0,1)=1
        NKSYM(1,1)=2
        NKSYM(0,2)=4
        NKSYM(1,2)=3
        NKSYM(0,3)=3
        NKSYM(1,3)=4
        NKSYM(0,4)=2
        NKSYM(1,4)=1
C
C   SET THE VALUES FOR PROLATE SYMMETRY TO "KGROUP" CONVERSION
C     USING THE ARRAY NSYMK(II,JJ), WHERE II IS THE INTEGER
C     PARITY (EVEN OR ODD) OF THE TOTAL ANGULAR MOMENTUM Q.N.
C     AND JJ IS THE SYMMETRY NUMBER (SEE ABOVE).
        NSYMK(0,1)=1
        NSYMK(1,1)=4
        NSYMK(0,2)=4
        NSYMK(1,2)=1
        NSYMK(0,3)=3
        NSYMK(1,3)=2
        NSYMK(0,4)=2
        NSYMK(1,4)=3
        GO TO 11
```

```
C
10        CONTINUE
          IF( INEAR .EQ. 0 )  GO TO 212
C   OBLATE LIMITS ON DELTA TAU
          IDEL(1,1) = 1
          IDEL(1,2) = 1
          IDEL(1,3) = 1
          IDEL(1,4) = 1
          IDEL(2,1) = 1
          IDEL(2,2) = 1
          IDEL(2,3) = 1
          IDEL(2,4) = 1
          IDEL(3,1) = 1
          IDEL(3,2) = 1
          IDEL(3,3) = 1
          IDEL(3,4) = 1
          IDEL(4,1) = 1
          IDEL(4,2) = 1
          IDEL(4,3) = 1
          IDEL(4,4) = 1
C
C   OBLATE CORRELATIONS BETWEEN "KGROUP" AND SYMMETRY
212       NKSYM(0,1)=1
          NKSYM(1,1)=4
          NKSYM(0,2)=2
          NKSYM(1,2)=3
          NKSYM(0,3)=3
          NKSYM(1,3)=2
          NKSYM(0,4)=4
          NKSYM(1,4)=1
C
          NSYMK(0,1)=1
          NSYMK(1,1)=4
          NSYMK(0,2)=2
          NSYMK(1,2)=3
          NSYMK(0,3)=3
          NSYMK(1,3)=2
          NSYMK(0,4)=4
          NSYMK(1,4)=1
C
11        CONTINUE
C
C   SET DIPOLE VALUES FOR THE POSSIBLE TRANSITION DIRECTIONS.
C     THE "NEAR" TOP AXIS IS ALWAYS MADE THE Z AXIS, AND THE
C     INTERMEDIATE AXIS (B AXIS) IS ALWAYS X.
C
          IF(RKA) 1,1,5
C   PROLATE ROTORS
C    ABSORPTION MOMENTS FIRST
1         IF(ITMA.EQ.2) GO TO 3
          IF(ITMA.EQ.3) GO TO 4
```

```
C         Z-AXIS IS THE A-AXIS
          IDPA(2)=0.
          RDPA(2)=1.
          KFAC=0
          DPSYM = 1.
          GO TO 9
C         X-AXIS IS THE B-AXIS
3         IDPA(1)=0.
          IDPA(3)=0.
          RDPA(1) = -DSQ2
          RDPA(3) = DSQ2
          KFAC=1
          DPSYM = -1.
          GO TO 9
C         Y-AXIS IS THE C-AXIS
4         IDPA(1)=-DSQ2
          IDPA(3)=-DSQ2
          RDPA(1)=0.
          RDPA(3)=0.
          KFAC=1
          DPSYM = 1.
C
C   PROLATE EMISSION MOMENTS
9         IF(ITMB.EQ.2) GO TO 102
          IF(ITMB.EQ.3) GO TO 103
          RDPB(2) = 1.
          IDPB(2) = 0.
          NPMN=0
          NPMX=0
          GO TO 99
102       RDPB(1) = -1.*DSQ2
          RDPB(3) = 1.*DSQ2
          NPMN=-1
          NPMX=1
          GO TO 99
103       IDPB(1) = -1.*DSQ2
          IDPB(3) = -1.*DSQ2
          NPMN=-1
          NPMX=1
          GO TO 99
C
C   OBLATE ROTOR
5         CONTINUE
          IF(ITMA.EQ.2) GO TO 7
          IF(ITMA.EQ.3) GO TO 8
C         Y-AXIS IS THE A-AXIS
          IDPA(1)=-DSQ2
          IDPA(3)=-DSQ2
          RDPA(1)=0.
          RDPA(3)=0.
          KFAC=1
          DPSYM = 1.
          GO TO 109
```

```
C       X-AXIS IS THE B-AXIS
7       IDPA(1)=0.
        IDPA(3)=0.
        RDPA(1) = -DSQ2
        RDPA(3) = DSQ2
        KFAC=1
        DPSYM = -1.
        GO TO 109
C       Z-AXIS IS THE C-AXIS
8       IDPA(2)=0.
        RDPA(2)=1.
        KFAC=0
        DPSYM = 1.
C
C    OBLATE EMISSION MOMENT
109     IF(ITMB.EQ.2) GO TO 202
        IF(ITMB.EQ.3) GO TO 203
        IDPB(1) = -1.*DSQ2
        IDPB(3) = -1.*DSQ2
        MPMN=-1
        MPMX=1
        GO TO 99
202     RDPB(1) = -1.*DSQ2
        RDPB(3) = 1.*DSQ2
        MPMN=-1
        MPMX=1
        GO TO 99
203     RDPB(2) = 1.
        IDPB(2) = 0.
        MPMN=0
        MPMX=0
99      CONTINUE
C
C    CALCULATE THE NUMBER OF ROTATIONAL STATES FOR ANY (N,KGRP)
        DO 5511 N = 0, NMAX + 1
           IKMAX(N,1) = INT(FLOAT(N)/2.) + 1
           IKMAX(N,2) = INT(FLOAT(N+1)/2.)
           IKMAX(N,3) = IKMAX(N,2)
           IKMAX(N,4) = IKMAX(N,1) - 1
5511    CONTINUE
C
C   INPUT EIGENVALUES AND EIGENVECTORS OF THE
C     ASYMMETRIC TOP GROUND STATE
C
        OPEN(UNIT=22,FILE='ASYMG.DAT',ACCESS='SEQUENTIAL',
     1   RECORDTYPE='SEGMENTED',EXTENDSIZE=200,FORM='UNFORMATTED',
     1   TYPE='OLD')
```

```
C   E(NMAX+1) IS NEEDED TO FIX MAXIMUM ENERGY
        DO 12 N = 0, NMAX + 1
        KGMX=4
        NN=N
        IF(N.EQ.0) KGMX=1
        IF(N.EQ.1) KGMX=3
        DO 12 KGRP=1,KGMX
        IKM=IKMAX(N,KGRP)
        READ(22) KKGRP, (EG(NN,ITAU,KKGRP), ITAU=1,IKM),
     1   ((EIVECG(NN,ITAU,IK,KKGRP), IK=1,IKM), ITAU=1,IKM)
        PM=-1.
        IF(KGRP.EQ.1.OR.KGRP.EQ.3) PM=1.
C
C   GET SYMMETRIC TOP COEFFICIENTS FROM + AND - COMBINATIONS
C   AND CONVERT THE IK INDEX TO SYMMETRIC TOP K VALUES
        DO 16 ITAU=1,IKM
        EIVECG(NN,ITAU,0,4)=0.
C       WRITE(16,41)  EG(NN,ITAU,KGRP)
        DO 16 IIK=1,IKM
        IK=IKM+1-IIK
        K=2*IK-1
        IF(KGRP.EQ.1) K=2*(IK-1)
        IF(KGRP.EQ.4) K=2*IK
        IF(KGRP.EQ.1.AND.IK.EQ.1) GO TO 18
        GO TO 17
18      EIVECG(NN,ITAU,0,1)= EIVECG(NN,ITAU,1,1)
        EIVECG(NN,ITAU,1,1)=0.
        GO TO 16
17      EIVECG(NN,ITAU,-K,KGRP)=PM*DSQ2*EIVECG(NN,ITAU,IK,KGRP)
        EIVECG(NN,ITAU,K,KGRP)=DSQ2*EIVECG(NN,ITAU,IK,KGRP)
16      CONTINUE
12      CONTINUE
        CLOSE(UNIT=22, DISP='SAVE')
C
C   ZERO ELEMENTS OF UNDEFINED KGROUPS (NECESSARY?)
        DO 35 ITAU = 1, (NMAX+1)/2 + 1
        DO 35 K = -1*(NMAX), NMAX
        EIVECG(0,ITAU,K,2)=0.
        EIVECG(0,ITAU,K,3)=0.
        EIVECG(0,ITAU,K,4)=0.
35      EIVECG(1,ITAU,K,4)=0.
C
        DO 622 I=0,2,2
        DO 622 J = -1, 1
        DO 622 II = -1, 1
        DO 622 JJ=-2,2
622     T3J11(I,J,II,JJ) = 0.
```

```
C
        DSQ3 = 1./SQRT(3.)
        DSQ30 = 1./SQRT(30.)
        T3J11(0,0,0,0)= -1.*DSQ3
        T3J11(0,1,-1,0)= DSQ3
        T3J11(0,-1,1,0)= DSQ3
        T3J11(2,0,0,0) = 2.*DSQ30
        T3J11(2,1,-1,0)= DSQ30
        T3J11(2,-1,1,0)= DSQ30
        T3J11(2,-1,-1,2)= 1./SQRT(5.)
        T3J11(2,1,1,-2) = 1./SQRT(5.)
        MPMX2=2*MPMX
C
        Q2SUMLE0 = 0.
        DO 655 MMP=MPMN,MPMX,2
          Q2SUMLE0 = Q2SUMLE0 + ( RDPB(2-MMP)*RDPB(2+MMP) -
     1               IDPB(2-MMP)*IDPB(2+MMP) )*T3J11(0,MMP,-MMP,0)
655     CONTINUE
C
C    ONLY EVEN IMU NEEDED WHEN EXCITED STATES ARE OF SAME KGROUP
        DO 304 IMU = -2, 2, 2
        Q2SUMLE2(IMU) = 0.
        DO 304 MMP=MPMN,MPMX,2
           NNP = MMP + IMU
           IF(ABS(NNP)-MPMX) 350,350,304
350        Q2SUMLE2(IMU) = Q2SUMLE2(IMU) + ( RDPB(2-MMP)*RDPB(2+NNP)
     1             - IDPB(2-MMP)*IDPB(2+NNP)  )*T3J11(2,MMP,-NNP,IMU)
304     CONTINUE
C
C   SET INITIAL PARAMETERS
        RWIDTH = FLOAT(NR+1)*CT001
        NRP1 = NR + 1
        NT = 3
        TTMIN = 0.3
        STEPMIN = .6*DELCONST(2)
        BB(1) = A0
        BB(2) = B0
        BB(3) = C0
        IFLAG = 0
        ITER = 0
        IF( TMIN .LT. TTMIN )  TMIN = TTMIN
        DO 6188 I = -1, 1
6188      T(I+2) = TMIN + FLOAT(I)*DELT
C   INITIALIZE CHI-SQUARED
        CALL ATT3( 3, BB(1), BB(2), BB(3), T, TMIN, CHIMIN, ISH )
C
C   FITTING LOOP STARTS HERE. SET TEMPERATURES AND
C    TRY NEW DIRECTION UNLESS ITER TOO BIG.
60166   CHIOLD = CHIMIN
        T0 = T0 + FLOAT( ISH ) * CT001
        WRITE(18,6050)  BB, TMIN, AINFIN, ISH, CHIMIN
60177   IF( TMIN .LT. TTMIN )  TMIN = TTMIN
        DO 60188 I = -1, 1
60188   T(I+2) = TMIN + FLOAT(I)*DELT
C
60155   ITER = ITER + 1
        IF( ITER .LT. 10 )  GO TO 6017
        WRITE(18,6016)  ITER
6016    FORMAT( ' Iteration limit of ', I2, ' reached. ' )
        STOP
C
6017    IFLAG2 = 0
        STEPSIZE = 6.*DELCONST(2)
        WRITE(22,8861)
8861    FORMAT( / ' LOOKING FOR A NEW DIRECTION.' )
        DO 6018 I = 1, 3
6018    AA(I) = BB(I)
        III = 0
        CHIMIN1 = 100000000.
        DO 6022 I = 1, 3
        DO 6022 II = -1, 1, 2
        AA(I) = AA(I) + FLOAT(II)*DELCONST(I)
        TTEMP = T(1)
        T(1) = T(2)
        CALL ATT3( 1, AA(1), AA(2), AA(3), T, TDUM, CHIMIN, IDUM )
        T(1) = TTEMP
        III = III + 1
        CHISQR1(III) = CHIMIN
        IF( CHIMIN .LT. CHIMIN1 ) CHIMIN1 = CHIMIN
        IF( CHIMIN .LT. CHIOLD )  IFLAG = 1
        AA(I) = BB(I)
6022    CONTINUE
        STEP(1) = CHISQR1(1) - CHISQR1(2)
        STEP(2) = CHISQR1(3) - CHISQR1(4)
        STEP(3) = CHISQR1(5) - CHISQR1(6)
        STEPNORM = 0.
        DO 6024 I = 1, 3
6024    STEPNORM = STEPNORM + STEP(I)*STEP(I)
        IF( STEPNORM .EQ. 0.)  GO TO 7070
        STEPNORM = SQRT(STEPNORM)
        DO 6025 I = 1, 3
        DIR(I) = STEP(I)/STEPNORM
6025    STEP(I) = DIR(I) * STEPSIZE
        WRITE(18,6040)  ITER, DIR
6040    FORMAT('[',I2,']',' NEW DIRECTION TO MIN: ', 3(F7.5, 1X))
C
        IF( IFLAG .NE. 0 )  GO TO 7020
C   CHI-SQUARED IS HIGHER ALL AROUND THE CURRENT POSITION.
C   CHECK FOR OPTIMUM TEMPERATURE, THEN TRY GRADIENT
C     AGAIN IF NECESSARY
        TTEMP = T(2)
        T(2) = T(3)
        CALL ATT3( 2, BB(1), BB(2), BB(3), T, TMIN, CHIMIN, IDUM )
        IF( CHIMIN .LT. CHIOLD )  GO TO 7080
        T(2) = TTEMP
6999    WRITE(18,7000)  CHIOLD, BB, T(2)
```

```
7000    FORMAT(' The center point, with chi-squared ', F8.3,
     1     ' is the best fit.'/ ' Final values: ', 3( F10.5, 1X ),
     2                      ',   T = ', F5.2, ',  Ainfin = ', F6.4)
        STOP
C
7070    IF( IFLAG .EQ. 0 ) GO TO 6999
        WRITE(18,7071)
7071    FORMAT
     1 (' The gradient is zero, but chi-squared is not minimum.')
        STOP
C
C    GO ANOTHER STEP IN TEMPERATURE IF NOT TOO LOW ALREADY.
7080    CHIOLD = CHIMIN
63131   IF( TMIN .GE. TTMIN )  GO TO 61111
        WRITE(18,62121)  CHIOLD, TMIN, TTMIN
62121   FORMAT( ' Chi-squared = ', F15.6, ' for temperature ',
     1                 F4.2, ', below Tmin = ', F4.2 )
        STOP
C
61111   T(1) = 2.*TMIN - TTEMP
        TTEMP = TMIN
        CALL ATT3( 1, BB(1), BB(2), BB(3), T, TDUM, CHIMIN, IDUM )
C   CONTINUE TO STEP AS LONG AS CHI-SQUARED IMPROVES;
C      OTHERWISE LOOK FOR NEW DIRECTION
        IF( CHIMIN .GT. CHIOLD )  GO TO 60177
        CHIOLD = CHIMIN
        TMIN = T(1)
        GO TO 63131
C
C    THERE IS ROOM FOR IMPROVEMENT IN CHI-SQUARED; TAKE A STEP.
7020    IFLAG = 0
7021    DO 7022 I = 1, 3
7022    BB(I) = BB(I) + STEP(I)
C
C   CHECK ORDER OF ROTATIONAL CONSTANTS
        IF( BB(1) .GT. BB(2)  .AND.  BB(2) .GT. BB(3) )  GO TO 6000
C
C   CONSTANTS OUT OF ORDER. REORDER TEMPORARILY AND CHECK
C   CHI-SQUARED. IF LOWER, LOOK FOR NEW DIRECTION FROM THAT POINT.
        DO 7222 I = 1, 3
          AA(I) = BB(I)
7222    CONTINUE
        CMIN = 10000.
        CMAX = 0.
        DO 7322 I = 1, 3
           IF( AA(I) .GT. CMIN )  GO TO 7322
           CMIN = AA(I)
           IIMIN = 1
           IF( AA(I) .LT. CMAX )  GO TO 7322
           CMAX = AA(I)
           IIMAX = I
7322    CONTINUE
        DO 7422 I = 1, 3
           IF( I .EQ. IIMIN  .OR.  I .EQ. IIMAX )  GO TO 7422
           AA(2) = AA(I)
7422    CONTINUE
        AA(1) = CMAX
        AA(3) = CMIN
        CALL ATT3( 3, AA(1), AA(2), AA(3), T, TMIN, CHIMIN, ISH )
        IF( CHIMIN .GE. CHIOLD ) GO TO 6001
C
C   KEEP THE NEW POINT IF IN RANGE; OTHERWISE STOP
        DO 6002 I = 1, 3
6002      BB(I) = AA(I)
C       IF( 1./BB(1) .GT. 1./BB(3) - 1./BB(2) )  GO TO 5432
C       WRITE(18,60001)
C       STOP
C
5432    IF( BB(1) .LT. A1  .OR.  BB(1) .GT. A2 )  GO TO 7023
        IF( BB(2) .LT. B1  .OR.  BB(2) .GT. B2 )  GO TO 7023
        IF( BB(3) .LT. C1  .OR.  BB(3) .GT. C2 )  GO TO 7023
        GO TO 60166
C
C   LOOK CAREFULLY FOR MINIMUM ONLY WHEN SURE TO BE NEAR CONVERGENCE
6201    IF( STEPSIZE .LT. STEPMIN ) GO TO 6011
C   BACKUP AND TRY SMALLER STEP
6301    DO 6005 I = 1, 3
        BB(I) = BB(I) - 0.8 * STEP(I)
6005    STEP(I) = STEP(I)/5.
        STEPSIZE = STEPSIZE/5.
C
C    CALCULATE CHI-SQUARED AFTER A STEP HAS BEEN TAKEN
6000    CALL ATT3( 3, BB(1), BB(2), BB(3), T, TMIN, CHIMIN, ISH )
        IF( CHIMIN .LT. CHIOLD ) GO TO 6015
C
C   NEW POSITION IS WORSE THAN PREVIOUS ONE;
C    ACTION TO TAKE DEPENDS ON STEPSIZE AND IFLAG2
6001    IF( IFLAG2 .EQ. 0 ) GO TO 6201
C   NOT AT POSITION OF LAST GRADIENT SEARCH SO DON'T NEED
C     STEPSIZE TOO SMALL
        IF( STEPSIZE .LT. 4.*DELCONST(2) ) GO TO 6011
        GO TO 6301
C
C   CAN'T FIND LOWER CHI-SQUARED. IF A NEW DIRECTION IS BEING
C      TRIED, STOP.  OTHERWISE, TRY A NEW DIRECTION.
6011    DO 6006 I = 1, 3
6006      BB(I) = BB(I) - STEP(I)
        IF( IFLAG2 .NE. 0 )   GO TO 60155
C  IFLAG2 = 0 MEANS THIS IS A NEW DIRECTION.
        WRITE(18,6012) CHIMIN1, STEPSIZE, BB
6012    FORMAT( ' Chi min is ', F10.4,' within ',F5.4,' of ',
     1                                                3(F6.4, 2X) )
        STOP
C
```

```
C   CHI-SQUARED IS LOWER; KEEP ON THIS PATH UNLESS OUT OF RANGE.
6015    CHIOLD = CHIMIN
        T0 = T0 + FLOAT( ISH ) * CT001
        WRITE(18,6050)  BB, TMIN, AINFIN, ISH, CHIMIN
6050    FORMAT( ' Chi-squared is improved for constants : ',
     1     3( F7.5, 2X )/ '   T = ', F5.2, '  Ainfin = ', F6.4,
     2      ',   Shift = ', I2, ',   chi-squared = ', F12.6 / )
C       IF( 1./BB(1) .GT. 1./BB(3) - 1./BB(2) )  GO TO 60077
C       WRITE(18,60001)
C60001  FORMAT( ' -- but the constants do not form a valid set.' )
C       STOP
C
60077   IF( BB(1) .LT. A1  .OR.  BB(1) .GT. A2 )  GO TO 7023
        IF( BB(2) .LT. B1  .OR.  BB(2) .GT. B2 )  GO TO 7023
        IF( BB(3) .LT. C1  .OR.  BB(3) .GT. C2 )  GO TO 7023
        IFLAG2 =  1
        DO 67177 I = -1, 1
        IF( TMIN .LT. TTMIN )  TMIN = TTMIN
67177   T(I+2) = TMIN + FLOAT(I)*DELT
        STEPSIZE = 2.*STEPSIZE
        DO 60255 I = 1, 3
60255   STEP(I) = STEPSIZE*DIR(I)
        GO TO 7021
C
C   ITERATION HAS LED BEYOND INDICATED RANGE.
7023    WRITE(18,7024)
7024    FORMAT(' -- but the point is out of range. ')
        END
C
C
C
        SUBROUTINE ATT3( NT, A1, B1, C1, T, TMIN, CHIMIN, ISHMIN )
C
        REAL NG,NI,NJ,KG,KIP,KJ,NU,NJFAC,KKSUMS,NITNIP1
        REAL IDPA, IDPB, IF1, NURES, NUMAX, IFF
        DIMENSION  RF(3,24), IFF(3,24), F6JPL(3,3,0:2)
        DIMENSION  KMAXG(4), KMAXJ(4), F6JPR(3,3,0:2)
        DIMENSION  DECAYPL(5000), DECAYPR(5000), ROFT(5000), T(3)
        DIMENSION  FMDPL(3,50000),FMDPR1(3),FMODPL(3),FMODPR(3)
        DIMENSION  BOLT(3), CHISQR(-1:1)
        COMMON  T3J11(0:2,-1:1,-1:1,-2:2), KFAC, DPSYM, NMAX, NSKIP,
     1     NRP1, IKMAX(0:46,4), Q2SUMLE2(-2:2), Q2SUMLE0, CT001,
     2     T0, RWIDTH, SUMD, NPTSD, AINFIN, IPOL, ITMA, IJSYM(3,4),
     3     NKSYM(0:1,4), NSYMK(0:1,4), RDPA(3), IDPA(3), RDPB(3),
     4     IDPB(3), NURES, NUMAX, MPMN, MPMX, MPMX2, STATWT(4),
     5     IDEL(4,4), EG(0:46,24,4), EIVECG(0:46,24,-46:46,4)
        COMMON /RJMS/  NI, NJ, LL, NG
        COMMON /EIG/  E(0:46,24,4), EIVEC(0:46,24,-46:46,4)
        COMMON /FILL/  F, G, H
C
        INUMAX = 0
        SQ2=SQRT(2.)
        DSQ2=1./SQ2
```

```
C
C   CALCULATE TIME RANGES
C    THE COMPUTED TIME MUST START ONE RESPONSE WIDTH
C    BEFORE T_0 (PLUS 1 CHANNEL AND EXTEND 1 CHANNEL
C    PAST THE DATA TO ALLOW FOR SHIFT.)
        IF( T0 .NE. 0. ) GO TO 67
        T0CCH = 0.
        N0 = 0
        GO TO 77
C
67      IF( T0 .LT. RWIDTH )  GO TO 68
        N0 = NRP1
        T0CCH = ( T0 - RWIDTH )/ CT001
        GO TO 77
C
68      T0CH = ( T0 + .0001 )/CT001
        N0 = INT(T0CH)
        T0CCH = T0CH - FLOAT(N0)
C
77      NPTS = NPTSD + N0 + 1
C
C   CALCULATE EIGENVALUES AND EIGENVECTORS OF THE ASYMMETRIC TOP
C
        RKA=( 2.*B1 - A1 - C1 )/( A1 - C1 )
        IF(RKA) 310,310,320
C    RKA<0 IMPLIES THE MOLECULE IS NEARER A PROLATE TOP
C      - A PROLATE TOP EIGENBASIS IS USED FOR THE EXPANSION
310     F=(RKA-1.)/2.
        G=1.
        H=(RKA+1.)/2.
        GO TO 330
C
C    RKA>0 IMPLIES THE MOLECULE IS NEARER AN OBLATE TOP
C      - AN OBLATE TOPEIGENBASIS IS USED FOR THE EXPANSION
320     F=(RKA+1.)/2.
        G=-1.
        H=(RKA-1.)/2.
330     CONTINUE
C
        CALL ATEIG(NMAX,A1,B1,C1)
        DO 22 N=0,NMAX+1
        KGMX=4
        NN=N
        IF(N.EQ.0) KGMX=1
        IF(N.EQ.1) KGMX=3
        DO 22 KGRP=1,KGMX
        IKM=IKMAX(N,KGRP)
        PM=-1.
        IF(KGRP.EQ.1.OR.KGRP.EQ.3) PM=1.
C
C   GET SYMMETRIC TOP COEFFICIENTS FROM + AND - COMBINATIONS
```

```
C   AND CONVERT THE IK INDEX TO SYMMETRIC TOP K VALUES
        DO 26 ITAU=1,IKM
        EIVEC(NN,ITAU,0,4)=0.
        DO 26 IIK=1,IKM
        IK=IKM+1-IIK
        K=2*IK-1
        IF(KGRP.EQ.1) K=2*(IK-1)
        IF(KGRP.EQ.4) K=2*IK
        IF(KGRP.EQ.1.AND.IK.EQ.1)  GO TO 28
        GO TO 27
28      EIVEC(NN,ITAU,0,1)= EIVEC(NN,ITAU,1,1)
        EIVEC(NN,ITAU,1,1)=0.
        GO TO 26
27      TEMP = DSQ2*EIVEC(NN,ITAU,IK,KGRP)
        EIVEC(NN,ITAU,-K,KGRP) = PM*TEMP
        EIVEC(NN,ITAU,K,KGRP) = TEMP
26      CONTINUE
        TMX = IKMAX(NN,KGRP)
22        CONTINUE
C
C   ZERO ELEMENTS OF UNDEFINED KGROUPS (NECESSARY?)
        DO 35 ITAU = 1, (NMAX+1)/2 + 1
        DO 35 K = -1*(NMAX + 1), NMAX + 1
        EIVEC(0,ITAU,K,2)=0.
        EIVEC(0,ITAU,K,3)=0.
        EIVEC(0,ITAU,K,4)=0.
35      EIVEC(1,ITAU,K,4)=0.
C
        DO 6201 JT = 1, NT
           DO 620 I=1,50000
620           FMDPL(JT,I)=0.
6201       FMDPR1(JT)=0.
C
        EMAX = EG(NMAX+1,1,1)
C
C     CYCLE THROUGH ALL GROUND STATE LEVELS AND THEIR TRANSITIONS
C
        DO 305 NNG=0,NMAX,NSKIP
        NMIN=NNG-1
        IF(NNG.EQ.0) NMIN=1
        NG=FLOAT(NNG)
        NGEO = JMOD(NNG,2)
C
C    SET HIGHEST K IN SYMMETRIC TOP EXPANSION OF
C      GROUND STATE EIGENFUNCTIONS
        KMAXG(1)= 2*IKMAX(NNG,4)
        KMAXG(2)= 2*(IKMAX(NNG,2)) - 1
        KMAXG(3)= KMAXG(2)
        KMAXG(4)= KMAXG(1)
        KKKMAX=4
        IF(NNG.EQ.1) KKKMAX=3
        IF(NNG.EQ.0) KKKMAX=1
C
```

```
C    DEFINE ALL CONSTANTS DEPENDING ON NG ONLY
        TWONG = NG + NG
        DEMFAC1 = 1. / SQRT( (TWONG + 3.)
     1                              *( TWONG + 2.)*( TWONG + 1.) )
        T3J00A = SQ2*( NG + 1.)*DEMFAC1
        T3J01A = SQRT( ( NG + 2.)*( NG + 1.) )*DEMFAC1
        IF( NNG .EQ. 0 )  GO TO 391
        DEMFAC2 = 1. / SQRT( ( NG + 1.)*( TWONG + 1.)*NG  )
        DEMFAC3 = 1. / SQRT( ( TWONG + 1.)*NG*( TWONG - 1.) )
        T3J00B = NG*DEMFAC3
        T3J01B =  1. / SQRT( 4.*NG + 2.)
        T3J01C = DSQ2*SQRT( NG*( NG - 1.) )*DEMFAC3
C
391     DO 305 KGRPG=1,KKKMAX
C   GET THE SYMMETRY OF THE GROUND STATE LEVEL
        ISYMG= NKSYM(NGEO,KGRPG)
C
C   GET THE SYMMETRY OF TRANSITION MOMENT ALLOWED
C     EXCITED STATE LEVELS
C       WRITE(20,8867)  ITMA, ISYMG
C8867   FORMAT( ' ITMA = ', I2, ' ISYMG = ', I2 )
        ISYMIJ= IJSYM(ITMA,ISYMG)
        EXPFAC1 = (-1)**(KMAXG(KGRPG))
C
        DO 308 ITAUG=1,IKMAX(NNG,KGRPG)
C
        ENRGY = EG(NNG,ITAUG,KGRPG)
        IF( ENRGY .GT. EMAX )  GO TO 308
C
        STNGFAC = STATWT(ISYMG)*(-1.)**NGEO  *(2.*NG+1.)
        DO 555 JT = 1, NT
555     BOLT(JT) = STNGFAC*EXP( -1.*ENRGY / ( 20.84*T(JT) ) )
C
C    FILL THE F6J, RF, AND IFF ARRAYS FOR THE CURRENT GROUND STATE
        DO 3040 NNJ = NMIN, NNG + 1
        INDEX = NNJ - NNG + 2
        NJ = FLOAT(NNJ)
C
C    THE FIRST INDEX OF F6J IS ALWAYS > OR = TO THE SECOND.
        DO 3333  NNI = NNJ, NNG + 1
           NI = FLOAT(NNI)
           INDEX2 = NNI - NNG + 2
           LMIN = 0
           IF( NNI .NE. NNJ )  LMIN = 2
           DO 3333  LL = LMIN, 2, 2
              F2 = (2.*FLOAT(LL)+1.)* T3J11(LL,0,0,0)*SIXJ(DDD)
              F6JPL(INDEX2,INDEX,LL)  = F2*T3J11(LL,0,0,0)
              F6JPR(INDEX2,INDEX,LL)  = F2*-1.*T3J11(LL,1,-1,0)
3333    CONTINUE
C
C   IS NNJ EVEN OR ODD?
        NJEO = JMOD(NNJ,2)
C       GET THE KGROUP CORRESPONDING TO THE ALLOWED IJ SYMMETRY AND
```

```
C       THE VALUE FOR NNJ
C       WRITE(20,8868)  NJEO, ISYMIJ
C8868   FORMAT( ' NJEO = ', I2, ' ISYMIJ = ', I10 )
        KGRPJ = NSYMK(NJEO,ISYMIJ)
        IF(IKMAX(NNJ,KGRPJ) .EQ. 0) GO TO 3040
C
        FAC11=1.
        IF(NNJ.EQ.NNG) FAC11=-1.
C
        EXFAC1=(-1.)**(NNJ+KMAXG(KGRPG)+1)
        EXFAC2=(-1.)**(NNG+KMAXG(KGRPG)+KFAC)
        EXFAC3=(-1.)*EXFAC2
C
        DO 3030 ITAUJ = 1, IKMAX(NNJ,KGRPJ)
C
        RF1 = 0.
        IF1 = 0.
C
        DO 303 KKG = KMAXG(KGRPG), 1, -2
C
        DO 303 KKJ = KKG - KFAC, KKG + KFAC, 2
        IF( ABS(KKJ) - NNJ )   710, 710, 303
710     KJ = FLOAT(KKJ)
        KG = FLOAT(KKG)
        IQ = KKJ - KKG
        FAC1=1.
C
        IF(IQ) 720,727,723
720     KJ = -KJ
        KG = -KG
        FAC1=FAC11
C
C     KJ = KG + 1
723     IF( NNG - NNJ ) 724,725,726
C       NJ > NG
724     T3JIG = EXFAC3*SQRT( (NG+KJ)*(NG+KJ+1) )*DEMFAC1
        GO TO 750
C       NJ = NG
725     T3JIG = FAC1* EXFAC3*SQRT( (NJ-KG)*(NJ+KG+1) )*DSQ2*DEMFAC2
        GO TO 750
C       NJ < NG
726     T3JIG = EXFAC1*SQRT( (NJ-KG)*(NJ-KG+1) )*DSQ2*DEMFAC3
        GO TO 750
C
C     FOR  KJ = KG  i.e. Q = 0 (ABSORPTION ALONG Z)
727     IF( NNG - NNJ )  728, 729, 730
C       NJ > NG
728     T3JIG = EXFAC3*SQRT( (NG-KJ+1)*(NG+KJ+1)*2.)*DEMFAC1
        GO TO 750
C       NJ = NG
729     T3JIG = EXFAC2*KG*DEMFAC2
        GO TO 750
C       NJ < NG
```

```
730     T3JIG = EXFAC1*SQRT( (NJ+KG+1)*(NJ-KG+1) )*DEMFAC3
C
750     F1 = T3JIG*
     1   EIVECG(NNG,ITAUG,KKG,KGRPG)*  EIVEC(NNJ,ITAUJ,KKJ,KGRPJ)
        IF1 = IDPA(2-IQ)*F1  + IF1
        RF1 = RDPA(2-IQ)*F1  + RF1
303     CONTINUE
        IF1 = IF1 + IF1
        RF1 = RF1 + RF1
        IF( KGRPG .NE. 1 )  GO TO 3020
C
C     KGRPG IS 1: ADD APPROPRIATE KG = 0 TERMS
        IF(KFAC)  9999, 3010, 3015
C     KFAC IS 0, IDPA = 0  --->   ADD KJ = KG = 0 TERM
3010    IF( NNG - NNJ )  3011, 3020, 3012
C       NJ > NG
3011    T3JIG = EXFAC3*T3J00A
        GO TO 3013
C       NJ < NG
3012    T3JIG = EXFAC2*T3J00B
3013    RF1 = RF1 + RDPA(2)*T3JIG*EIVECG(NNG,ITAUG,0,1)*
     1                                 EIVEC(NNJ,ITAUJ,0,KGRPJ)
        GO TO 3020
C
C     KFAC IS 1  --->  ADD KJ = 1, KG = 0 TERM
3015    IF( NNG - NNJ )  3016, 3017, 3018
C       NJ > NG
3016    T3JIG = EXFAC3*T3J01A
        GO TO 3019
C       NJ = NG
3017    T3JIG = EXFAC3*T3J01B
        GO TO 3019
C       NJ < NG
3018    T3JIG = EXFAC3*T3J01C
C
3019    F1 = T3JIG*EIVECG(NNG,ITAUG,0,1)*EIVEC(NNJ,ITAUJ,1,KGRPJ)
        IF1 = IF1 + 2.*IDPA(1)*F1
        RF1 = RF1 + 2.*RDPA(1)*F1
C
3020    RF(INDEX,ITAUJ) = RF1
        IFF(INDEX,ITAUJ) = IF1
3030    CONTINUE
3040    CONTINUE
C
C     START EXCITED STATE SUMS
        DO 302 NNJ=NMIN,NNG+1
C     IS NNJ EVEN OR ODD
        NJEO = JMOD(NNJ,2)
C   GET THE KGROUP CORRESPONDING TO THE ALLOWED
```

```
C     SYMMETRY AND THE VALUE FOR NNJ
        KGRPJ= NSYMK(NJEO,ISYMIJ)
        IF( IKMAX(NNJ,KGRPJ) .EQ. 0 )  GO TO 302
        IDELJ = IDEL(KGRPG,KGRPJ)
        NDGJ = NNJ - NNG + 2
        NJ = FLOAT(NNJ)
C
        KMAXJ(1) = 2*IKMAX(NNJ,4)
        KMAXJ(2) = 2*( IKMAX(NNJ,2) ) - 1
        KMAXJ(3) = KMAXJ(2)
        KMAXJ(4) = KMAXJ(1)
        TWONJ = NJ + NJ
        TWONJFAC = (TWONJ+4.)*(TWONJ+3.)*(TWONJ+2.)*(TWONJ+1.)
        DEMFAC4 = 1./( (TWONJ+5.)*TWONJFAC )
        IF( NNJ .EQ. 0 ) GO TO 392
        DEMFAC5 = 1./( TWONJ*TWONJFAC )
        DEMFAC6 = SQRT( (TWONJ+4.)*DEMFAC5 / (TWONJ-1.) )
C
C    EXFAC8 SHOULD BE (-1)**( NNJ + KMAXI(KGRPI) ) BUT FOR
C     DIPOLES ALONG PRINCIPLE AXES  KMAXJ(KGRPJ) = KMAXI(KGRPI) SO:
392     EXFAC7 = (-1)**( NNJ + KMAXJ(KGRPJ) )
        EXFAC8 = EXFAC7
        NJFAC = Q2SUMLE0*EXFAC7 / SQRT( TWONJ + 1.)
        F7LEOPL = F6JPL(NDGJ,NDGJ,0)*NJFAC
        F7LEOPR = F6JPR(NDGJ,NDGJ,0)*NJFAC
C
        DO 301 NNI=NNJ,NNG+1
C   IS NNI EVEN OR ODD?
        NIEO = JMOD(NNI,2)
C       GET THE KGROUP CORRESPONDING TO THE ALLOWED IJ SYMMETRY AND
C       THE VALUE FOR NNI
        KGRPI= NSYMK(NIEO,ISYMIJ)
        IF(IKMAX(NNI,KGRPI) .EQ. 0) GO TO 301
        IDELI = IDEL(KGRPG,KGRPI)
        NDGI = NNI - NNG + 2
        NI=FLOAT(NNI)
        NITNIP1 = NI*( NI + 1.)
C
        FAC33=1.
        IF(NNI.EQ.NNJ+1) FAC33=-1.
C
        F1 = FAC33 *(2.*NI+1.)*( TWONJ+1.)
C
        DO 3070 ITAUJ=1,IKMAX(NNJ,KGRPJ)
        IF( ABS( ITAUJ - ITAUG ) .GT. IDELJ )  GO TO 3070
        ITAUIMIN=1
        IF(NNI.EQ.NNJ) ITAUIMIN=ITAUJ
C
        DO 307 ITAUI=ITAUIMIN,IKMAX(NNI,KGRPI)
        IF( ABS( ITAUI - ITAUG ) .GT. IDELI )  GO TO 307
        NU = ABS(E(NNI,ITAUI,KGRPI) - E(NNJ,ITAUJ,KGRPJ))
        IF( NU .GT. NUMAX ) GO TO 307
C
```

```
3060    KKSUMS = RF(NDGI,ITAUI)*DPSYM*RF(NDGJ,ITAUJ)  -
     1                               IFF(NDGI,ITAUI)*IFF(NDGJ,ITAUJ)
C
        IF( KKSUMS ) 645,307,645
C
645     F7PL=0.
        F7PR=0.
        FAC = 2.
C
        IF( NNJ + 1 - NNI ) 780, 770, 760
C
C     THIS SEGMENT IS FOR NI = NJ
760     IF( ITAUI .NE. ITAUJ )  GO TO 656
C
C     DIAGONAL TERM APPEARS ONLY ONCE IN SUMMATION
        FAC = 1.
C      L = 0
        F7PL = F7LEOPL
        F7PR = F7LEOPR
C
C      L = 2
656     IF(NNI+NNJ-2) 604, 793, 793
793     F7 = 0.
        DO 404 KKJ=-KMAXJ(KGRPJ), KMAXJ(KGRPJ), 2
C
405     DO 504 KKIP= KKJ-MPMX2, KKJ+MPMX2, 2
        IF(ABS(KKIP)-NNI) 406,406,504
406     KIP=FLOAT(KKIP)
        KJ=FLOAT(KKJ)
        IMU = KKIP - KKJ
C
        IF( IMU ) 764, 766, 765
764     KIP=-KIP
        KJ=-KJ
C      KIP = KJ + 2
765     T3JIJ = EXFAC7* SQRT( 6*(NI-KJ-1)*(NI-KJ)*
     1                           (NI+KJ+1)*(NI+KJ+2)  )*DEMFAC6
        GO TO 790
C
C      KIP = KJ
766     T3JIJ= EXFAC7*2.*( 3.*KJ*KJ - NITNIP1 )* DEMFAC6
C
790     F7 = F7 + Q2SUMLE2(IMU)*T3JIJ*EIVEC(NNI,ITAUI,KKIP,KGRPI)*
     1                                  EIVEC(NNJ,ITAUJ,KKJ,KGRPJ)
504     CONTINUE
404     CONTINUE
        GO TO 800
C
C     THIS SEGMENT IS FOR NI = NJ + 1
770     IF(NNI+NNJ-2)  301, 7931, 7931
7931    F7 = 0.
        DO 4041 KKJ=-KMAXJ(KGRPJ), KMAXJ(KGRPJ), 2
```

```
C
      DO 5041 KKIP= KKJ-MPMX2, KKJ+MPMX2, 2
      IF(ABS(KKIP)-NNI) 4061,4061,5041
4061  KIP=FLOAT(KKIP)
      KJ=FLOAT(KKJ)
      IMU = KKIP - KKJ
      FAC3=1.
C
      IF( IMU ) 7641, 7661, 7651
7641  FAC3 = -1.
      KIP=-KIP
      KJ=-KJ
C
C      KIP = KJ + 2
7651    T3JIJ=FAC3*2.*EXFAC8* SQRT( (NJ+KIP-1)*
     1                        (NJ+KIP)*(NJ+KIP+1)* (NJ-KIP+2)*DEMFAC5 )
        GO TO 7901
C      KIP = KJ
7661    T3JIJ= EXFAC8*(-2.)*KIP*SQRT( 6*(NJ-KIP+1)
     1                                *(NJ+KIP+1)*DEMFAC5 )
C
7901    F7 = F7 + Q2SUMLE2(IMU)*T3JIJ*EIVEC(NNI,ITAUI,KKIP,KGRPI)*
     1                                  EIVEC(NNJ,ITAUJ,KKJ,KGRPJ)
5041    CONTINUE
4041    CONTINUE
        GO TO 800
C
C     THIS SEGMENT IS FOR NI = NJ + 2
780     F7 = 0.
        DO 4042 KKJ=-KMAXJ(KGRPJ), KMAXJ(KGRPJ), 2
C
        DO 5042 KKIP= KKJ-MPMX2, KKJ+MPMX2, 2
        KIP=FLOAT(KKIP)
        KJ=FLOAT(KKJ)
        IMU = KKIP - KKJ
C
        IF( IMU ) 7642, 7662, 7652
7642    KIP=-KIP
        KJ=-KJ
C     KIP = KJ + 2
7652    T3JIJ = EXFAC8* SQRT( (NJ+KIP-1)*
     1                        (NJ+KIP)*(NJ+KIP+1)*(NJ+KIP+2)*DEMFAC4 )
        GO TO 7902
C
C      KIP = KJ
7662    T3JIJ= EXFAC8* SQRT( 6*(NJ-KIP+2)*
     1                      (NJ-KIP+1)*(NJ+KIP+2)*(NJ+KIP+1)*DEMFAC4 )
C
7902    F7 = F7 + Q2SUMLE2(IMU)*T3JIJ*EIVEC(NNI,ITAUI,KKIP,KGRPI)*
     1                                  EIVEC(NNJ,ITAUJ,KKJ,KGRPJ)
5042    CONTINUE
4042    CONTINUE
C
```

```
800     F7PL = F7PL + F6JPL(NDGI,NDGJ,2) * F7
        F7PR = F7PR + F6JPR(NDGI,NDGJ,2) * F7
C       WRITE(15,8883)  NNG, KGRPG, ITAUG
C       WRITE(15,8883)  NNI, KGRPI, ITAUI
C       WRITE(15,8883)  NNJ, KGRPJ, ITAUJ, 2, F7PL, F7PR
C8883   FORMAT( 1X, 4I4, 2F10.5 )
604     CONTINUE
        IF(F7PL) 560,307,560
C
560     INU=NINT(NU/NURES) +1
        IF(INU .GT. INUMAX)  INUMAX = INU
        DO 610 JT = 1, NT
           RRR = EXPFAC1*KKSUMS*F1*BOLT(JT)*FAC
           FMDPL(JT,INU) = FMDPL(JT,INU) + RRR*F7PL
610        IF( INU .EQ. 1 )  FMDPR1(JT) = FMDPR1(JT) + RRR*F7PR
C
307     CONTINUE
3070    CONTINUE
301     CONTINUE
302     CONTINUE
308     CONTINUE
305     CONTINUE
C
C   WE USE A FREQUENCY RESOLUTION OF (NURES) GHZ AND
C     A MAXIMUM OF (NUMAX) GHZ
        CONSTANT= 6.283185*CT001*NURES
C
        WRITE(22,8862)  T0, A1, B1, C1
8862    FORMAT( ' For T_0 = ', F7.3, ' and constants : ',
     1                                          3( F7.5, 2X ))
C
C   TRANSFORM TO TIME DOMAIN AND GET CHI-SQUARED FOR EACH
C     TEMPERATURE ( AND THREE SHIFT VALUES ( -1, 0, 1 ) IF NT = 3 )
        CHIMIN = 10000000000.
        DO 623 JT = 1, NT
C
        DO 621 I=1, NPTS
621     DECAYPL(I)=0.
C
        YMAX = 0.
        DO 602 J = 2, INUMAX
        IF( FMDPL(JT,J) .EQ. 0. ) GO TO 602
        OMEGA = FLOAT( J - 1 )*CONSTANT
        DO 605 I = 1, NPTS
605        DECAYPL(I) = DECAYPL(I) + FMDPL(JT,J)*
     1                          COS( OMEGA*( TOCCH + FLOAT(I-1) ) )
602     CONTINUE
C
C    CALCULATE DECAYS AND CONVOLUTE
        DO 2706 I = 1, NPTS
        DECAYPR(I) = -0.5*DECAYPL(I) + FMDPR1(JT)
```

```
2706     DECAYPL(I) = DECAYPL(I) + FMDPL(JT,1)
         CALL CONVOL( DECAYPR, NPTS )
         CALL CONVOL( DECAYPL, NPTS )
C        WRITE(20,8864)
C8864    FORMAT( // )
C        WRITE(20,8865)  ( DECAYPL(I), I = 1, NPTS )
C
         IF( IPOL - 1 )   2101, 2201, 2001
C
C     IPOL = 2  -- CALCULATE R(T)
C     DETERMINE NORMALIZATION TO MATCH DATA
2001     SUMSIM = 0.
         DO 2002 I = 1 + NO, NPTSD + NO
2002     SUMSIM = SUMSIM + ( DECAYPL(I) - DECAYPR(I))/
     1                              ( DECAYPL(I) + 2.*DECAYPR(I) )
         RINFIN = SUMSIM/NPTSD
         AINFINSIM = ( 1 + 2.*RINFIN )/( 1. - RINFIN )
         SCALEFAC = AINFINSIM/AINFIN
         III = 0
         IF( NT .EQ. 3 ) III = 1
         DO 1234 IA = -III, III
         SCALE = SCALEFAC*FLOAT(1000 + IA)/1000.
         DO 706 I = 1, NPTSD + 2
C   NO MUST ALWAYS BE GREATER THAN 1
         IARG = NO + I - 1
706      ROFT(I) = (DECAYPL(IARG) - SCALE*DECAYPR(IARG))/
     1                 (DECAYPL(IARG) + 2.*SCALE*DECAYPR(IARG))
C        WRITE(20,8865)  ( ROFT(I), I = 1, NPTSD + 2 )
C
         DO 7007 ISH = -III, III
         CHISQR(ISH) = FCHI(ISH,ROFT,NPTSD)
         IF( CHISQR(ISH) .GT. CHIMIN )  GO TO 7007
         CHIMIN = CHISQR(ISH)
         ISHMIN = ISH
         TMIN = T(JT)
7007     CONTINUE
         WRITE(22,8863)  T(JT), IA,
     1                     ( ISH, CHISQR(ISH), ISH = -III, III )
8863     FORMAT(  '   T = ', F5.2, ', Scale index = ', I2 /
     1       3('      Shift = ', I2, ',    chi-squared = ', F12.6 /))
1234     CONTINUE
         GO TO 623
C
C   PREPARE TO CALCULATE CHI-SQUARED BASED ON PARALLEL DECAYS
C   BY NORMALIZING THE SIMULATION.
2101     CONTINUE
         SUMSIM = 0.
         DO 2111 I = 1 + NO, NPTSD + NO
2111        SUMSIM = SUMSIM + DECAYPL(I)
         SCALEFAC = SUMD/SUMSIM
C        WRITE(21,8859) NO, NPTSD, NPTS, SUMD, SUMSIM, SCALE
C8859    FORMAT( ' NO, NPTSD, NPTS: ', I2, 2I4 /
C     1                  ' DATA, SIM, RATIO ',  2F15.3, F12.4 )
         III = 0
         IF( NT .EQ. 3 ) III = 1
         DO 2345 IA = -III, III
         SCALE = SCALEFAC*FLOAT(1000 + IA)/1000.
         DECAYPR(1) = 0.
         II = 2
         IF( NO .GE. 1 )  II = 1
         DO 2121 I = II, NPTSD + 2
2121        DECAYPR(I) = DECAYPL(NO+I-1)*SCALE
C        WRITE(20,8865)  ( DECAYPR(I), I = 1, NPTSD + 2 )
C8865    FORMAT( 8( 1X, F9.2 )/ )
C
         III = 0
         IF( NT .EQ. 3 ) III = 1
         DO 707 ISH = -III, III
         CHISQR(ISH) = FCHI(ISH,DECAYPR,NPTSD)
         IF( CHISQR(ISH) .GT. CHIMIN )  GO TO 707
         CHIMIN = CHISQR(ISH)
         ISHMIN = ISH
         TMIN = T(JT)
707      CONTINUE
         WRITE(22,8863)  T(JT), IA,
     1                     ( ISH, CHISQR(ISH), ISH = -III, III )
2345     CONTINUE
         GO TO 623
C
2201     WRITE(18,2202)
2202     FORMAT( ' No perpendicular fit segment written. ' )
         STOP
C
623      CONTINUE
         RETURN
C      THIS SEGMENT IS NOT REACHED UNLESS SOMETHING ISN'T WORKING.
9999     WRITE(18,999)
999      FORMAT( ' IRREGULAR TERMINATION AT LINE 9999.' )
         STOP
         END
C
C
         SUBROUTINE CONVOL(Y,NPTS)
C     CONVOLUTES THE CALCULATED FILES AND INPUT RESPONSE, WITH NO
C     DECAY. CONVOLUTED DATA IS RETURNED IN Y ARRAY.
C
         DIMENSION Y(5000),YI(5000)
         COMMON /CONVOL/ NR, R(500)
C
         DO 10 I = 1, NPTS
           YI(I)=0.
C
           IF( I .LT. NR )  GO TO 8
           DO 7 J = 1, NR
```

```
7          YI(I) = R(J)*Y(I-J+1)  + YI(I)
         GO TO 10
C
8        DO 9 J = 1, I
            YI(I)=R(J)*Y(I-J+1)  + YI(I)
9        CONTINUE
10     CONTINUE
       DO 15 I = 1, NPTS
15        Y(I) = YI(I)
C
       RETURN
       END
C
C
       FUNCTION FCHI(ISH,Y,N)
C   CALCULATES CHI-SQUARED USING WEIGHTS FROM THE  FILE SIGDEM
       DIMENSION   Y(5000)
       COMMON /CHI/  D(5000), SIGDEM(5000)
       CHITEMP = 0.
       DO 707 I = 1, N
707       CHITEMP = CHITEMP + ( Y(I+ISH+1) - D(I) )**2 / SIGDEM(I)
       FCHI = CHITEMP
       RETURN
       END
C
C
       SUBROUTINE ATEIG(NMAX,A1,B1,C1)
       DIMENSION A(4,29,29), ASYM(500), ALPHA(29,29), ESTATE(29),
    1   WK(500), IMAX(4)
       COMMON /EIG/  E(0:46,24,4), EIVEC(0:46,24,-46:46,4)
C
       DO 10 N = 0, NMAX + 1
C      WRITE(25,443)  N
C443   FORMAT( /'        N = ', 2X, I4 )
       FAC2=0.5*(A1-C1)
       FAC1=0.5*(A1+C1) * FLOAT(N*(N+1))
       IMAX(4)=INT(FLOAT(N)/2.)
       IMAX(2)=INT(FLOAT(N+1)/2.)
       IMAX(3)=IMAX(2)
       IMAX(1)=IMAX(4)+1
C
       KKKMAX=4
       IF(N.EQ.0) KKKMAX=1
       IF(N.EQ.1) KKKMAX=3
C
C  ZERO ALL ELEMENTS OF A
       DO 11 IKGRP = 1, KKKMAX
       IMX=IMAX(IKGRP)
       DO 1 I=1,IMX
       DO 1 J=1,IMX
1      A(IKGRP,I,J)=0.
11     CONTINUE
C
C   GET INITIAL MATRIX ELEMENTS
       NN=N
       CALL FILLMAT(NN,A)
C
C   DIAGONALIZE EACH OF THE FOUR SUBMATRICES REPRESENTING THE FOUR
C    ASYMETRIC TOP SYMMETRY CLASSIFICATIONS.
       DO 3, IKGRP=1,KKKMAX
C      WRITE(25,444)  IKGRP
C444   FORMAT( /' IKGRP = ', I2 )
       IMX=IMAX(IKGRP)
       IJ=0
C
C    PUT THE MATRIX FOR THE PARTICULAR IKGRP AND N IN SYMMETRIC
C     STORAGE MODE
       DO 5 I=1,IMX
       DO 5 J=1,I
       IJ=IJ+1
5      ASYM(IJ)=A(IKGRP,I,J)
C      ZERO THE EIGENVALUES  AND EIGENVECTORS
       DO 6 I=1,IMX
       ESTATE(I)=0.
       DO 6 J=1,IMX
6      ALPHA(I,J)=0.
C
C   DIAGONALIZE THE MATRIX
       CALL EIGRS(ASYM,IMX,2,ESTATE,ALPHA,29,WK,IER)
C   THE EIGENVECTORS ARE NORMALIZED (THEY ARE IN COLUMN FORM)
C
C      WRITE(25,445)   WK(1), IER
C445   FORMAT( F10.5, 2X, I5 )
C
C    CONVERT THE EIGENVALUES TO ACTUAL ENERGIES BY MULTIPLYING BY
C     (A-C)/2 AND ADDING .5*(A+C)*N*(N+1)C AND STORE THE CALCULATED
C     VALUES IN THE E AND EIVEC ARRAYS.
       DO 7 I = 1, IMX
       E(N,I,IKGRP) = ESTATE(I)*FAC2 + FAC1
       DO 7 J = 1, IMX
       EIVEC(N,I,J,IKGRP) = ALPHA(J,I)
7      CONTINUE
C      WRITE(25,457) ( E(N,I,IKGRP), I = 1, IMX )
C457   FORMAT( 6F13.5 )
C
3      CONTINUE
10     CONTINUE
       RETURN
       END
C
C
C
       SUBROUTINE FILLMAT(J,A)
C
C   ONLY THE LOWER TRIANGULAR ELEMENTS NEED TO BE FILLED. ELEMENTS
```

```
C     OF IKGRP'S 4 AND 2 ARE DERIVED FROM 1 AND 2, RESPECTIVELY.
        DIMENSION A(4,29,29)
        COMMON /FILL/  F, G, H
C
        RJJP1 = FLOAT( J*(J+1) )
        DO 10 IKGRP=1,2
        ISTART=1
        IF(IKGRP.EQ.1) ISTART=0
        ND=0
C
C   I IS THE K QUANTUM NUMBER OF CONTRIBUTING
C     SYMMETRIC TOP BASIS FUNCTIONS
        IF(ISTART.GT.J) GO TO 10
        DO 5 I=ISTART,J,2
           ND=ND+1
           A(IKGRP,ND,ND)= F*RJJP1 + (G-F)*FLOAT(I*I)
           JK=ND+1
C    CALCULATE THE OFF-DIAGONAL ELEMENT IF IN RANGE
           IF(I+2.GT.J) GO TO 20
           A(IKGRP,JK,ND)=0.5*H*  SQRT( FLOAT(J*(J+1) - (I+1)*(I+2))*
     1                                  FLOAT(J*(J+1) - (I+1)*I) )
5       CONTINUE
C
20      IF(IKGRP .EQ. 1)  GO TO 30
C
C   COPY A(IKGRP=2) TO A(IKGRP=3) AND ADJUST  FIRST ELEMENT OF BOTH
        DO 25 ND = 1, (J-1)/2
           JK = ND + 1
           A(3,JK,JK) = A(2,JK,JK)
25         A(3,JK,ND) = A(2,JK,ND)
        FAC = (0.5*H*RJJP1)
        A(3,1,1) = A(2,1,1) + FAC
        A(2,1,1)= A(2,1,1) - FAC
        GO TO 10
C
C   CHANGE A(1,2,1) AND FILL A(IKGRP=4)
30      A(1,2,1)= A(IKGRP,2,1)*SQRT(2.)
        DO 35 ND = 1, J/2 - 1
           JK = ND + 1
           A(4,JK,JK) = A(1,JK+1,JK+1)
35         A(4,JK,ND) = A(1,JK+1,JK)
        A(4,1,1) = A(1,2,2)
10      CONTINUE
        RETURN
        END
C
        FUNCTION SIXJ(DDD)
        REAL NJ,NI,NG
        COMMON /RJMS/  NI, NJ, LL, NG
        IF( LL-2 ) 102,2,2
2       S=NI+NJ+2.
        A=NI
        B=NJ
        C=2.
        D=NG
        GO TO 103
102     S=NI+NG+1.
        A=NI
        B=NG
        C=1.
        D=NJ
103     IF(B-D) 201,202,203
C
202     SIXJ=((-1)**(INT(S)))*SQRT(  (S+1)*(S-2*A)*(S-2*B)*(S-2*C+1)
     1               / ( B*(2*B+1)*(2*B+2)*(2*C-1)*2*C*(2*C+1)  ) )
        RETURN
C
203     SIXJ=((-1)**(INT(S)))*SQRT(  S*(S+1)*(S-2*A-1)*(S-2*A)
     1                / ((2*B-1)*2*B*(2*B+1)*(2*C-1)*2*C*(2*C+1))  )
        RETURN
C
201     SIXJ=((-1)**(INT(S)))*SQRT(  (S-2*B-1)*(S-2*B)*(S-2*C+1)*
     1     (S-2*C+2)/((2*B+1)*(2*B+2)*(2*B+3)*(2*C-1)*2*C*(2*C+1))  )
        RETURN
        END
```